Next Generation Photovoltaic Modules: Visualizing Deflection and Analyzing Stress

by

Xiaodong Meng

A Dissertation Presented in Partial Fulfillment
of the Requirements for the Degree
Doctor of Philosophy

Approved September 2019 by the
Graduate Supervisory Committee:

Mariana Bertoni, Chair
Zachary Holman
Terry Alford
Rico Meier

ARIZONA STATE UNIVERSITY

December 2019

ABSTRACT

Stress-related failure such as cracking are an important photovoltaic (PV) reliability issue since it accounts for a high percentage of power losses in the midlife-failure and wear-out failure regimes. Cell cracking can only be correlated with module degradation when cracks are of detectable size and detrimental to the performance. Several techniques have been explored to access the deflection and stress status on solar cell, but they have disadvantages such as high surface sensitivity.

This dissertation presents a new and non-destructive method for mapping the deflection on encapsulated solar cells using X-ray topography (XRT). This method is based on Bragg diffraction imaging, where only the areas that meet diffraction conditions will present contrast. By taking XRT images of the solar cell at various sample positions and applying an in-house developed algorithm framework, the cell‘s deflection map is obtained. Error analysis has demonstrated that the errors from the experiment and the data processing are below 4.4 and 3.3%.

Von Karman plate theory has been applied to access the stress state of the solar cells. Under the assumptions that the samples experience pure bending and plain stress conditions, the principal stresses are obtained from the cell deflection data. Results from a statistical analysis using a Weibull distribution suggest that 0.1% of the data points can contribute to critical failure. Both the soldering and lamination processes put large amounts of stress on solar cells. Even though glass/glass packaging symmetry is preferred over glass/backsheet, the solar cells inside the glass/glass packaging experience significantly more stress. Through a series of in-situ four-point bending test, the assumptions behind Von Karman theory are validated for cases where the neutral plane is displaced by the tensile and compressive stresses.

The deflection and stress mapping method is applied to two next generation PV concepts named Flex-circuit and PVMirror. The Flex-circuit module concept replaces traditional metal ribbons with Al foils for electrical contact and PVMirror concept utilizes a curved PV module design with a dichroic film for thermal storage and electrical output. The XRT framework proposed in this dissertation successfully characterized the impact of various novel interconnection and packaging solutions.

ACKNOWLEDGMENTS

First of all, I would like to give my deepest gratitude to my supervisor Dr. Mariana Bertoni. Not only she is such a great professor and mentor with tons of inspiring ideas for my research all the time, but also she has been a wonderful friend for the past five years. I really appreciate the guidance, patience, encouragement that she has offered to me. Most of the credit in this work goes to her.

Secondly, I would like to thank Dr. Zachary Holman, who offered me important roles in several of his projects and funded most of my work. I admire his critical way of thinking and it has been a great pleasure to work with him. A huge thank you goes to my other committee member Dr. Rico Meier and Dr. Terry Alford who provided insightful advice to my research and constructive feedback to this dissertation.

A special thank you goes to former postdocs Dr. Laura Ding and Dr. Michael Stuckelberger who spent their valuable time to guide me and kept me on track in the first few years. My first paper will not be published without them. I would like to thank Kathryn Fisher and Dr. Zhengshan Yu in Holman's group for their support in module fabrication and characterization. I also would like to thank Bill Dauksher at SPL who kept the laminator in good condition.

Thanks to Duncan Harwood at D2 Solar who provided a precious summer internship experience to me. Thanks to Myles Steiner, Kaitlyn VanSant and all other the staffs at NREL during HOPE workshop for showing me the state-of-art solar cells and PV module fabrication and characterization.

I am very grateful to be a member of the diverse DEfECT Lab. I would like to thank all DEfECTers for their unlimited support on providing samples, refining my presentations, correcting errors in my writing, and most importantly, drinking beers with me. You guys are the best.

Finally, I would like to express great thanks to my family. My parents offered unconditioned support in pursuing a PhD degree abroad, from initial decision making to my defense. A special shout-out to my 'chinese gang' who explore wonderful things with me in the US.

TABLE OF CONTENTS

Page

LIST OF TABLES viii

LIST OF FIGURES ix

CHAPTER

1 INTRODUCTION 1
    1.1 Silicon Based PV Modules 1
    1.2 Stress-Related Degradation in PV Modules 5
    1.3 Stress Characterization on Silicon Cell/Wafer 8
    1.4 Motivation and Goals 13
2 BACKGROUND ON X-RAY TOPOGRAPHY 15
    2.1 X-Ray Source 15
    2.2 X-ray Topography Theory 17
    2.3 Topography Contrast Imaging 19
3 VISUALIZING CELL DEFLECTION BY X-RAY TOPOGRAPHY 25
    3.1 Cell Deflection Calculation Model 26
    3.2 XRT Measurement Procedure 30
        3.2.1 Measuring $\leq$ 3” Solar Cells 32
        3.2.2 Measuring 6” Solar Cells 34
    3.3 Data Processing 35
        3.3.1 $K_{\alpha 1}$ Extraction Varied by Encapsulation 35
        3.3.2 Stacking $K_{\alpha 1}$ Signals and Interpolation 40
        3.3.3 ω Map to Deflection Map Varied by Tabbing 41
    3.4 Application Results and Discussion 46
        3.4.1 Example 1: Deflection Validation 48
        3.4.2 Example 2: Lamination Temperature 49

3.4.3 Example 3: Lamination Stack 52
3.4.4 Example 4: Accelerated Tests 53
4 ERROR AND SENSITIVITY ANALYSIS 55
4.1 Error Estimation 55
4.1.1 Error from Measurement 56
4.1.2 Error from Data Processing 57
4.2 Sensitivity Analysis 59
4.2.1 Number of X-ray Sweeps on Each XRT Image 61
4.2.2 Number of X-ray Raw Images 63
4.2.3 $K_{\alpha 2}$ Diffraction Lines 65
4.2.4 Distance between $K_{\alpha 1}$ Lines and $K_{\alpha 2}$ Lines 70
5 BENDING STRESS ANALYSIS ON ENCAPSULATED SOLAR CELLS 73
5.1 Thin Plate Bending Theory 73
5.2 Examples and Applications 77
5.2.1 Principal Stresses and Probability of Failure 79
5.2.2 Impact of Soldering, Lamination, and Damp Heat Testing .. 84
5.2.3 Stress-Electrical Performance Correlation 86
5.2.4 Impact of Stack, Encapsulant, and Glass Thickness 87
6 FROM BENDING STRESS TO ABSOLUTE STRESS 93
6.1 Four-Point Bending Theory 93
6.2 Setup Design and Modeling 94
6.2.1 In-situ Four-Point Bending Setup 94
6.2.2 Finite Element Analysis 98
6.2.3 Bending Distance Correction 99

- 6.3 Results and Discussion 100
  - 6.3.1 One-layer System: Bare Silicon Wafer 100
  - 6.3.2 Two-layer System: Silicon/Aluminum 102
  - 6.3.3 Three-layer System: Aluminum/Silicon/Aluminum 104

7 FLEX-CIRCUIT: MONOLITHIC SI MODULE WITH ALUMINUM FOIL 107
- 7.1 Introduction of Flex-Circuit Concept 107
- 7.2 Module Fabrication 110
- 7.3 Reliability Characterization and Lamination Optimization 114
- 7.4 Stress of Different Module Configurations 122

8 PVMIRROR: CURVED PV MODULES WITH STORAGE CAPABILITY 128
- 8.1 Introduction of PVMirror Concept 128
- 8.2 Module Fabrication 132
- 8.3 Optical Characterization and Lamination Optimization 138
- 8.4 Electrical Performance and Upscaling Capability 146

9 CONCLUSIONS 154

REFERENCES 157

APPENDIX

A SUMMARY OF ACHIEVEMENT 166

LIST OF TABLES

Table Page

1.1 Summary of the Deflection/Stress Determination Methods. 13

3.1 X-ray Transmittance through Different PV Components. 38

4.1 List of 10 $\omega_{\mathrm{sweep,n}}$ Angles Corresponding to $K_{\alpha1}$ and $K_{\alpha2}$ Signals. 68

4.2 List of 5 $\omega_{\mathrm{sweep,n}}$ Angles Corresponding to $K_{\alpha1}$ and $K_{\alpha2}$ Signals. 70

5.1 Sample List of Modules for Stress Analysis. 79

5.2 Max, Mean and Min of the Top 0.1% $\sigma_{\mathrm{b,1}}$ Values of Six PERC Modules. 91

6.1 List of Thickness Values of Four Silicon Wafer and Sputtered Al. 96

6.2 List of FEA Simulated and Von Karman σ_1 Values of Si Samples. 101

6.3 List of FEA Simulated and Von Karman σ_1 Values of Si/Al Samples. . . 103

6.4 List of FEA Simulated and Von Karman σ_1 Values of Al/Si/Al Samples. 105

8.1 Sample List of All PVMirror Modules in This Dissertation. 139

LIST OF FIGURES

Figure Page

1.1 Scheme of a Typical Crystalline Silicon PV Module Layout. 2

1.2 The Temperature and Pressure Profile of a PV Encapsulation Cycle. . . 5

1.3 Typical Failure Modes of Crystalline Wafer-based Photovoltaic Modules. 6

1.4 EL Images of a Cracked Solar Cell under Differently Biased Currents. . . 9

1.5 Scheme of a Laminate Prepared for DIC Measurement. 10

1.6 Stress Map of a Silicon Solar Cell by Raman. 11

1.7 FEA Modeled Stress of a Standard PV Module. 12

2.1 Historical Evolution of the Peak Brilliance in Various X-ray Sources. . . . 16

2.2 X-ray Radiation Spectrum from a Molybdenum Target. 17

2.3 Diagram of Bragg's Diffraction under Normal Condition. 18

2.4 Sketch of White Beam Topography using Synchrotron Light Source. . . . 18

2.5 Sketch of Lang Topography in Transmission Geometry (Laue Case). . . . 20

2.6 Sketch Illustrating Extinction Contrast Formation in XRT Images. 21

2.7 Diagram of Bragg Diffraction in Distorted Crystal Lattices. 22

2.8 A Typical Raw XRT Image from a Bent Solar Cell. 23

2.9 Comparison in XRT Images between Flat and Bent Solar Cells. 24

3.1 Schematic of the ω to Deflection Calculation Method. 28

3.2 Photo of the HITACHI Rigaku XRT-100 Used in This Dissertation. . . . 30

3.3 Sketch of Side View of Sample and X-ray Detector in the XRT System. 32

3.4 A Set of Raw XRT Images Collected at Different ω_{sweep} Values. 33

3.5 Photo of the Designed Sample Holder for 6" Solar Cell Measurement. . . 35

3.6 Flow Chart Used for Data Processing of Every XRT Image. 36

3.7 Difference between Skeletonizing and Thinning on Binary Images. 37

3.8 Data Process Flow on Cells without Encapsulation. 37

Figure Page

3.9 Data Process Flow for Encapsualted Solar Cells. 39

3.10 Demonstration of Stacking $K_{\alpha 1}$ Lines and Interpolation of ω Values. . . . 40

3.11 EL and XRT Image of a PERC Silicon Solar Cell. 42

3.12 ω and Deflection Maps of Three Separately Processed Solar Cells. 43

3.13 Data Processing on Soldered Solar Cell Using Global References. 44

3.14 Data Processing on Soldered Solar Cell Using Busbar References. 45

3.15 Photo and Cross-section of a Partially Soldered and Encapsulated Cell. 46

3.16 Deflection Comparison between Three Proposed Methods. 47

3.17 Scheme of Sample Used for Deflection Calculation Validation. 48

3.18 Validation of XRT Analyzed Deflection Maps with Profilometry. 50

3.19 Correlation between Cell Deflection and Lamination Temperature. 51

3.20 Correlation between Cell Deflection and Lamination Stack. 52

3.21 Correlation between Cell Deflection and DH1000 Test. 53

4.1 Four Deflection Maps Showing the Errors from Measurement. 57

4.2 Standard Deviations of Deflection from Four Measurements. 58

4.3 Four Deflection Maps Showing the Errors from Data Processing. 59

4.4 Standard Deviation of Deflection from the Same Measurement. 60

4.5 Photo of Image Plate and Replaced Semiconductor X-ray Detector. 60

4.6 Three Raw XRT Images Taken with Different Number of X-ray Sweeps. 62

4.7 Five Deflection Maps by Different Number of X-ray Sweeps. 62

4.8 Mean Deviation of Deflection as a Function of Number of X-ray Sweeps. 63

4.9 Six Deflection Maps by Different Number of Images. 64

4.10 Mean Deviation of Deflection as a Function of Number of XRT Images. 65

4.11 Raw XRT Images Taken at Two ω_{sweep} Angles. 66

4.12 Deflection Maps Processed with $K_{\alpha1}$ and/or $K_{\alpha2}$ from 10 XRT Images. 67

4.13 Mean Deviations of the Three Deflection Maps Against Reference...... 68

4.14 Deflection Maps Processed with $K_{\alpha1}$ and/or $K_{\alpha2}$ from 5 XRT Images... 69

4.15 Mean Deviations of the Three Deflection Maps Against Reference...... 70

4.16 XRT Raw Image of a Silicon Wafer and a Cross-section Line. 71

4.17 XRT Raw Image of an Encapsulated Cell and a Cross-section Line..... 72

5.1 Statistical Analysis on the Direction of Cell Cracks. 73

5.2 Scheme of a Silicon Wafer Cross-section Showing Stress Distribution. .. 74

5.3 Lamination Stacks of Six Full-size 6” PV Modules. 78

5.4 Photos of Six 6” PERC PV Modules.................................. 79

5.5 Deflection and Component Stresses in PERC-S1...................... 80

5.6 Diagram of Component Stresses and Principal Stresses............... 81

5.7 $\sigma_{\mathrm{b},1}$ and $\sigma_{\mathrm{b},2}$ Maps of PERC-S1. 81

5.8 Histogram of Stress Values and Probability of Failure of PERC-S1. 82

5.9 Cross-section View of the Deflection, $\sigma_{\mathrm{b},1}$ and $\sigma_{\mathrm{b},2}$ Maps of PERC-S1. . 83

5.10 $\sigma_{\mathrm{b},1}$ Stress Map of PERC-S1 after Each Process. 84

5.11 Maximum and Top 0.1% $\sigma_{\mathrm{b},1}$ Values in SHJ-S1...................... 85

5.12 $\sigma_{\mathrm{b},1}$ Maps, EL Images and Series Resistance Maps of Two Mini-modules. 87

5.13 Experimental and Fitted Relationship Between Rs and $\sigma_{\mathrm{b},1}$........... 87

5.14 Stress Distribution inside Glass/Backsheet and Glass/Glass PV Modules. 88

5.15 $\sigma_{\mathrm{b},1}$ Maps of Six PERC 6” PV Modules. 89

5.16 Histogram of the $\sigma_{\mathrm{b},1}$ Values ($\geq$100 MPa) in Six 6” PERC Modules. ... 90

5.17 Distribution of Top 0.1% $\sigma_{\mathrm{b},1}$ Values in Six 6” PERC Modules......... 91

5.18 $\sigma_{\mathrm{b},2}$ Maps of Six PERC 6” PV Modules. 92

Figure Page

6.1 Scheme of Four-point Bending Setup and Anticipated Stress Distribution. 94
6.2 SolidWorks Drawing and Photos of Four-point Bending Holder. 95
6.3 Photo and Diagram of Four-point Bending on Si Samples. 96
6.4 Deflection, $\sigma_{\mathrm{b},1}$ and $\sigma_{\mathrm{b},2}$ of a Bent Silicon Wafer. 97
6.5 FEA Simulated Deflection Maps of a Silicon Wafer. 99
6.6 Simulated $\sigma_{\mathrm{b},1}$ Map of a Silicon Wafer by FEA. 99
6.7 Bending Distance Correction on Deflection Maps. 100
6.8 σ_1 of Si Samples as Function of Bending Distance and Technique. 101
6.9 Photo and Diagram of Four-point Bending on Si/Al Samples. 102
6.10 σ_1 of Si/Al Samples as Function of Bending Distance and Technique. . . 103
6.11 Photo and Diagram of Four-point Bending on Al/Si/Al Samples. 104
6.12 σ_1 of Al/Si/Al Samples as Function of Bending Distance and Technique. 105
6.13 Mean σ_1 as Function of Bending Distance and Number of Al Layers. . . . 106
7.1 Predicted Ag Usage Per Solar Cell in the Next Ten Years. 108
7.2 The Front and Back Side of Zebra IBC Solar Cells. 109
7.3 Schematic of a Traditional PV Stack and Flex-circuit Module Stack. . . . 110
7.4 Schematic of a Reference Flex-circuit Lamination Process. 111
7.5 Photos of the Flex-circuit Laminate at Different Steps. 112
7.6 EL and IV Result of Flex-circuit Modules through TC200 Test. 113
7.7 Photo of a Flex-circuit Module after TC100 with Wrinkles on Al Foil. . 114
7.8 Optical and SEM Images Showing the Cause of Delamination. 115
7.9 Photos of Al Electrodes Fabricated with Different Processes. 116
7.10 Photos of Al Electrodes Fabricated with Various Encapsulants and Foils. 117
7.11 EL, PL, IV Results Demonstrating Effectiveness of Lamination Frame. . 118

7.12 Fabrication of Flex-circuit Modules Using Approach 1. 120
7.13 Fabrication of Flex-circuit Modules Using Approach 2. 121
7.14 Fabrication of Flex-circuit Modules Using Approach 3. 122
7.15 EL Images of Four Lamination Approaches Before and After TC200. . . 123
7.16 Stack of Flex-circuit and Reference Modules for Stress Analysis. 124
7.17 Deflection of Flex-circuit and Reference Modules. 125
7.18 $\sigma_{\mathrm{b},1}$ of Four Flex-circuit and Reference Modules. 126
7.19 Histogram of $\sigma_{\mathrm{b},1}$ in Four Flex-circuit and Reference Modules. 127
8.1 Schematic of the PVMirror System on a Solar Tracker. 129
8.2 Spectral Efficiency of IBC and SHJ Solar Cells and CSP. 130
8.3 Transmittance and Reflectance of the Dichroic Film and Ag. 131
8.4 Angle Dependent Reflectance and Transmittance of the Dichroic Film. . 132
8.5 Dichroic Film's Shrinkage Profile by Temperature and Cycles. 133
8.6 Raman and Optical Characterization on the Dichroic Film. 134
8.7 Peel Strength Result of Different Encapsulant on the Dichroic Film. . . . 136
8.8 Temperature Profiles of Flat and Curved Laminates during Lamination. 137
8.9 Lamination Stack of Traditional PV and PVMirror. 138
8.10 Schematic and Photo of a Reference Flat PVMirror Module. 140
8.11 Schematic of Four Lamination Approaches and Associated Flat Modules. 141
8.12 Working Principle of the Hartmann Test on Curved Surfaces. 143
8.13 Increased Shape Error Percentage in Eight Curved PVMirror Modules. 144
8.14 Shape Error Increase as a Function of Shape Error Specification. 145
8.15 Optical Loss Analysis of Extra Layer(s) of EVA in PVMirror Modules. . 146
8.16 Direct Optical Comparison of PVMirror and AgMirror. 147

8.17 Modeled and Measured Performance of a 9-cell PVMirror Module. 149
8.18 Photo and EL Image of a 144-cell Utility-scale PVMirror Module. 150
8.19 Electrical Performance of a 144-cell PVMirror Module. 150
8.20 A PVMirror Power Plant System Model and Modeled System Efficiencies. 152

Chapter 1

INTRODUCTION

1.1 Silicon Based PV Modules

Photovoltaic (PV) cells, which convert solar energy into electricity, are one of the most promising renewable energy resources. Driven by the vast source of energy provided by the sun, abundant silicon resources and continuously decreasing price, solar PV is one of the fastest growing energy technologies [1]. Due to the steady reduction in cost, solar PV had a global electricity market share of 1.5% in 2016 and this number is expected to rise to 69% by 2050 [2].

Realizing the promise of solar PV requires demonstrating its profitability, which depends on low degradation rates and high module efficiency. These factors are assessed with a metric called the levelized cost of electricity (LCOE). The LCOE of utility-scale PV was 7 cents/kWh in 2016, closing in on the Sunshot target of 3 cents/kWh by 2030 [3]. The LCOE of a PV system is defined as the lifecycle cost of a solar project divided by the lifetime energy production of the solar project [4]. It not only includes system efficiency, but also counts in module manufacturing cost, degradation rate and service lifetime. The module manufacturing cost mainly includes the cost of raw materials (e.g. silicon wafer, encapsulant, glass), production line operation, transport, and installation [5]. The service lifetime of a PV module is determined by its yearly performance - the PV module is expected to be retired when its efficiency is not conducive to profit. In general, higher module efficiency and lower degradation rates lead to higher LCOE.

$$\text{LCOE} = \frac{\text{Lifecycle cost of solar project}}{\text{Lifetime energy production of solar project}} \tag{1.1}$$

The solar cells are soldered and encapsulated into PV modules to improve reliability and achieve better integrity. A traditional glass-backsheet PV module includes the stack of glass / encapsulant / cell / encapsulant / backsheet. The current silicon module efficiency record is 24.4% [6]. A detailed lamination stack is shown in Figure 1.1. The module assembly process includes tabbing and encapsulation, which are described below.

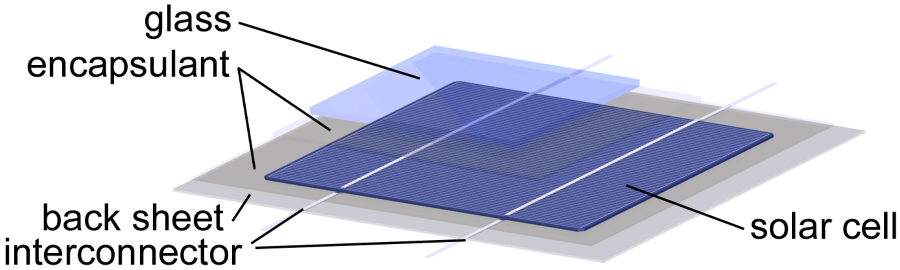

Figure 1.1: Scheme of a typical crystalline silicon PV module layout consisting of front glass, encapsulant, interconnector, solar cell, and backsheet [7].

Several types of solar cells are available on the market. Wafer based silicon solar cell technologies have dominated the PV market with more than 80% for decades [8]. Currently, back surface field (BSF) solar cells have the largest market share, with more than 70% [5]. Advanced cell technologies offering higher efficiency, including passivated emitter rear cell (PERC), silicon heterojunction (SHJ) and interdigitated back contact (IBC) silicon solar cells, are gradually penetrating the market with more sophisticated architectures like the record-breaking n-type rear IBC from Kaneka (η = 26.7%) [6; 9].

Wafer based silicon solar cells often have screen printed Ag-based fingers and are tabbed into strings before module assembly. The tabbed Cu ribbons facilitate electron extraction. The tabbing process varies by cell technology and connection type. For example, PERC cells are tabbed with metal ribbon strips directly on the front and back busbars. The SunPower IBC solar cells have both positive and negative contacts on the back such that no metal rests on the front surface. Newly developed shingle technology puts one cell on top of another and uses an electrical conductive adhesive (ECA) instead of regular metal ribbons to lower tabbing process temperature resistance.

The encapsulant adheres the glass to solar cells while offering electrical isolation to the cell and being transparent. Some of the encapsulant available on the market includes ethylene vinyl acetate (EVA), thermoplastic polyolefin (TPO), polyolefin elastomer (POE), Ionomer, polyvinyl butyral (PVB) and PDMS (polydimethyl silicone) / silicone. EVA was the most popular encapsulant in 2017 with a market share of more than 95% [5]. However, EVA's market share is decreasing as it has been found to show discoloration and PID issues in the field [10]. ITRPV predicts that polyolefin-based encapsulants are going to have an increased share of more than 25% by 2028 because of its improved reliability performance (for instance, free of potential induced degradation) [5]. Typical encapsulants come in the form of polymer sheets prior to lamination that soften and solidify during a high-temperature lamination process except the silicone, which comes in liquid format and cures at room temperature.

Solar cells and encapsulants are sandwiched between a piece of glass and a layer of backsheet to provide mechanical support and reduce water vapor transmission. The front glass is often made of low iron, tempered glass with SiO_2 anti-reflection (AR) coatings to provide high transparency and good electrical isolation while maintaining good mechanical support. A typical glass/backsheet module uses 3.1 mm thick glass in the front. Thinner glasses are becoming more and more popular to reduce material cost and weight. In 2028, more than a third of new PV modules will be made with glass between 2 and 3 mm thick [5]. The backsheet is a white polymer sheet made from tedlar-based materials like tedlar/PET/tedlar (TPT), tedlar/PET/EVA, and other PET-based materials.

A high-temperature and high-pressure lamination process is applied to assemble all layers together, which is critical to achieve high efficiency and low degradation rate. The traditional lamination cycle contains three phases as shown in Figure 1.2. In the vacuum phase, the laminate is lifted up by metal pins on the lower chamber and separated from the heating plate. The temperature of the laminate slowly increases from ambient temperature to the encapsulant's softening temperature (60–80°C). At the same time, the chamber is evacuated to eliminate air voids inside the laminate. The slow temperature ramp rate is designed to avoid glass warping issues. After 3–5 min of vacuum, the curing phase starts. The metal pins are retracted and a maximum pressure of 1 bar is gradually applied to the laminate by the upper silicone bladder. The high pressure is to further squeeze out air bubbles and facilitate homogenous heat transfer from the heating plate to the laminate. In the curing cycle, the encapsulant quickly reaches its curing temperature (130–160°C) and goes through a critical solidification process. The lamination profile (temperature and pressure over time) is tuned to obtain the desired EVA quality at the end of the lamination process. After lamination, the module is cooled down to ambient temperature and completed with an Al frame and junction box.

The lamination process is often optimized by gel content percentage and/or adhesion strength. The gel content of laminated encapsulant can be measured by differential scanning calorimetry (DSC) [11; 12]. Higher gel content indicates higher lamination quality and has been suggested to be linked to a lower degradation rate. The commonly targeted gel content is >80%. A strong adhesion to the interfaces is crucial to prevent modules from delamination. Cross-link-based materials like POE

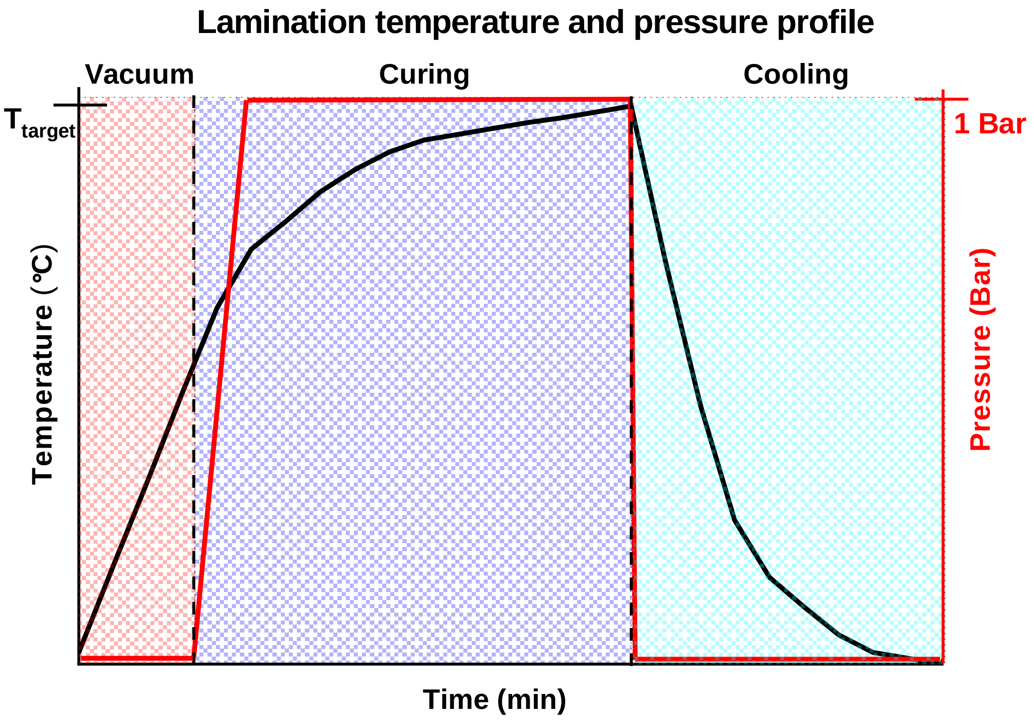

Figure 1.2: The temperature and pressure profile of a representative PV encapsulation cycle. The black and red lines represent the measured temperature and pressure on the laminate [11].

and EVA form strong chemical bonds to the interfaces, which offer stronger adhesion than non-cross-linked materials like TPO and ionomer. The latter materials rely on thermoplastic bonding characteristics that use ionic, hydrogen, and/or Van der Waals forces for adhesion [13]. For that reason, EVA and POE are the encapsulants preferred by the market.

1.2 Stress-Related Degradation in PV Modules

During the course of operation, PV modules are susceptible to degradation depending on the module's working environment, material quality, manufacturing process, installation. The median PV module degradation rate is currently 0.5%/yr obtained from 2000 modules in the field [14]. The degradation of PV modules in the field can be caused by multiple stressors. Figure 1.3 shows the typical failure modes of crystalline wafer-based PV modules at different stages of operation lifetime [15]. The total power output of the module is the integrated area under the power curve. As we can see, failure modes such as cell interconnect breakage can greatly impact the power output in short amounts of time and suddenly render the PV module useless. By contrast, failure modes such as glass AR coating degradation and light-induced degradation (LID) slowly degrades the module efficiency throughout its whole lifetime.

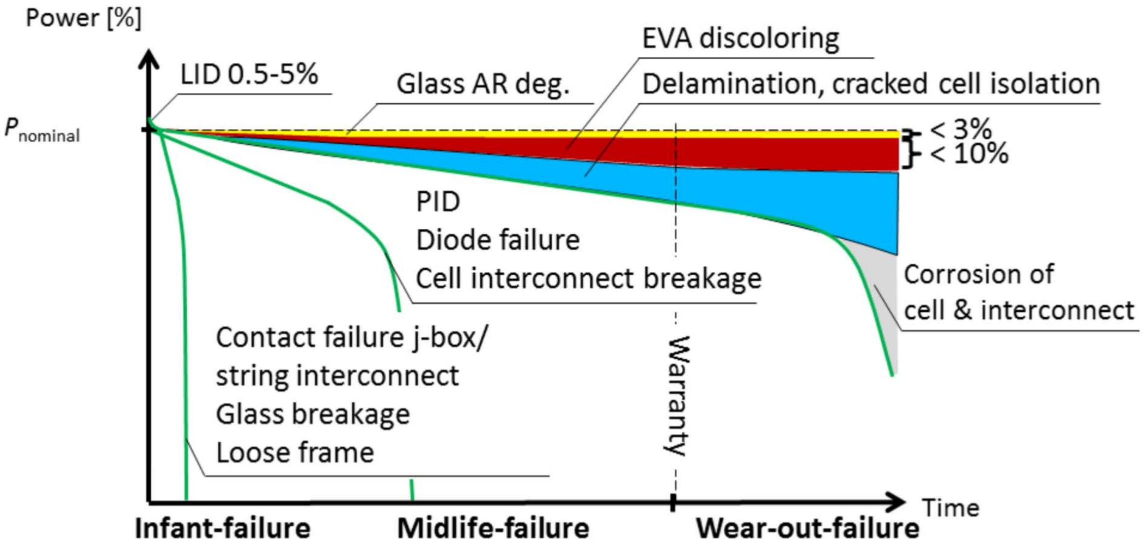

Figure 1.3: Typical failure modes of crystalline wafer-based photovoltaic modules at different stages of service lifetime [15].

It is important for PV module manufactures to understand those failures modes. Infant failures take place at the beginning of the working life of a PV module. If a PV module has a defective junction box, bad string interconnect or glass breakage during manufacturing and installation, the module's performance is likely to drop quickly. Those failures can be easily identified. Most of the modules deployed in the field fail either in the midlife-failure stage or in the wear-out-failure stage, which makes it difficult to track the cause and make improvements.

Therefore, standard accelerated stress tests (IEC 61215 for crystalline silicon modules) were developed to compare different module qualities and eliminate infant-stage failure [16]. The IEC 61215 qualification test includes a sequence of damp heat (DH), mechanical load, hail, thermal cycling, UV exposure, humidity freeze, and hot spot tests. A power loss of more than 5% in an individual test or a total power loss of more than 20% is considered as failure [17]. There is no direct evidence showing that a PV module that fails the accelerated stress tests will definitely fail in the field during 25 years of operation. However, passing those tests indicates that the PV product has met the requirements to be financed and sold in the market. Manufactures run accelerated stress tests on their PV modules multiple times and/or longer duration to promote the robustness of their PV products.

Stress-related degradation accounts for a high percentage of power losses in the midlife-failure and wear-out-failure regimes [18; 19]. It introduces failure modes such as cracked cell isolation, cell interconnect failure and delamination. Corresponding accelerated tests are designed to put individual stressors on modules to identify potential failure modes. For example, the mechanical load test puts forces on the modules to simulate mechanical stress-related degradation such as cracked cell isolation; thermal cycles (-40°C to 80°C temperature cycles) applies thermal stress on solder joints to simulate cell interconnect failure; and the DH1000 (85°C and 85% relative humidity for 1000 hours) test is performed to test delamination through loss of adhesion [17].

Cracks are the clearest result of stress on solar cells and should be avoided at all cost. Most cell cracks originate from the tabbing process [20]. Different tabbing processes introduce various amounts of stress on solar cells. The mismatch of thermo-mechanical properties between the wiring and the silicon during the soldering process is a well-known cause for microcracks formation [21–23]. Similar to other brittle materials, when the tensile stress exceeds a critical stress value, cracks are formed.

Such regions with cell cracks can seriously affect output performance [24]. Crack propagation, on the other hand, has been attributed to the combination of stresses on the module and the asymmetric nature of the module architecture – stiff glass on the front and more pliable backsheet on the back [23; 25]. For that reason, the module configuration with glass on both sides are becoming the mainstream to reduce stress gradients on cells [5].

Electroluminescence (EL) imaging is the go-to characterization method to identify cell cracks. EL images are taken by passing current through the p-n junction and capturing the subsequent luminescence photons. Cell areas with lower resistance have more current passing through, resulting in stronger luminescence signal on the EL images. Figure 1.4 shows the EL images of a cracked solar cell under different currents. Based on the severity of the effect of the crack on cell performance, cell cracking is categorized into three modes. Crack modes A, B, and C represent no cell isolation, partial cell isolation and total cell isolation, respectively. Crack mode C completely isolates the broken cell part and results in no current collection in that area, which is the worst scenario and should be avoided at all costs. In this regard, the correlation of module degradation to cell cracking is only evident when cracks are of detectable size and detrimental to the performance [21; 26].

1.3 Stress Characterization on Silicon Cell/Wafer

For decades, techniques such as DSC, Soxhlet extraction, solvent swelling, and dynamic mechanical analysis were used to characterize the encapsulant quality and as feedback to optimize the lamination process [27–29]. However, those techniques are destructive and only address the optimization of the encapsulant, giving no information about solar cell status. The encapsulant solidification, for example, usually translates into shrinkage, resulting in stress on the solar cells that cannot be mea-

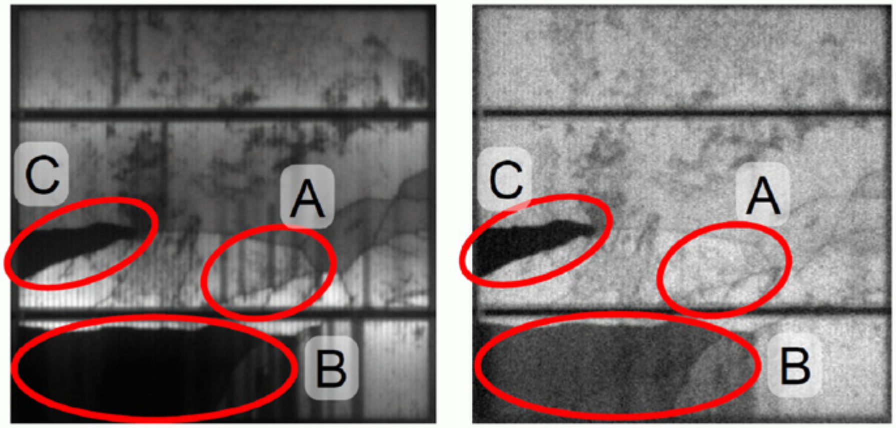

Figure 1.4: EL images of the a solar cell with crack modes A, B, and C. Left EL image was taken at Isc; right at 10% of Isc [21].

sured by the above-mentioned techniques. The actual stress state of the solar cells is unknown. Therefore, it is essential to experimentally characterize and understand the stresses that the solar cells see during proecessing and operation to prevent cell cracks in their early stages.

The forces acting on the solar cells are conducive to deformation and deflection, thus measuring deformation under encapsulation is critical to access the stress states. Eitner et al. and Meier et al. used a digital image correlation (DIC) technique to measure the deformation of solar cells in PV modules [30–32]. The sample preparation of DIC method is shown in Figure 1.5. The technique requires a random speckle pattern (paint for example) on the surface of the measured object. The deformation of the solar cells is determined by tracking the change in the pattern's shape/location during thermal loading and mechanical loading. The accuracy of the measurement is reported as 1 μm. Note that a transparent backsheet is used since DIC is based on visible light reflection. While DIC is useful in terms of tracking the cell deformation in the plane of the solar cell (expansion or shrinkage), DIC requires special sample preparation such that it is not suitable for in-line inspection.

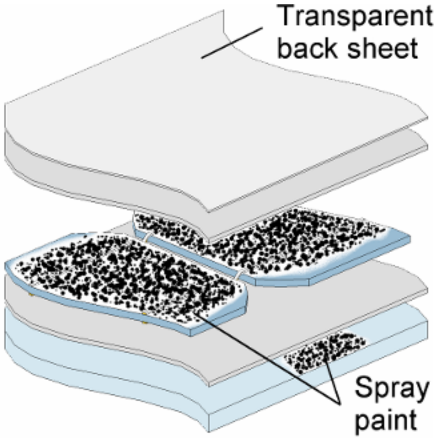

Figure 1.5: Scheme of a laminate prepared for DIC measurement [30].

Another cell deflection measurement technique is optical profilometry, which is based on the position or angle change of a laser beam (a point or a line) reflected from the measured surface. Optical profilometers are commercially available such as the LJ-V7000 series from Keyence. After a quick calibration of initial height and surface angle, an optical profilometer can measure a 6" solar cell in seconds. However, this type of optical measurement is strongly sensitive to the reflections from multiple interfaces, especially when measuring laminated solar cells through the front glass and encapsulant. The situation is even worse if the solar cells have AR coatings, which dramatically reduce the intensity of reflected light.

More recently, Beinert et al. used Raman microscopy to spatially map the stress on laminated silicon solar cells [33; 34]. By measuring the spontaneous Raman scattering, a Raman spectrum is obtained as a function of wavenumber ($1/\lambda$). Stress-induced lattice constant change is reflected as peak shifting on the Raman spectrum. Peak shifting to lower wavenumber indicates tensile stress and shifting to higher wavenumber indicates compressive stress. Figure 1.6 shows the relative stress map of a silicon solar cell obtained by Raman spectroscopy. This technique has several disadvantages that limit its application: (a) slow data acquisition rate because the point laser has to scan the whole solar cell (12 hours for a 2.1 cm×2.1 cm cell area); (b) no indication of stress direction; (c) relative stress values instead of absolute stress values; and (d) localized sample heating from the laser that may compromise measured stress values.

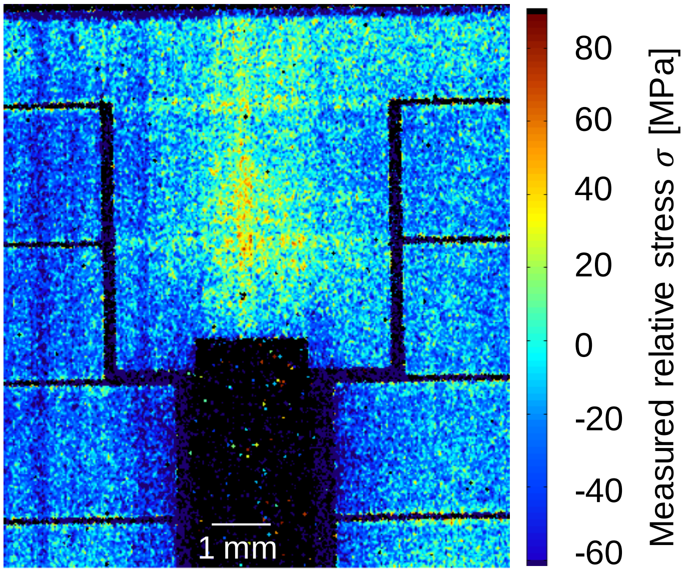

Figure 1.6: Raman area scan at the end of busbar on a silicon solar cell. The color code represents the interconverted relative stress. The black lines are the metallization fingers and busbar/ribbon, where no Raman spectra are measured [33].

Stoehr et al. and Kruger et al. applied a photoelasticity method to optically measure the mechanical stresses and strains on silicon wafers [35; 36]. Photoelasticity is based on birefringence caused by mechanical stress (or strain). It describes a stress-dependent change in the indices of refraction of materials with loading direction. During the test, a 1550 nm laser beam is used as the light source and transmits through the silicon wafer (silicon is an IR transparent material). However, the method is limited in some solar cell types like PERC and Al-back surface field (BSF) because they have Al covering the back and Al is not IR transparent. With the additional IR absorptance from the front glass in PV modules, this method is mainly limited to silicon wafers.

Due to the difficulty of experimentally probing the stress and deflection of encapsulated solar cells, the correlation between these cracks and the underlying stresses that originate them has mostly been determined by finite element analysis (FEA) [37; 38]. To generate stress maps of a PV module, FEA requires the material properties, module process windows, and loading conditions. Figure 1.7 shows the strain/stress distribution for a laminated PV module and first principal stress of a 60-cell module calculated by FEA [23]. The high-stress values at the four corners are introduced by the material shrinkage during assembly. Once a model of the PV module is built, it is convenient to test different encapsulants/temperatures/backsheets. However, FEA often does not reflect real module stress conditions because it ignores the human error and it is difficult to obtain accurate material properties (especially for polymers).

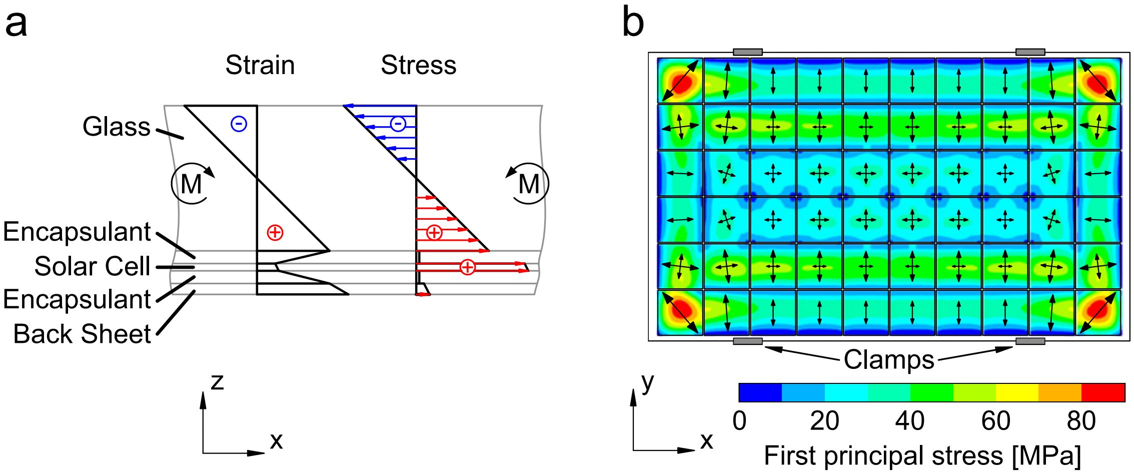

Figure 1.7: (a) Schematic of strain and stress distribution in a laminated PV module when bent in Y direction; (b) FEA modeled stress in a standard PV module with a clamped Al frame under 5.4 kPa area load. The color code represents the magnitude of the first principal stress at the bottom of the cells and the representative direction for the first and the second principal stress is depicted by arrows [23].

Table 1.1: Summary of the deflection/stress determination methods discussed above.

Method Name	Advantage	Disadvantage
DIC	fast	sample modification
Optical Profilometry	fast	surface sensitivity
Raman Microscopy	resolution	surface sensitivity; heat; slow; no σ direction
Photoelasticity	fast	metal and glass block IR light
FEA	large scale	modeled results

1.4 Motivation and Goals

Although we are eager to access the stress of encapsulated silicon solar cells, there is a lack of an effective, nondestructive cell characterization method. While EL is useful to correlate underperforming regions to cracked cell areas using 2D maps, this technique provides no information regarding the crack origin or stress states, nor the ability to visualize defective cells before full assembly of the devices.

In an attempt to develop an efficient and non-destructive method of characterizing stress/deflection on encapsulated silicon solar cells, this thesis presents a cell deflection mapping method by X-ray topography. The theory of X-ray topography will be introduced in Chapter 2. The experimental details, deflection calculation algorithm, and validation method will be discussed in Chapter 3. Error and sensitivity analysis will be discussed in Chapter 4.

In this work, the mechanical stress is calculated by the cell defleciton from XRT. In Chapter 5, bending stresses are calculated through the application of Von Karman plate theory, assuming solar cells are thin plates and under pure bending conditions. To explore validity of using thin plate theory and its assumptions, a series of four-point bending experiments followed by FEA calculations are shown in Chapter 6.

As the speed of the module technology evolution is accelerating, new PV module designs are developed and rolled into the market very quickly. While many of them pass accelerated testing, their stress-related failure modues are widely unknown. In this thesis, we argue that understanding the stress evolution for a given architecture can be instrumental to select the optimized bill of materials and minimize the stress-induced failure through the lifetime of the module. The glass/glass PV modules and two novel PV module technologies named flex-circuit PV modules and PVMirror modules will be analyzed and discussed in Chapter 5, Chapter 7, and Chapter 8, respectively.

Chapter 2

BACKGROUND ON X-RAY TOPOGRAPHY

X-ray topography (XRT) has been used in many applications, such as for inspecting defects in various crystalline materials and monitoring crystal quality. It is able to characterize residual strain, dislocations, surface damage and saw marks in silicon [39; 40]. X-rays are high-energy electromagnetic radiation that has wavelengths ranging from 0.01 nm to 10 nm, which is equivalent to frequencies ranging from 3×10^{16} Hz to 3×10^{19} Hz and energies ranging from 100 eV to 100 keV. Hard X-rays (energy between 10 keV and 100 keV) are able to travel through objects without being absorbed or scattered, the main reason for being widely used in medical imaging such as computed tomography (CT). Since X-rays have wavelengths comparable to the crystal lattice dimensions in materials, they are also widely used for material research purposes including X-ray microscopy and X-ray crystallography to determine the structure and characterize defects. In this chapter, we introduce the background of X-ray topography in preparation for visualizing cell deflection in Chapter 3.

2.1 X-Ray Source

X-rays are generated by three kinds of sources: X-ray tubes, rotating anodes, and synchrotrons. Synchrotron light sources generate X-rays by bending high energy electrons (GeV), which emits a tunable wavelength of X-rays. Although synchrotron light sources offer much more brilliant ($\gg 10^{10}$ times, see Figure 2.1) and coherent X-rays than laboratory X-ray sources [41], widespread implementation of synchrotron radiation in industry would be nearly impossible due to their extremely high capital and space requirements (1 Km ring).

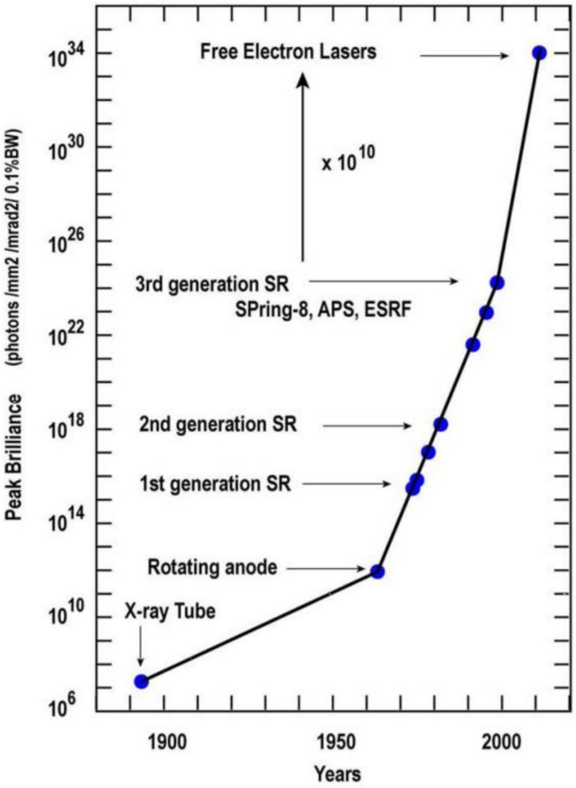

Figure 2.1: Historical evolution of the peak brilliance in various X-ray sources [41].

Laboratory X-ray sources produce X-rays using either an evacuated tube or a rotating anode. Fundamentally, those X-rays are generated by bombarding a target material with highly accelerated electrons. As free electrons are emitted from a cathode and accelerated by an electrical field (40 kV to 60 kV), they collide with a metal target made of a characteristic material (for example, Cu or Mo). These free electrons excite core electrons near the nucleus of an atom. To fill the vacated state, other electrons must release energy in the form of X-rays, producing (a) a continuous spectrum consisting of Bremsstrahlung radiation and (b) emission lines characteristic of electronic transitions in the anode material. The X-ray radiation spectrum by Mo at 35kV is shown in Figure 2.2. The $K_{\alpha 1}$ and K_{β} peaks represent the energy transitions in a Mo atom from the L shell to the K shell and from the M shell to the K shell, respectively. The intensity of the characteristic radiation is much higher than

Bremsstrahlung radiation such that the characteristic radiation peaks, especially the K_α peak can be isolated. The wavelengths of laboratory X-ray sources are not tunable and are fixed by the anode material.

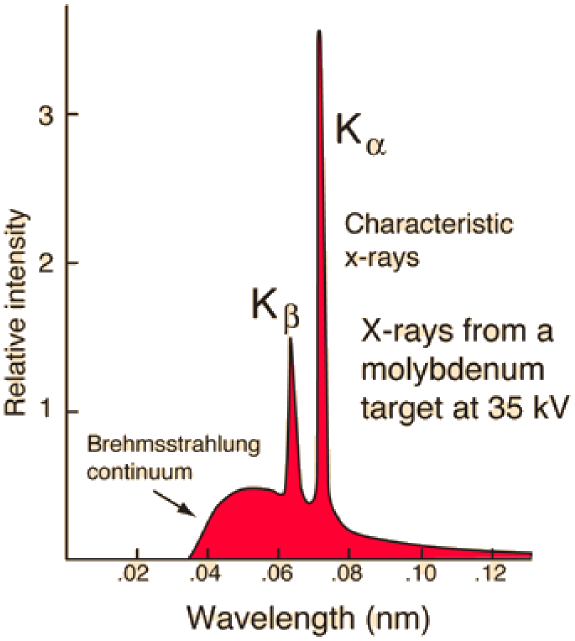

Figure 2.2: Bremsstrahlung radiation and characteristic radiation from a molybdenum target at 35 kV [42].

2.2 X-ray Topography Theory

XRT is an imaging technique based on Bragg diffraction. When X-rays strike a material, they interact with the atoms and are scattered by some atoms in certain crystal planes. When the incident angle, interplanar distance and the wavelength of X-ray fulfill the Bragg condition, X-rays are diffracted and exit the crystal in the direction differing from the direction of X-ray incidence by 2θ, as shown in Figure 2.3.

The Bragg condition is expressed as:

$$2dsin(\theta) = n\lambda \tag{2.1}$$

where n is a positive integer, λ is the wavelength of the incident X-ray, θ is the diffraction angle and d is the interplanar distance.

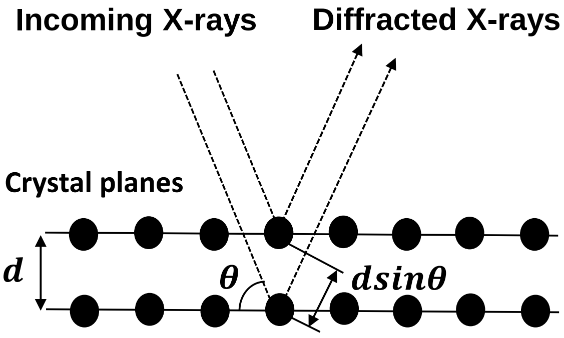

Figure 2.3: Diagram of Bragg's diffraction under normal condition.

Both white beam topography and Lang topography are widely used. A sketch of white beam topography, which is mostly implemented with a synchrotron radiation source [43], is shown in Figure 2.4. White beam topography is the simplest X-ray imaging technique for crystals [44]. A wide, homogeneous, low divergent, high power beam is applied to bulk crystals for defects or dislocation analysis. This topography method does not require sample orientation and the diffraction signal of the whole crystal is visible simultaneously, but it demands high-quality X-rays.

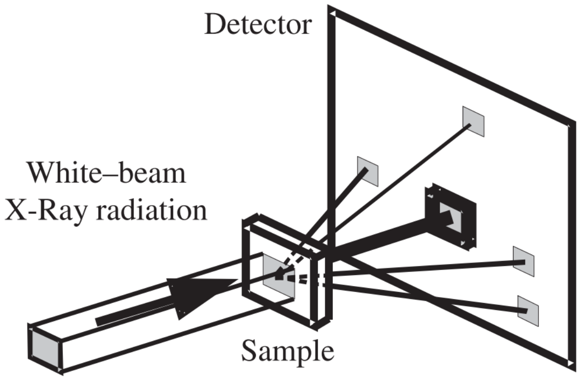

Figure 2.4: Sketch of white beam topography using synchrotron light source [45].

Lang topography, on the other hand, mostly uses laboratory X-ray sources. It operates in two geometries: reflection geometry (Bragg case) when the X-ray beam enters and leaves through the same surface, and transmission geometry (Laue case) when the beam enters and leaves through opposite surfaces of the sample. A sketch of Lang topography using transmission geometry is demonstrated in Figure 2.5. The X-rays travel through the tube, first slit, sample holder, stage, and second slit and then reach the detector. The angle ω indicates the sample rotation in Y direction, with the axis being perpendicular to the paper. The angle ϕ indicates the sample rotation in Z direction, with the axis being perpendicular to the sample surface. The angles ω and ϕ are perpendicular to each other. The first slit is used to restrict the radiation field of the X-ray beam incident on the sample and control the horizontal divergence. A width-limiting slit and a height-limiting slit can be configured depending on the size of the sample. The second slit is used to reduce the effects of beam scattering onto the image plate and to provide protection against direct exposure to X-ray beams. Since the X-ray beam is vertical, the X-ray detector and the sample on the stage simultaneously translate perpendicularly to the ω and ϕ rotation axes such that the incoming X-ray beam can sweep the whole sample without interfering with the X-ray diffraction angles. This is called extended X-ray imaging. Compared to white beam topography, Lang topography requires extra time for angle alignment and simultaneous translation. However, it does not necessarily need a synchrotron light source.

2.3 Topography Contrast Imaging

Both X-ray films and semiconductor detectors are used to collect spatial X-ray intensities. X-ray films typically contain silver halide crystal grains. When the film is exposed to X-ray radiation, the halide is ionized and free electrons are trapped in crystal defects. Silver ions are attracted to these defects and result in clusters of Ag-"free" area [47]. Once the images are developed, areas with more Ag atom

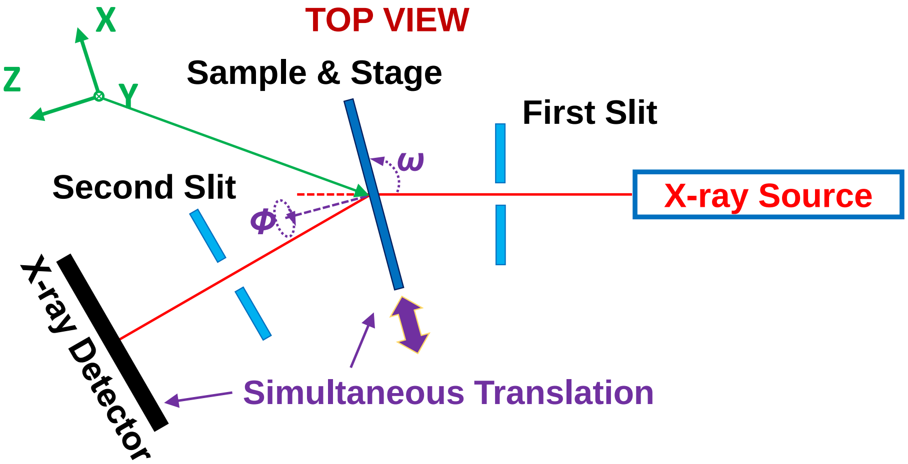

Figure 2.5: Sketch of Lang topography in transmission geometry (Laue case) using a laboratory X-ray source, which is the XRT geometry used in this dissertation. Note that this is a top view of the XRT setup [46]. An orthogonal cartesian coordinate system is defined at the center of the sample holder and rotates/translates according to the position of the sample.

appear dark. Semiconductor detectors can be divided into two categories. Direct semiconductor detectors made of silicon or germanium (doped with lithium) detect X-rays by X-ray generated electron-hole pairs. Indirect semiconductor detectors use a scintillator to convert X-rays into visible light and a phosphor to convert visible light into electrons. In general, semiconductor detectors have the advantage of fast data acquisition over films but suffer from lower resolution.

Diffraction gives rise to the signal intensity in an XRT image. Unlike the CT sweep, whose working principle is based on X-ray absorption contrast, XRT makes use of the intensity profile of the diffracted X-ray signal. Unlike the traditional X-ray diffraction (XRD) method, which collects diffraction intensity as a function of diffraction angle, XRT collects a spatial map of the diffraction intensity (ideally the whole sample).

Figure 2.6 illustrates the contrast mechanism of XRT imaging using the Lang method. When a perfect crystal is illuminated by a homogeneous X-ray beam, the XRT image has no contrast. Extinction image contrast arises when (a) the thickness of the sample changes over the image or/and (b) parts of the crystal are diffracting X-ray with various intensities due to distortions in the crystal lattice by defects [48]. In case (a), the intensity of the diffracted beam increases as the thickness of the sample increases. In case (b), the defects can be boundaries, dislocations, cracks or clusters. Apart from the detector and setup geometry, the image quality also depends on the nature of the defects. The contrast of the defect only increases when the local orientation of the defect is different from the average orientation by more than the Darwin width (full width at half-maximum of the total X-ray peak profile) of the X-rays used [49; 50].

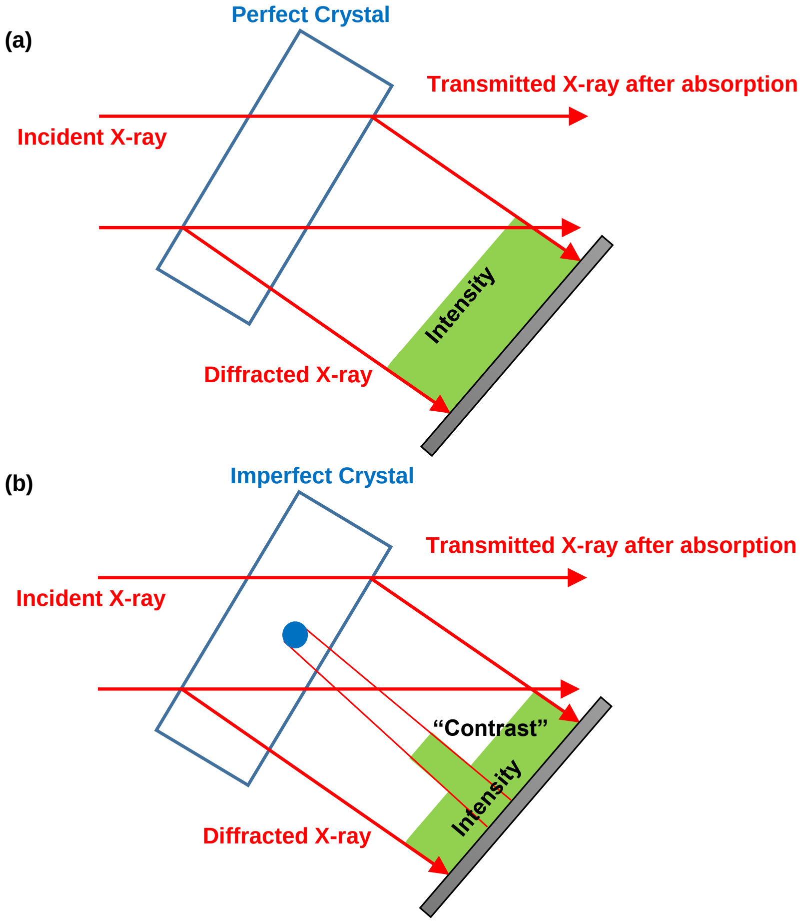

Figure 2.6: Sketch illustrating extinction contrast formation in XRT images from (a) a perfect crystal and (b) a crystal with defect. The green area indicates the X-ray intensity on the detector.

As well as the extinction contract, orientation contrast also contributes to the image contrast. Orientation contrast often affects the image when the crystal is deformed or under a stress field. When a crystal contains parts with different lattice orientations (wafer deflection, see Figure 2.7), the topography contrast increases: only the elements of the crystal that meet Bragg's condition will contrast in intensity from the background of the image. No other elements will show up in the image.

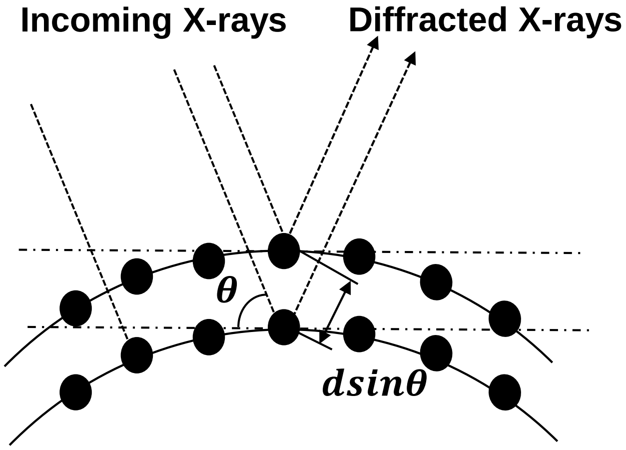

Figure 2.7: Diagram of Bragg diffraction in distorted crystal lattices.

Due to energy level splitting in the L shell, the K_α peak splits into $K_{\alpha 1}$ and $K_{\alpha 2}$ components with wavelengths of 0.070 93 nm and 0.071 359 nm, respectively ($K_{\alpha 1}$ has twice the intensity as $K_{\alpha 2}$). When no monochromator is used in the XRT system, the incident X-ray source contains both the $K_{\alpha 1}$ and $K_{\alpha 2}$ wavelengths, as shown in Figure 2.8(a). The $K_{\alpha 1}$ has a stronger signal (2:1) than $K_{\alpha 2}$ such that only $K_{\alpha 1}$ is aligned vertically for the diffraction conditions to achieve better contrast ratios and only $K_{\alpha 1}$ should show up on the XRT image. However, if the sample is bent, only parts of the sample can meet Bragg's condition at the $K_{\alpha 1}$ wavelength and appear on the XRT image due to other parts of the sample having different values of $d \times \sin\theta$. Additionally, a different part of the sample may meet Bragg condition at $K_{\alpha 2}$ wavelength and show up on the XRT image as well. Figure 2.8(b) shows a typical raw

XRT image collected from a bent silicon solar cell. As we expected, a dark line and a light line appear in the image, representing $K_{\alpha 1}$ and $K_{\alpha 2}$, respectively. The widths of the lines and the distance between them are associated with the peak widths of $K_{\alpha 1}$ and $K_{\alpha 2}$ in the X-ray spectrum and the curvature of the sample. The more the solar cell is bent, the narrower the line width and the shorter the distance that will be observed.

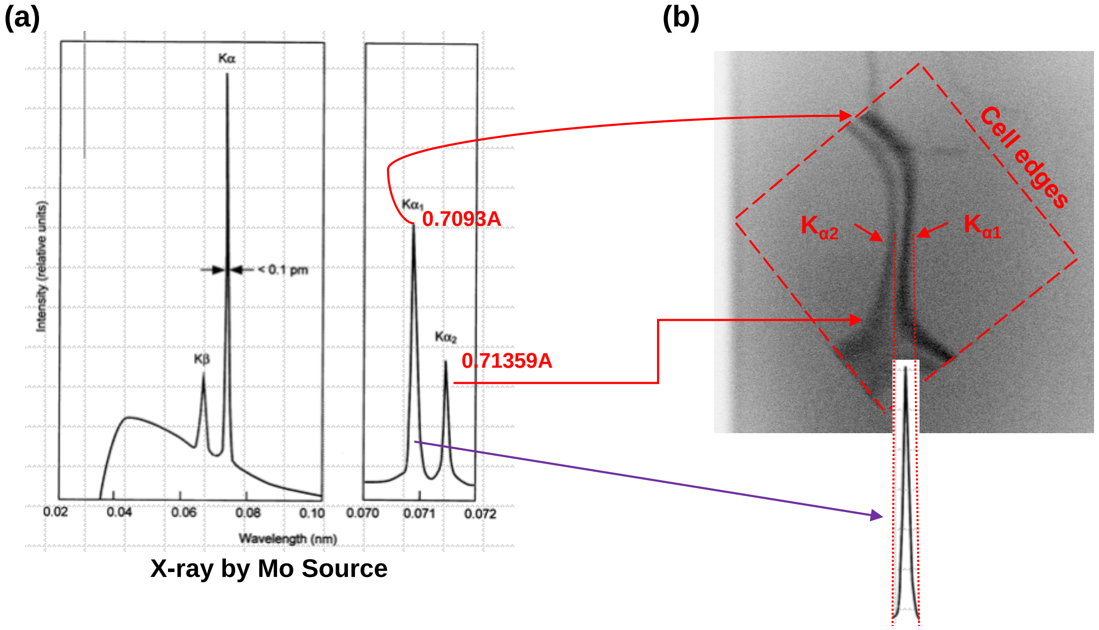

Figure 2.8: (a) X-ray spectrum of Mo source; (b) a typical raw XRT image from a bent solar cell. Red dashed lines indicate the cell edges.

To further illustrate orientation contrast, a flat solar cell and a bent solar cell as well as their raw XRT images are shown in Figure 2.9. Both images were taken after the same alignment on $K_{\alpha 1}$. For the flat solar cell, since every spot meets Bragg condition after initial alignment, the whole solar cell shows up on the image with a very strong signal. For the bent solar cell, both $K_{\alpha 1}$ and $K_{\alpha 2}$ show up in the raw XRT image, as previously described. Note that the glass and encapsulants, as the packaging materials, attenuate X-ray signal and therefore reduce the contrast on XRT images. The location of the X-ray signal is not affected. The XRT imaging technique is also capable of identifying cracks in the wafers, which show up as discontinuities in the diffraction pattern. No cracks were observed in these particular samples.

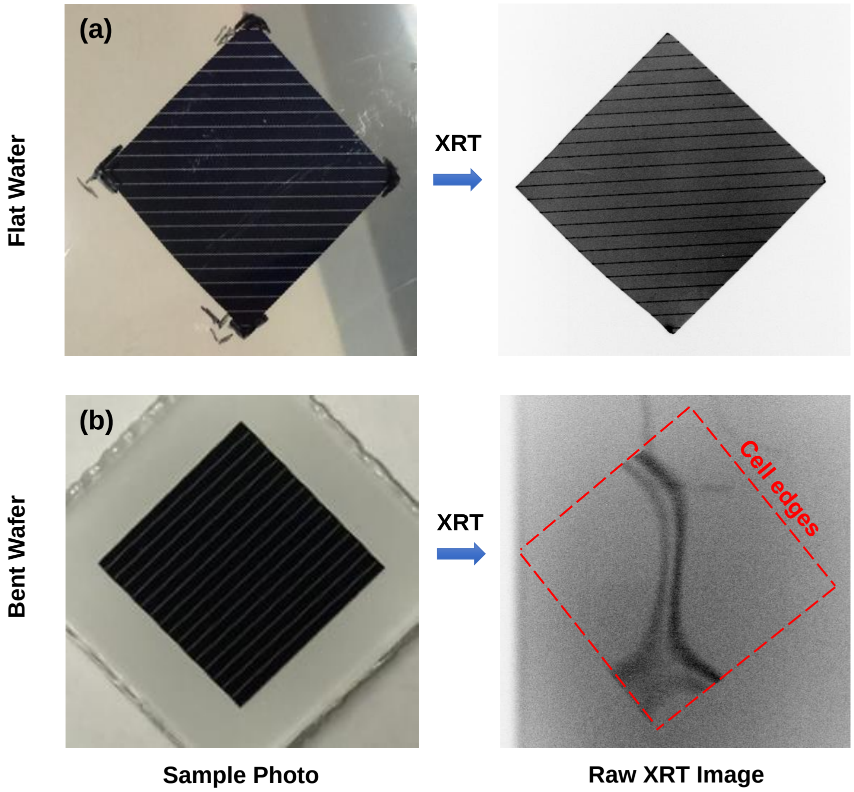

Figure 2.9: Photo and raw XRT image of (a) a bare, flat silicon solar cell and (b) an encapsulated, bent solar cell.

Chapter 3

VISUALIZING CELL DEFLECTION BY X-RAY TOPOGRAPHY

X-ray topography based technologies have been used in the past to characterize residual strain, dislocations, surface damage, and saw marks in thin films and wafers [40; 51]. It has been demonstrated to be capable of measuring curvatures ($\sim 1\,\mathrm{m}^{-1}$) in thin films and silicon wafers with high sensitivity and accuracy [52]. McNally et al. calculated the warpage of encapsulated silicon chip packages by using synchrotron-based B-spline X-ray diffraction imaging technology and examined the individual transmission section topography in the silicon die sweeps [53; 54]. They were able to measure the silicon deflection in one direction but had difficulties in mapping the deflection. More recently, Colli et al. demonstrated the possibility of using synchrotron XRT technology to image cracks on encapsulated solar cells [55]. Synchrotron-based XRT has demonstrated faster data acquisition rates and submicrometer resolution due to higher flux compared to regular in-house tools [56]. We expect that both acquisition rate and spatial resolution can be enhanced by at least one order of magnitude at the state-of-the-art synchrotron beamlines.

However, it is neither necessary nor feasible to implement synchrotron-based XRT in a PV module production line. Tippabhotla et al. calculated the residual stress evolution near soldering joints on silicon solar cells by analyzing the crystal plane misorientation angles with synchrotron X-ray micro-diffraction [38]. As the authors stated, such experiments cannot be performed on a large scale because of the limitations of time and resources (synchrotron X-ray source). We argue that full cell deflection and stress mapping with high resolution can be achieved by utilizing a systematic sweeping and calculation method based on laboratory-based X-ray topography. In this chapter, we leverage the throughput of our in-house XRT system to visualize the deflection induced by various lamination profiles and materials.

3.1 Cell Deflection Calculation Model

For a fixed X-ray source and a flat sample in an XRT system, the wavelength of incident X-ray, the interplanar distance, and the diffraction angle are set as constants. However, that is not the case for curved samples. As discussed in Chapter 2, when the measured solar cell is curved, only parts of the sample can meet the Bragg condition and appear on the XRT image at different wavelengths ($K_{\alpha 1}$ and $K_{\alpha 2}$). The reason why multiple wavelengths of X-rays are appearing at the same time is because each wavelength is compensating the angular misalignment induced by the curvature, assuming the interplanar distance remains constant. In other words, it is possible to manually correct the angle misalignment while taking XRT images focusing on X-rays of one wavelength (for example, $K_{\alpha 1}$ line). The angle misalignment can be maneuvered by adjusting the angle ω (see Figure 2.5). By XRT imaging at different ω values, every part of the curved solar cell can fulfill the Bragg condition. The location of the XRT signal is associated with ω angles, which means a ω map that contains the bending behavior of the whole solar cell can be obtained.

Here we discuss the calculation method to transform the above-mentioned ω map into the actual deflection map experienced by the solar cell. Silicon has a face-centered diamond-cubic crystal structure with a lattice constant of 0.5431 nm. A typical silicon solar cell uses (001) silicon wafers since they are easy to texture (silicon (111) plane is the favored KOH etching plane). Therefore, we describe the method for the particular case of the (004) plane of silicon, but it can be readily adapted to other diffraction planes.

The Cartesian coordinate system used in this calculation is defined in Figure 3.1 with the center of the solar cell as the origin (reference). The deflection at this pixel equals zero by definition, and the deflections of all other pixels in Z direction are referenced to it (Figure 3.1). Next, we present our method to access the relative deflection in Z direction, first between two neighboring pixels including the reference point, and then between two neighboring pixels away from the reference point. The coordinate system is fixed to the solar cell as the cell rotates from wafer position at ω_0 to wafer position at ω_m, and then to wafer position at ω_{m+1} (the coordinate system rotates together with the wafer). Note that the glass rotates together with the wafer but only the glass at wafer position ω_0 is shown. The calculation relies on the precise angular position variation of the experimental setup and geometric calculations. The deflection calculation is performed subsequently for each pixel acquired on the X-ray detector.

In Figure 3.1, the gray lines represent incident X-rays coming from the source and diffracted X-rays leaving towards the X-ray detector. The brown curved solid line represents the cross-section of the silicon wafer at ω_0 and the corresponding brown dashed line (Tangent 0) is the tangent at the reference point position P_0. The ω value when the sample meets the Bragg condition at the origin is denoted ω_0. From position P_0, a diffracted spot is recorded on the X-ray detector at pixel P'$_0$ if the incoming X-ray and sample meet the Bragg condition. The brown double dashed line is normal to Tangent 0.

As the sample rotates in ω counterclockwise towards the position ω_m, the wafer position where Bragg's law is now met, shifts to P_m and the recorded diffraction spot on X-ray detector shifts to P'$_m$, with the green curved solid line indicating the new wafer cross-section. The variable m is defined as the number of pixels on the X-ray detector between P'$_0$ and P'$_m$. The green double dashed lines are perpendicular to

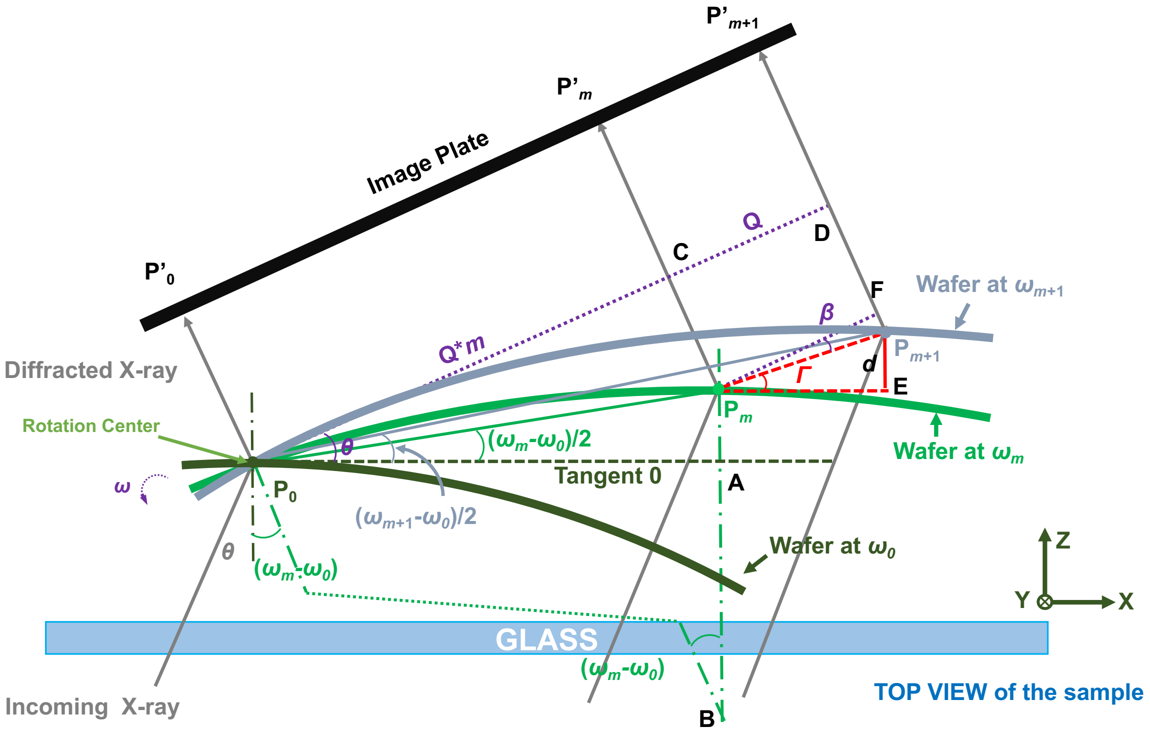

Figure 3.1: Schematic of cross-sections of the same laminated silicon wafer at three different rotation ω values: ω_0, ω_m, and ω_{m+1}, illustrating the deflection calculation method. Please note that P_0 is the origin of the coordinate system and the center of rotation. The X-ray beam (gray) coming from bottom of the figure is diffracted to the top of the figure, reaching the X-ray detector perpendicularly. θ is the Bragg diffraction angle (15° in this case). The coordinate system in the bottom-right corner is bonded to the wafer as it rotates, fixing P_0 as the origin.

the wafer at P_0 and P_m, respectively. Those two lines meet each other at distant point B. P_0B crosses Tangent 0 at A forming a 90° angle. P_mE is the tangent line at Pm.

As the sample further rotates towards position ω_{m+1}, the wafer position where the Bragg condition is now met shifts to pixel position P_{m+1}, shown by the blue curved solid line. P_{m+1}E is normal to P'_{m+1}E. Purple dashed lines are perpendicular to the diffracted X-rays, intersecting at C, D, and F. It is apparent that $\angle CP_0A = \theta$. β (purple font) represents the angle between P_mP_{m+1} and P_0F; Γ (red font) represents the angle between $P_{m+1}P_m$ and P_mE; Q represents the pixel size on the X-ray detector.

We now consider the discrete the small distance between pixels given by the resolution of the X-ray detector and approximate the distance between diffraction points on the X-ray detector as Q×m. d represents the relative deflection from P_m to P_{m+1} in Z direction, which is also $P_{m+1}E$.

Let us consider first the deflection from P_0 to P_1. Based on the assumption of two neighboring pixels sharing the same curvature, we have P_0B equals P_1B. Then, if we consider these three triangles: P_0P_1A, P_0P_1B and P_0AB, we find the following relation:

$$\angle P_0P_1A = \frac{\omega_1 - \omega_0}{2} \tag{3.1}$$

Using triangles P_0CP_1 and P_0P_1A that share the same side P_0P_1, we derive the expression of the deflection P_1A at position P_1:

$$P_1A = \frac{Q \times \sin((\omega_1 - \omega_0)/2)}{\cos(\theta - (\omega_1 - \omega_0)/2)} \tag{3.2}$$

Now let's consider two non-reference points, P_m and P_{m+1}, as shown in Figure 4.7. To determine the deflection d, we utilize the parallelism of P_mC and $P_{m+1}D$ and the triangle $P_mP_{m+1}F$ to get:

$$\beta = \tan^{-1}(\frac{P_{m+1}F}{Q}) = \tan^{-1}(\frac{P_{m+1}D - P_mC}{Q}) \tag{3.3}$$

For d, the deflection of P_{m+1} with respect to P_m, we consider the triangles $P_mP_{m+1}E$ and $P_mP_{m+1}F$, where P_mP_{m+1} is the common line:

$$d = P_mP_{m+1} \times \sin\sigma = Q \times \frac{\sin(\theta - \beta)}{\cos\beta} \tag{3.4}$$

Using these equations, we can determine the deflection d between the two points defined by Q, the Bragg diffraction angle θ, and the experimentally rotated ω needed to get P_{m+1} into diffraction conditions from P_0.

Through the above calculation method, the deflection between adjacent points can be determined in the direction of ω rotation (X direction in this case). To construct a full deflection map, the deflection between adjacent points in the Y direction is also needed. Thus, two sets of ω maps are required to fully obtain cell deflection. To be specific, we first calculate the deflection at the vertical middle line of the wafer using ω from the Y direction. Then we treat all the pixels on that middle line as the reference points for all lines in the X direction and perform the transformation calculation across the whole wafer using ω in X direction.

3.2 XRT Measurement Procedure

The XRT setup used for this study is a HITACHI Rigaku XRT-100. The tool is capable of doing XRT measurements in both Laue case and Bragg case configurations. The photo of the setup is shown in Figure 3.2.

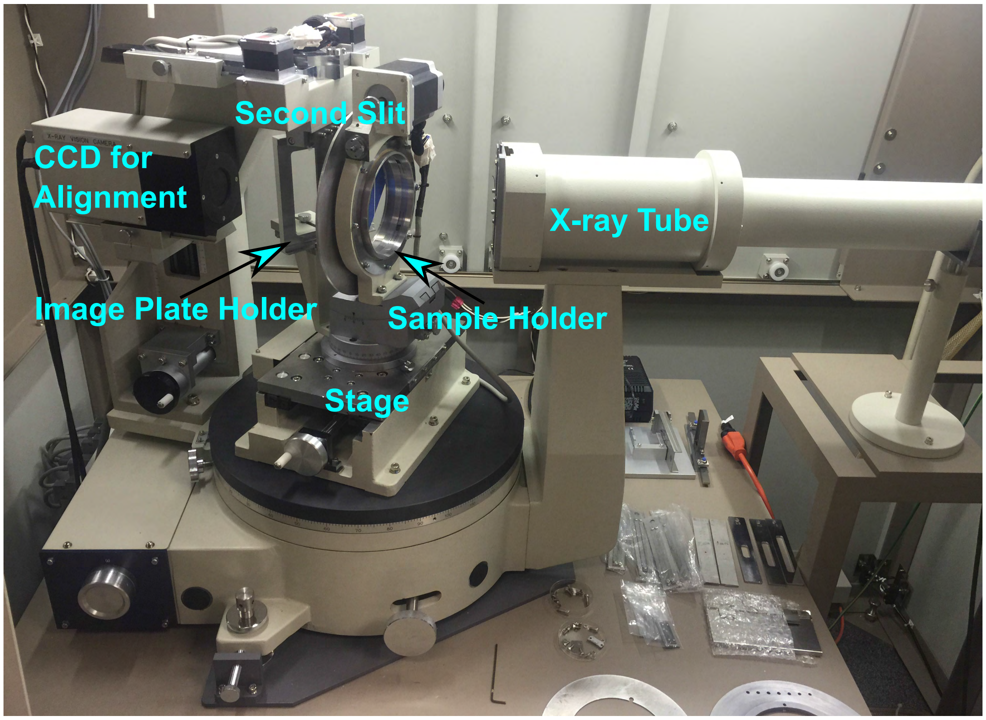

Figure 3.2: Photo of a HITACHI Rigaku XRT-100 used in this dissertation.

This dissertation mainly focuses on the Laue case, which was previously introduced in Figure 2.5. A Mo source ($h\upsilon = 17\,481\,\mathrm{eV}$) with a flux of $\sim 10^9$ photons/s is used as the X-ray source. In this case, the X-ray source generates a vertical point-sourced vertical beam with a cross-section of 1 mm × 100 mm. No monochromator is installed. The sample is held between two Mylar-foils that are extended on a pair of holder rings (10 cm in diameter). The holder is able to mount square-shaped solar cells up to 7.5 cm×7.5 cm. The sample stage (4" circular holder in diameter) can do angular ω and ϕ rotation as indicated in Figure 2.5 to align the sample with the Bragg condition. A 2315 Varex Imaging Flat Panel X-ray Detector with a resolution of 75 μm is used as the X-ray detector.

The spatial resolution in the XRT image is limited by the resolution of the detector, the experimental geometry, and the intrinsic diffraction effects. The spatial resolution cannot be higher than the resolution of the detector. The geometric spatial resolution of an XRT system is calculated by

$$x = \frac{S}{D}a \tag{3.5}$$

where a is the distance between the sample and detector, D is the distance between the sample and X-ray source, and S is the dimension of the X-ray source. The best spatial resolution of any XRT system is achieved by a small X-ray source, a large sample distance, and a small detector distance. The geometric spatial resolution of this system ($a = 80\,\text{mm}$, $D = 1100\,\text{mm}$, $S = 0.5\,\text{mm}$) is determined to be approximately 36 μm, indicating the current resolution is limited by the XRT detector. The incident X-ray is horizontally confined by the first slit width (1 mm by default), limiting the horizontal divergence to 0.0521°; the incoming X-ray is vertically defined by the first slit with a height of 100 mm, defining the vertical divergence as 5.72°.

There is a trade-off between the measurement time, X-ray signal-to-background ratio, X-ray sweeping speed, and the number of ω_{sweep} angles. Error and sensitivity analysis of this XRT measurement will be discussed in Chapter 4.

3.2.1 *Measuring $\leq$ 3" Solar Cells*

The HITACHI Rigaku XRT-100 tool used in this dissertation is primarily designed for defects and dislocation inspection in flat crystalline materials. However, our XRT measurement procedure mainly focuses on deflected silicon wafers/cells. Due to the different demand in raw XRT images, the current XRT imaging system sets constraints on our experiment and further limits the application of XRT in PV applications in terms of sample size. The current XRT system limits the size of the measured square solar cell to 3". Also, the incident X-ray beam has the cross-section of 100 mm × 1 mm, which also limits the vertical dimension of the sample to ≤ 10 cm.

When the solar cell is no larger than 3", it will be held between two Mylar-foils (default mounting option). The side view shown in Figure 3.3 illustrates the interaction between the X-rays and the sample. Since most crystalline silicon solar cells are made from (100) silicon wafers, the (004) crystal plane, which is perpendicular to the sample surface, is chosen for this study. For silicon (004) plane, the lattice constant is 0.5430 nm and the diffraction angle 2θ is 30.29°. Alignment is performed by rotating ω and ϕ angles such that the incoming X-ray beam fulfills the Bragg condition and a vertical X-ray beam of $K_{\alpha 1}$ appears on the X-ray detector.

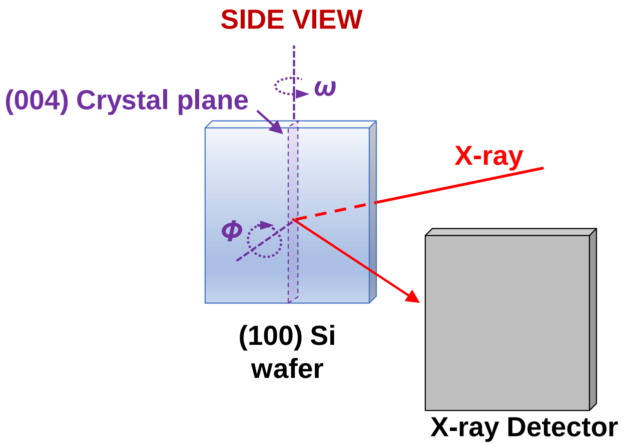

Figure 3.3: Sketch of side view of sample and X-ray detector in the XRT system.

As mentioned earlier, the position of $K_{\alpha 1}$ X-ray signal on the raw image is a function of ω angle. To map the $K_{\alpha 1}$ signal on the whole sample, a set of raw XRT images showing $K_{\alpha 1}$ diffraction patterns was collected on the X-ray detector by rotating the sample around ω (Figure 3.4) at discrete ω_{sweep} values.

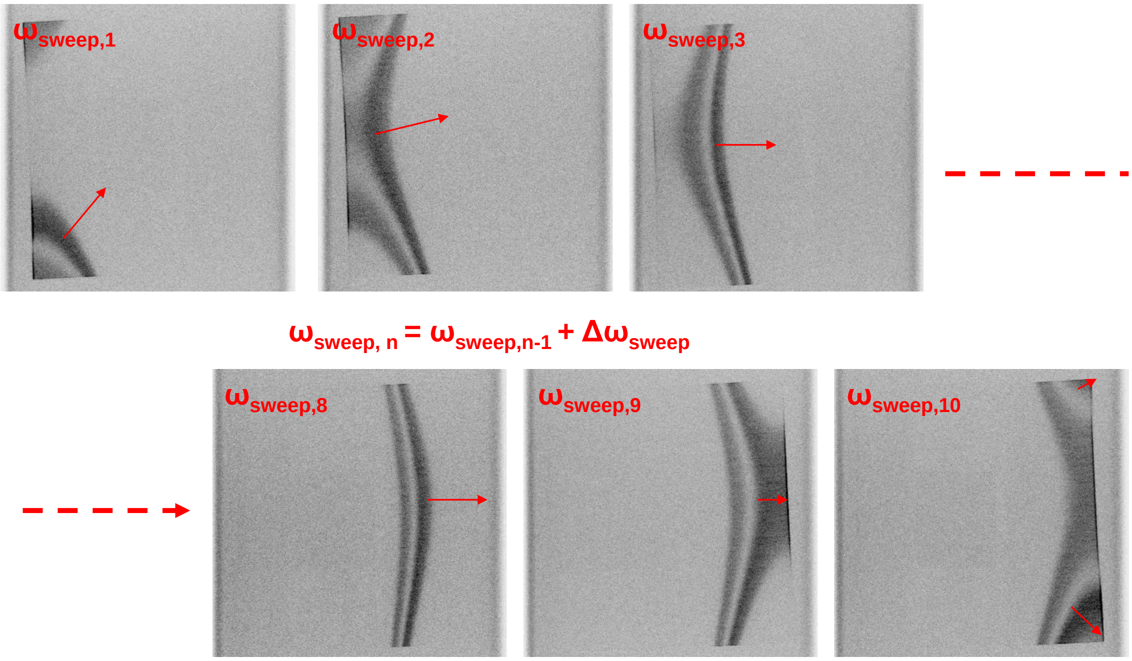

Figure 3.4: A set of raw XRT images collected at different ω_{sweep} values. The ω_{sweep} values are determined by total $\triangle\omega \div$ total number of raw XRT images.

For each image, the sample stage and X-ray detector (but not the second slit) move together in a controlled translation to sweep X-rays through the whole sample. The X-ray source is stationary. By default, 10 images were taken with the X-rays sweeping in X direction and 8 images were taken with the X-rays sweeping in the Y direction after ϕ rotation. A smaller number of images was used in the second set due to its less contribution to the deflection calculation. The X-rays translational sweeping speed is set as 2 mm/s and 2-6 number of sweeps are generally used depending on the test subject (to be discussed in Chapter 3.3.1). Note that we are not sweeping 2θ as in a standard XRD measurement. Next, the sample was rotated by 90° in ϕ, and another series of X-ray diffraction images was collected (by repeating the X-ray sweeping at another series of ω_{sweep} values). Two sets of XRT images were collected because each set only contains the curvature information of the solar cell in the direction of X-ray sweeping.

Note that the image of the solar cell on the detector is a projection thus the dimensions differ according to the projection angle. Vertically, the projected image of the solar cell is larger because of the point X-ray source. The projection angle (correction ratio) is determined by the distance between the cell and X-ray source and the vertical dimension of the cell. Horizontally, the projected image of the solar cell is smaller because of the angle between the cell and the X-ray detector. Those distortions can be easily corrected by scaling to the actual size of the solar cell.

Also, note that the cell in the XRT image shifts horizontally under ω rotations due to different angles between the sample (the rotating object) and the X-ray detector (no rotation). Increasing the $\triangle\omega_{\text{sweep}}$ value will shift the projected cell to the left part of the solar cell. Since $\triangle\omega_{\text{sweep}}$ is a constant value in a data set, the amount of shift is also constant (linear approximation). Therefore, the effect can be corrected during data processing.

3.2.2 Measuring 6” Solar Cells

Commercial solar panels contain solar cells with sizes of 6”. It is imperative to explore and extend our XRT method to actual modules. In the case of the full-sized 6” solar cells, a 6” cell sample holder was designed to replace the current sample holder. As shown in Figure 3.5(a), the 6” cell holder is a ring design with two sets of bars perpendicular to each other that support one corner of the 6” cell modules (6” solar cells are laminated with 8” front glass in this dissertation). The two bars can shift through slots to accommodate PV modules in other sizes. The two handles on the bar ends are used to clamp the PV module to the ring. One corner of the 6” cell module is imaged at a time and four measurements are required for a 6” cell.

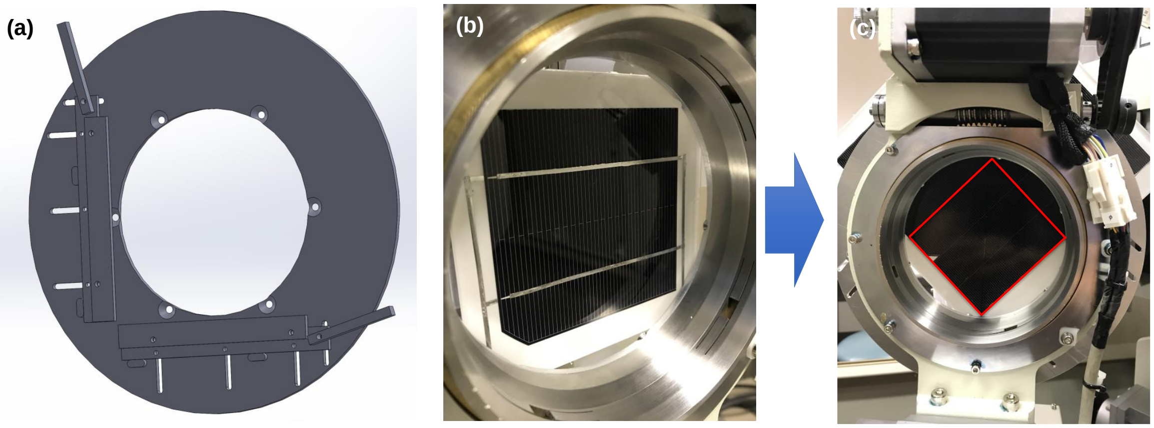

Figure 3.5: (a) SolidWorks drawing of the 6” cell module holder for the existing XRT system; (b) photo of a 3” cell module installed in the XRT system; (c) photo of a 6” cell module installed in the XRT system using the holder fabricated according by (a).

3.3 Data Processing

3.3.1 $K_{\alpha 1}$ Extraction Varied by Encapsulation

Those $K_{\alpha 1}$ lines were originally extracted out of the background (alignment is based on $K_{\alpha 1}$) by a watershed technique. The process was carried out in ImageJ using a watershed plugin with manual thresholding on each segment of $K_{\alpha 1}$ lines, which is time inefficient. To speed up the process, Matlab is used to directly extract the $K_{\alpha 1}$ lines from raw XRT images. A series of morphological image processing procedures are utilized to increase the signal-to-background contrast ratio on the raw image. A flow chart summarizing the data processing flow using Matlab is shown in Figure 3.6. Note that encapsulation plays an important role in the data process because the glass thickness significantly reduces the contrast intensity (see Section 4.2.4). The data process is categorized into two scenarios: with and without encapsulation.

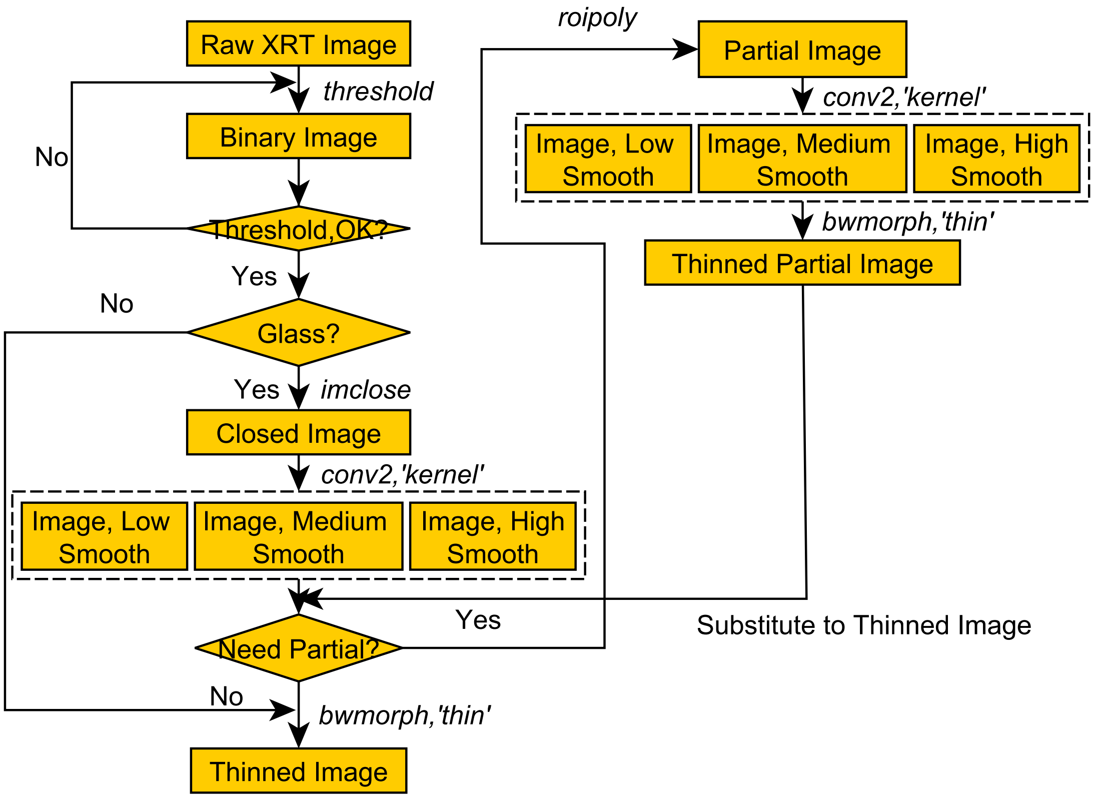

Figure 3.6: Flow chart for data processing of every XRT raw image using MatLab.

Solar Cells without Encapsulation

Thinning and *skeletonizing* are often used to extract a representative line out of an area. In this case, we are trying to extract $K_{\alpha 1}$ lines (to represent the diffraction signals at the wavelength of peak $K_{\alpha 1}$ intensity) out of the dark $K_{\alpha 1}$ areas in raw XRT images. Figure 3.7 shows a comparison between them. Starting from the same binary image, the *skeletonizing* is more sensitive to the edges than *thinning*. After removing unnecessary spurs, the result from *skeletonizing* is obviously losing some of the features of the original image. Therefore, *thinning* instead of *skeletonizing* is used to fit the peak $K_{\alpha 1}$ signals.

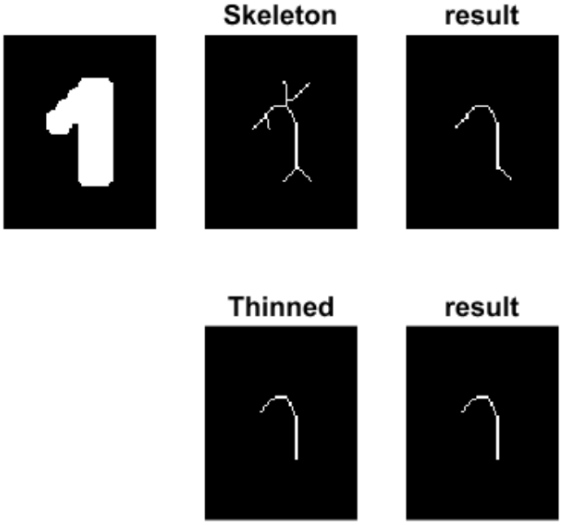

Figure 3.7: Process flow demonstrating the difference between skeletonizing and thinning on binary images.

Figure 3.8 shows the data extraction process used on a silicon solar cell without encapsulation [57]. From left to right, the raw XRT image goes through the procedure of *threshold* and thinning. *Thresholding* extracts the shape of $K_{\alpha1}$ areas; *thinning* transforms the porfile of the $K_{\alpha1}$ signal into a line. As we can see, the line in Figure 3.8(c) well preserves the shape of $K_{\alpha1}$.

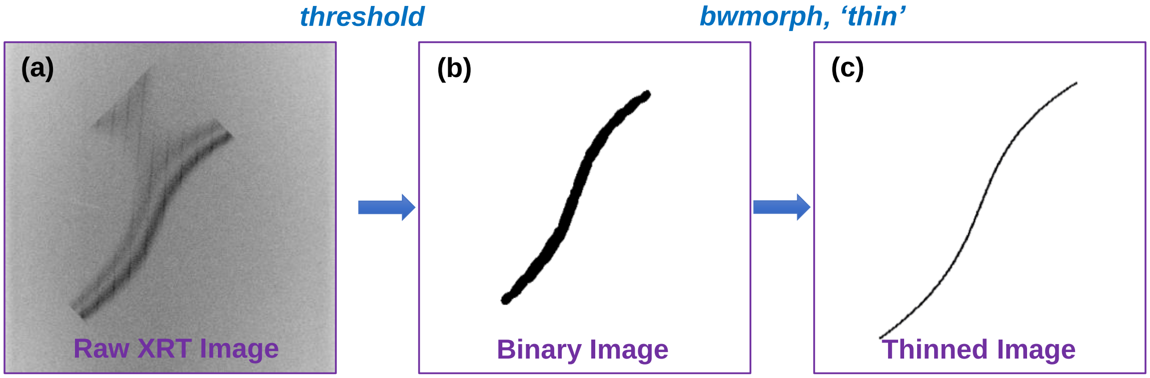

Figure 3.8: Process flow to extract $K_{\alpha1}$ signals in raw XRT images taken on silicon solar cells without encapsulation.

Encapsulated Solar Cells

The data analysis gets complicated when the measured silicon solar cell is encapsulated. The laboratory-based X-ray source has relatively low beam intensity such that it is very sensitive to X-ray absorption and scattering in the glass and encapsulant. The signal-to-background contrast ratio is much lower in the encapsulated solar cell raw XRT images. Note that the signal originates from X-ray diffraction and the background originates from the transmitted X-ray through the second slit (see Figure 2.5 for geometry). To quantify that, the X-ray transmittance of different materials used in PV modules is measured and shown in Table 3.1. High-quality low-iron B270 glass, which is decent for PV modules, has the lowest X-ray transmittance among the tested glasses. To maximize the X-ray signal reaching the detector, Borosilicate glasses are used in all PV modules for XRT measurement. Although there are other options such as acrylic sheets that could also serve as the front protector, their mechanical properties are greatly different from rigid glass.

Table 3.1: X-ray transmittance through different PV components of various thicknesses.

Material	thickness (mm)	X-ray Transmittance(%)
Tempered glass	3.2	6.7
Borosilicate glass	3.2	17.3
B270 glass	3.2	3.1
Laminated EVA	0.4	95.9
Laminated backsheet	0.4	92.8
PERC solar cell	0.2	66.7

A different data process is used for analyzing encapsulated solar cells as shown in Figure 3.9. If the raw images are processed in the same flow used for non-encapsulated cells as shown in Figure 3.9(a-c), net lines instead of a representative line would be extracted. Those net lines may cause artifacts in the following interpolation process and should be avoided at no cost. Therefore, extra steps including *imclose* (Figure 3.9(d)) and *conv2* (Figure 3.9(e)) are added to the process flow. The *imclose* fills the empty pixels between bright data points; the *conv2* rounds up the boundaries of the $K_{\alpha 1}$ area such that the following *thinning* process has minimum spurs input. The thinned image in Figure 3.9(f) resulting from the new process represents better results than Figure 3.9(c).

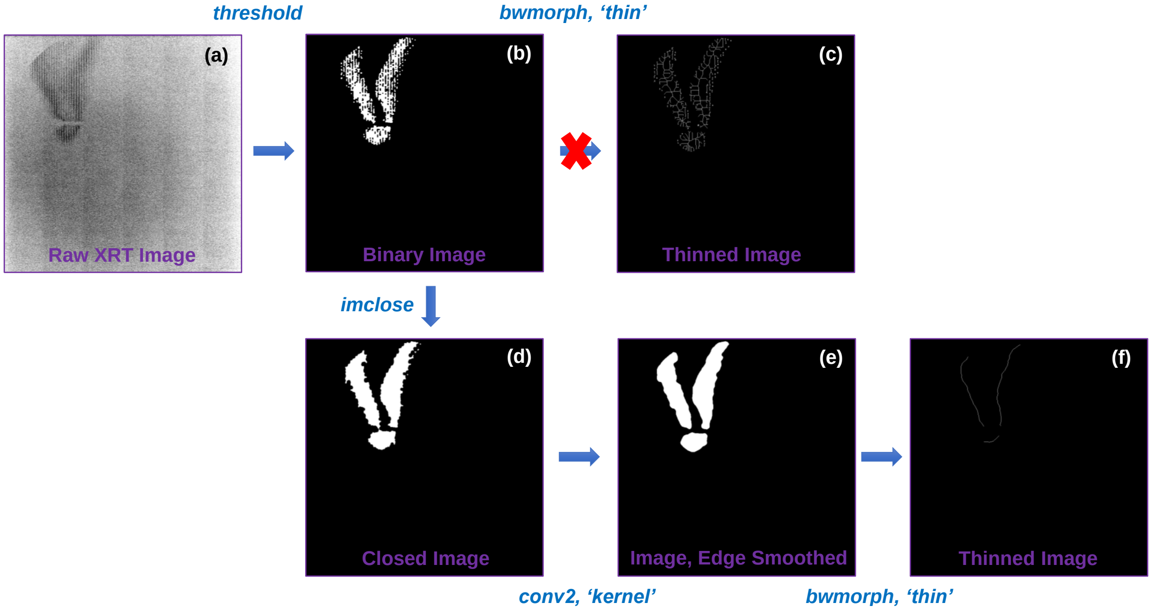

Figure 3.9: Process flow to extract $K_{\alpha 1}$ signals from raw XRT images taken on encapsulated silicon solar cells.

Note that the *conv2* is very sensitive to the line width of the X-ray signal. For thin lines, aggressive *conv2* will dilate the signal area and results in incorrect $K_{\alpha 1}$ lines. In fact, a narrow diffraction line (before the thinning process) requires a lower level of edge smoothing. Therefore, a partial image thinning process is included in the process flow. For that reason, parts of the lines on the closed images are taken out and processed with *conv2* at a different level, as shown on the right side Figure 3.6.

3.3.2 Stacking $K_{\alpha 1}$ Signals and Interpolation

The above data extraction processes are applied to every single raw XRT image such that a series of images with $K_{\alpha 1}$ lines at discrete ω_{sweep} values is obtained (Figure 3.10(a)). Figure 3.10(b) shows the diffraction lines resulting from the overlay of the lines extracted from individual images. Each diffraction line originates from the spots on the cell that met the Bragg condition at a particular ω_{sweep} angle; different spots on the sample meet Bragg's conditions at different ω_{sweep} angles. As we can see in Figure 3.10(b), the diffraction lines are curved and twisted in various directions. Figure 3.10(c) shows the 3D ω map that is constructed by a thin-plate spline interpolation [58] that extracted $K_{\alpha 1}$ diffraction lines (shown as black lines) to the entire area [46]. Each ω value inside the sample edge (gray dashed line) represents the angular conditions where Bragg diffraction on the sample takes place in Figure 3.10(b). Please note that Figure 3.10(b) and (c) show the same data with (b) showing the measured ω_{sweep} values and (c) showing the interpolated ω values. The ω map reveals that the sample is significantly bent. Note that such ω maps do not show the sample's deflection in Cartesian coordinates but in angles.

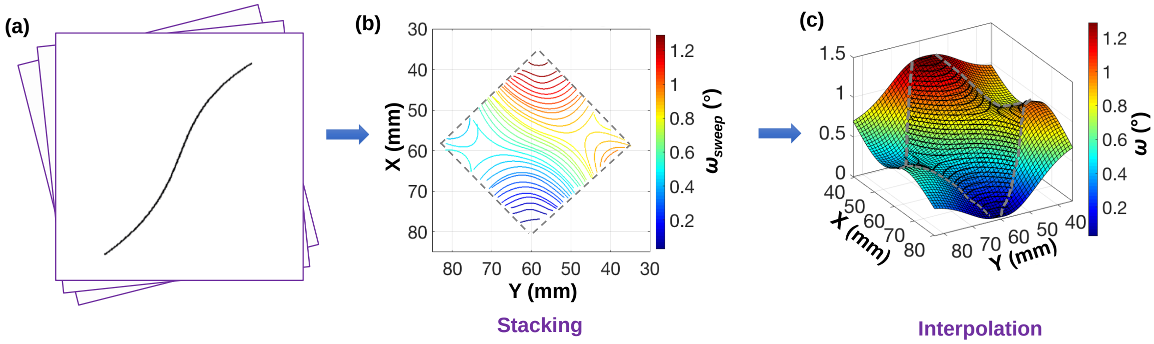

Figure 3.10: (a) a series of images with extracted $K_{\alpha 1}$ lines; (b) processed ω_{sweep} map of stacked Bragg diffraction $K_{\alpha 1}$ lines; (c) interpolated 3D ω map. Gray dashed lines indicate sample edges. The ω values outside of gray dashed lines are extrapolated from the fitting process without physical meaning.

3.3.3 ω Map to Deflection Map Varied by Tabbing

Solar Cells without Tabbing

As mentioned before, two ω maps are needed to calculate deflection such that two sets of raw images were collected. The same process flow was applied to the other set of XRT raw images that was obtained after 90° ϕ rotation. The diffraction information of each set is processed into 2 separate ω maps for the 2 different ϕ positions. Only from the combination of two ω maps from distinct ϕ angles, we can reconstruct the full deflection using the deflection model described in Section 3.1.

Solar Cells with Tabbing

Metal ribbons are soldered on solar cells to facilitate photo-generated carrier extraction. Due to the intensity limitation of the lab-based X-ray source, the metal ribbons absorb most of the incident X-ray and cannot be evaluated. Figure 3.11 shows a clear example of this ribbon-blocking issue. On the EL image in Figure 3.11(a), we can clearly identify the two ribbons as dark lines because they block the fluorescence signal illuminated from silicon. The same phenomenon takes place on the XRT image in Figure 3.11(b) where the signals of both $\mathrm{K}_{\alpha 1}$ and $\mathrm{K}_{\alpha 2}$ lines are missing at metal ribbon locations. As a result, the ω information under metal ribbons cannot be captured for interpolation.

The ω values in the ribbon areas can be extrapolated using the same thin-plate interpolation method. However, without the discrete ω_{sweep} values, extrapolation could easily increase the uncertainty and errors in the final deflection maps. For that reason, the ribbon areas will be blanked and shown as no data.

It is challenging to develop the whole-cell deflection map without the ω values in the ribbon area. In Chapter 3.1, we introduced the deflection calculation method of

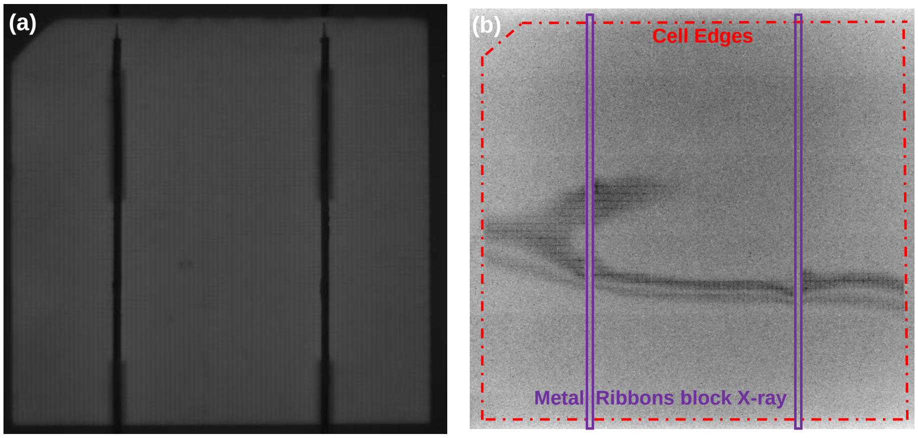

Figure 3.11: (a) El image and (b) raw XRT image of a soldered and encapsulated 3" PERC silicon solar cell.

using the cell center as the reference point and calculating the deflection of each pixel referencing to its neighbor pixel. Without the ribbon area serving as 'the bridge' connecting the data on each side of ribbons, the cell deflection beyond ribbons cannot be calculated. In this case, three approaches are developed to solve this issue: Deflection-Full, Deflection-Global, and Deflection-Busbar.

Deflection-Full interpolates the ω values at the ribbon areas. The thin-plate spline interpolation function performs surface interpolation on two criterions: matching the developed surface with the input data values and lowest surface roughness. It is observed that ω values on each side of the ribbon area differ dramatically due to ribbon-induced mechanical stress. When the interpolation is performed in the Deflection-Full approach, the spline function tends to smooth out the ω difference (generate artifacts), which is crucial in extracting mechanical behaviors. This also influences the sequential deflection values beyond the ribbon area.

Both Deflection-Global and Deflection-Busbar calculate the deflection of the soldered solar cell as individual solar cells that are separated by the ribbons. In this way, the interpolation artifacts can be completely avoided. The detailed process is shown in Figure 3.12. Figure 3.12(a) demonstrates a ω map with the ribbon area blanked out. The left, middle, and right cells are designated with Cell-1, Cell-2, and Cell-3. The three solar cells are then calculated independently using the ω values in the designated areas. For example, Deflection-1's reference point with 0 value in Z direction is the center of cell-1 instead of the entire cell. Then the deflections of three cells are combined as the deflection of the entire cell. Now that the new deflection map has three reference points with 0 value in Z direction – the three cells need to be aligned to one reference point.

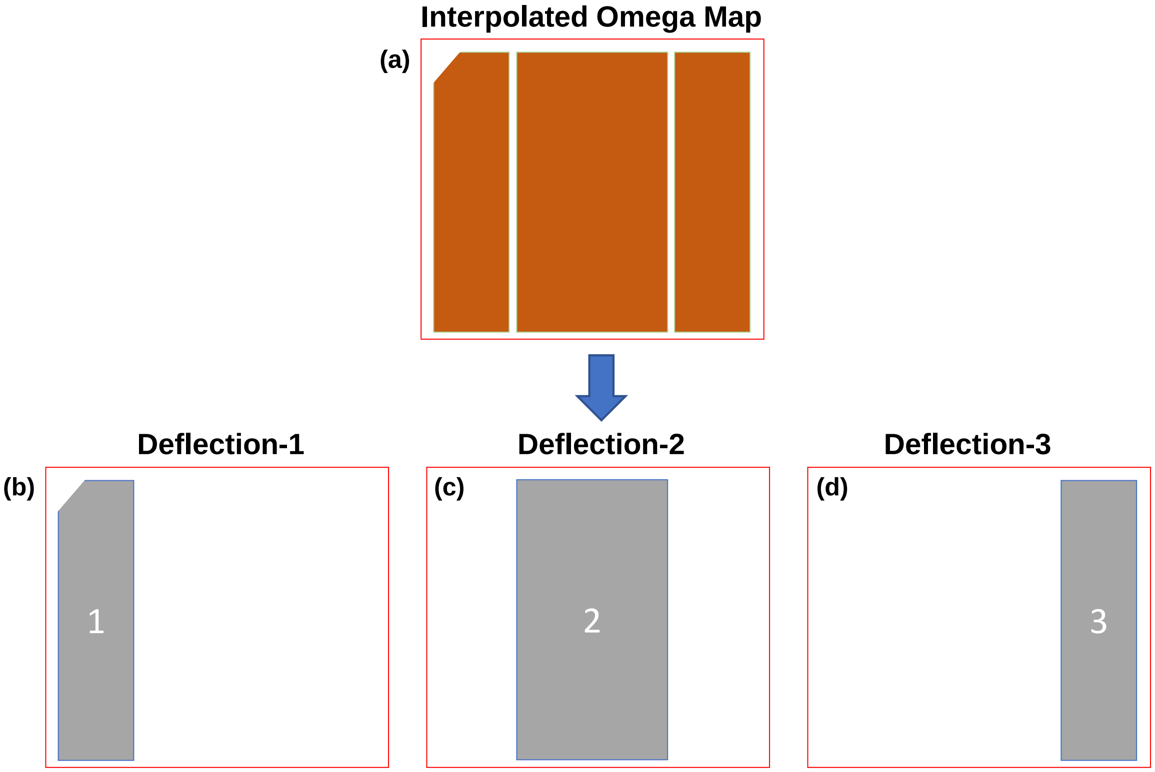

Figure 3.12: (a) Interpolated ω map of a soldered silicon solar cell; (b-d) three deflection maps calculated by treating the whole cell as three separated solar cells.

The Deflection-Global approach aligns the three cells by referring to the values in Deflection-Full map as shown in Figure 3.13. In this case, four deflection maps are generated: Deflection-1, Deflection-2, Deflection-3 and Deflection-Full (Figure 3.13(a-b)). The values of three reference points in the Deflection-Full maps are extracted and used to shift the whole Deflection-1 and Deflection-3 maps in Z direction.

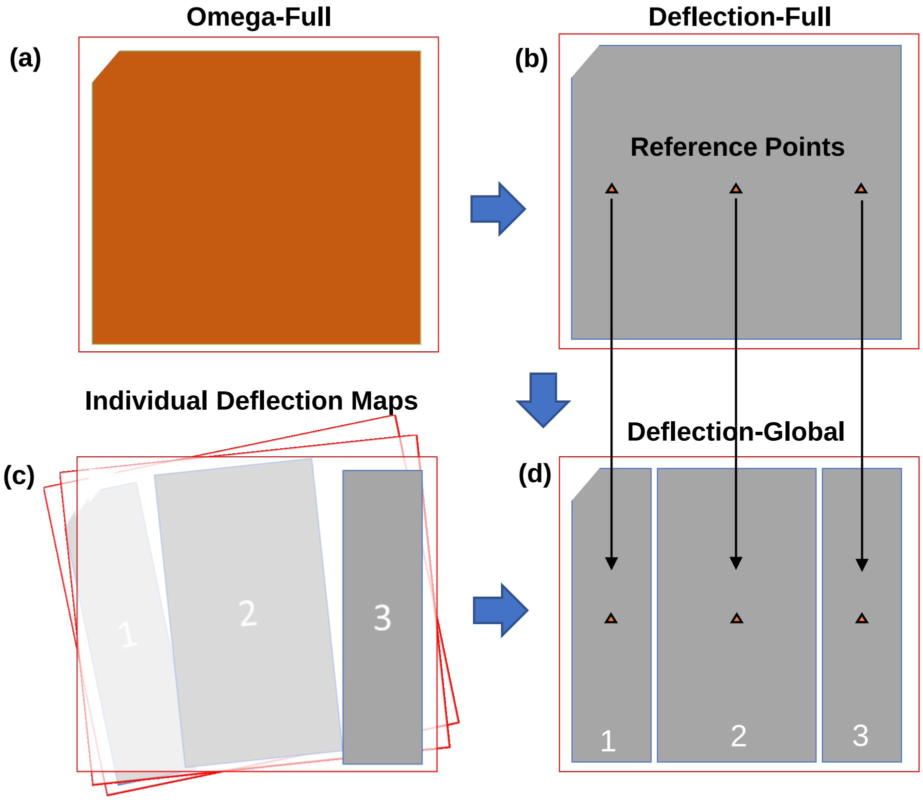

Figure 3.13: (a) Interpolated ω map of a soldered silicon solar cell with extrapolated ω values under ribbons; (b) calculated deflection-full map from (a); (c) stack of three deflection maps of individually treated cells; (d) calculated deflection-global map using three reference points from Deflection-full map.

The Deflection-Busbar approach aligns three cells by assuming that the solar cells under ribbons are flat and horizontal. In other words, the cell deflection values on either side of ribbons are identical. In this case, the Deflection-1 and Deflection-3 maps are shifted in Z direction by the values of the triangles in Figure 3.14.

Apart from aligning in Z direction, a surface rotation is added for both Deflection-1 and Deflection-3 maps. During the deflection calculation, the orientation of the sample is set by the normal direction of the reference point. The three deflection maps have three reference points such that they are calculated at three different orientations. The surface rotation is carried out by referring to the corresponding ω values on the Omega-Full map, as shown in Figure 3.13(a).

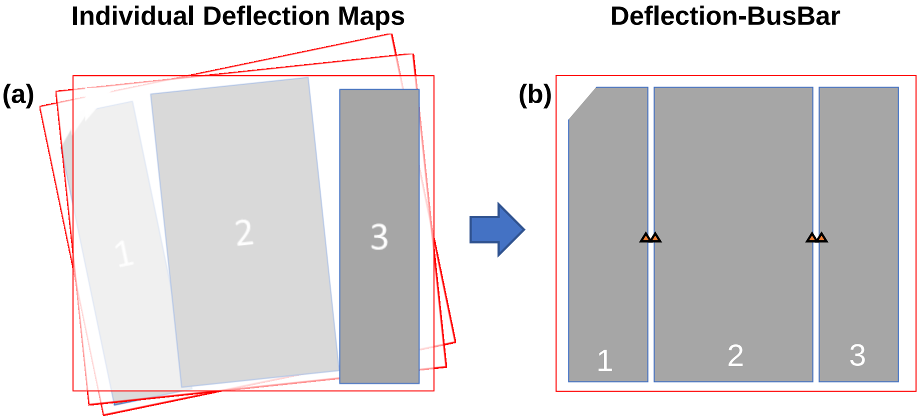

Figure 3.14: (a) Stack of three deflection maps of individually treated cells; (b) calculated deflection-BusBar map using reference points on either side of busbar.

Now we have to choose one of the three approaches. It is obvious that the Deflection-Full approach has the most artifacts/errors because of the extrapolation under ribbon areas and should not be considered. However, three deflections values in the Deflection-Full map are used in the Deflection-Global approach. In order to choose between Deflection-Busbar and Deflection-Global, a partially soldered silicon solar cell was fabricated, measured with XRT and processed with all three processes. A photo of the sample and a schematic of the side view of the module is shown in Figure 3.15. The ribbons only cover a bottom portion of the front busbar and a top portion of the back busbar. The middle portions of the front and back busbar are not soldered such that its deflection on the Deflection-Full map is not susceptible to extrapolation.

The calculated Deflection-Full, Deflection-Global and Deflection-Busbar maps are shown in Figure 3.16(a-c). Visual inspection does not reveal the advantage of the Deflection-Global approach and the Deflection-Busbar approach over each other. A cross-section (purple dashed line) is investigated at the same location of the three maps in ribbon-free areas and the deflection profile is shown in Figure 3.16(d). Note that the curvatures of three curves differ the most in the vicinity of the busbars

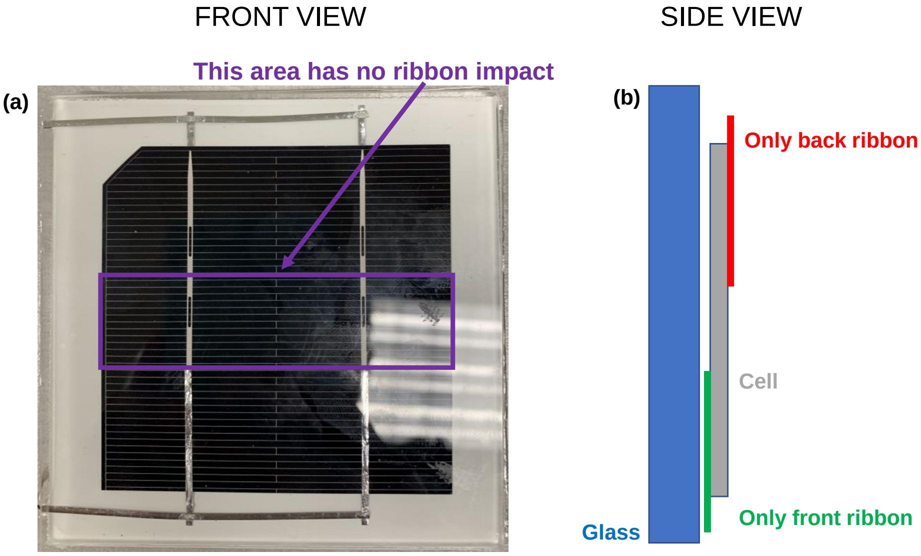

Figure 3.15: (a) Top view and (b) side view of a partially soldered and encapsulated silicon solar cell.

because the probed Deflection-Full profile is still influenced by the ribbon interpolation. For the Cell-1 area on the left, both the Deflection-Global map and the Deflection-Busbar map are close to the Deflection-Full map. For the Cell-3 area, the Deflection-Global map demonstrated more agreement to the Deflection-Full map than the Deflection-Busbar map. Therefore, we consider the Deflection-Global approach as the more accurate process with a maximum deviation of 0.02 mm with respect to the Deflection-Full map. And the Deflection-Global approach will be applied to all following deflection maps. For convenience, the Deflection-Global maps will be named as Deflection maps.

3.4 Application Results and Discussion

The lamination process is crucial in determining the performance and reliability of PV modules. The lamination quality is influenced by the following factors: (a) lamination temperature, (b) lamination pressure, (c) lamination time and (d) lamination stack. A well-controlled and optimized lamination process should lead to good

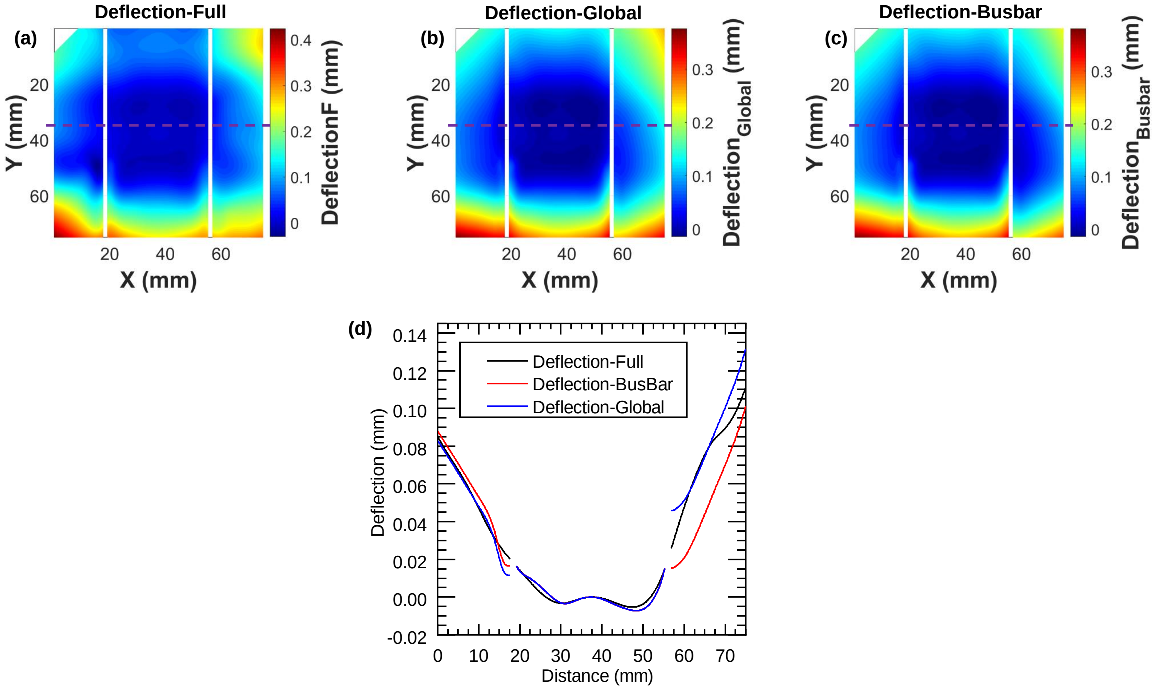

Figure 3.16: (a) Deflection-Full map calculated from Figure 3.13(a); (b) calculated deflection-Global map; (c) calculated deflection-BusBar map. Note that blue means the solar cell is bent toward the front glass and red means the solar cell is bent away from front glass. (d) cross-section of the deflection on the silicon solar cell as indicated in (a-c) at Y = 37.5 mm.

electrical contact (no shunting), no cell cracks, minimum stresses on solar cells, and low degradation rate (both in the field and accelerated tests) in finished modules [59]. When new PV module concepts are promoted, the lamination stack usually differentiates from traditional ones. The lamination temperature and time are often adjusted for acceptable quality (>80% gel content for EVA) in the encapsulant [59]. Altering those parameters may completely change solar cells' surrounding environment, resulting in different cell behaviors (deflection, stress, resistance, etc.). Though the rest (e.g. resistance) can be readily characterized by techniques such as EL, the deflection and stress are difficult to measure due to the lack of testing methods. In this section, we first validate our XRT calculation method with established experimental methods. And then, with the help of XRT, we characterize the impact of varying

(a) lamination temperature; (b) lamination stack and (c) accelerated testing on the deflection of encapsulated silicon solar cells.

3.4.1 Example 1: Deflection Validation

In order to validate our deflection calculation, we characterized an intentionally bent silicon wafer by profilometry and XRT analysis, following the above-mentioned calculation method. As shown in Figure 3.17, the silicon wafer (31.8 mm × 31.8 mm × 180 μm) was mounted on a glass substrate (50.8 mm × 50.8 mm), with the solar cell's center elevated from the glass by multiple layers of tape of 0.3 mm in total. The cell's four corners were glued to the glass by epoxy, and two of the cell's sides were pressed toward the glass during epoxy solidification to purposely induce a two-dimensional deflection.

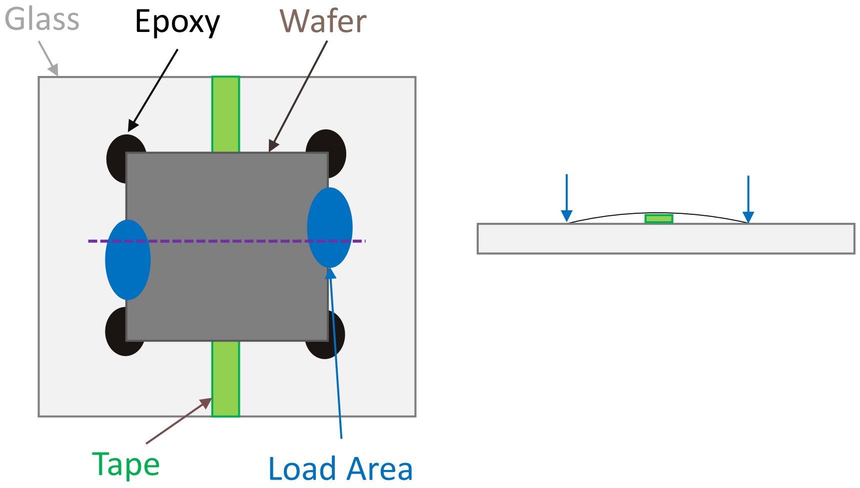

Figure 3.17: Scheme of the Sample used for validating the XRT deflection calculation method with profilometry measurement.

Both XRT and profilometry results are shown in Figure 3.18. As we can see from the XRT analyzed deflection map (Figure 3.18(b)), the wafer has its minima positions on the opposing sides depicted by the white ellipses in Figure 3.18(a), where we intentionally applied pressure. Note that Figure 3.18(b) was measured from the front side of the glass, which means the incident X-rays go through the glass and then to the silicon wafer. Blue means the wafer was bent toward the glass; red means the wafer was bent away from the glass. The four corners have higher Z values than these minima edge points due to the thickness of the epoxy between the wafer and the glass. We performed profilometry measurements along three lines A, B, and C as shown in red in Figure 3.18(a) and (b). We extracted the data corresponding to the same lines from our reconstructed deflection map from XRT in Figure 3.18(b). The reconstructed deflection from XRT matches well with the measured one by profilometry in terms of depth and shape, showing a maximum deviation of $<0.025\,\text{mm}$. Errors from profilometry measurements and from XRT analysis contribute to this difference. The relative error in C is larger than the other two because of the shifted peak, which we attribute to the errors from interpolation. Overall, this demonstrates that our XRT reconstruction method is able to reproduce the deflection of the specimen indicating that XRT is a powerful way of inspecting the deflection in a silicon wafer in a non-destructive way.

3.4.2 Example 2: Lamination Temperature

The lamination temperature is one of the most important parameters in determining the lamination quality of PV modules. Several failure modes such as delamination are associated with the time-temperature and time-pressure profiles. Higher temperature favors higher gel contents, but it may cause potential higher stresses on the solar cell because of larger thermal expansion and shrinkage of the backsheet and encapsulant due to different thermal materials properties. Three $5\,\text{cm}\times5\,\text{cm}$ modules following the traditional PV stack (glass/EVA/cell/EVA/ backsheet) were laminated at three different temperatures (100°C, 145°C, 160°C) for XRT analysis and the data are shown in Figure 3.19 [60]. The EVA encapsulant starts curing at 110°C [11]. As

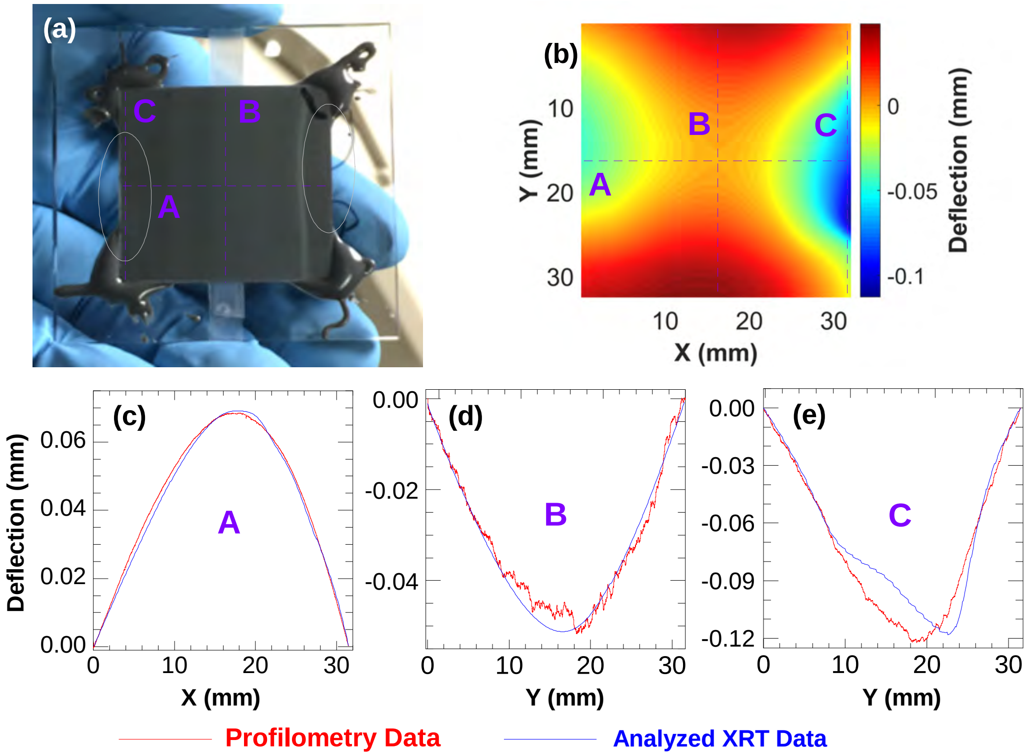

Figure 3.18: (a) Picture of an intentionally bent silicon wafer; (b) map of the calculated deflection on the wafer; (c), (d), (e) are profilometry measured and analyzed XRT data showing the wafer deflection along the marked as purple dash lines shown in (a) and (b).

the temperature increases, the total deflection on the cell (maximum Z value minus minimum Z value) increases; the corners of the cell are bent towards the front glass while the center is bent toward the back.

Although intrinsic stress (e.g. stresses introduced by cell fabrication) could potentially lead to deflection too, we attribute it here to the lamination process as the pristine cells were not bent. We expect this bending feature to be a combination of two effects: (i) the soften EVA was pressed out of the laminate because the applied pressure was higher at the module edges (edge pressing); (ii) the shrinkage of backsheet put more compressive stress on the cell back, which pulls the cell corners backward during solidification. The cause of the first item is due to the thickness of the finished modules not being homogeneous – the corners are thinner than the center. A bowing behavior on the backsheet (concave towards the glass) is observed. If the first item dominates, the cell corners will bend towards the glass, just like the backsheet. The cause of the second item is due to the fact that the CTE of the backsheet is ~11 times larger than the glass [61]. If the second item is true, the cell corners will bend towards the backsheet. The measured deflection results are in favor of the first item, indicating that the edge pressing dominates and leads to this bowing result. The total deflection of 100°C module is around 0.03 mm while the deflection of 145°C and 160°C modules are above 0.06 mm. A positive correlation between the total deflection and lamination temperature (Figure 3.19(d)) is identified. This suggests that the lamination induced deflection on the cell is associated with the temperature – the higher temperature the more deflection on the cell.

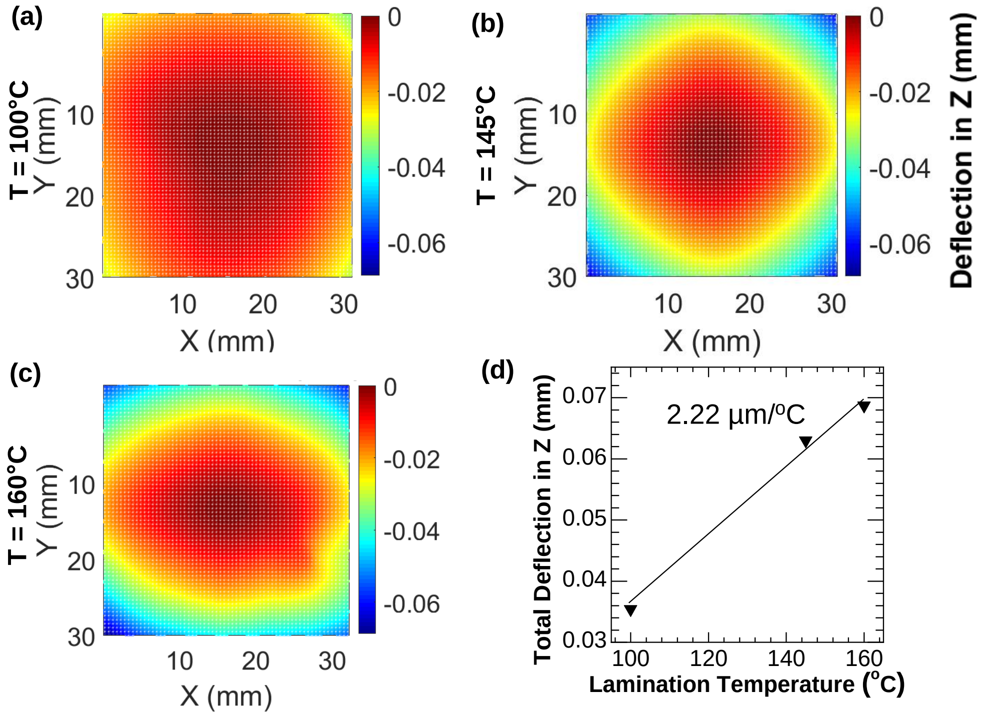

Figure 3.19: XRT analyzed deflection maps of three 5 cm×5 cm modules laminated with EVA at three temperatures: (a) 100°C; (b) 145°C and (c) 160°C. The corners are bent toward the glass. Bright means high and dark means low in the Z direction (point in the plane of this paper). (d) Figure showing the total deflection as a function of lamination temperature using the cell deflection from (a), (b) and (c).

3.4.3 Example 3: Lamination Stack

The lamination stack is also an important factor when it comes to cell deflection and analysis. Here we apply our XRT analysis method to quantitatively evaluate the effect of different lamination stacks of the PVMirror stack and the standard stack on cell deflection. PVMirror modules are newly developed module structure with extra layers of encapsulant and polymeric film in the lamination stack, which will be discussed in Chapter 8. We characterized two 5 cm×5 cm modules following traditional PV stack and PVMirror stack and the results are shown in Figure 3.20 [60]. From visual inspection, both modules look flat. However, the XRT deflection maps of both laminated cells reveal that they are actually bent, with the cell's corners towards the glass and cell's center away from the glass. The cell inside Figure 3.20(a) shows 60 μm total deflection from the corner to the center, while the value in Figure 3.20(b) is 0.14 mm, i.e. 230% as large as in Figure 3.20(a). As discussed earlier, the edge

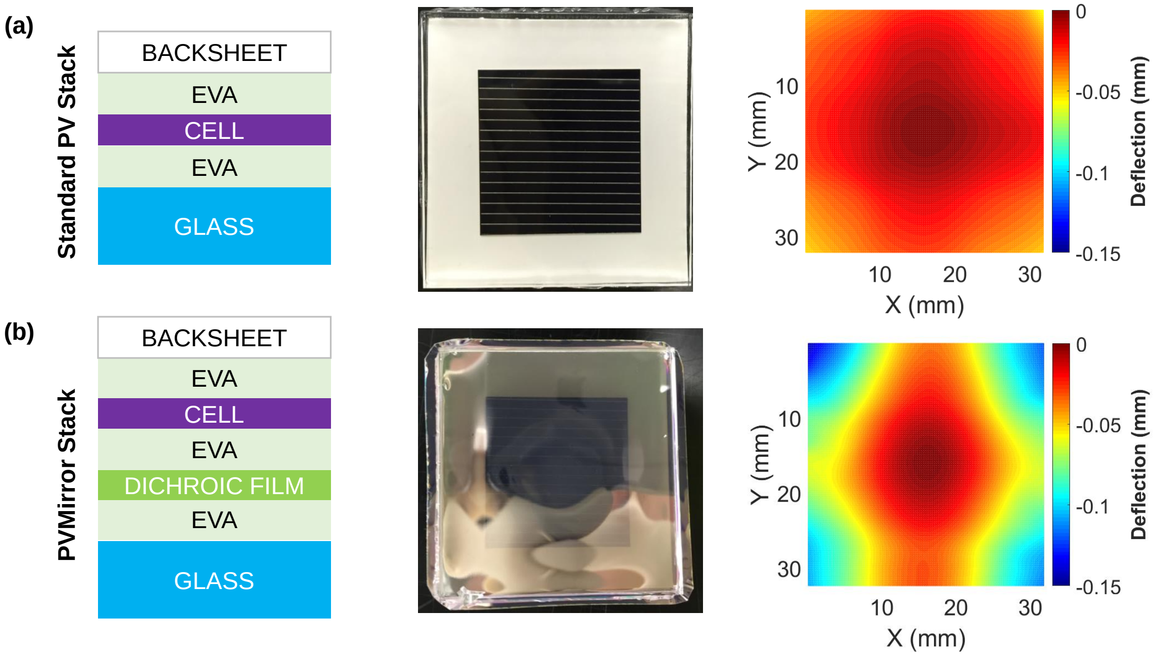

Figure 3.20: Lamination stack, photos and deflection maps of 5 cm×5 cm PV module fabricated with (a) traditional PV stack and (b) PVMirror stack, respectively.

pressing dominates the cell bending in those 5 cm×5 cm modules. As more encapsulant is used in the stack, more encapsulant is pressed out of the module, resulting in increased deflection of the cell. It is interesting to isolate the edge pressing from the result to see the effect of different CTE values in materials. A frame of different height around the module and/or larger modules could be used to minimize the edge pressing in future work.

3.4.4 Example 4: Accelerated Tests

Most of the modules that failed in the DH1000 test experience water ingression and encapsulant degradation (e.g. adhesion loss) [16]. Replacing the encapsulant and backsheet with materials of lower water vapor transmission rate and better chemical bonding is often the solution. Here we tend to investigate the process through the view of solar cells in terms of deflection. Figure 3.21(a) and (b) show the deflection map of Figure 3.20(a) and (b) after damp heat (DH1000, 1000 hours of 85°C/85% RH) test [60].

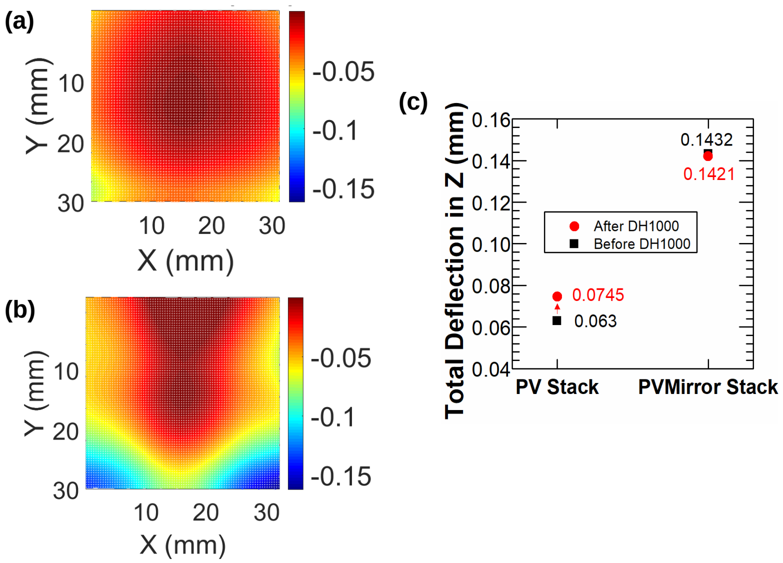

Figure 3.21: Deflection map of PV module following (a) a traditional stack and (b) PVMirror stack post DH1000; (c) analyzed figure showing the total deflection changes between PV stack and PVMirror stack, both before and after DH1000 test.

The DH1000 test is designed to stress the PV module to reveal potential lamination problems such as delamination and corrosion. The total cell deflection comparison before and after DH1000 (Figure 3.21(c)) indicates that there is no significant change ($<0.03\,\mathrm{mm}$) in terms of total deflection. However, the deflection map of the solar cell varies a lot, suggesting that the distribution of stresses acting on the cell change through time. Both modules' top half area on the deflection map show increased Z values. The curing process is a thermal cross-linking process. Even the optimized lamination recipe can hardly deliver 100% gel content in EVA; the left-over uncured EVA can still soften at a temperature of 85°C [13]. Additionally, the polymer's shape changes under elevated temperature and humidity environment. All of those factors contribute to the delamination in PV modules eventually [62].

Chapter 4

ERROR AND SENSITIVITY ANALYSIS

In Chapter 3, we introduced a non-destructive method of using X-ray topography to inspect cell deflection in encapsulated PV modules. The deflection mapping method shows comparable results with profilometry measurement with a maximum physical deviation of $<0.025\,\text{mm}$ and is able to quantitatively measure the amount of cell deflection influenced by different lamination parameters. More importantly, the statistical error, both from XRT measurement and data processing, should be quantified such that the measured cell deflection can be trustworthy. Meanwhile, the sensitivity analysis of important parameters should also be quantified to further improve the speed and quality of this deflection mapping method.

In this Chapter, a 3" PERC silicon solar cell laminated with the traditional stack (glass/EVA/cell/EVA/backsheet) was used as the reference module for error and sensitivity analysis. The module was laminated at 145°C for 11.5 minutes (curing time). By default, the XRT measurement takes 18 images (10 in the first set and 8 in the second set with a 90° ϕ angle difference). Each image was taken under 8 X-rays sweeps at a sweeping speed of 2 mm/s. Note that the error and sensitivity analysis demonstrated in this chapter only applies for PV modules of this kind – the result may vary depending on module configurations.

4.1 Error Estimation

A lower statistical error means lower variation in the deflection values from multiple measurements on the same sample. The statistical error of this XRT method originates from the measurement and the data processing.

4.1.1 Error from Measurement

The errors from the measurements originate from improper mounting, imprecise motor behavior in angle rotation, incorrect discrete ω_{sweep} values and incorrect translating range. Every angle rotation is performed according to the center of the sample holder. If the sample is not placed at the holder center, both ϕ and ω values will be off and a 90° ϕ rotation will not be reached. Incorrect discrete ω_{sweep} values will result in missing features in the deflection maps, especially in the high-stress areas. Incorrect translation range will reduce the X-ray intensities or lose X-ray signals on the left and right (in X direction) of the solar cell, resulting in incorrect deflection.

In this subsection, the reference module was measured four times by the default conditions and processed using the same Matlab code. Note that the module was demounted and remounted for each measurement. The four deflection maps are shown in Figure 4.1. No significant visual deviations are identified. Note that the errors from the mounting discussed here contain the errors from manual thresholding.

To quantify the mounting effect on the deflection measurement, the standard deviations of the four maps are calculated on a pixel by pixel basis as shown in Figure 4.2(a). A maximum deviation of 0.016 mm is observed. The cross-sections of the four deflection maps perpendicular to the busbars that are selected at the highest deviation point are shown in Figure 4.2(b). The deviations on the right edge are attributed to the combination of incorrect sweeping range, improper mounting, and manual processing. The high deviation in the cell-2 region is attributed to the incorrect discrete ω_{sweep} values. In conclusion, the statistical deviations from measuring and processing the same sample are estimated to be within 0.016 mm.

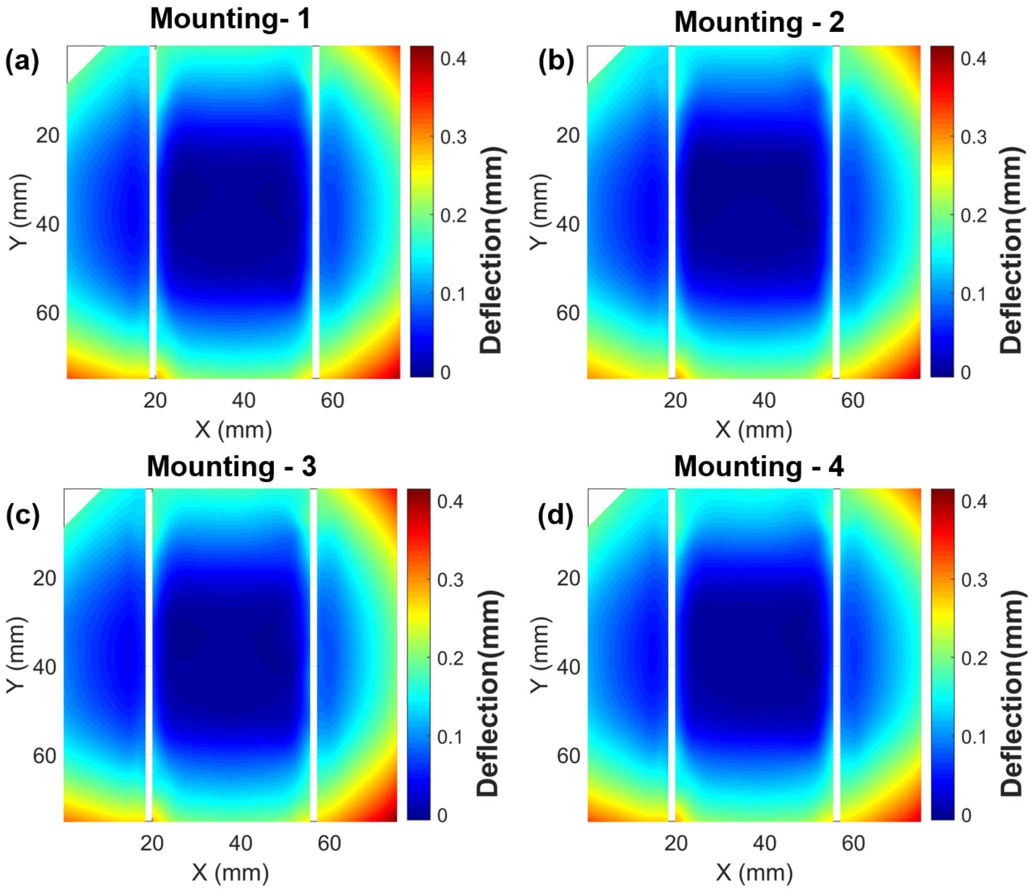

Figure 4.1: Four deflection maps (a-d) processed by the same Matlab code using the four set of measured data from a 3” PERC soldered solar cells.

4.1.2 Error from Data Processing

Ideally, applying the same data process to the same data set should result in the same deflection. In data processing, the statistical deviations come from manual thresholding, thinning, and interpolation. The threshold value that is determined manually varies from image to image because each image has different $K_{\alpha 1}$ X-ray intensities. The thinning is dependent on the shape and edge roughness of the $K_{\alpha 1}$ signal on the binary image. Interpolation may introduce a certain amount of artifacts in the ω maps due to the definition of surface fitting. In this case, the manual thresholding process is determined to have the largest amount of deviations.

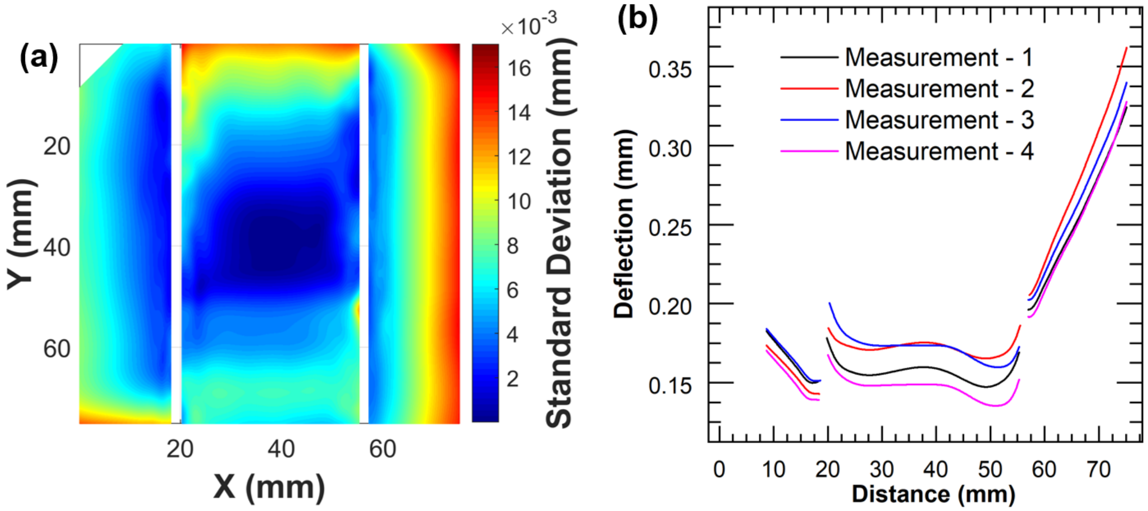

Figure 4.2: (a) Standard deviation of the four deflection maps shown in Figure 4.1 on a pixel by pixel basis; (b) the cross-secitons of the four deflection maps at Y = 0 mm, as the purple dashed line indicated in (a).

In this subsection, the data set from a single complete XRT measurement using default conditions was processed 4 times using the same Matlab code to investigate the errors introduced by manual thresholding. The calculated deflection of the four processes are shown in Figure 4.3. Visual inspection indicates that all four maps are similar, except the bottom-left corner where the deflection is higher in the Data Process-1 map and the Data Process-2 map. Visual inspection indicates that all four maps have smaller variation than the maps in Figure 4.1. No significant features are missing or added in any of the maps.

To quantify the deviations from manual thresholding, the standard deviations of the four maps are calculated on a pixel by pixel basis as shown in Figure 4.4(a). Most of the standard deviation values on the solar cell are under 0.006 mm, except the bottom left corner with up to 0.01 mm. The deviation values are smaller than the values in Figure 4.2(a) because they include the deviation from measurements. The cross-sections of the four deflection maps that are selected at the highest deviation point are shown in Figure 4.4(b). The deviations by manual thresholding are

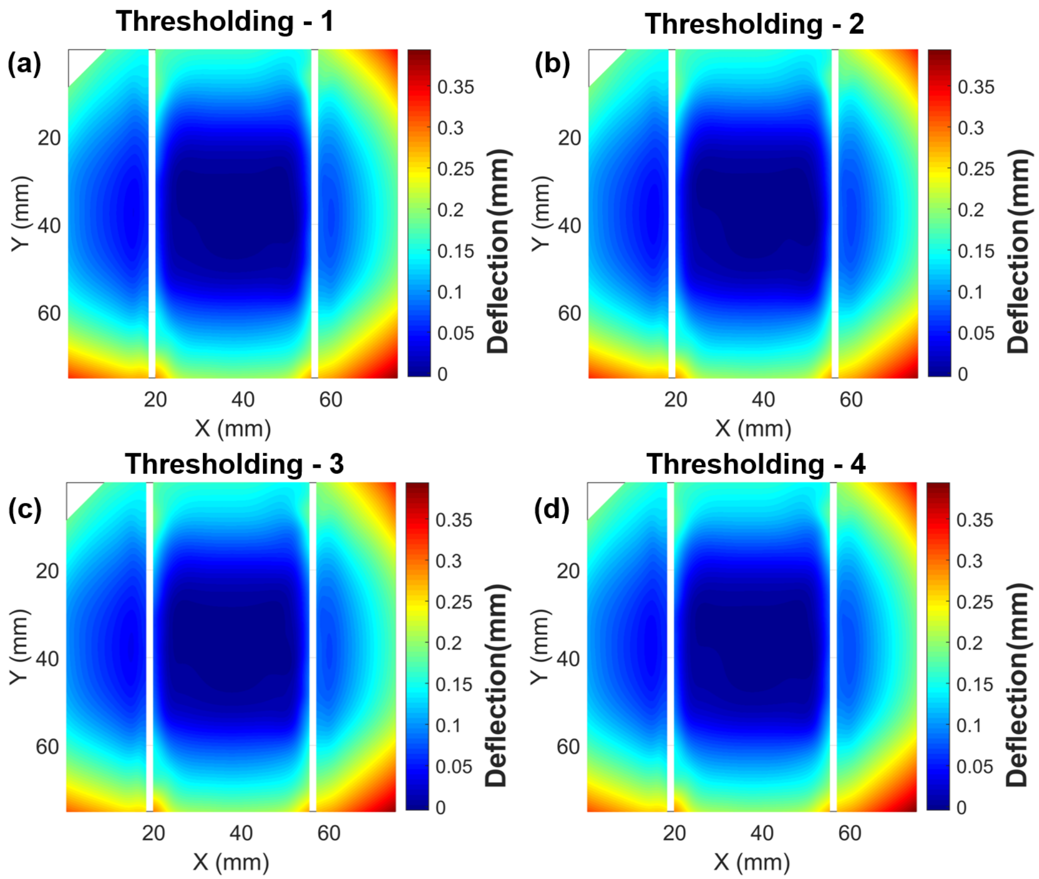

Figure 4.3: Four deflection maps (a-d) processed by the same Matlab code using the same set of measured data from a 3” PERC soldered solar cells.

below 3.3%, considering the measured maximum deflection is about 0.4 mm and the deflection on the bottom-left corner is about 0.3 mm.

4.2 Sensitivity Analysis

The most limiting factor of this deflection mapping method is the low data acquisition. The Rigaku XRT-100 originally used an image plate for a higher resolution of 50 μm (primarily for defect detection). The image plate requires 3-5 min to accumulate the X-ray signal, 4 min to develop the XRT image, and 3 min to erase the X-ray signal. The XRT acquisition time could be 3 times longer if the PV module’s glass dramatically decreases X-ray intensity.

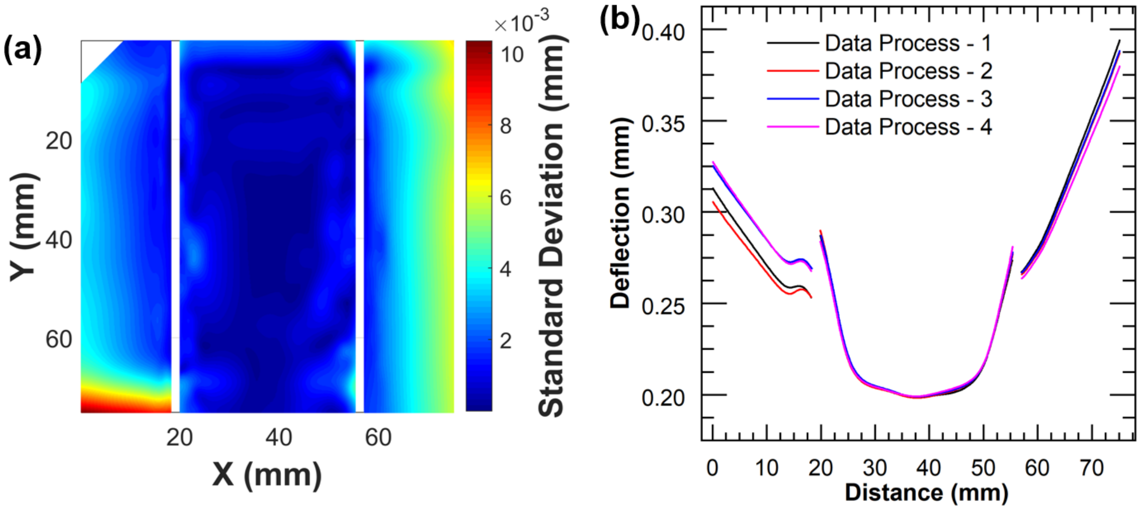

Figure 4.4: (a) Standard deviation of the four deflection maps shown in Figure 4.3 on a pixel by pixel basis; (b) the cross-secitons of the four deflection maps at Y = 78 mm, as the purple dashed line indicated in (a).

To facilitate the process, the semiconductor detector with a 75 μm resolution is used to replace the image plate (Figure 4.5(b)). Since the XRT deflection mapping method focuses on the location of the X-ray signals instead of the intensities, the XRT deflection method is less sensitive to resolution. Without developing and erasing the image plate, an image can now be obtained within 5 min, which reduces the 6" cell module imaging time down to 7-8 hours. However, this is still far too slow compared to other module characterization methods, such as solar simulators and EL imaging.

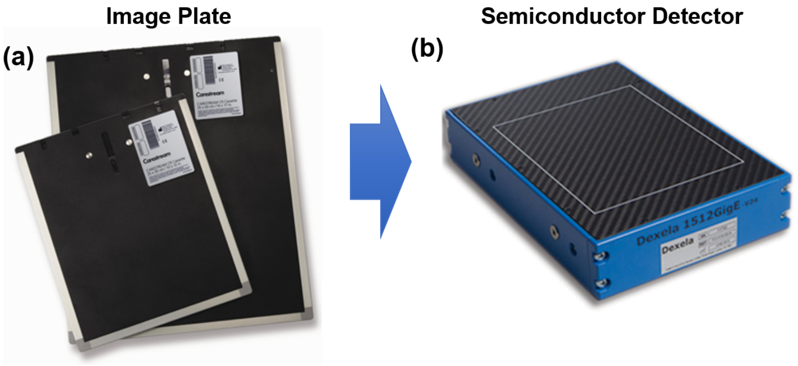

Figure 4.5: Image of (a) the image plate that was installed in the XRT system by default and (b) the succedaneous Dexela 1512 semiconductor detector.

Therefore, in this chapter, the sensitivity of important parameters XRT measurement is investigated on the deflection results.

The data acquisition time of this XRT method is determined by the number of XRT images × X-ray exposure time for each image. As mentioned earlier, it takes 18 images to process a 3" PERC solar cell and each image takes 8 X-ray sweeps at a speed of 2 mm/s. Both the number of X-ray sweeps and sweeping speed contribute to the X-ray exposure time for each image. The exposure time can influence the quality of the thresholding and thinning process. A larger number of sweeps can increase the signal-to-background ratio on raw XRT images such that a more consistent thresholding can be achieved.

4.2.1 Number of X-ray Sweeps on Each XRT Image

In this case, we study the impact of the number of X-ray sweeps while keeping the sweeping speed constant. The reference module was measured five times varying the number of X-ray sweep from 1 to 10 while keeping other parameters constant. Surprisingly, the quality of XRT images degrades as a function of operation time. The signal-to-background ratio decreases from a morning measurement to an afternoon measurement. Figure 4.6 shows the photos of the raw image taken with different numbers of sweep in the order of measurement. In this case, the XRT image with 8 × sweep was taken first, followed by 1 × sweep and then 10 × sweep. The image with 1 × sweep shows the lowest signal-to-background ratio due to low X-ray doses. However, the image with 10 × sweep shows more noise than the image with 8 × sweep due to the decreased detector imaging quality. This degradation phenomenon is attributed to the heat in the detector. This degradation also contributes to the measurement deviation as we discussed in Chapter 4.1.2.

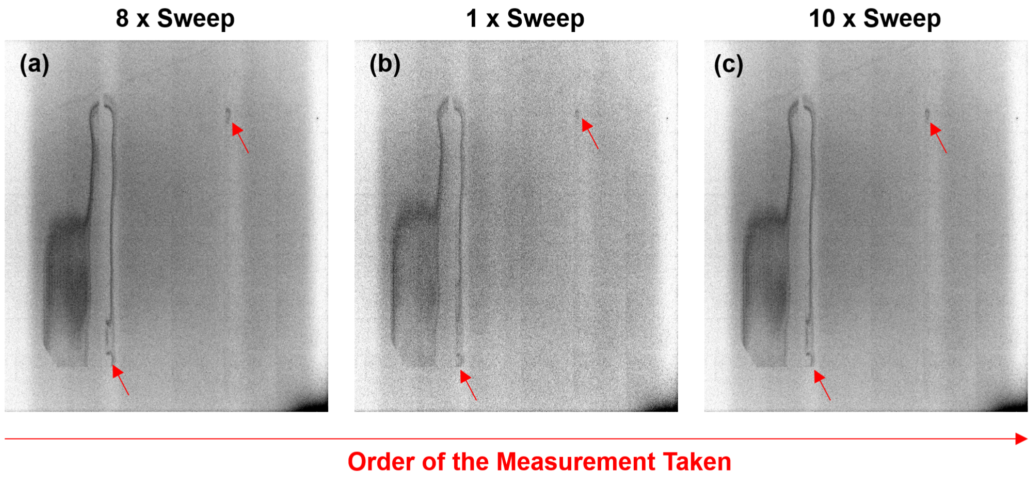

Figure 4.6: Three raw XRT images taken with different number of X-ray sweeps in the order of measurement sequence.

The corresponding deflection maps are shown in Figure 4.7. Visual inspection indicates moderate deflection variation at cell corners (in red color). The deflection maps taken with a smaller number of sweeps do not demonstrate a significant difference compared to the deflection maps taken with a larger number of sweeps. To quantify the impact of sweeping number on the deflection maps, the mean absolute

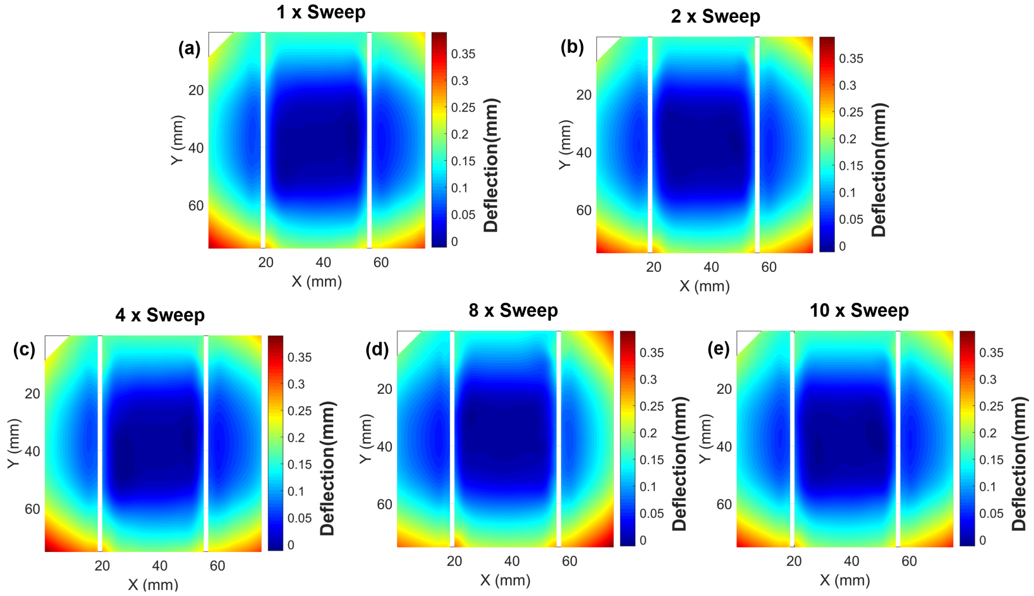

Figure 4.7: Five deflection maps (a-e) processed using the raw XRT image measured at different number of X-ray sweeps from a 3" PERC soldered solar cells.

deviation of the deflection maps are calculated with respect to the deflection with 8 × sweep (Figure 4.7(d) is considered to be the most accurate result from the quality of raw XRT images), shown in Figure 4.8. The mean deviation values show a mixed trend against the number of X-ray sweep, which is a combined result of heat degrading the quality of raw images and more X-ray sweeps increasing the quality of images.

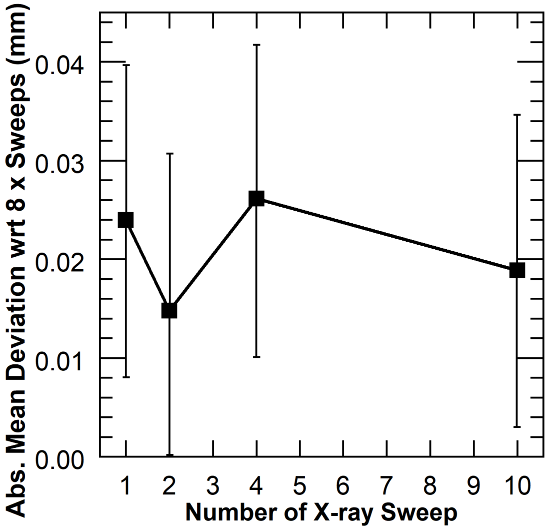

Figure 4.8: Mean absolute deviation of the first four deflection maps in Figure 4.9 with respect to the last deflection map.The error bars are defined by the maximum standard deviation observed in Figure 4.2(a).

4.2.2 Number of X-ray Raw Images

A larger number of XRT raw images increases the density of the X-ray signal (the number of discrete ω_{sweep}) on the stacking image (Figure 3.10(b)) and therefore increases the accuracy of interpolation. Ideally, a finite number of images can provide the discrete ω_{sweep} on every pixel of the solar cell such that no interpolation is further needed. However, due to the time limit of data acquisition, it is nearly impossible to achieve. In fact, there should be an optimal number of XRT raw images that offers enough X-ray signals and requires minimum measurement time.

To study the impact of the XRT image number on XRT results, the reference module was measured with 38 images (30 images in the first set and 8 images in the second set) and processed into a deflection map. Meanwhile, a certain number (5, 6, 10, 15) of the 30 images in the first set were selected systematically and processed into deflection maps. The 5 deflection maps are shown in Figure 4.9. Visual inspection indicates that a larger number of images bring more consistency to the deflection

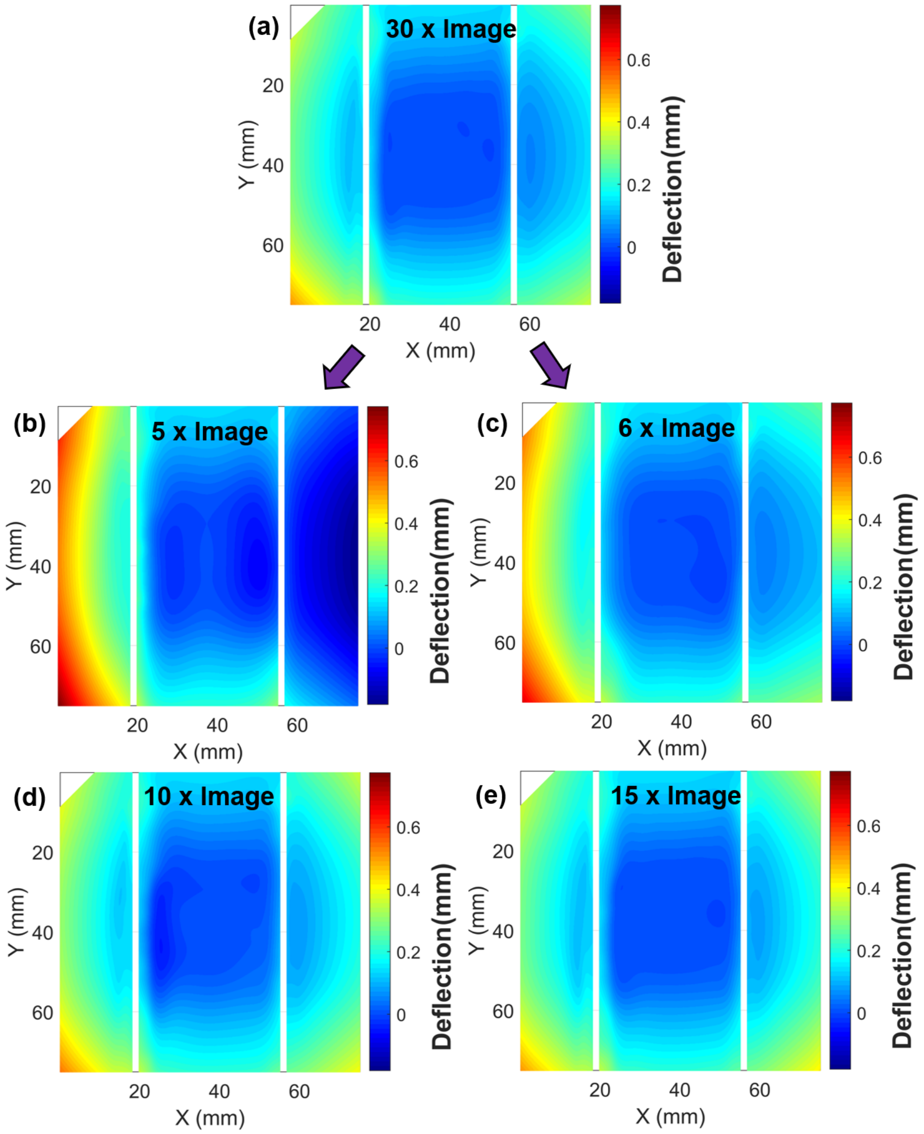

Figure 4.9: Six deflection maps (a-f) processed using different number of raw XRT image measured from a 3” PERC soldered solar cells.

map. The maps with large image numbers show very similar deflection maps; the maps with small image numbers show large variation especially on the cell left.

To quantify the impact of the X-ray signal intensity on the deflection map, the absolute mean deviation of every pixel on the first five maps, with respect to the last image (Figure 4.9(f), is considered as the most accurate result) is calculated and shown in Figure 4.10. The mean deviation decreases as the number of XRT images increases. A mean deviation of 0.1 mm is observed at a low number of images. The first data point of 3 is low because of coincidence. The curve flattens out when the number of image numbers is higher than 10, indicating that the number of 10 is an optimal value considering the least amount of deviation and the least number of images (faster data acquisition).

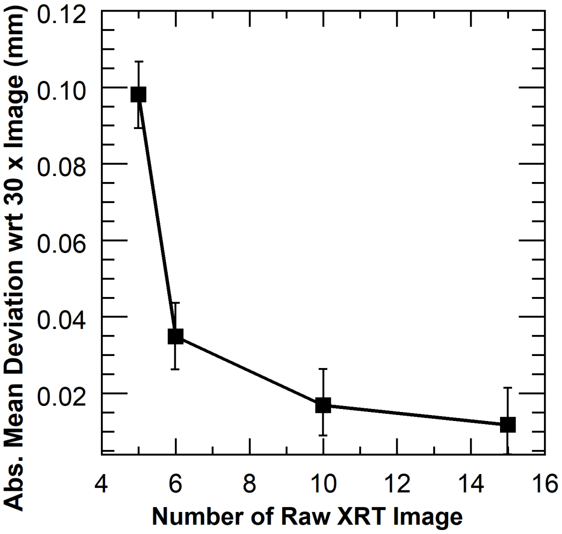

Figure 4.10: Mean absolute deviation of the first five deflection maps in Figure 4.9 with respect to the last deflection map. The error bars are defined by the maximum standard deviation observed in Figure 4.4(a).

4.2.3 $K_{\alpha 2}$ Diffraction Lines

Each raw XRT image has both $K_{\alpha 1}$ and $K_{\alpha 2}$ lines. Also, the $K_{\alpha 2}$ signal originates from Bragg diffraction but at a different X-ray wavelength. Meaning, $K_{\alpha 2}$ lines also contain important information regarding the cell deflection. It is important to investigate the contribution of $K_{\alpha 2}$ lines to this deflection method and the possibility of achieving the same deflection with less data acquisition time.

The ω_{sweep} values of $K_{\alpha 2}$ need to be obtained in the raw XRT images because every image was taken at the ω_{sweep} value referring to $K_{\alpha 1}$. According to Bragg condition, we have:

$$2dsin(\theta_{\alpha 1}) = n\lambda_{\alpha 1} \tag{4.1}$$

$$2dsin(\theta_{\alpha 2}) = n\lambda_{\alpha 2} \tag{4.2}$$

Where $\lambda_{\alpha 1}$ and $\lambda_{\alpha 2}$ are the wavelength of $K_{\alpha 1}$ and $K_{\alpha 2}$, $\theta_{\alpha 1}$ and $\theta_{\alpha 1}$ are their corresponding diffraction angle. Both equations are true at the same time on each image. By the definition of alignment, $\theta_{\alpha 1}$ is the diffraction angle of 15.145° for silicon (004) crystal planes. Combining Equation 4.1 and 4.2, $\theta_{\alpha 2}$ can be calculated to be 15.2368°, which is 0.0938° constantly larger than $\theta_{\alpha 1}$. Therefore, the ω_{sweep} values of $K_{\alpha 2}$ can be readily obtained from the ω_{sweep} values of $K_{\alpha 1}$. The 0.0938° can be confirmed by two raw XRT images, as shown in Figure 4.11. Figure 4.11(a) was taken when

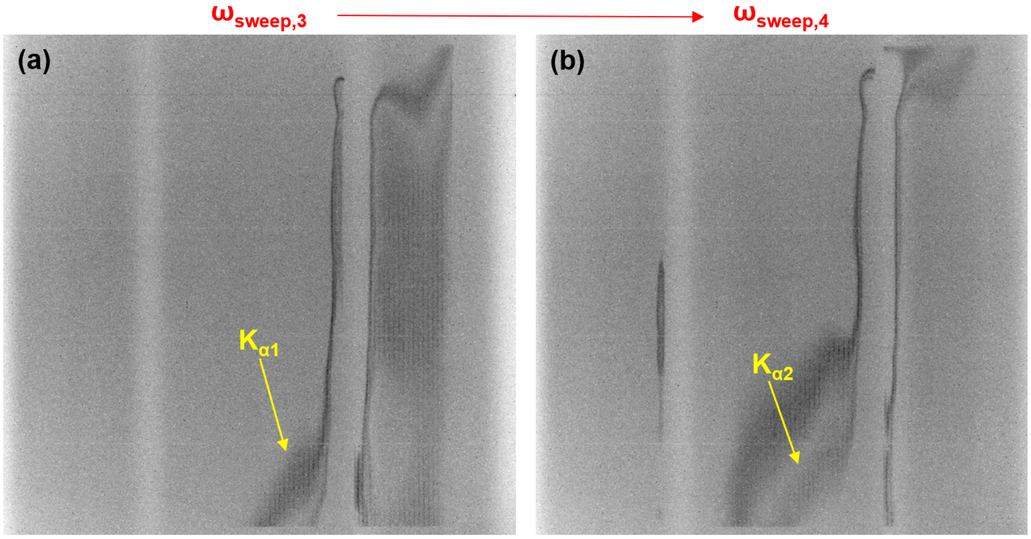

Figure 4.11: Raw XRT images taken at (a) $\omega_{\text{sweep},3}$ and (b) $\omega_{\text{sweep},4}$ using the same sample.

ω_{sweep} = -0.13° and Figure 4.11(b) was taken when ω_{sweep} = -0.02°. With the $\Delta\omega_{\text{sweep}}$ value close to 0.0938°, the position and shape of $K_{\alpha1}$ in the left image are close to the position and shape of $K_{\alpha2}$ in the right image.

The data set used in Figure 4.1(a) was selected to study the contribution of $K_{\alpha2}$ on the deflection results. The ω_{sweep} values for both $K_{\alpha1}$ (obtained at measurement) and $K_{\alpha2}$ (obtained by the calculation discussed above) are shown in Table 4.1. In this case, three deflection maps were processed using either only $K_{\alpha1}$, only $K_{\alpha2}$, or $K_{\alpha1}$ + $K_{\alpha2}$. And the three deflection maps are compared with the 30 × Image deflection map (considered to be the most accurate deflection map), as shown in Figure 4.12.

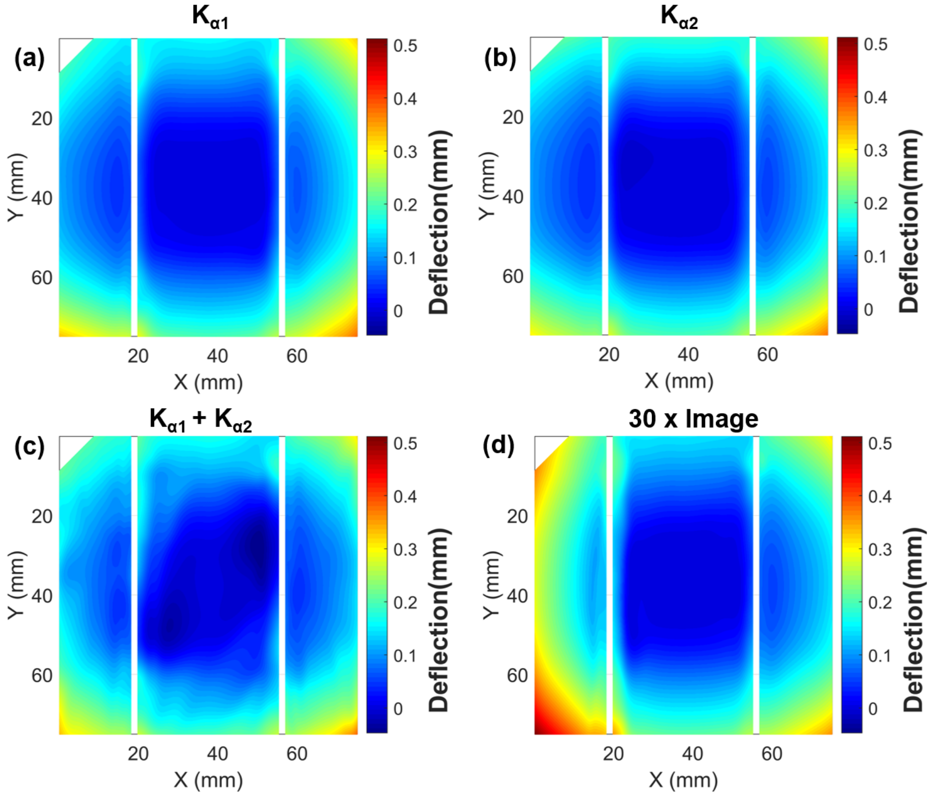

Figure 4.12: Three deflection maps processed using (a) only $K_{\alpha1}$ lines, (b) only $K_{\alpha2}$ lines and (c) both $K_{\alpha1}$ and $K_{\alpha2}$ signals in Table 4.1; (d) is the same deflection map in Figure 4.9(a).

Since both $K_{\alpha1}$ and $K_{\alpha2}$ have the same $\Delta\omega_{\text{sweep}}$ value and it is very close to 0.0938°, Figure 4.12(a) and (b) are very similar. For that reason, adding $K_{\alpha2}$ to $K_{\alpha1}$ should yield similar variations in the deflection maps (Figure 4.12(c)) compared to the $K_{\alpha2}$ map and $K_{\alpha1}$ map. This phenomenon is attributed to the overlapping of $K_{\alpha1}$ and $K_{\alpha2}$ signals.

Table 4.1: List of ω_{sweep} angles corresponding to $K_{\alpha1}$ and $K_{\alpha2}$ signals. Note that NaN means no data.

X-rays	$\omega_{\text{sweep},1}$	$\omega_{\text{sweep},2}$	$\omega_{\text{sweep},3}$	$\omega_{\text{sweep},4}$	$\omega_{\text{sweep},5}$	$\omega_{\text{sweep},6}$	$\omega_{\text{sweep},7}$	$\omega_{\text{sweep},8}$	$\omega_{\text{sweep},9}$	$\omega_{\text{sweep},10}$
$K_{\alpha1}$	-0.35	-0.24	-0.13	-0.02	0.09	0.2	0.31	0.42	0.53	0.64
$K_{\alpha2}$	NaN	-0.1462	-0.0362	0.0738	0.1917	0.2938	0.4038	0.5138	0.6238	0.7328

The deflection map observation is later confirmed by mean deviation analysis. In this case, the absolute mean deviation is calculated with respect to the 30 × Image deflection map. All three deflection maps show the similar mean deviation value around 0.035 mm. This result indicates that adding $K_{\alpha2}$ to $K_{\alpha1}$ is not improving the accuracy of this XRT method. Therefore, this is not recommended when $\Delta\omega_{\text{sweep}}$ is close to 0.0938°.

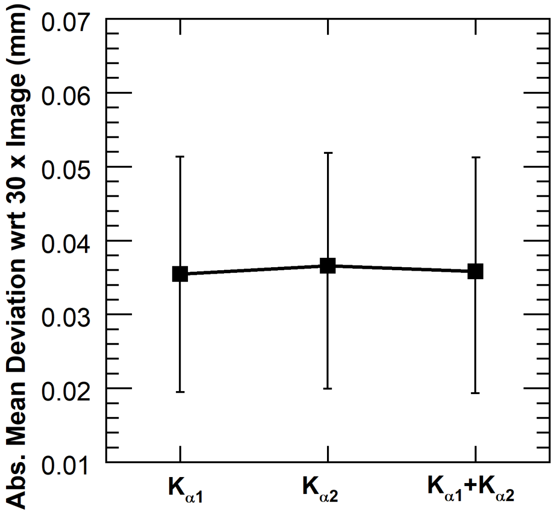

Figure 4.13: Mean absolute deviation of the three two deflection maps in Figure 4.12 with respect to the deflection map in Figure 4.9(a).

However, we argue that adding $K_{\alpha2}$ to $K_{\alpha1}$ should work when $\Delta\omega_{\text{sweep}}$ is much larger or smaller than 0.0938°. For demonstration, the above data set is re-processed using half of the number of raw XRT images as interpolation input. For clarity, the updated ω_{sweep} values are shown in Table 4.2. In this case, the new $\Delta\omega_{\text{sweep}}$ is doubled to be 0.22°. The deflection maps using the re-processed data set and the 30 × Image deflection map are shown in Figure 4.14. It is apparent that the three maps have significant variations in the colors and shapes between each other. The $K_{\alpha1}$ deflection map has more red on the right side while the $K_{\alpha1}$+$K_{\alpha2}$ deflection map has no red.

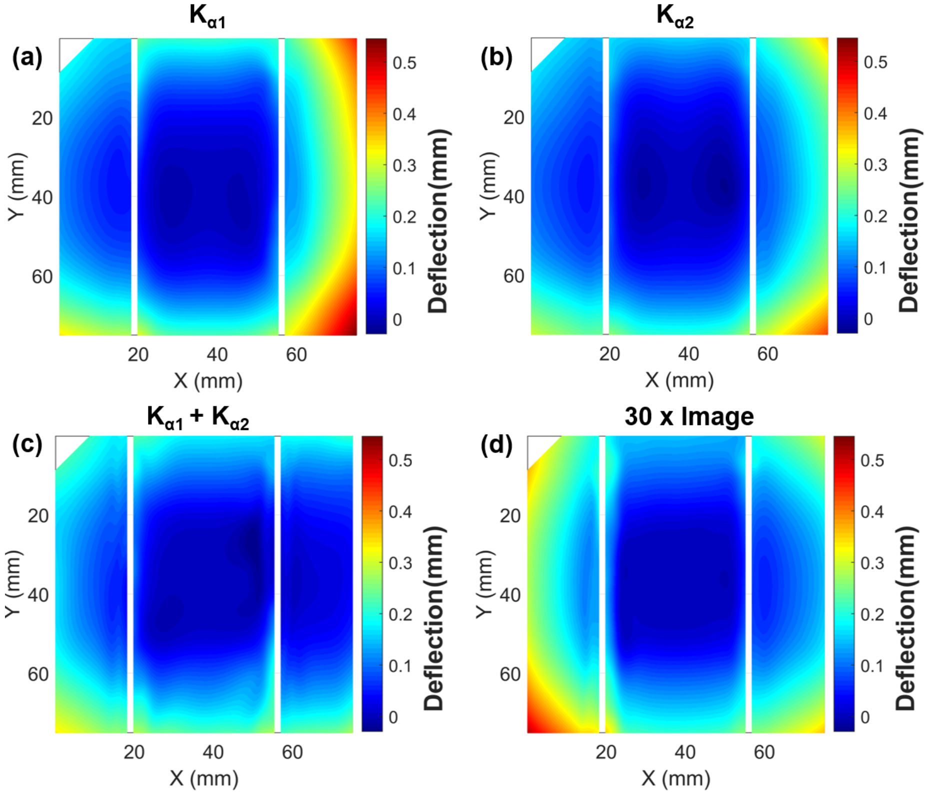

Figure 4.14: Three deflection maps processed using (a) only $K_{\alpha1}$ lines, (b) only $K_{\alpha2}$ lines and (c) both $K_{\alpha1}$ and $K_{\alpha2}$ signals in Table 4.2 ; (d) is the same deflection map in Figure 4.9(a).

Again, the absolute mean deviations of the three deflection maps are calculated with respect to the 30 × Image deflection map. Note that the same error bar is used for all three deflection maps because the data process is less sensitive to the X-ray exposure time (as long as the X-ray signals are distinguishable in the data processing,

Table 4.2: List of ω_{sweep} angles corresponding to $K_{\alpha1}$ and $K_{\alpha2}$ signals when processed with only half of the measured images. Note that NaN means no data.

X-rays	$\omega_{\text{sweep},1}$	$\omega_{\text{sweep},2}$	$\omega_{\text{sweep},3}$	$\omega_{\text{sweep},4}$	$\omega_{\text{sweep},5}$	$\omega_{\text{sweep},6}$	$\omega_{\text{sweep},7}$	$\omega_{\text{sweep},8}$	$\omega_{\text{sweep},9}$	$\omega_{\text{sweep},10}$
$K_{\alpha1}$	NaN	-0.24	NaN	-0.02	NaN	0.2	NaN	0.42	NaN	0.64
$K_{\alpha2}$	NaN	-0.1462	NaN	0.0738	NaN	0.2938	NaN	0.5138	NaN	0.7338

as shown in Section 4.2.1). As expected, the deviations increased dramatically with the fewer number of raw XRT images. The $K_{\alpha1}$+$K_{\alpha2}$ deflection map show the smallest mean deviation of 0.045 mm. The $K_{\alpha1}$ deflection map has a larger deviation than the $K_{\alpha2}$ map because the $K_{\alpha2}$ signals covered the solar cell areas with important bending profiles. Therefore, we conclude that $K_{\alpha2}$ signals are beneficial in improving the accuracy of the measurement when $\Delta\omega_{\text{sweep}}$ is much larger or smaller than 0.0938°.

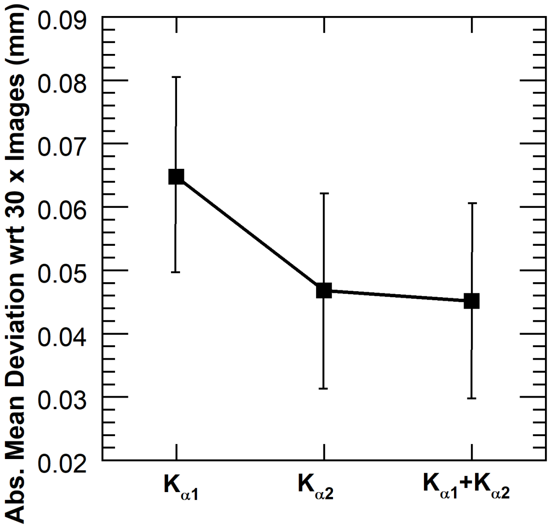

Figure 4.15: Mean absolute deviation of the three two deflection maps in Figure 4.14 with respect to the deflection map in Figure 4.9(a).

4.2.4 Distance between $K_{\alpha1}$ Lines and $K_{\alpha2}$ Lines

As mentioned earlier, both $K_{\alpha1}$ and $K_{\alpha2}$ signals are present due to the absence of monochromator. In this case, a raw XRT image of a one-dimensionally bent silicon wafer (see Chapter 6 for more details) is shown in Figure 4.16(a) and the X-ray intensity of the red dashed line is shown in (b). Due to the high signal-to-background contrast ratio being around 10, both $K_{\alpha 1}$ and $K_{\alpha 2}$ signals are identified. Note that the XRT image is taken at one ω_{sweep} value, referring to the $K_{\alpha 1}$ peak. In Figure 4.16(b), the $K_{\alpha 1}$ is at 5.325 mm and the $K_{\alpha 2}$ is at 6.375 mm. At the same time, the ω values between the two peaks are determined to be 0.1017°. Assuming a uniform curvature, the curvature between the two points can be calculated as $1.69\,\text{m}^{-1}$, using the equation:

$$\kappa = \frac{1}{r} = \frac{\Delta\omega/2}{\Delta d/2} \tag{4.3}$$

where $\Delta\omega$ is the ω difference between two pixels and Δd is the distance between the two pixels in the XRT image.

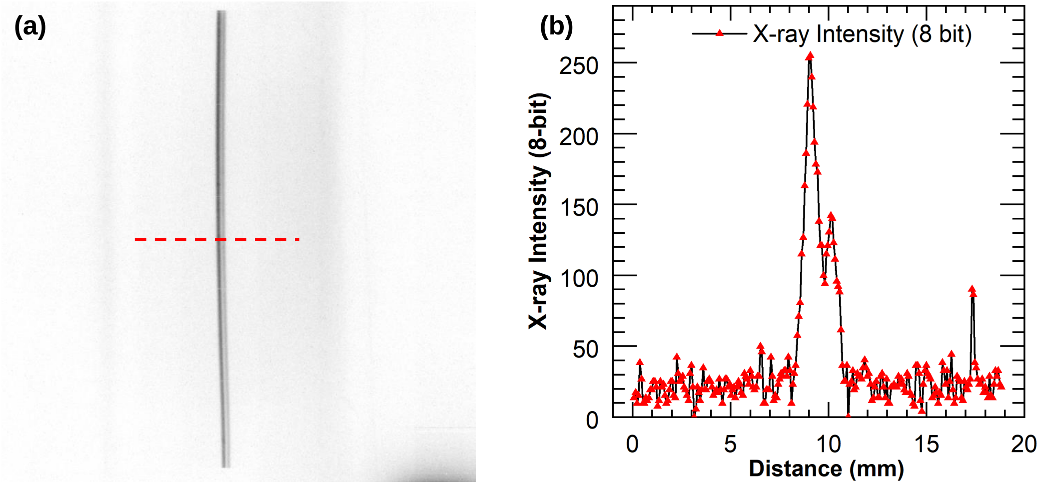

Figure 4.16: (a) a XRT raw image of a silicon wafer and (b) a cross-section line of both $K_{\alpha 1}$ and $K_{\alpha 2}$ signals. Red triangles are real data points and the dark line is fitted result.

Therefore, it is possible to build a connection between curvature and X-ray intensities in a single raw image and calculate the curvature without other images. This brings another approach of calculating deflection maps of encapsulated solar cells. However, a relationship between X-ray intensity and X-ray wavelength has to be established ahead of time and only the curvature in the direction of the two probed points can be obtained. Additionally, this methodology can only be applied to the pixels when the diffraction signal appears. Multiple images at different ω_{sweep} angles are still required.

Encapsulation brings difficulty to the above-mentioned method. Figure 4.17 shows a raw XRT image of the encapsulated silicon solar cell with double glasses. Due to the significant X-ray attenuation through two layers of glass, the signal-to-background ratio is less than 2. Visually, both $K_{\alpha1}$ and $K_{\alpha2}$ lines can still be identified because human eyes are very sensitive to image contrast. However, the computer program will have a problem with identifying both lines. As shown in Figure 4.17, the X-ray intensity is noisy such that no useful peak information can be extracted. Therefore, the process introduced in Chapter 3.3 is recommended to process the XRT images of encapsulated solar cells.

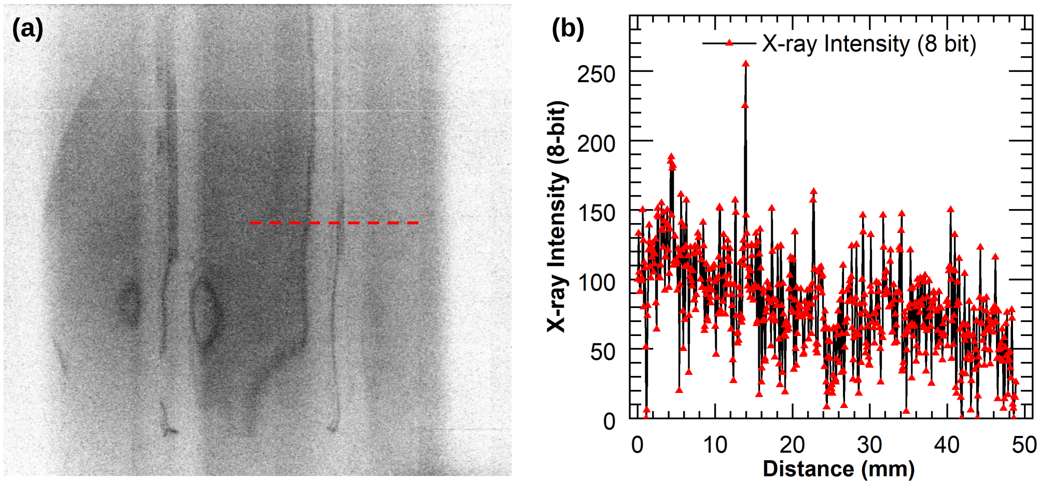

Figure 4.17: (a) a XRT raw image of an encapsulated solar cell in a glass/glass stack and (b) a cross-section line of both $K_{\alpha1}$ and $K_{\alpha2}$ signals. Red triangles are real data points and the dark line is fitted result.

Chapter 5

BENDING STRESS ANALYSIS ON ENCAPSULATED SOLAR CELLS

Soldering and lamination processes have previously been reported to introduce stresses on the solar cells, especially around the ribbon areas [63]. It is reported that 50% of cell cracks are parallel to the metal ribbons and only 20% of them propagate diagonally to the ribbons following the $\langle 111 \rangle$ family of directions [20]. The goal of this section is to characterize the mechanical stress from different stressors such as soldering and lamination stack. To make this possible, the Von Karman plate theory is used to transform the deflection information into bending stresses.

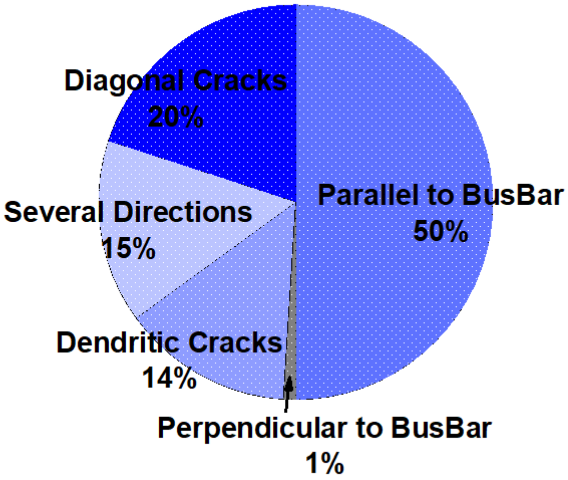

Figure 5.1: Statistical analysis on the direction of cell cracks [20].

5.1 Thin Plate Bending Theory

After deflection maps are obtained, the next question is how to calculate stress from deflection. The solar cell deflection is a combined result of the exerted stresses from various sources, such as encapsulant shrinkage, lamination pressure, and tabbing.

However, not every stressor causes cell deflection. Cell deflection only takes place when the net stress is not zero. For example, Figure 5.2 illustrates a wafer having positive stress (tensile) on the bottom surface and negative stress (compressive) on the top surface, assuming a plate system with only plain stresses present. The net stress is considered as the effect of the two. The tensile stresses stretch the crystal lattice and compressive stresses push atomic arrangements closer together. As a result, the silicon wafer will bend towards the top surface, showing a net deflection. When compressive stresses, or tensile stresses, are present on both surfaces, the net stress is the addition of the two. When equal stresses are present, no deflection will occur.

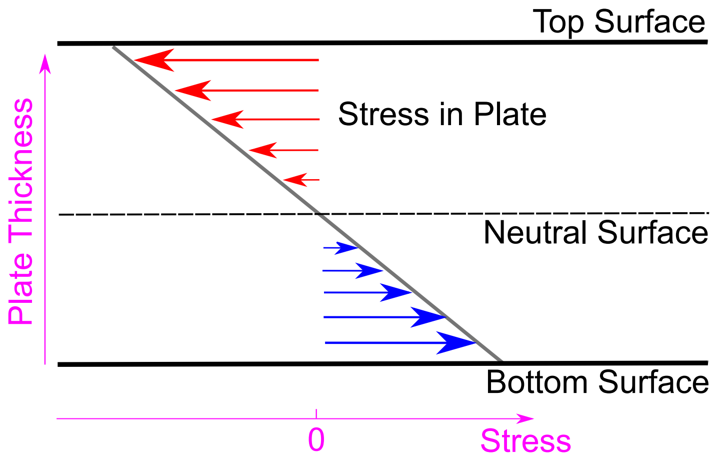

Figure 5.2: Scheme of a silicon wafer cross-section showing stress values as a function of horizontal and vertical distance. Positive stress values are tensile and nagative stress values are compressive. Neutral surface is the plane of zero stress.

In this study, the bending stress values are calculated from the deflection. Instead of absolute stresses exerted on the sample, the bending stresses are the relative stress values between the top and bottom sample surface. The bending stress on the top surface is defined as

$$\sigma_b = \frac{\sigma_{top} - \sigma_{bottom}}{2} \tag{5.1}$$

where σ_{b} is the bending stress value at the top surface on the probing point, σ_{top} and

σ_{bottom} are the absolute stress values of the top and bottom surface on the probing point.

The bending stress tensors are calculated using Von Karman thin-plate theory. The theory is a set of nonlinear partial differential equations describing large deflections of thin flat plates. The main assumptions are [64]:

1. The plate is thin (True: length/thickness >100 for solar cell).
2. The magnitude of the transverse deflection is of the same order as the thickness of the solar cell (True: observed cell deflection in our case is $100 \sim 250\,\mu$m).
3. The gradient of in-plane displacement is small (True: when no cracks are present).
4. The cell deflection is under pure bending condition (Not necessarily true. Therefore, we focus only on the evaluation of bending stresses at this point). Note that the bending stress values of the back and front surface have opposite stress values of the same magnitude for equilibrium under pure pending conditions. The neutral surface is located in the middle of the solar cell.

To further simplify our calculations, we further assume that:

1. The solar cell is under plane stress condition (True: length/thickness >100 for solar cells). Hence, the 3D problem can be reduced to be a 2D problem, which can be illustrated as:
$$\begin{bmatrix} \sigma_{11} & \sigma_{12} & \sigma_{13} \\ \sigma_{21} & \sigma_{22} & \sigma_{23} \\ \sigma_{31} & \sigma_{32} & \sigma_{33} \end{bmatrix} \Rightarrow \begin{bmatrix} \sigma_{11} & \sigma_{12} & 0 \\ \sigma_{21} & \sigma_{22} & 0 \\ 0 & 0 & 0 \end{bmatrix} \tag{5.2}$$
2. The thickness of the cell does not change (First order approximation, the wafer thickness typically varies less than 15% [65]).

3. The cell is isotropic and homogeneous (Not necessarily true. The silicon is an anisotropic material and the solar cells contains multiple layers of different materials).

The stress-strain relationship for an isotropic material can be described by Hooke's law:

$$\begin{bmatrix} \sigma_{11} \\ \sigma_{22} \\ \sigma_{33} \\ \sigma_{23} \\ \sigma_{13} \\ \sigma_{12} \end{bmatrix} = \frac{E}{(1-v-2v^2)} \times \begin{bmatrix} 1-v & v & v & 0 & 0 & 0 \\ v & 1-v & v & 0 & 0 & 0 \\ v & v & 1-v & 0 & 0 & 0 \\ 0 & 0 & 0 & 1-2v & 0 & 0 \\ 0 & 0 & 0 & 0 & 1-2v & 0 \\ 0 & 0 & 0 & 0 & 0 & 1-2v \end{bmatrix} \times \begin{bmatrix} \epsilon_{11} \\ \epsilon_{22} \\ \epsilon_{33} \\ \epsilon_{23} \\ \epsilon_{13} \\ \epsilon_{12} \end{bmatrix} \tag{5.3}$$

where E is the silicon's isotropic Young's modulus and v is silicon's isotropic Poisson's Ratio. However, during the alignment process of XRT measurement, the orientation of the silicon solar cell was known (the (004) crystal planes are aligned to the vertical X-ray beam). Therefore, an effective E of 130 GPa and an effective v of 0.28 are used in this dissertaion [66; 67].

Based on these delineated assumptions, the displacement of any point on the cell is given by:

$$\mu_1 = -t\frac{\partial z}{\partial x}, \mu_2 = -t\frac{\partial z}{\partial y}, \mu_3 = 0 \tag{5.4}$$

where μ is the displacement value and t is the distance value between the mid-plane to the probing point on the cell. For example, t equals to half of the cell thickness when evaluating surface deflection [64].

From the compatibility relations, the strains are given by:

$$\epsilon_{11} = \frac{\partial \mu_1}{\partial x} = -t\frac{\partial^2 z}{\partial x^2} \tag{5.5}$$

$$\epsilon_{22} = \frac{\partial \mu_2}{\partial y} = -t\frac{\partial^2 z}{\partial y^2}, \tag{5.6}$$

$$\epsilon_{12} = \frac{\partial \mu_1}{\partial x} + \frac{\partial \mu_2}{\partial y} = -2t\frac{\partial^2 z}{\partial y \partial x}, \tag{5.7}$$

$$\epsilon_{33} = \epsilon_{13} = \epsilon_{23} = 0 \tag{5.8}$$

Only ϵ_{11}, ϵ_{22} and ϵ_{12} have non-zero values and all other stress components are zero. From Hooke's law, the expressions for the six stress tensor components are:

$$\sigma_{11} = -\frac{E}{1-\upsilon^2}t(\frac{\partial^2 z}{\partial x^2} + \upsilon\frac{\partial^2 z}{\partial y^2}), \tag{5.9}$$

$$\sigma_{22} = -\frac{E}{1-\upsilon^2}t(\frac{\partial^2 z}{\partial y^2} + \upsilon\frac{\partial^2 z}{\partial x^2}), \tag{5.10}$$

$$\sigma_{12} = -\frac{E}{1+\upsilon}t\frac{\partial^2 z}{\partial y \partial x}, \tag{5.11}$$

$$\sigma_{33} = \sigma_{13} = \sigma_{23} = 0 \tag{5.12}$$

This relation allows us to transform the previously measured deflection map into bending stress maps. Following standard nomenclature, when the stress value is higher than zero, the stress is tensile; when the stress value is negative, the stress is compressive. The nature of plate theory assumes that the mid-plane of the specimen is the neutral plane with zero stress. And the deflection map generated by XRT is the defleciton at the mid-plane of the specimen. If one side of the plate has tensile stress, the other side will have compressive stress. Note that the stresses we are covering in this study are purely generated by the deflection of the solar cell.

5.2 Examples and Applications

Sample Preparation

Silicon heterojunction (SHJ) solar cells (6") with wafer thicknesses of 200 μm were prepared at the Solar Power Lab at Arizona State University and laser-cut into

2.5” coupons. Commercial PERC solar cells (6”) with wafer thicknesses of 200 μm and Al back surface field (BSF) solar cell (5”) with wafer thickness of 220 μm were laser-cut into 3” coupons and 2.5” coupons, respectively. The solar cell coupons were soldered to standard solar cell interconnectors (solder surrounded copper ribbons with a thickness of 0.15 mm and a width of 1.5 mm) and laminated into mini-modules. The ribbons are soldered to the cell using a soldering gun at 450°C. Mini-modules of encapsulated cells were built using heat-resistant borosilicate flat glass (3” × 3”) following a standard PV module stack (Glass/EVA/Cell/EVA/Backsheet). A NPC LM-110X161-S module laminator was used for module assembly. Six full-size 6” PERC silicon solar cells with four bubars were soldered and encapsulated by DuPont, following the stack demonstrated in Figure 5.3. Photos of the six modules are shown in Figure 5.4. Note that all of the modules have front ribbons connected to the top thicker ribbons, except the 2mmGGEVA module and the 3mmGBEVA module. A list of modules used in this chapter are shown in Table 5.1.

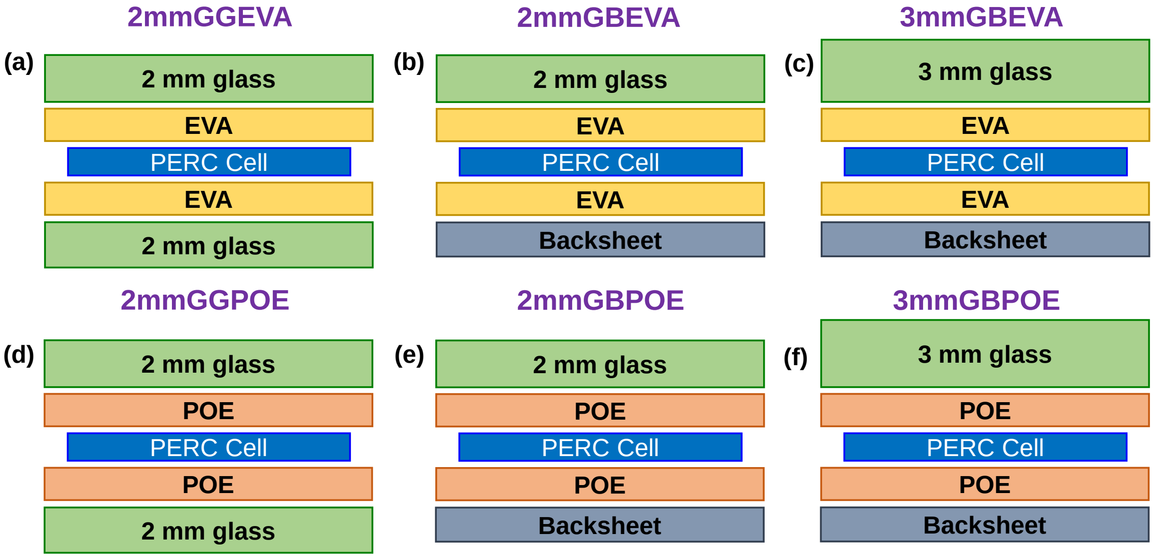

Figure 5.3: Lamination stacks of six full-size PERC PV modules: (a) 2mmGGEVA, (b) 2mmGBEVA, (c) 3mmGBEVA, (d) 2mmGGPOE, (e) 2mmGBPOE and (f) 3mmGBPOE.

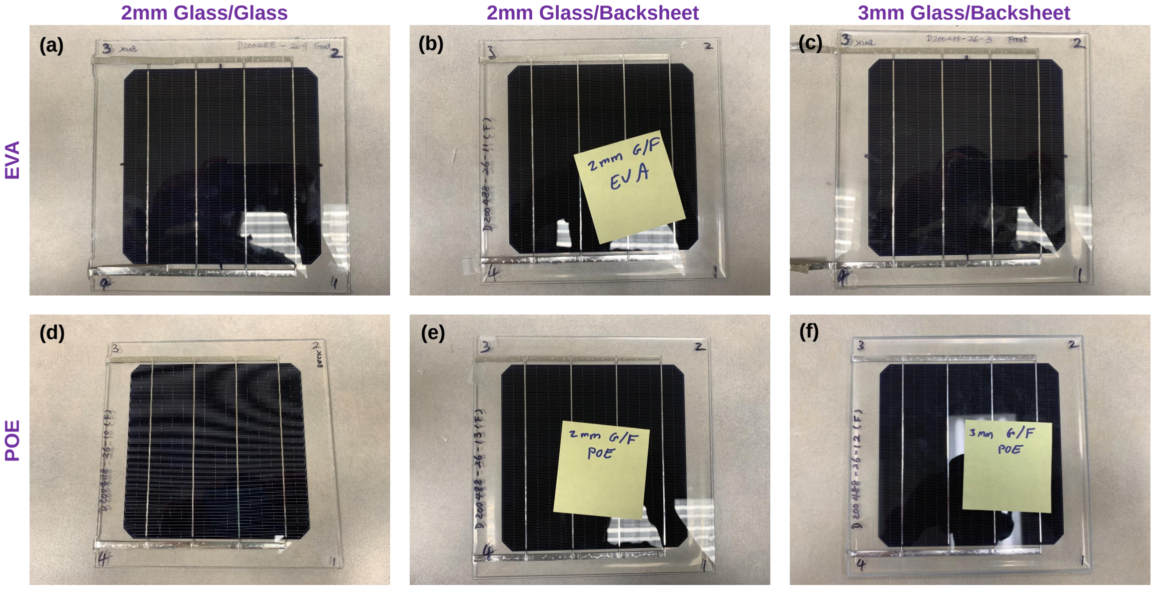

Figure 5.4: Photos of six 6" PERC PV modules fabricated using the stack shown in Figure 5.3.

Table 5.1: List of 3 mini-modules and 6 full-size modules used in this chapter for bending stress analysis.

2.5" BSF cell	**2.5" SHJ cell**	**3" PERC cell**	**6" PERC cell**
BSF-S1	SHJ-S1	PERC-S1	2mmGGEVA, 2mmGBEVA, 3mmGBEVA 2mmGGPOE, 2mmGBPOE, 3mmGBPOE

5.2.1 Principal Stresses and Probability of Failure

Figure 5.5 shows the deflection map of module PERC-S1 with two metal ribbons (both front and back). The bending stress components σ_{11}, σ_{22} and σ_{12} are calculated by Von Karman theory, as shown in Figure 5.5(b-d). The direction of each bending stress component is shown in Figure 5.5(e). The ribbons are located in the middle of the solar cell and are represented as white strips. The color bar indicates the value of the stress on each pixel. Most of the pixels related to relatively high stress in all three bending stress maps are in the vicinity of the ribbons. Since the solar cell is assumed to be under plain stress, the directions of the stresses are all contained in the surface plane. The σ_{11} is perpendicular to the ribbon (in X direction). The σ_{22} is parallel to the ribbon (in Y direction). The σ_{12} is the shear stress in the direction of turning the element. The factors of ribbon thickness, ribbon width, solar cell thickness, soldering uniformity, soldering temperature, pressing force, and lamination pressure contribute to the stress values shown in the maps.

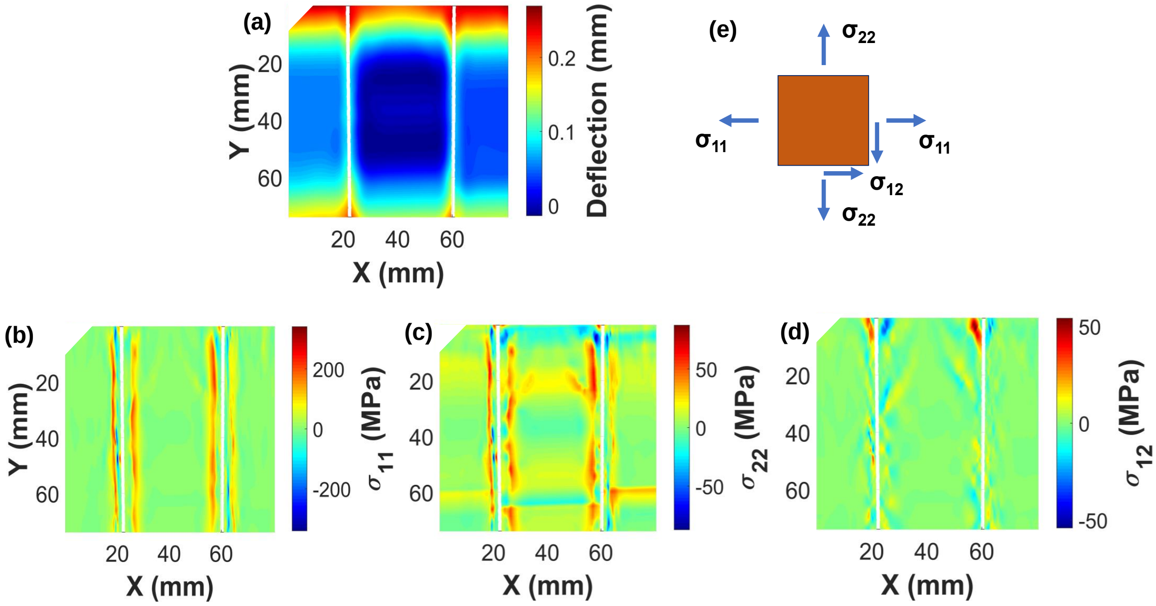

Figure 5.5: (a) Deflection and (b) σ_{11}, (c) σ_{22} and (d) σ_{12} bending stress maps of the front surface in a 3" PERC silicon solar cell (PERC-S1) in encapsulation; (e) the direction of the three bending stress components.

Though the calculated bending stress components can provide information of the stress state that the solar cell experiences, they give few information about the probability of failure or indicate crack initiation and propagation. In order to do that, principal stresses are commonly used [23]. The principal stresses are calculated by diagonalization of the stress tensor as shown in Equation 5.13:

$$\begin{bmatrix} \sigma_{11} & \sigma_{12} & 0 \\ \sigma_{21} & \sigma_{22} & 0 \\ 0 & 0 & 0 \end{bmatrix} \Rightarrow \begin{bmatrix} \sigma_{11} & 0 & 0 \\ 0 & \sigma_{2} & 0 \\ 0 & 0 & 0 \end{bmatrix} \tag{5.13}$$

where σ_1 and σ_2 are the first and second principal stresses, respectively. The magnitude of the two principal stresses are the two eigenvalues of the new 2D stress tensor.

σ_1 is larger than σ_2 by definition. Physically, they are the two normal stresses when an element is rotated to a position where the shear stress is zero (Figure 5.6).

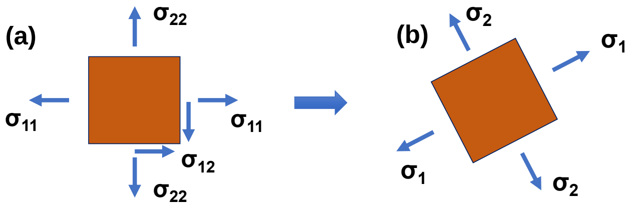

Figure 5.6: Diagram showing the direction of (a) three component stresses and (b) corresponding two principal stresses.

The principal stresses of PERC-SI are calculated and presented in Figure 5.7. Similar to the stress components, only the areas around the ribbons have high-stress values. σ_1 seems to be dominated by σ_{11}, whereas σ_2 seems to be dominated by σ_{22}. The highest stress value observed in this sample is ~250 MPa. Those high stress values are caused by the lamination pressure pressing on the metal ribbons and the thermal effect from the soldering process. During soldering, the ribbons and the solar cell were heated up to 450°C and then cooled down to room temperature. Since the ribbons have a much larger CTE value than silicon (17×10^{-6}K^{-1} for copper and 2.56×10^{-6}K $^{-1}$ for silicon at 20°C), the ribbons tend to contract more than the silicon cell, causing a large concentration of tensile stress around those areas [61].

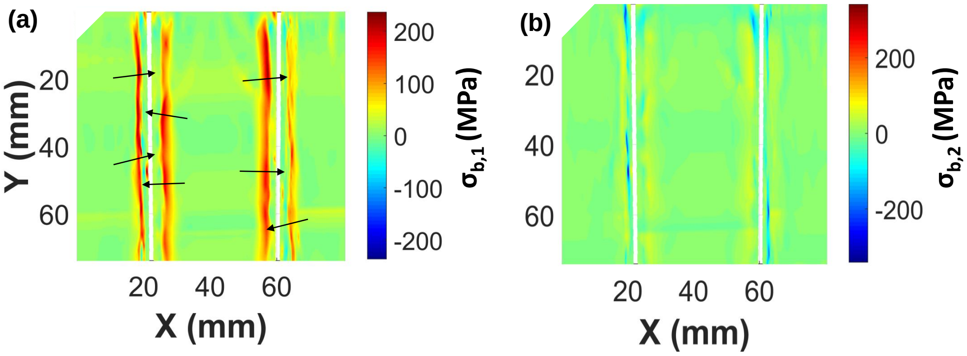

Figure 5.7: $\sigma_{b,1}$ and $\sigma_{b,2}$ maps of mini-module PERC-S1 calculated from the stress components in Figure 5.5. The black arrows in (a) indicate direction of σ_1.

The σ_1 map gives a map of the highest stress value from which the probability of failure can be calculated using a Weibull distribution function [23]. Actually, σ_1 is often compared to the fracture strength of a brittle material to evaluate the probability of failure. The higher the σ_1 value, the higher the probability of generating cracks [23]. The fracture strength of silicon solar cell is highly dependent on the structure of the solar cell (defects, cell layout, etc.); the range of values have been reported to span from 166 to 1000 MPa [68–70]. Figure 5.8 shows the histogram of pixel counts as a function of $\sigma_{\mathrm{b},1}$ values in Figure 5.7(a). The highest $\sigma_{\mathrm{b},1}$ value is 238 MPa, which is relatively small compared to the reported fracture strength. Most of the solar cell areas (99.9%) have stress values under 200 MPa. Using the experimental data from the Reference [23], the probability of failure was calculated as a function of σ_1 and shown in Figure 5.8. Following the Weibull distribution, the probability values are close to zero when σ_1 is below 200 MPa and the highest observed value is 1.8%. Assuming the bending stress is the only stress contribution to failure, 0.1% of the solar cell areas have a significant probability of failure that contribute to critical failure and should be reduced at all cost.

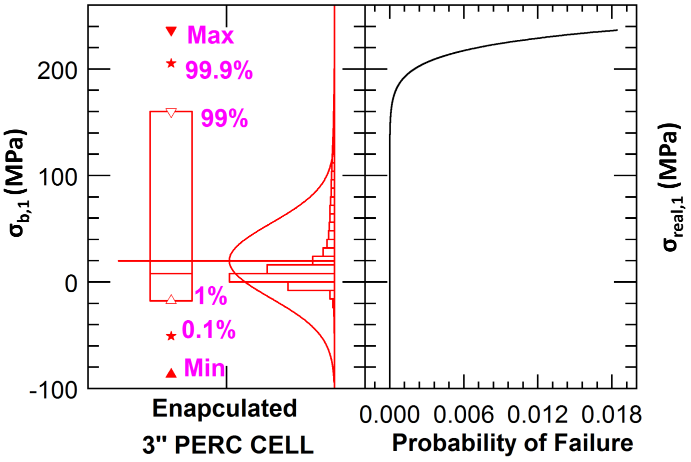

Figure 5.8: Histogram of $\sigma_{\mathrm{b},1}$ values in PERC-S1 by pixel counts and its corresponding probability of failure calculated by Weibull distribution using the experimental data in Reference [23].

To better illustrate the deflection and bending stress development around the ribbons, deflection and stress cross-sections perpendicular to the busbars are drawn and shown in Figure 5.9(b). The cell bending features around those two ribbons can be easily identified. The solar cell is deflected away from the front glass around the ribbons while on the cell edges and cell center are almost flat. This bending feature is caused by the lamination process where the lamination pressure is exerted on the cell from metal ribbons.

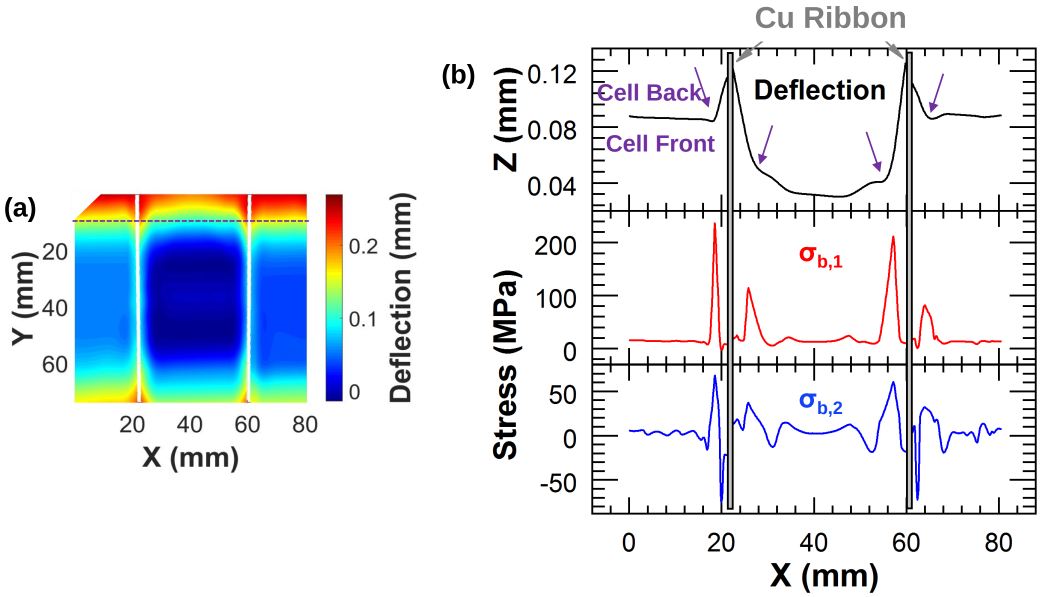

Figure 5.9: (a) Deflection map of the module in Figure 5.5, the dashed line indicates the position of cross-section; (b) the deflection, $\sigma_{\mathrm{b},1}$ and $\sigma_{\mathrm{b},2}$ values on the purple dashed lines perpendicular to the ribbons, as shown in (a).

Both $\sigma_{\mathrm{b},1}$ and $\sigma_{\mathrm{b},2}$ curves are shown below the deflection curve. Most of the cell areas have small stress values except the areas around the ribbons. Two high tensile peaks on each side of the ribbons are identified. Those high tensile values are introduced during the soldering and lamination process. The silicon directly below or very close to the ribbons experience compressive stresses because the ribbon tends to contract more than silicon when temperature is cooling down.

5.2.2 Impact of Soldering, Lamination, and Damp Heat Testing

Now we have quantitatively demonstrated the deflection and stresses that the silicon cell experiences after soldering and lamination. Those values are combined results from soldering and lamination such that their individual impact on the solar cell is unknown. Additionally, how those stress values behave under accelerated testing such as DH1000, is unknown. Therefore, the bending stress of sample SHJ-S1 (one busbar) was evaluated after soldering, after lamination, and after DH1000 test.

Figure 5.10 shows the $\sigma_{\mathrm{b},1}$ maps of SHJ-S1 after each process. After soldering, we can clearly see the high-stress areas at random spots around metal ribbons, which are associated with the high-temperature soldering process. The reason why most of the areas around ribbons have small $\sigma_{\mathrm{b},1}$ values is because the solar cell's bottom and top surface have nearly similar stress values. After lamination, the high-stress areas expanded to the vicinity of entire ribbons, which could be attributed to the lamination pressure exerted on ribbons. The high $\sigma_{\mathrm{b},1}$ areas re-distributed after DH1000 probably due to the softness of encapsulant (EVA's glass transition temperature is about 60°C).

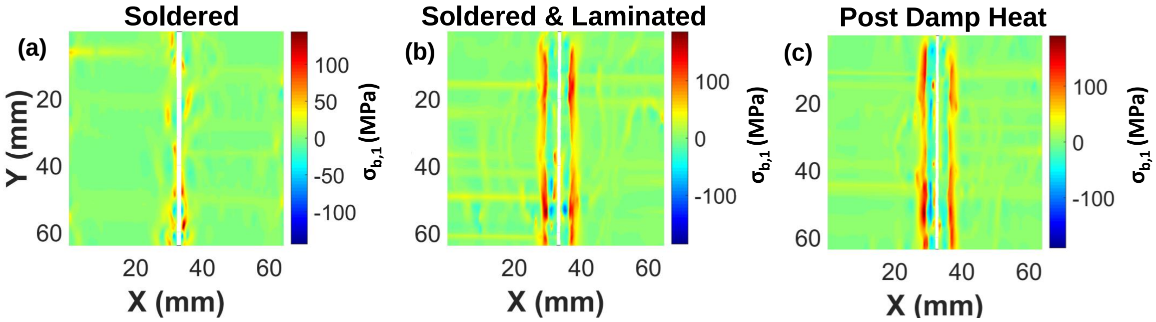

Figure 5.10: $\sigma_{\mathrm{b},1}$ stress maps of PERC-S1 measured and analyzed (a) after soldering, (b) after lamination, and (c) after DH1000.

Figure 5.11 shows the maximum and top 0.1% of $\sigma_{\mathrm{b},1}$ values on SHJ-S1 after each process. After soldering, the maximum stress reached 140 MPa while the top 0.1% stress is close to 70 MPa, which is 50% of the maximum value. Both two probing values showed an increasing trend after lamination, indicating that the lamination process further introduced more stress on the solar cell. The maximum $\sigma_{b,1}$ increased to 185 MPa (31% increase) and top 0.1% $\sigma_{b,1}$ increased to 135 MPa (93% increase). Statistically, the soldering process is more influential on solar cells than the lamination process. Surprisingly, the $\sigma_{b.1}$ values did not change significantly after damp heat test. The movement in encapsulant (result from softening and curing) majorly changed the stress distribution instead of stress magnitude in solar cell.

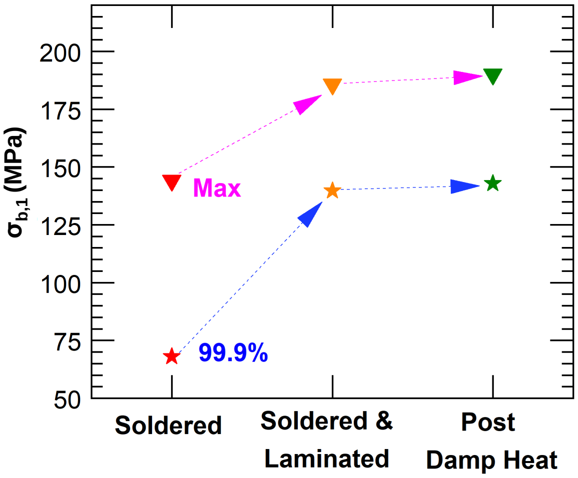

Figure 5.11: Maximum and top 0.1% $\sigma_{b,1}$ stress values of SHJ-S1 measured and analyzed after soldering, after lamination, and aftrr DH1000 test.

The above analysis on SHJ-S1 demonstrated a significant impact of soldering and lamination on cell stress. The soldering-induced stress could be mitigated by using lower soldering temperature; the lamination-induced stress could be mitigated by using thinner metal ribbons. While accelerated testing is meant to degrade modules, we did not observe significant variation in module stress values. However, more data points are needed to conclude the above statement and other accelerated tests such as TC100 should be considered for more trustworthy analysis.

5.2.3 Stress-Electrical Performance Correlation

Cell cracking has a negative correlation with module performance – the more cell cracks in a PV module the less power the module generates [21]. However, the relationship between stress that causes cell cracking and module efficiency is unclear due to the lack of experimental stress characterization method. Here we correlate the bending stress values with the electrical performance on a pixel by pixel basis. In this case, the series resistance (Rs) is chosen to be the performance indicator. The hypothesis is that high stresses on solar cell influence the interfaces within the cell structure and increase local Rs values.

Figure 5.12 shows the $\sigma_{\mathrm{b},1}$ maps, EL images and Rs maps of PERC-S1 and BSF-S1. The Rs mapping method was described in the reference here [71]. Same as previously discussed, high-stress values are in the vicinity of metal ribbons. No crack or dark areas are observed on the EL images. BSF-S1 showed overall lower resistance than PERC-S1 due to differences in cell structure. Rs values are much lower around the busbars than the cell edges due to shorter distances of carrier extraction.

The top 0.1% percent of high-stresses values on both solar cells are plotted as a function of Rs in Figure 5.13. Each experimental data point is taken from the same spot in the $\sigma_{\mathrm{b},1}$ map and Rs map. A linear fit (red line) to all the experimental data indicates a negative relationship between Rs and $\sigma_{\mathrm{b},1}$, which is inconsistent with our hypothesis. In fact, $\sigma_{\mathrm{b},1}$ is higher and Rs is lower when the probing area is close to the busbars – the Rs is dominated by the distribution of metalization such that the impact of stress on Rs is convoluted. Other electrical performance indicators, such as LBIC/LBIV, could be applied and will be explored in the future.

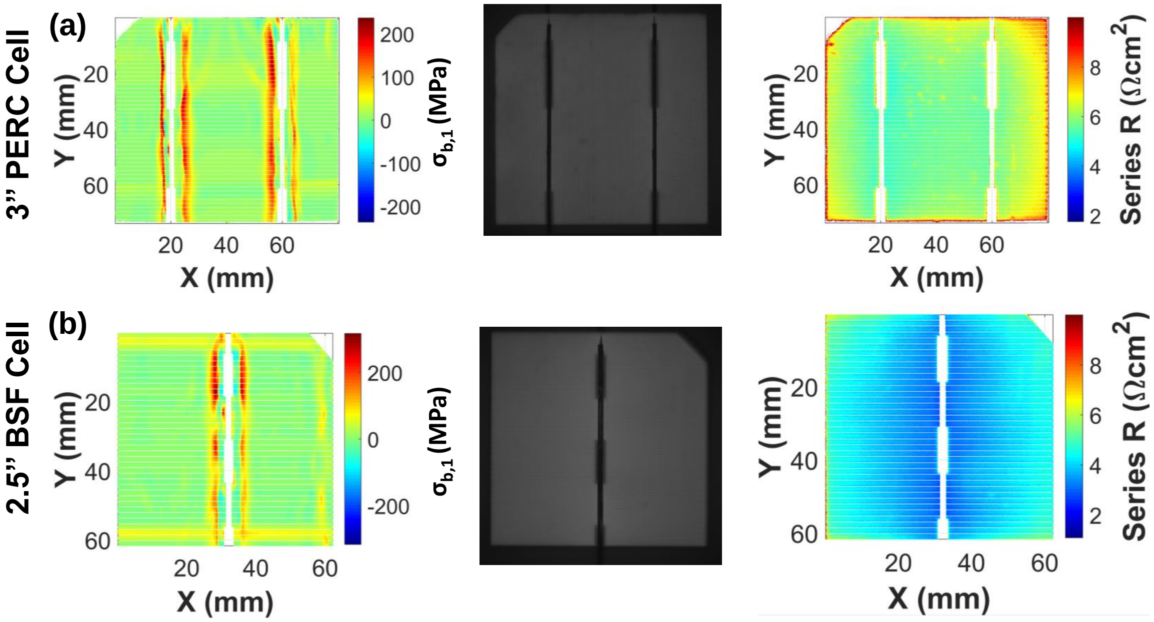

Figure 5.12: $\sigma_{b,1}$ maps, EL images and series resistance maps of (a) PERC-S1 and (b) BSF-S1.

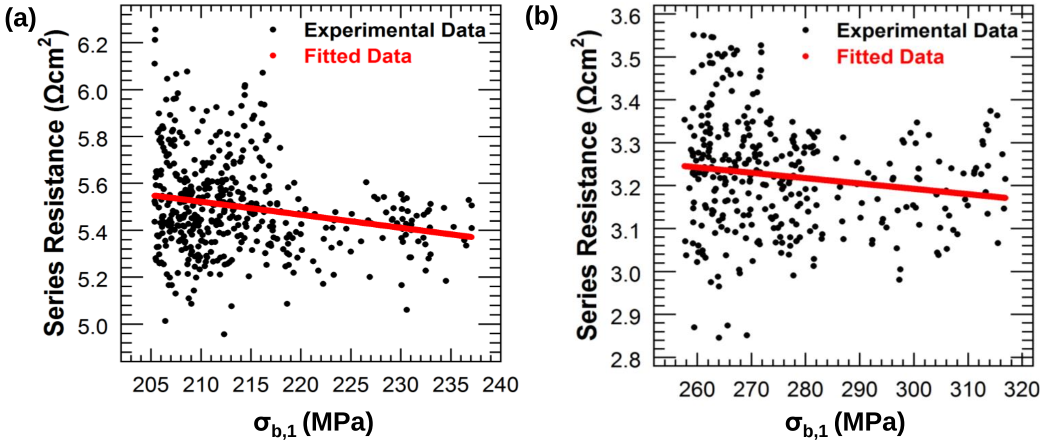

Figure 5.13: Experimental and fitted Rs values as a function of $\sigma_{b,1}$. Note that only the top 0.1% of the $\sigma_{b,1}$ values are included.

5.2.4 Impact of Stack, Encapsulant, and Glass Thickness

As the traditional mono-facial solar cell production line can be modified to fabricate bifacial solar cells with minimum additional cost for improved performance, glass/glass (GG) modules are becoming popular in the PV community to take advantage of the bifacial solar cells [5]. Meantime, many PV companies such as Solarwatt are advertising GG modules as a robust solution to reduce cell cracks under mechanical loading. They claim that due to the symmetrical structure in GG modules, the neutral stress plane (the plane of zero stress) will locate at the solar cells instead of glass upon mechanical loading (Figure 5.14), which dramatically reduces the stress on solar cell and results in less cell cracks.

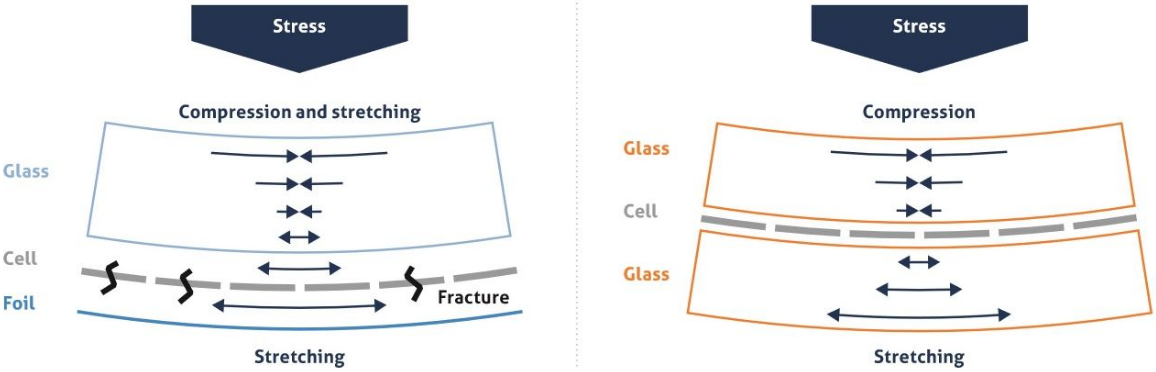

Figure 5.14: Stress distribution inside GB PV modules and GG PV modules.

However, we expect the stress values on solar cells to be higher in GG modules after fabrication because: (1) the solar cells are not exactly symmetrical because of front and back ribbons; (2) unlike flexible bakchseet, the rigid back glass cannot mitigate the lamination pressure, which means more pressure will be exerted on the solar cell through metal ribbons. To test our hypothesis, six full-size 6" PERC cells were fabricated in different combinations of encapsulants and packaging solutions, and analyzed using XRT (using the 6" sample holder). Note that four quaters of each solar cell were measured separately and the analyzed stress maps were physically attached together to show the information as a whole.

The $\sigma_{\mathrm{b},1}$ maps of the modules are shown in Figure 5.15. Note that the same color bar is used for every $\sigma_{\mathrm{b},1}$ map. The GB modules have most of the high-stress values around the ribbon areas. It can be imagined that those high $\sigma_{\mathrm{b},1}$ are caused by the back ribbons pushing at the solar cell. Though an encapsulation layer and a flexible basksheet layer are positioned next to the back ribbons, the lamination pressure is still exerted on the solar cells. For GG modules, in contrast, the high-stress values are mostly located at the end of back ribbons, which corresponds to the bottom part of module 2mmGGEVA and the upper part of module 2mmGGPOE. Similar to the edge pressing phenomenon during GG module lamination, the solar cell at the end of the back ribbons experiences more pressure than the rest, resulting in significant higher stress values. We attribute this stress behavior to the flexible polymer layers of backsheet that their mechanical properties change during the lamination process. The backsheet conforms to the shape of the back ribbons that the back glass cannot do. The high $\sigma_{\mathrm{b},1}$ in GG modules are mostly next to ribbons whereas the high $\sigma_{\mathrm{b},1}$ in GB modules are away from ribbons. Meanwhile, strips of compressive stresses are observed between the ribbon and high $\sigma_{\mathrm{b},1}$ areas in all modules. The same stress behavior is also observed in SHJ-S1 samples (Figure 5.10), which showed up after lamination.

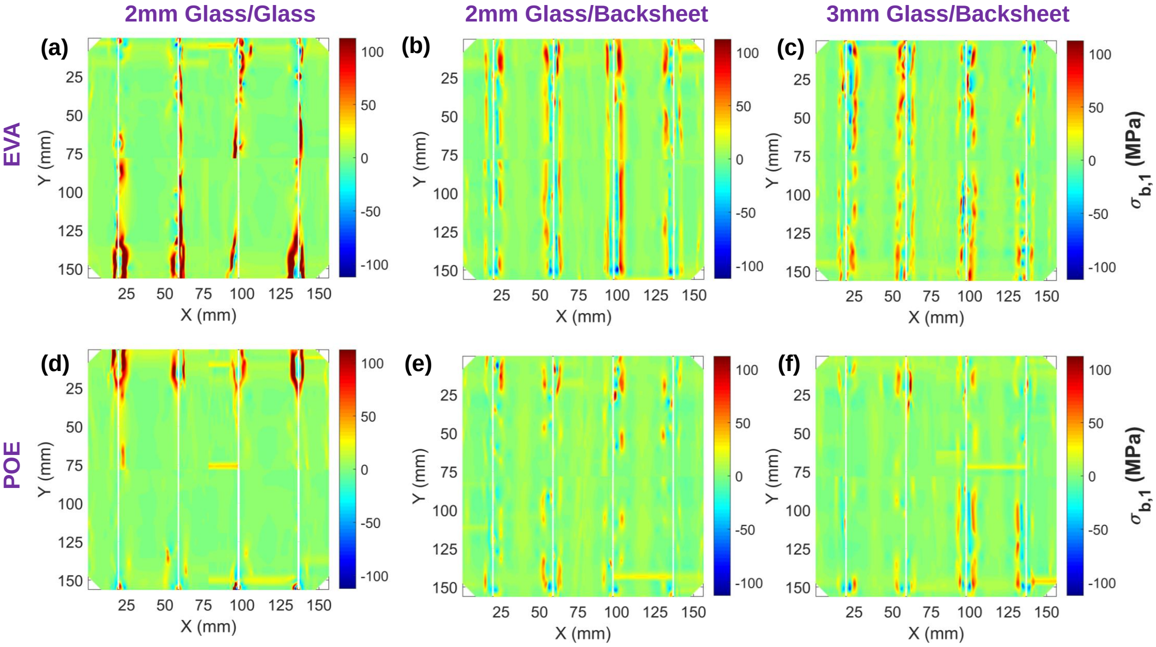

Figure 5.15: $\sigma_{\mathrm{b},1}$ maps of six PERC 6” PV modules shown in Figure 5.4.

As for EVA and POE comparison, we can clearly see that EVA modules experience higher $\sigma_{\mathrm{b},1}$ than POE modules, especially in the GG configuration. The EVA modules have more high-stress areas than POE modules. We attribute this to the higher stiffness coefficient in EVA material than POE. We do not observe a significant correlation between glass thickness and $\sigma_{\mathrm{b},1}$ in Figure 5.15.

The histogram of the $\sigma_{\mathrm{b},1}$ ($\geq$80 MPa) values are plotted as a function of pixel counts with a bin size of 50 MPa (Figure 5.16). Note that the pixel size is 100 μm × 100 μm. It is clear that higher $\sigma_{\mathrm{b},1}$ values have less pixel counts, following a normal distribution. At the 100 MPa region, all modules have pixel counts over 10000 except module 2mmGBPOE and 3mmGBPOE. Meanwhile, the module 2mmGBEVA is experiencing 50% more high-stress (around 100 MPa) counts than the 3mmGBEVA module, indicating PV modules with thinner glasses are more susceptible to high cell stresses.

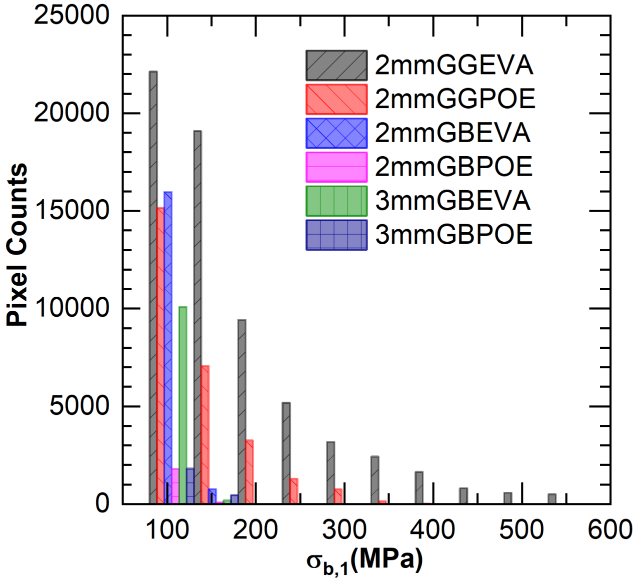

Figure 5.16: Histogram of the stress values ($\geq$100 MPa) of six 6" PERC modules as a function of pixel counts.

The top 0.1% values of six $\sigma_{\mathrm{b},1}$ maps in Figure 5.15 are extracted and shown in Figure 5.17. *Within* those values, the maximum, mean and minimum $\sigma_{\mathrm{b},1}$ are

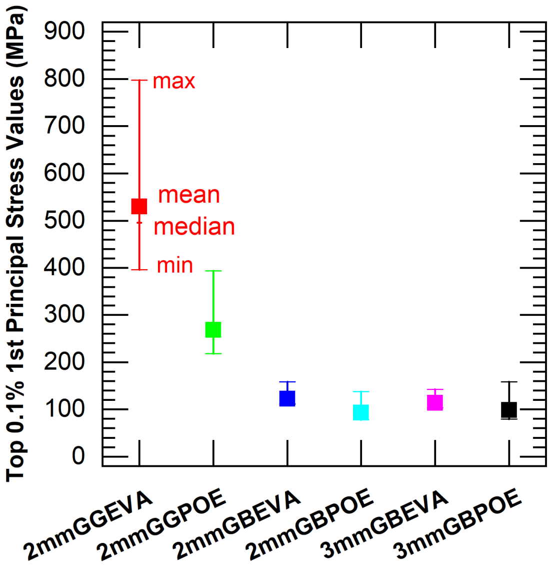

Figure 5.17: Distribution of the top 0.1% $\sigma_{\mathrm{b},1}$ values in six 6” PERC modules.

marked in the figure and shown in Table 5.2. Initial inspection shows that the $\sigma_{\mathrm{b},1}$ values in GG modules are much higher than those in GB modules, which supports our hypothesis. GB modules have $\sigma_{\mathrm{b},1}$ as high as ∼129 MPa whereas GG modules have $\sigma_{\mathrm{b},1}$ as high as ∼651 MPa. Considering the max $\sigma_{\mathrm{b},1}$ maybe outliers and may not represent the real trend, the mean $\sigma_{\mathrm{b},1}$ values are used for stress analysis. GG modules have 190-320% higher cell stress values than 2mm GB modules. EVA modules put 50-100% more stress on cells than POE modules. The 2mm glass GB modules and

Table 5.2: Maximum, mean and minimum of the top 0.1% $\sigma_{\mathrm{b},1}$ values of six PERC modules shown in Figure 5.17.

Module List	**Max $\sigma_{\mathrm{b},1}$ (MPa)**	**Mean $\sigma_{\mathrm{b},1}$ (MPa)**	**Min $\sigma_{\mathrm{b},1}$ (MPa)**
2mmGGEVA	651.15	432.26	323.41
2mmGGPOE	319.93	218.51	177.52
2mmGBEVA	129.04	99.97	90.79
2mmGBPOE	112.28	76.23	63.93
3mmGBEVA	116.07	93.07	84.17
3mmGBPOE	121.11	80.175	64.887

3mm glass GB modules have mixed results and do not show a strong correlation in $\sigma_{\mathrm{b},1}$ magnitudes.

The $\sigma_{\mathrm{b},2}$ maps of six 6" modules are shown in Figure 5.18. Similar to $\sigma_{\mathrm{b},1}$, most of the non zero $\sigma_{\mathrm{b},2}$ are located at the end of busbars. The GB modules have significantly more pixels of compressive stresses than GG modules next to the ribbon areas due to the backsheet. Since compressive stress is not the direct cause of cell cracks, it is less important than tensile stress.

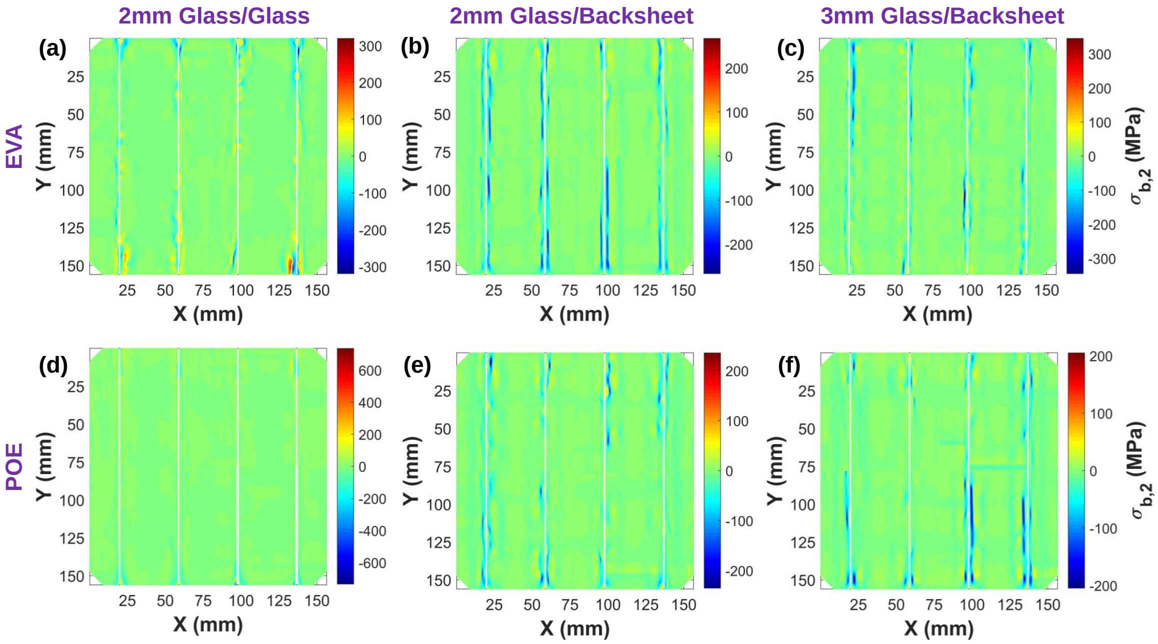

Figure 5.18: $\sigma_{\mathrm{b},2}$ maps of six PERC 6" PV modules shown in Figure 5.4.

Chapter 6

FROM BENDING STRESS TO ABSOLUTE STRESS

In Chapter 5, the method of calculating bending stresses from XRT calculated cell deflection was demonstrated and applied to multiple applications. The method made a major assumption that the solar cell is under pure bending conditions, which is not necessarily true for solar cells. Firstly, most of the solar cells do not have a symmetrical structure. Secondly, the tabbing and lamination processes often put both mechanical and thermal stresses on cells. Therefore, it is important to understand the nature of bending stresses on the solar cells and evaluate the errors from the assumption. In this chapter, we perform stress analysis on bare silicon wafers using four-point bending. The XRT analyzed stress values will be compared with finite element analysis (FEA) simulated stress values. The $\sigma_{\mathrm{b},1}$ values will be compared with FEA σ_1 as a function of technique, bending distance, and thicknesses of sputtered Al.

6.1 Four-Point Bending Theory

A four-point bending test is an important method of quantitatively introducing areas of uniform stress on subjects. It is often used in evaluating brittle materials (Si for instance), where the flexible strength and crack initiation are highly related to the maximum stresses. A diagram of four-point bending is shown in Figure 6.1. In principle, two bars are positioned on the top to push the sample downwards and two bars are positioned on the back with a larger span to provide fixed support. When the inner span is half of outer span, the $\sigma_{\mathrm{b},1}$ values on the bottom surface can be expressed by:

$$\sigma_1 = \frac{3PL}{4bd^2} \tag{6.1}$$

where P is the applied force, L is the outer span distance, b and d are the width and thickness of the sample.

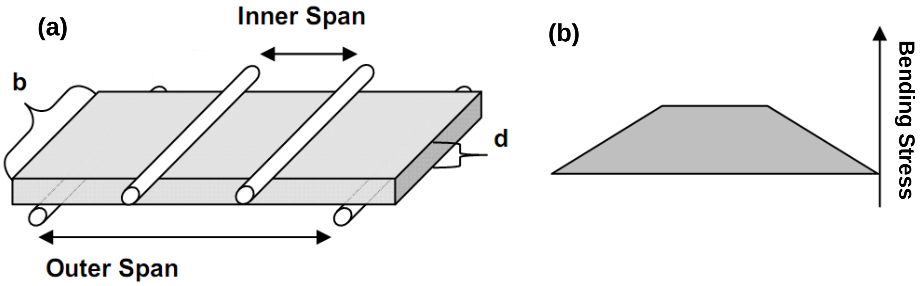

Figure 6.1: Scheme of a four-point bending setup and the expected stress field of the measured wafer across the bending direction [72].

In contrast to three-point bending, four-point bending test provides an area of uniform bending stress along the central part of the sample, as shown in Figure 6.1 [72]. The friction from loading bars also contribute to the measured results. The impact of friction stress can be expressed as

$$\frac{\sigma_{\mathrm{f}}}{\sigma_{\mathrm{b}}} = \frac{4df}{3L} \tag{6.2}$$

where f is the friction coefficient between the bars and sample. Considering the value of d/L (0.00188) is very small, the contribution of friction stress is ignored in the following discussion.

6.2 Setup Design and Modeling

6.2.1 In-situ Four-Point Bending Setup

An in-site four-point bending setup was designed for XRT measurement while systematically bending the sample. As shown in Figure 6.2, the setup consists of two Al plates with two bars bolted on each of them. To reduce the friction between contact, each bar was rounded and polished. The two plates are connected by four pins with bearings. The distance between two plates (bending distance) is determined by the four screws next to the pins. To precisely control the bending distance, four Al hollow pins of the same length are fabricated and positioned between two plates. If the plate distance is D at zero bending position, the physical length of the pins are determined by D-0.28 mm, D-0.5 mm, D-0.75 mm. Note that the bending distance 0.75 mm defines the largest deflection that the XRT setup can detect (ω rotation: ±3.5°). The sample holder is designed to bend 88 mm × 88 mm silicon wafers. Note that only the sample area between inner span (45 mm × 88 mm) is imaged and analyzed.

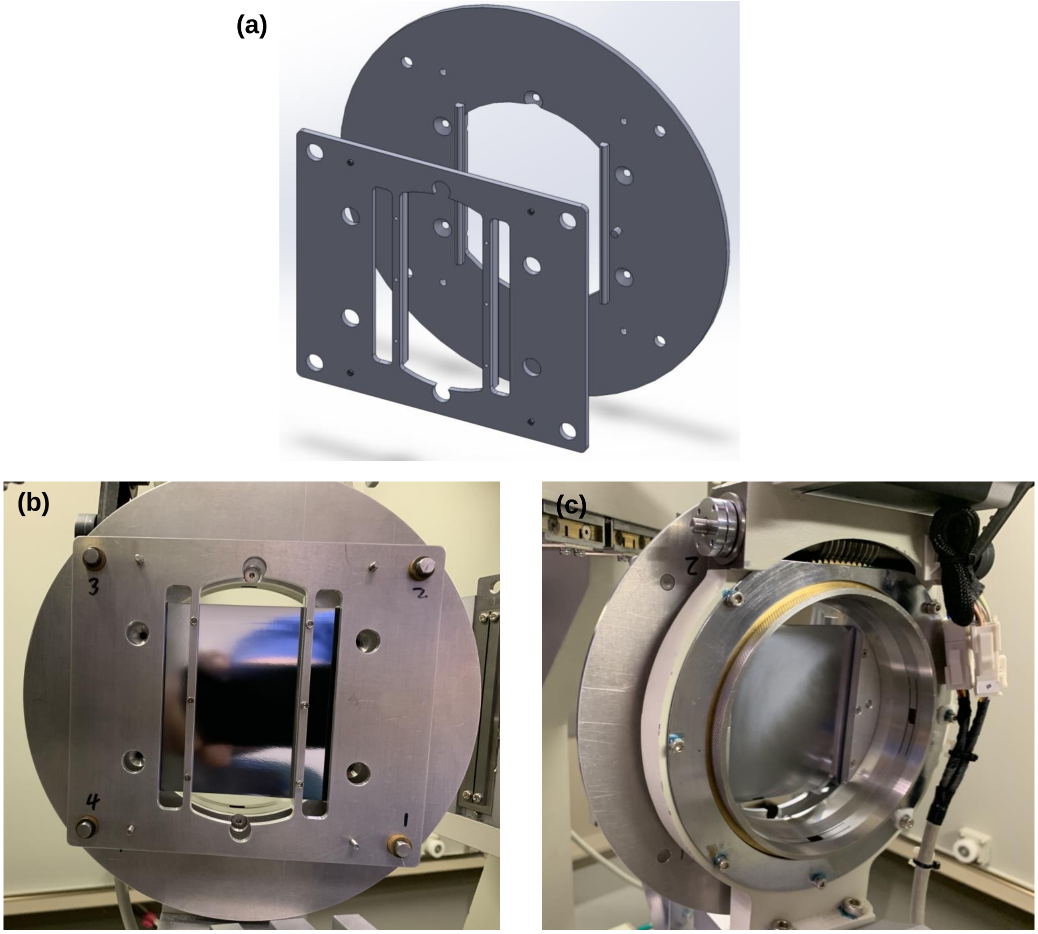

Figure 6.2: (a) SolidWorks drawing of the designed in-situ XRT four-point bending holder; (b) back and (c) front view of the bending holder mounted on XRT tool with a silicon wafer.

For pure bending conditions, four silicon wafers were etched and chemically polished down to around 150 μm by HF/Nitric Acid (HNA). The list of sample thickness can be found in Table 6.1. Figure 6.3 shows the photo of a polished Si sample and the diagram of the four-point bending setup referring to the incident X-rays. In this case, the inner span is 50 mm and the outer span is 80 mm. The side of Si wafer facing incident X-rays is assigned to the front-side. An Al layer of 17 μm was sputtered on the front-side of four Si wafer (Si → Si/Al) to displace the neutral plane toward the front-side. Another Al layer of 34 μm was sputter on the back-side of four Si wafer (Si/Al → Al/Si/Al) to displace the neutral plane toward the back-side. Each sputtering process was followed by an XRT measurement. A total of 36 XRT measurements were carried out on 12 samples (Si×4, Si/Al×4, Al/Si/Al×4) using three bending distances (0.28, 0.5, 0.75 mm).

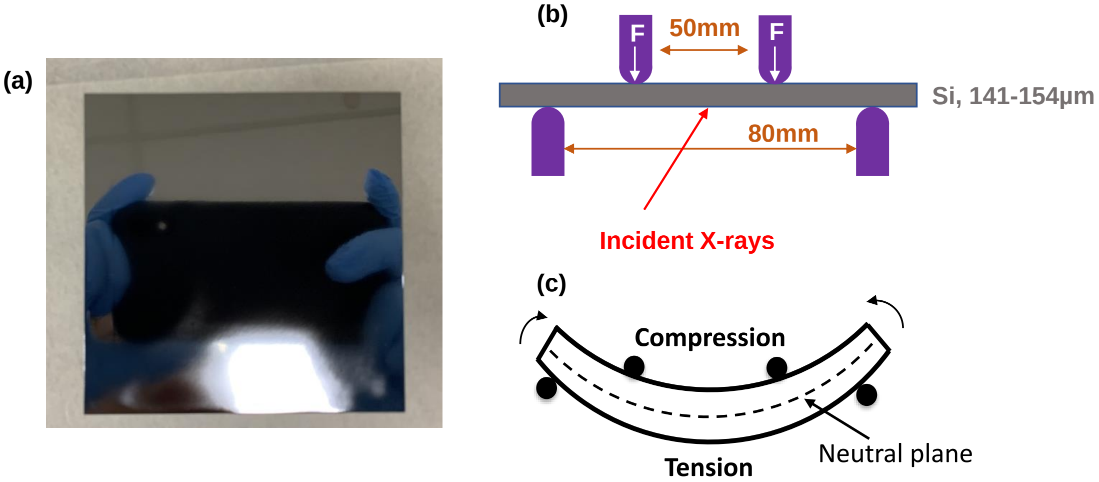

Figure 6.3: (a) Photo of a Si sample, (b) diagram and (c) stress field of the Si sample mounted on the four-point bending holder.

Table 6.1: List of thickness values of four silicon wafer and sputtered Al used in this chapter.

	Si1	**Si2**	**Si3**	**Si4**	**Front-side Al**	**Back-side Al**
Thickness (μm)	154	150	141	151	17	34

Figure 6.4 shows an exemplary XRT deflection map, $\sigma_{b,1}$ map, and $\sigma_{b,2}$ map of a four-point bending measurement using the 0.75 mm hollow pins. Instead of a uniform bending distribution in X direction across the whole silicon wafer, the deflection values at the top and bottom regions are smaller than the values in the middle. We attribute this phenomenon to the deflection of wafer edges in Y direction. The unusual deflection distribution at the top and bottom areas is explained by the $\sigma_{b,2}$ in Figure 6.4(c), where compressive stresses instead of tensile stresses are observed. In this case, the $\sigma_{b,2}$ is dominated by the component stress in Y direction and caused the sample bending toward -Z direction. In contrast, the middle part of the Si wafer shows a uniform/homogeneous bending profile, which corresponds to the plateau area in the bending stress curve in Figure 6.1. For this reason, the average $\sigma_{b,1}$ value inside the dashed purple rectangular in Figure 6.4(c) is used and noted as "Von Karman Stress".

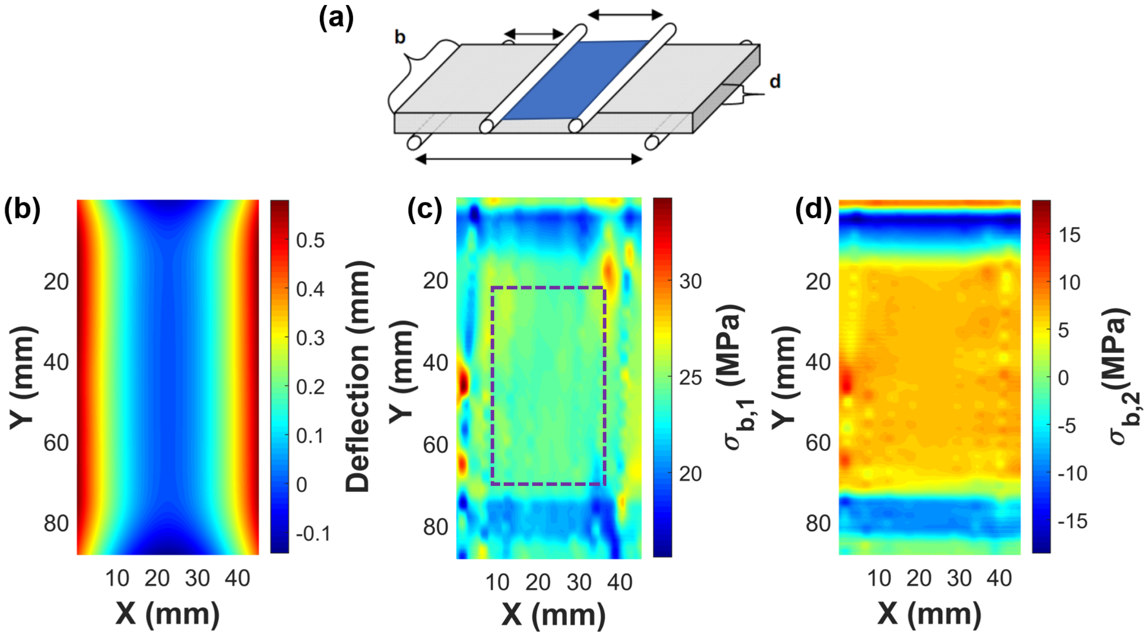

Figure 6.4: (a)Four-point bending diagram highlighting the blue areas as imaged area; (b) Deflection, (c) $\sigma_{b,1}$ and (d) $\sigma_{b,2}$ maps of sample Si1 measured and analyzed by XRT using 0.75 mm distance pins.

6.2.2 *Finite Element Analysis*

The deflection and $\sigma_{\mathrm{b},1}$ map of each XRT measurement is simulated by ANSYS. The SolidWorks drawing of the four-point bending setup (Figure 6.2(a)) is directly imported into ANSYS as the geometry. The Si material used an anisotropic elasticity:

$$\begin{bmatrix} 166000 & 64000 & 64000 & 0 & 0 & 0 \\ 64000 & 166000 & 64000 & 0 & 0 & 0 \\ 64000 & 64000 & 166000 & 0 & 0 & 0 \\ 0 & 0 & 0 & 80000 & 0 & 0 \\ 0 & 0 & 0 & 0 & 80000 & 0 \\ 0 & 0 & 0 & 0 & 0 & 80000 \end{bmatrix} \text{(MPa)} \tag{6.3}$$

The sputtered Al used an isotropic Young's modules of 71 000 MPa and Poisson's ratio of 0.33. The contacts between four bars and each sample are defined as no-separation (allowing slide but no separation). The contact between Si and Al is defined as bonded. For each solution, fix supports are applied to the outer bars and different amounts of deformation in -Z direction are applied to the inner bars.

The simulated deflection maps of Si1 using the set of 0.75 mm hollow pins are shown in Figure 6.5. The left map was simulated without boundary conditions (0 deformations in Y direction) on the sample's edges while the right map was simulated with boundary conditions on the sample's edges. Figure 6.5(a) shares the same contour as Figure 6.4(b) while the Figure 6.5(b) shows the ideal deflection map resulting from the four-point bending. This further explains the unusual deflection distribution at the top and bottom regions in Figure 6.4(c). For more accurate results, all FEA in this chapter are calculated with the boundary conditions.

The simulated $\sigma_{\mathrm{b},1}$ map of Figure 6.5(b) is shown in Figure 6.6(a). The cross-section curve matches the anticipated stress field in Figure 6.1, indicating a well-

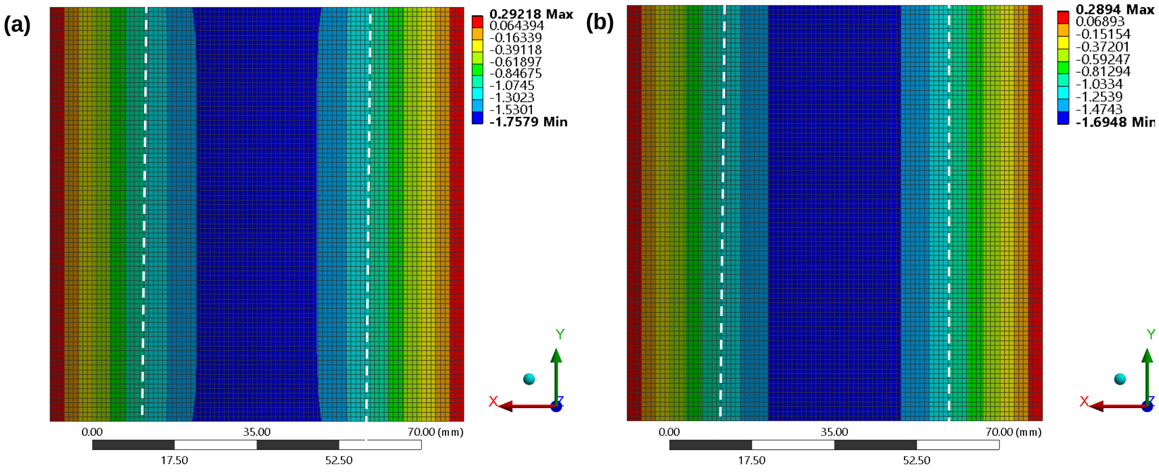

Figure 6.5: FEA simulated deflection maps of the sample Si1 (a) without and (b) with boundary conditions on the top/bottom edges. The white dashed lines indicate the position of inner bars during measurement.

defined four-point bending model. To compare the FEA σ_1 results with XRT, the $\sigma_{\mathrm{b},1}$ value at the plateau area is used and noted as ”FEA stress”.

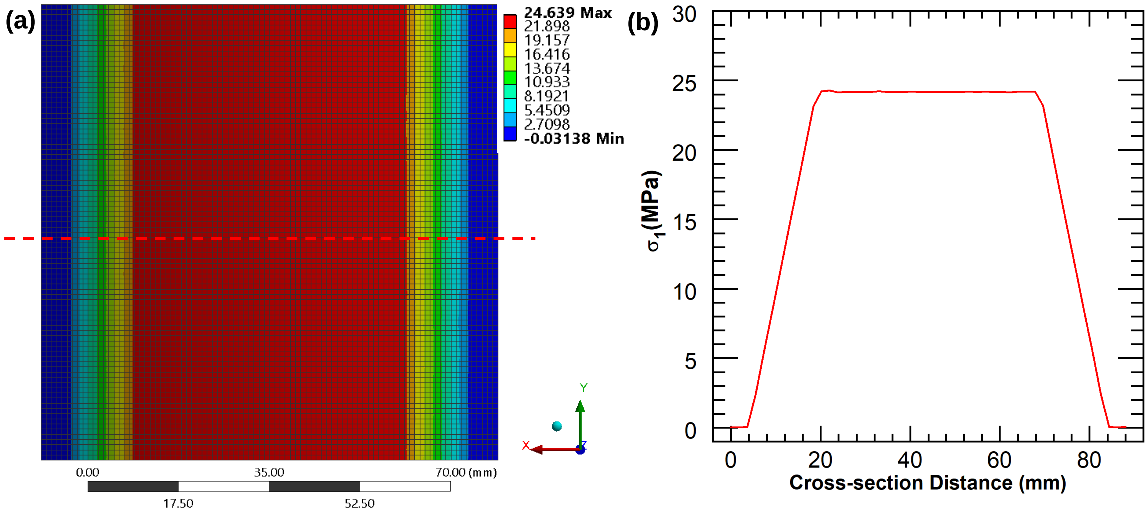

Figure 6.6: Simulated $\sigma_{\mathrm{b},1}$ map of the sample Si1 by FEA and (b) the $\sigma_{\mathrm{b},1}$ values on the red dashed line in (a).

6.2.3 Bending Distance Correction

Tightening the screws results in larger bending distance, which means the actual bending distance of inner bars in -Z direction is larger than the bending distance set by four Al pins. To correct the bending distance, the cross-section of XRT analyzed deflection in the sample Si1 using 0.75 mm pins is shown in Figure 6.7. In addition, the deflection cross-sections of the bending distances from 0.85 mm to 1.25 mm are simulated by FEA and displayed in the same figure. As we can see, the XRT deflection using 0.75 mm pins matches the FEA deflection of 1 mm bending distance. That means a 0.25 mm should be added. Therefore, the bending distance of 0.28, 0.5, and 0.75 mm using pins are now reassigned as 0.53, 0.75, and 1 mm.

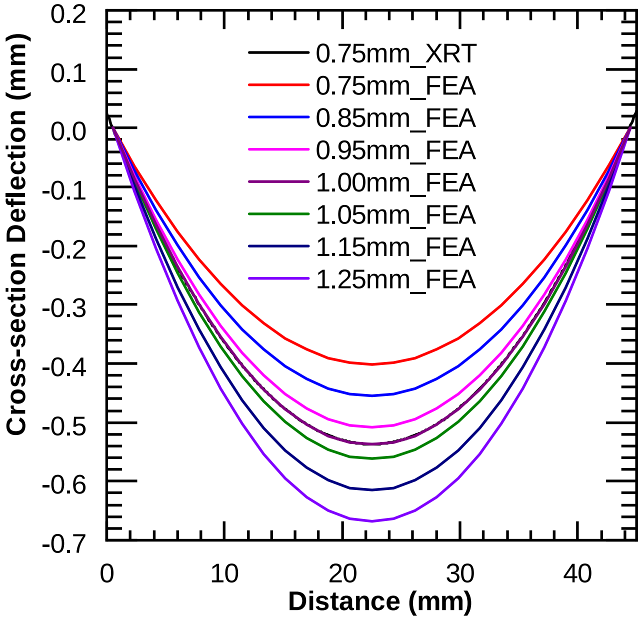

Figure 6.7: Deflection cross-sections of the sample Si1 by XRT and FEA at various bending distances.

6.3 Results and Discussion

6.3.1 One-layer System: Bare Silicon Wafer

The results of Von Karman stresses and FEA stresses of bare Si wafers at three bending distances are listed in Table 6.2. In this case, the Si wafers are under pure bending conditions. By definition, Von Karman stress is defined by (σ_{F}-σ_{B})/2, and the FEA stress is σ_F. That means that the Von Karman stress should be the same value as the FEA stress. As shown in Table 6.2, the analyzed Von Karman stress values showed 0.5-3% deviations from the FEA simulated stress, which is expected. The relatively small deviations in stress are attributed to different amounts of forces used in positioning the two bending bars.

Table 6.2: List of FEA simulated and Von Karman σ_1 values of four Si samples at three bending distances.

Bending (mm)	**Technique**	**Si1**	**Si2**	**Si3**	**Si4**	**Mean**
0.53	VK	13.770	13.519	11.775	12.73	12.9485
	FEA	12.818	12.485	12.485	12.484	12.5680
0.75	VK	17.903	17.750	17.597	17.511	17.6903
	FEA	18.137	17.667	17.668	17.665	17.7843
1.00	VK	24.297	24.126	22.162	23.448	23.5083
	FEA	24.185	23.556	23.558	23.554	23.7133

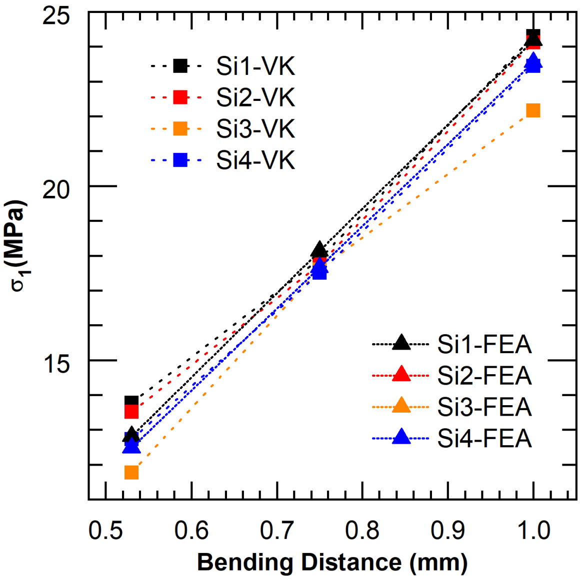

Figure 6.8: σ_1 values of four Si samples as a function of bending distance and technique. Rectangles indicate XRT results and triangles indicate FEA results.

Since the four-point bending is a linear model, the measured and simulated σ_1 values are also expected to be linear as a function of bending distance. The σ_1 values in Table 6.2 are plotted in Figure 6.8 as a function of bending distance. Both the Von Karman stress and FEA stress form a straight line, which indicates good consistency in Von Karman stress analysis.

6.3.2 Two-layer System: Silicon/Aluminum

The Al layer of 17 μm was sputtered on the front-side of the silicon wafers to shift the neutral plane away from the mid-plane. Figure 6.9 shows the photo of a sputtered Si/Al sample and the position of the sample referring to incident X-rays during loading. Note that the Al is in contact with the outer bars and the sputtered Al layers is porous. Also, note that the Si/Al samples contain a bowing effect from the sputtering process. The bowing effect was realized by transforming the thermal stress into bending stress.

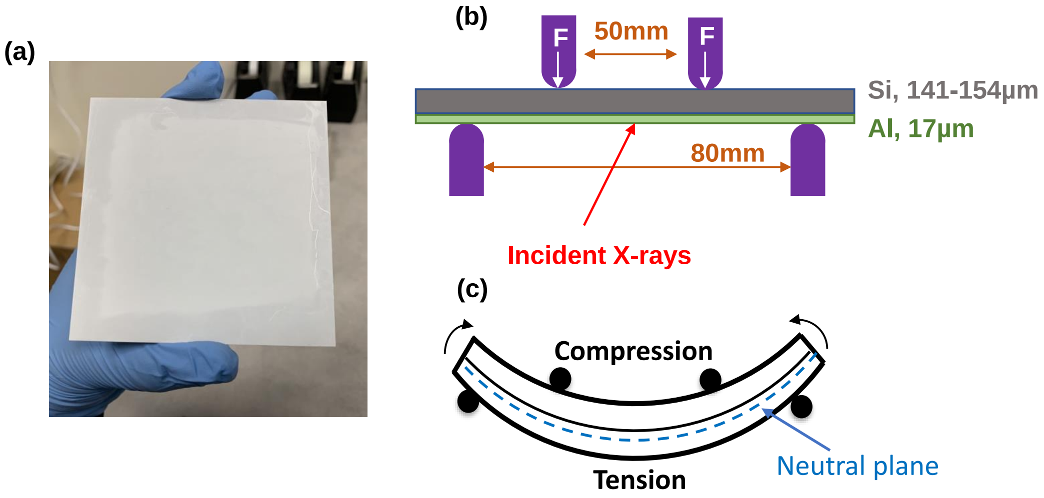

Figure 6.9: (a) Photo of a Si/Al sample, (b) diagram and (c) stress field of the Si/Al sample mounted on the four-point bending holder.

In this case, the Von Karman stress values of the four samples have larger deviations from the FEA stress values up to 18.3%, as shown in Table 6.3 and Figure 6.10.

The increased deviations are attributed to the definition of different types of stresses. The Von Karman stress probes the difference between σ_{F} and σ_{B}, while FEA stress probes only the σ_{F}. As the neutral plane was displaced towards the front-side of silicon wafers, the σ_{F} values decrease and σ_{B} increase at the same bending distance. As a result, the FEA stresses decrease and deviations are larger than pure Si wafers.

Table 6.3: List of FEA simulated and Von Karman σ_1 values of four Si/Al samples at three bending distances.

Bending (mm)	**Technique**	**Si/Al1**	**Si/Al2**	**Si/Al3**	**Si/Al4**	**Mean**
0.53	VK	14.613	113.394	12.500	13.689	13.5490
	FEA	11.960	11.626	10.878	11.626	11.5225
0.75	VK	20.054	19.115	17.570	19.177	18.9790
	FEA	16.925	16.453	15.393	16.453	16.3063
1.00	VK	26.614	26.621	23.987	25.615	25.7093
	FEA	22.567	21.937	20.524	21.937	21.7413

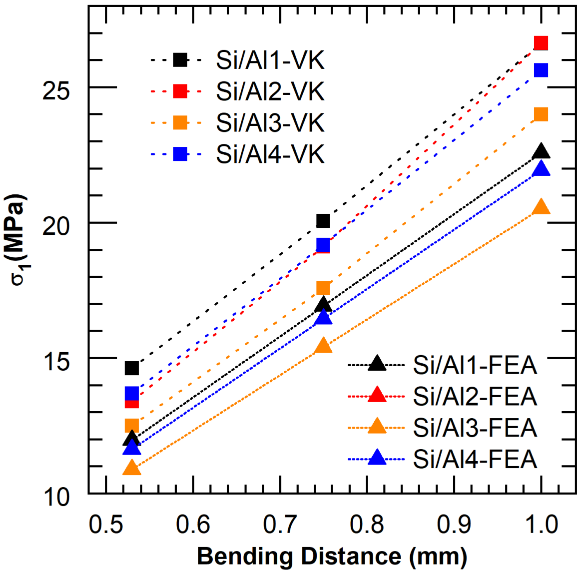

Figure 6.10: σ_1 values of four Si/Al samples as a function of bending distance and technique. Rectangles indicate XRT results and triangles indicate FEA results.

Now we consider the bending stress value in FEA results of SiAl1 at the bending distance of 1 mm. The σ_F is 22.614 MPa and the σ_B is -25.902 MPa. By the definition in Equation 5.1, the bending stress in FEA results is calculated to be 24.258 MPa, which is higher than the bending stress of 24.185 MPa in Table 6.2. If we only focus on the bending stress, both Von Karman stress and FEA stress increased after Al sputtering.

6.3.3 Three-layer System: Aluminum/Silicon/Aluminum

Another Al layer of 34 μm was sputtered on the other side of SiAl samples to shift the neutral plane away from the mid-plane. Figure 6.11 shows the photo of a sputtered Al/Si/Al sample on the back-side and the position of the sample during loading. Note, the Al/Si/Al samples also contain the bowing effect from the sputtering process. However, the bowing effect in the Al/Si/Al samples was realized by transforming the only part of the thermal stress into bending stress – the rest of thermal stress will be present during the following bending test.

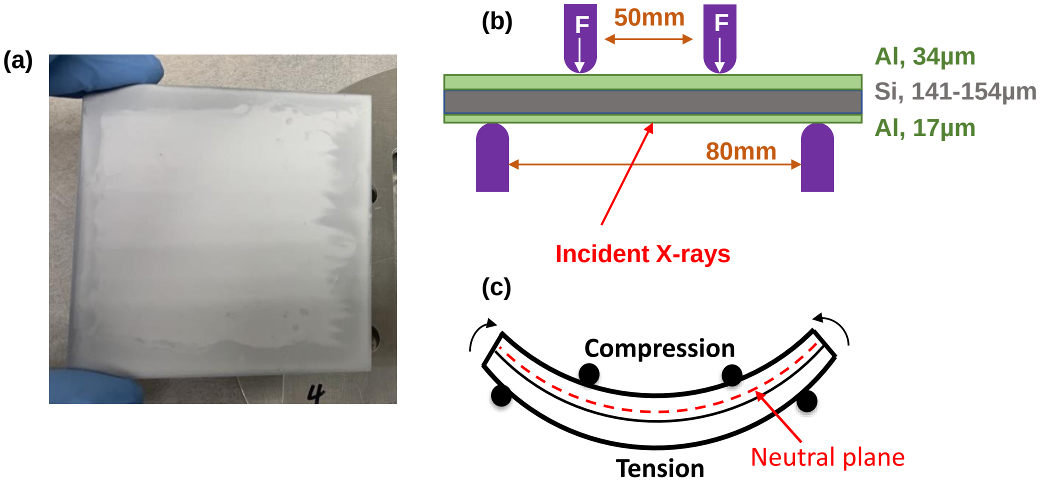

Figure 6.11: (a) Photo of a Al/Si/Al sample, (b) diagram and (c) stress field of of the Al/Si/Al sample mounted on the four-point bending holder referring to X-rays.

Both Von Karman stress and FEA stress values increased after sputtering another Al layer, as shown in Table 6.4 and Figure 6.12. In contrast to the previous data set, the deviations between two stress values in Al/Si/Al samples decreased to a maximum value of 5.4%. This phenomenon is attributed to the increased σ_F and decreased σ_B, which are results from the neutral plane shifting towards the back-side of silicon wafers. Note that thermal uniform stresses that were induced by the sputtering process also contribute to the deviations here.

Table 6.4: List of FEA simulated and Von Karman σ_1 values of four Al/Si samples at three bending distances.

Bending (mm)	Technique	Al/Si/Al1	Al/Si/Al2	Al/Si/Al3	Al/Si/Al4	Mean
0.53	VK	14.223	14.494	13.141	13.843	13.9253
	FEA	13.690	13.359	12.615	13.442	13.2765
0.75	VK	20.500	20.826	18.011	19.872	19.8023
	FEA	19.372	18.904	17.852	19.021	18.7873
1.00	VK	27.155	26.558	24.270	25.614	25.9060
	FEA	25.83	25.206	23.802	25.362	25.0500

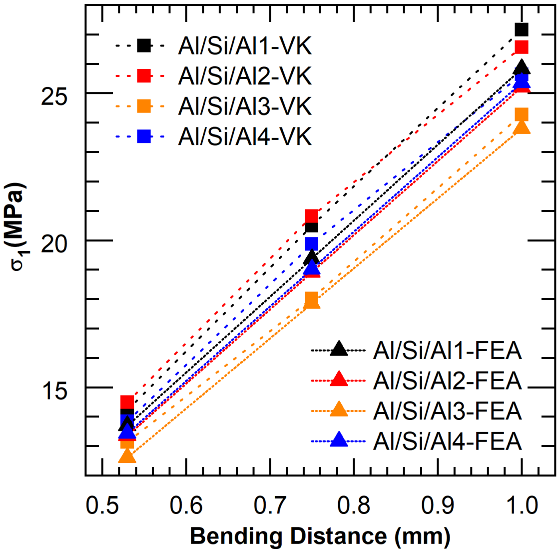

Figure 6.12: σ_1 values of four Al/Si/Al samples as a function of bending distance and technique. Rectangles indicate XRT results and triangles indicate FEA results.

Figure 6.13 shows the Von Karman stress and FEA stress values as a function of samples and techniques. It is clear that the Von Karman stresses show the smallest deviation of $\leq 3\%$ with the FEA stresses in bare Si wafers, which is exactly the assumption of Von Karman bending stress calculation. However, pure bending conditions are rarely seen in actual solar cells. The Al/Si/Al samples, which best represent actual solar cells with metal layers on the back-side, demonstrated deviations of $\leq 5.4\%$. These series of four-point bending test offers preliminary errors by assuming pure bending conditions in solar cells. Additionally, this analysis only focuses on bending stresses and ignores the thermal stress induced by the soldering and lamination process.

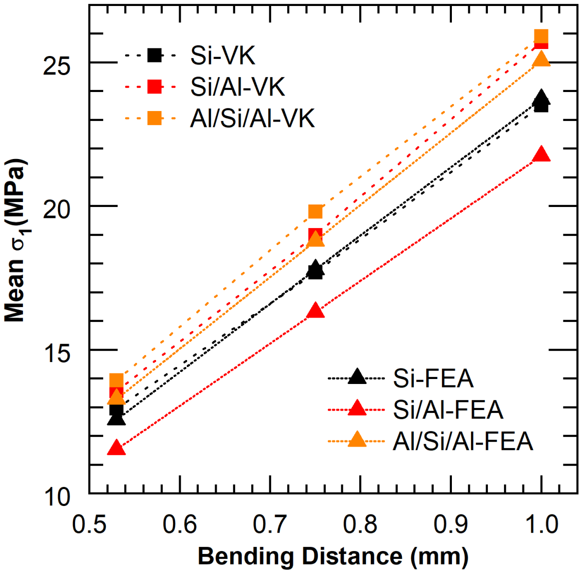

Figure 6.13: Mean σ_1 values of four silicon wafers as a function of bending distance and number of Al layers. Rectangles indicate XRT results and triangles indicate FEA results.

Chapter 7

FLEX-CIRCUIT: MONOLITHIC SI MODULE WITH ALUMINUM FOIL

The PV industry currently uses approximately 10% of annual worldwide Ag production [26]. Metallization, mainly Ag, on solar cells represents a significant part of PV modules production cost. Studies have shown that the median usage of Ag was 0.1g per cell in 2017 [5]. According to ITRPV, the average Ag price of \$533 /kg results in the cost of 4.5 cents/cell, which is 20% of the cost of a mc-Si PERC cell. To reduce the amount of Ag used in PV modules, alternative cell structures, and metal options have been explored such as Cu conductive backsheets with electrically conductive adhesive (ECA) interconnects and Cu-plated grids on solar cells [73]. Though Cu-plated grids have reached series resistance comparable to Ag, reliability issues such as copper contamination in silicon and poor finger adhesion are still a challenge [74]. Cu backsheets with ECA are still expensive because of the cost of Cu and Ag content in ECA. Al is generally a third the price of Cu with 60% the conductivity of Cu, which makes it a potential substitute for Cu backsheet replacement.

Meanwhile, the metal ribbons on solar cells put large quantities of stress on solar cells and play an important role in generating cracks and reduce the yield of PV modules. The stress could be higher if metal ribbons on each side of the solar cell are not symmetrical. For example, larger than 600 MPa σ_1 values are observed at the vicinity of the end of the back ribbons in glass/glass packaging.

7.1 Introduction of Flex-Circuit Concept

A new module concept called flex-circuit is proposed as an alternative to reduce the Ag usage on solar cells as well as improve reliability through replacing regular metal

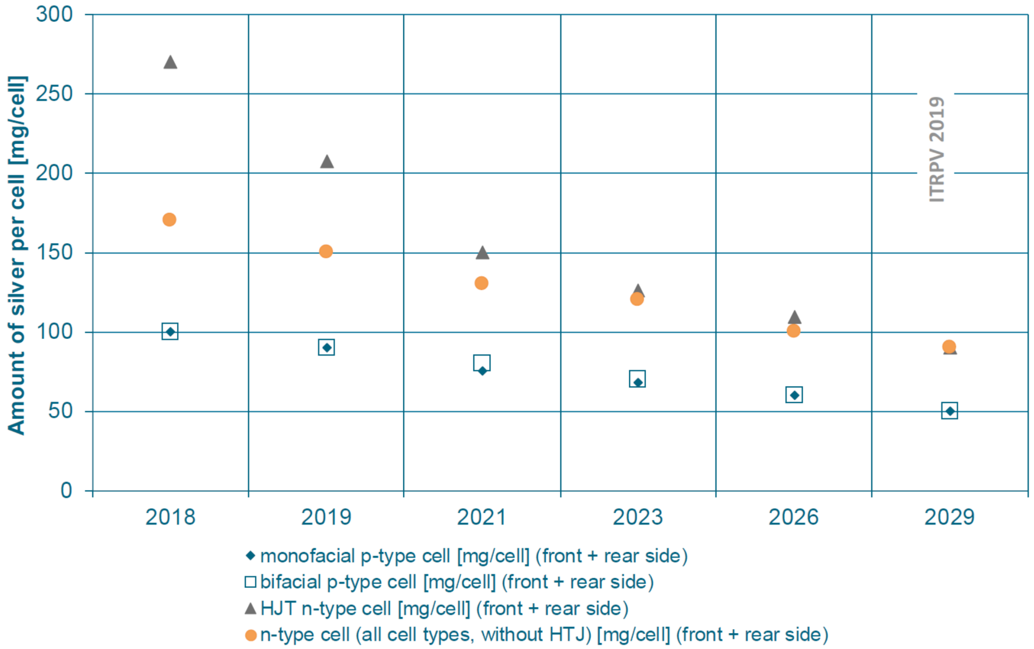

Figure 7.1: Predicted Ag usage per solar cell in the next ten years, taken from ITRPV [5].

ribbons with perforated Al foils. The concept uses an interdigitated back contact (IBC) based silicon solar cell fabricated at ISC Konstanz (Zebra cells), as shown in Figure 7.2 [75]. The Zebra cells use 156 × 156 mm n-type Cz wafer and have an average efficiency of 21-22%. The Zebra cells' front side are similar to the SunPower IBC cells with anti-reflection coating and no metal on top surface, but Zebra cells' back-side use four pairs of Ag busbars (each pair has one positive busbar and one negative busbar) and parallel Ag fingers instead of Ag grids and soldering pads in SunPower IBC cells. As shown in Figure 7.2, the Zebra cells have three different Ag usage configurations from standard busbar with industry-standard amount of Ag to no Ag busbar at all. A 3 mm wide isolation layer on each busbar is applied to isolate the busbar from fingers of opposite polarization. Among the three configurations, thin busbar cells and no busbar cells are used in this thesis.

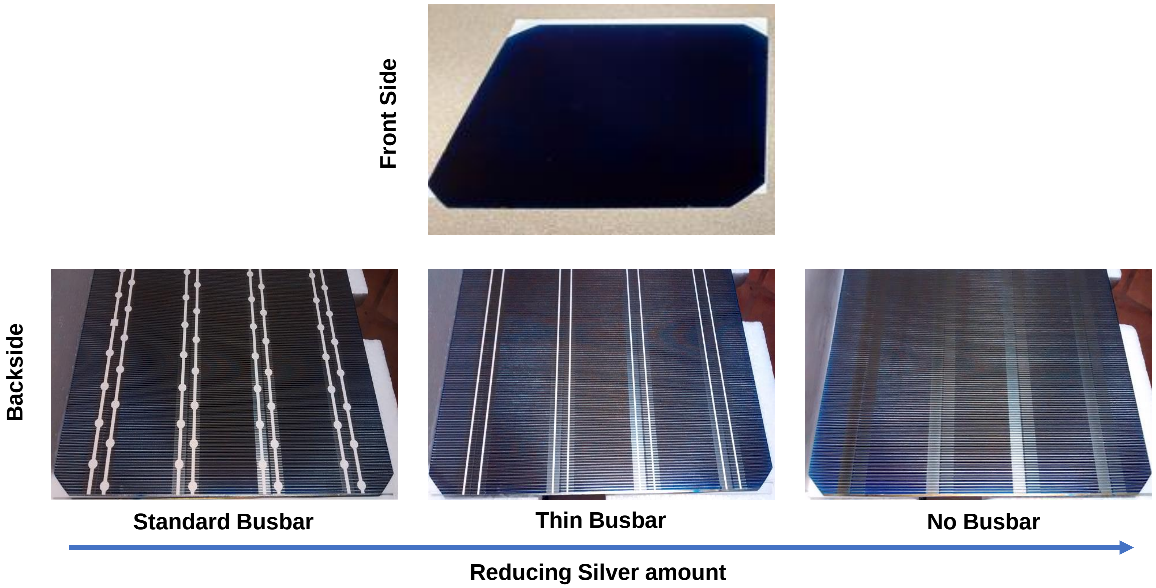

Figure 7.2: The front and back side of Zebra IBC solar cells from ISC Konstanz in three Ag configurations: standard busbar, thin busbar and no busbar.

The flex-circuit concept chooses IBC solar cells for its unique module stack because the Al electrodes cannot be positioned in front of the solar cell. A traditional PV stack and the flex-circuit PV stack using IBC solar cells are shown in Figure 7.3. Compared to traditional PV modules (Figure 7.3(a)), the flex-circuit PV module highlights a double glass module configuration with Al foil electrodes as interconnection on cell back. The whole Al foil is isolated into two parts for positive and negative terminals and extends out of the laminate for electrical connection. The glass thickness is reduced to 2 mm for cost reduction and weight management. Polyolefin based encapsulant (TPO/POE) is primarily used as it has lower moisture ingress rate and no acetate acid production compared to commonly used EVA, which theoretically could cause delamination and corrosion as module failure [73]. But for research and development purposes, EVA is also used because it is the most widely used encapsulant in modules.

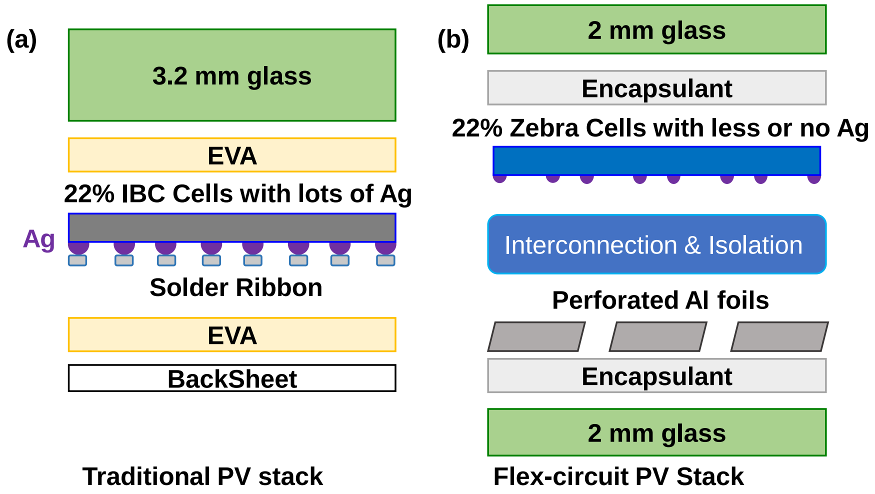

Figure 7.3: Schematic of (a) the traditional PV lamination stack and (b) flex-circuit PV module stack in a double glass format.

The key challenge of this concept lies in the interconnection between the solar cells and the Al electrode. On one hand, the Al electrode must have low electrical resistivity with the Ag on the busbar areas (busbars or fingers). On the other hand, the Al electrode must be isolated from the Ag fingers located other than the busbar area to avoid shunting.

7.2 Module Fabrication

A NPC LM-110X161-S module laminator was used for module assembly. Tempered glasses (textured on one side) and 2 mm boronsilicate glasses are used for flex-circuit modules. Ultra-high vacuum Al foils in three thicknesses from All Foilsare tested and to make the electrodes: 12.5, 45, and 70 μm. Encapsulants used in this section include Ethyl Vinyl Acetate, EVA9100 from 3M (EVA) and Polyolefin Elastomer from Cybrid (POE).

The reference fabrication of single-cell flex-circuit PV modules include two lamination cycles, one embossing, and one laser isolation. The sequence of each step is shown in Figure 7.4 [73]. Al foil sheets were cut to 240 mm × 156 mm, and 600 μm tall busbars were embossed into the foil using a 2-sided die. The pattern in the die is the same as the busbar pattern on the cells. Embossed foils were laminated to the back glass of the module with the female side of the die left in place during the lamination so that the raised areas filled with encapsulants. The positive and negative terminals were then separated using a 532 nm laser. Photos of the embossed Al foil with the pattern matching the Zebra cells and laser isolated Al electrodes are shown in Figure 7.5(a) and (b), respectively.

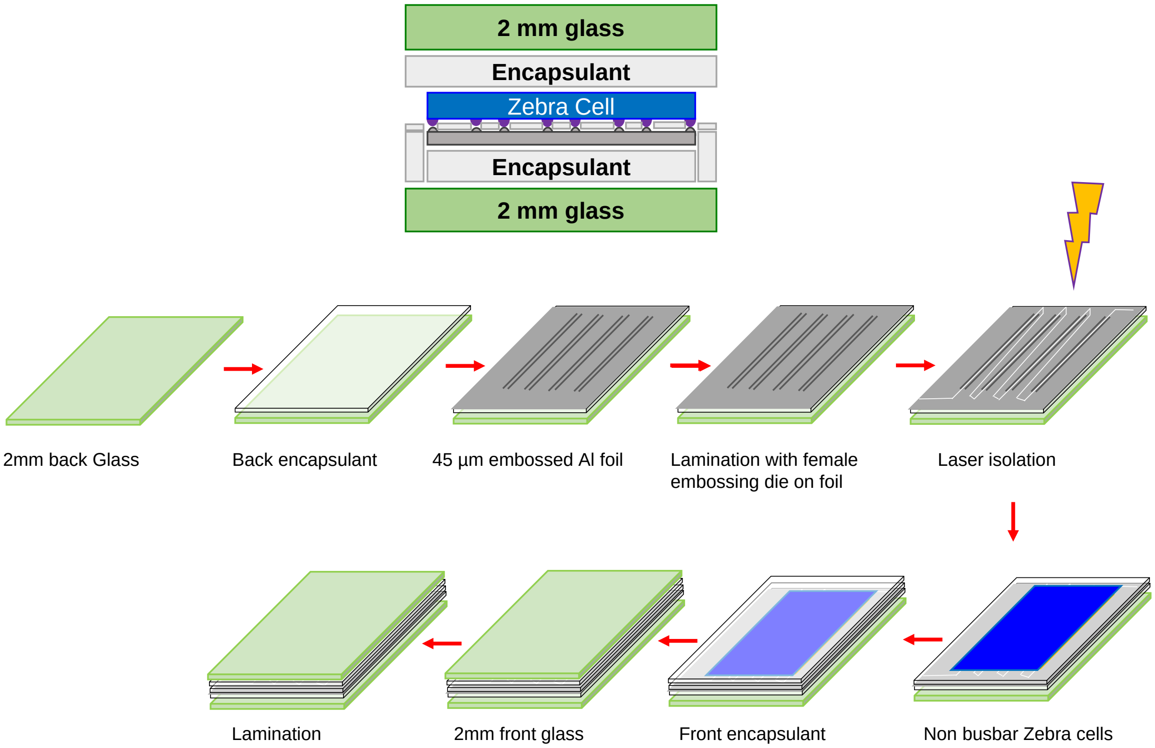

Figure 7.4: Schematic a reference flex-circuit lamination process featuring two lamination cycles, a laser isolation, and a embossing process.

After laser isolation, encapsulant was cut by hand to cover the flat areas of the electrode but not the embossed busbars (such that the encapsulant does not block the contact between the cell and the Al foil). The cells were aligned to the electrode simply by lining up the edge of the cell with the edge of the foil. Front encapsulant and glass were added before laminating modules at 145°C for 11.5 min (curing time)

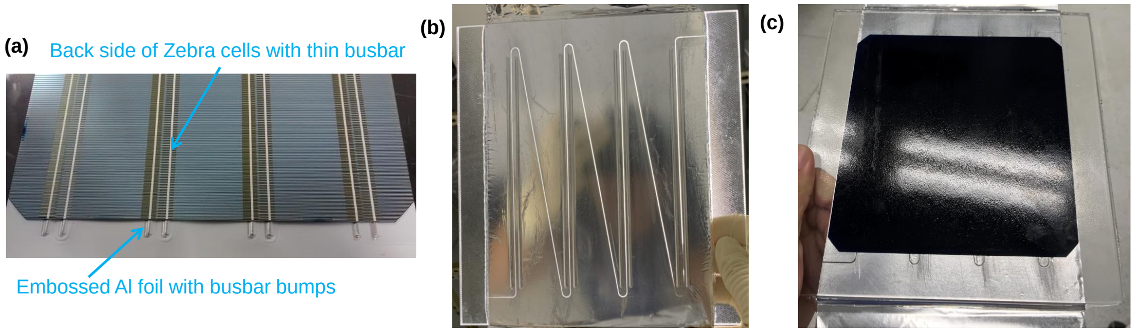

Figure 7.5: Photos of (a) an embossed Al foil matching the busbar pattern on Zebra cell, (b) a laser isolated Al electrode, and (c) a finished flex-circuit module.

for modules with EVA and 160°C for 12 min (curing time) for modules containing POE. A photo of the finished single-cell flex-circuit module is shown in Figure 7.5(c). Note that the electrical contact between the Al electrode and the solar cell is achieved by lamination pressure pushing the Al foil onto the cell.

Initial module lamination has shown great results in both EL and IV measurements using thin busbar Zebra cells. No cracks and shunts are observed in the EL image (Figure 7.6(a) and (d)), indicating the lamination process results in full contact between the Al foil and the solar cell. The solar cell shows a slightly darker area in the center, indicating higher resistance. Note that the crack on the cell bottom was present in the PL image before lamination.

After lamination, the module with thin busbars was subjected to IEC standard thermocycling (TC) (85°C to -40°C at 1160°C/min with 10 min soak at minimum and maximum temperatures). TC100 (100 cycles) is often used to test the thermal stability of interconnections in PV modules. Each cycle takes approximately 4 hours. Failure modes such as cell breakages, metal ribbon detachment, and delamination are often observed during TC tests. The above flex-circuit PV module was put through a TC200 test and its EL and IV curves were measured after TC100 and after TC200. The results are shown in Figure 7.6(b) and (c). After TC100, severe delamination

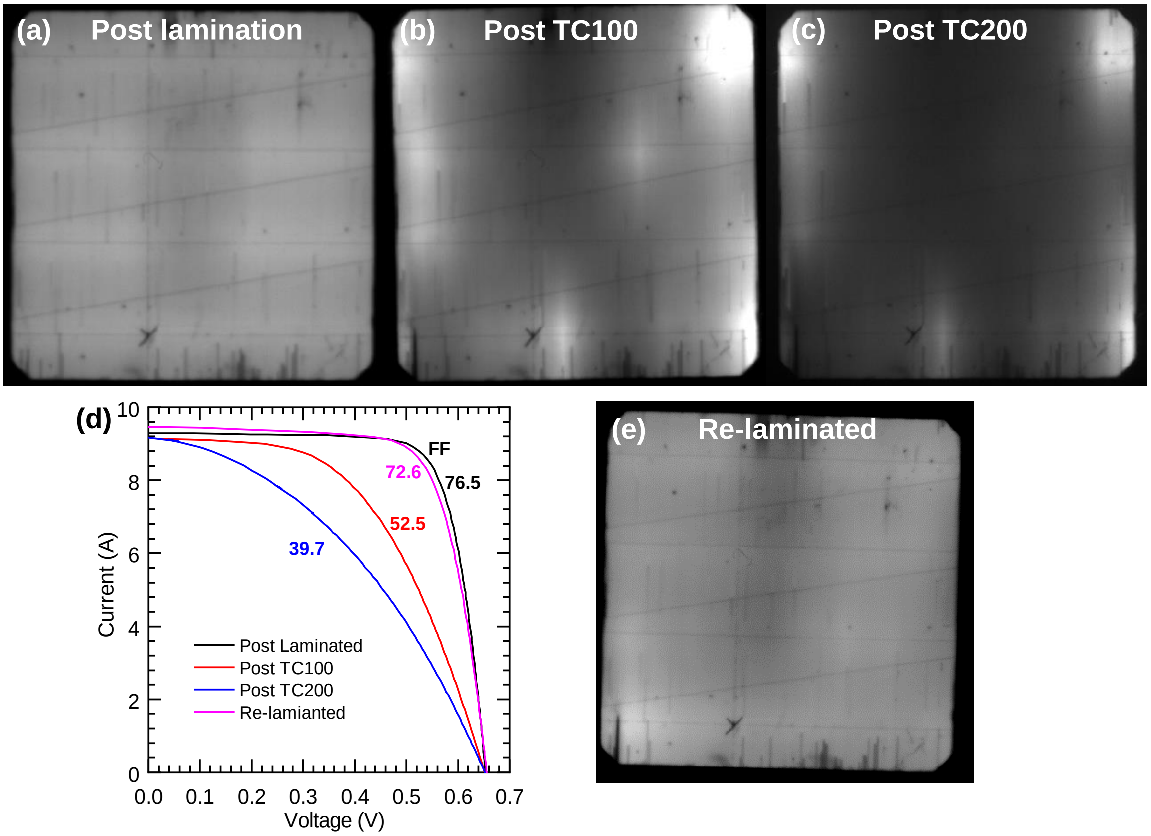

Figure 7.6: EL images of a flex-circuit PV module (thin busbar cell) taken (a) after lamination, (b) after TC100, (c) after TC200, and (e) re-laminated. (d) are their corresponding IV curves.

occurs in the center of the module, as indicated by those dark areas. The delamination behavior becomes even worse after TC200. The center part of the cell goes almost dark while several corners and edge areas still hold the contact. The delamination phenomenon is further confirmed by the IV measurement, where the fill factor (FF) of the PV module dropped from 76.5% to 52.5% and then to 39.7%. Surprisingly re-laminated the flex-circuit module results in restoring most of the interconnection degradation, suggesting that the delamination is caused by the Al foil losing pressure contact with the cell.

Apart from the increased contact resistance in the EL images, wrinkles on the Al foil were also observed as shown in Figure 7.7. Those wrinkles are located perpendicular to the laser isolation trenches and busbars. The wrinkles could be the cause of losing electrical contact as shown in the EL images.

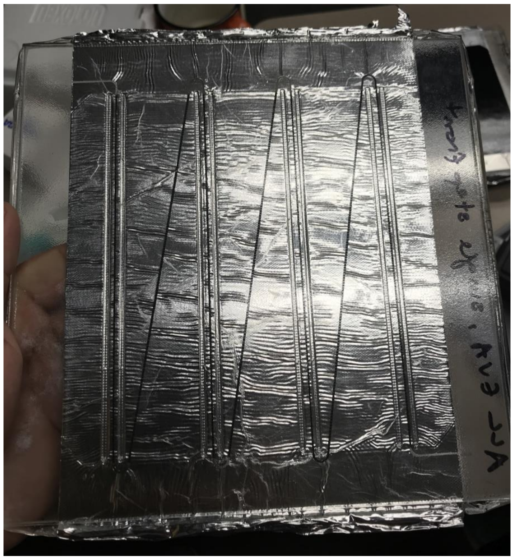

Figure 7.7: Photo of a flex-circuit module after TC100 test featuring wrinkles on the Al foil.

To have a better understanding of the interconnection degradation, polished cross-sections of the module on contact areas were imaged by optical microscope and SEM as shown in Figure 7.8. For comparison, Figure 7.8(a) shows images from a healthy busbar (bright area on EL image) and Figure 7.8(b) shows the images from a degraded busbar (dark area on EL image). The images of the healthy busbar show that the Al electrode has physical contact with Ag; the images of the degraded busbar show that the Al electrode has no physical contact with Ag. It is confirmed that the increased series resistance after TC testing is caused by the Al electrode detaching from the Ag on the solar cell.

7.3 Reliability Characterization and Lamination Optimization

As the TC cools down and heats up the test subjects with a 125°C temperature difference, delamination may be caused by the different thermal properties in the

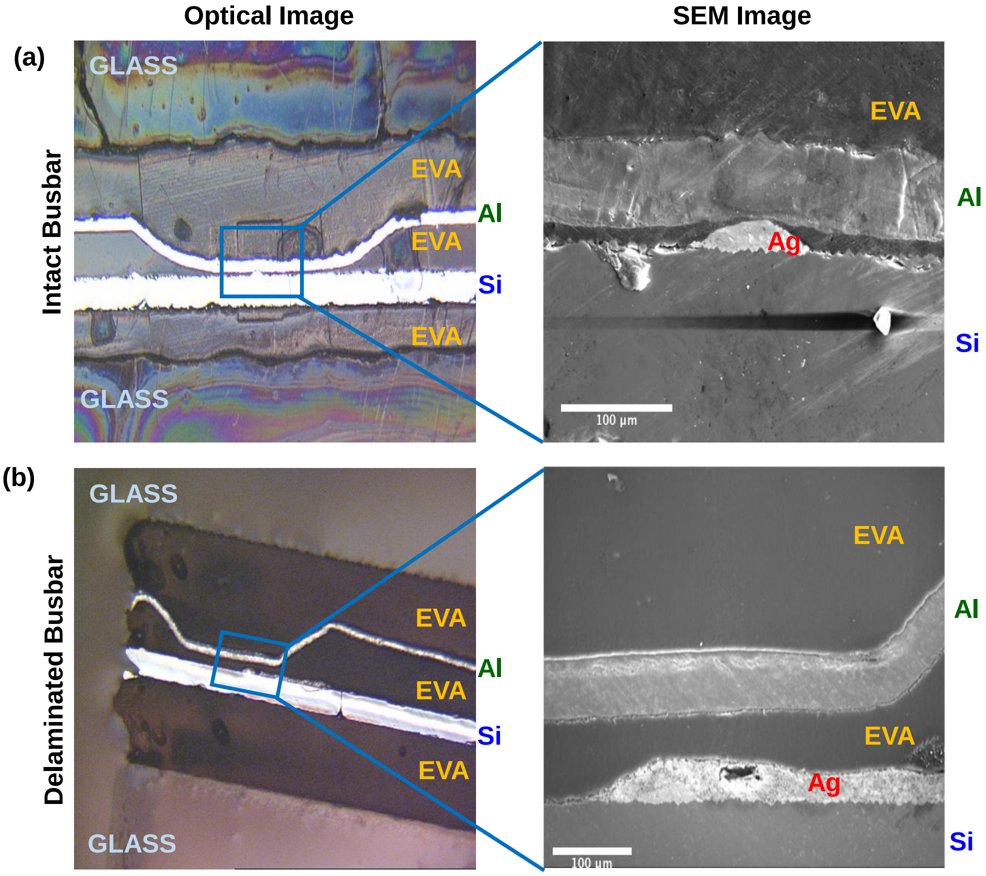

Figure 7.8: Optical and SEM images of the cross-sections of (a) healthy busbar area with low series resistance and (b) degraded busbar area with high series resistance.

encapsulant and Al. The encapsulant, EVA, for example, has a coefficient of thermal expansion (CTE) of 280 μm/m°C according to the product manual. Al, alternatively, has CTE of 21-25 μm/m°C, which is an order of magnitude smaller than the encapsulant. The encapsulant contracts and expands much more than the Al foil during temperature ramps. When the stress caused by the movement of encapsulant is larger than the adhesion strength between the foil and Ag, which is likely to take place under elevated temperature, delamination occurs. Furthermore, the fact that the delamination starts from the cell center leads the cause of delamination to the uneven pressure on the laminate during the lamination process. The silicone membrane puts more force on the glass corners and edges than the center (from edge pressing), resulting in higher pressure (better contact) on the cell edges and lower pressure (poor contact) in the cell center area than cell center.

Based on the discussion, we hypothesize the delamination could be explained by the following: (1) processed-induced stress on the foil from laser isolation and/or embossing; (2) different CTEs in the encapsulant and the foil; (3) edge pressing during glass-glass module lamination.

To test the first hypothesis, three electrodes following the stack of Al foil / EVA / glass were fabricated, tested through TC100 test and visually inspected. For comparison, one electrode was processed only with the laser isolation (Figure 7.9(a)), one electrode was processed only with embossing (Figure 7.9(b)) and one electrode was processed with both (Figure 7.9(c)). All three electrodes exhibit a similar amount of wrinkles after the same amount of TC stress testing, indicating that neither laser isolation nor embossing is the cause of wrinkling.

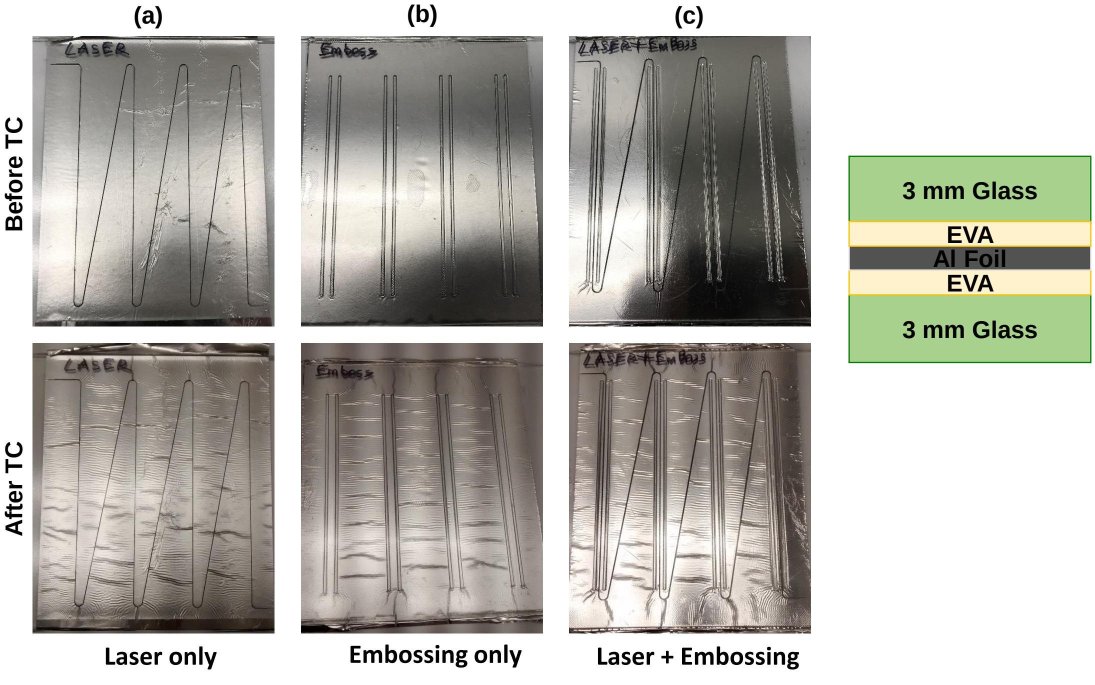

Figure 7.9: Photo of 20 cm×20 cm Al electrodes before and after the TC test. The electrodes were fabricated with the stack shown on the right and processed by (a) laser isolation, (b) embossing and (c) laser isolation + embossing.

If the second hypothesis is true, one could reduce the plane stress by choosing the encapsulant and Al foil in different thicknesses and properties. With the same amount of shear force present, a thicker foil should experience a smaller amount of stress. Six samples following the stack of glass/encapsulant/Al foil/encapsulant/glass were fabricated and characterized by the TC test. Three encapsulants (EVA, POE, ION) and three foil thicknesses (12.5, 45, and 70 μm) were tested. The foil statuses were recorded before and after TC, as shown in Figure 7.10. Samples (a), (b) and (c) are compared for different encapsulants. Those three encapsulants have slightly different CTE, Young's modulus values and different thicknesses. As shown in the Figure 7.10, the three encapsulants have little impact on the wrinkles. Samples (a), (d) and (e) are compared for different foil thicknesses. The 12.5 μm sample shows some wrinkles at a smaller scale and the 70 μm one shows no wrinkles at all. It is

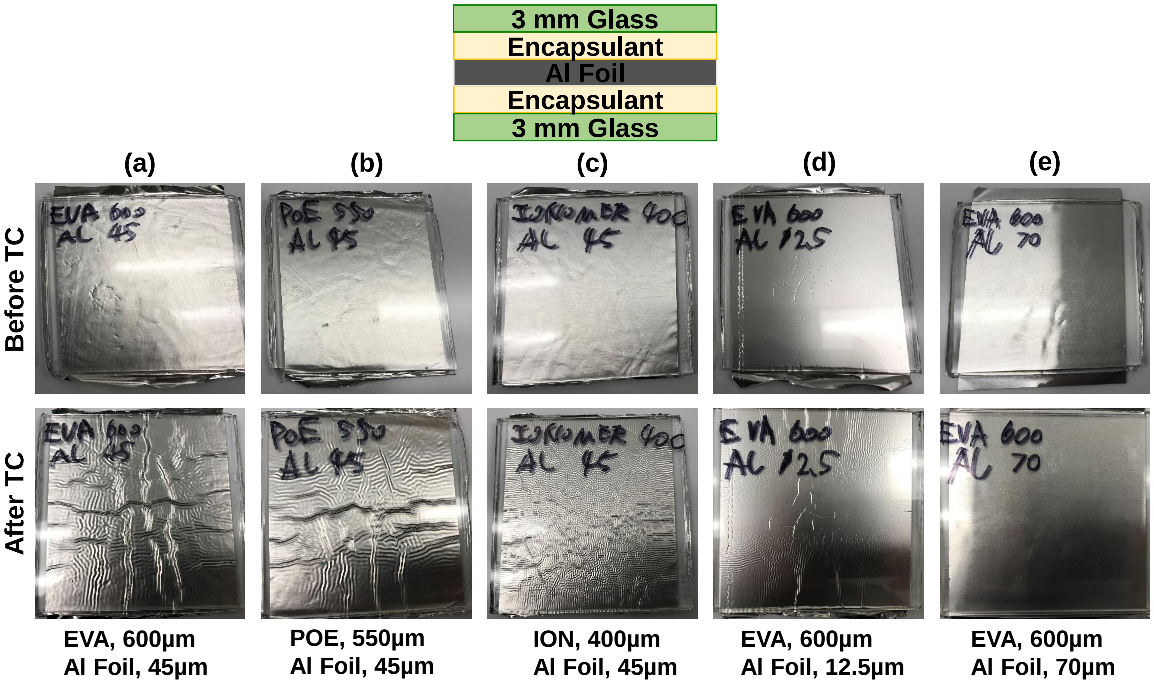

EVA, 600µm
Al Foil, 45µm

POE, 550µm
Al Foil, 45µm

ION, 400µm
Al Foil, 45µm

EVA, 600µm
Al Foil, 12.5µm

EVA, 600µm
Al Foil, 70µm

Figure 7.10: Photos of 5 cm×5 cm Al electrodes before and after the TC test. The electrodes were fabricated with different encapsulants and foils, following the stack shown on the top. No laser isolation and embossing were applied.

confirmed that the wrinkle comes from different CTEs in the materials and thicker foil can eliminate wrinkles.

Next, we focused on the third hypothesis by mitigating edge pressing by placing glass substrates with the same thickness of the laminate around it, serving as a lamination frame (see Figure 7.11). In this way, the uneven pressure transferred to the frame. To test this hypothesis, three modules were fabricated: one without the frame using a 45 μm foil as a reference, and two with the frame using 45 and 70 μm foils. Note that no-busbar Zebra cells from the same batch were used in this case to raise the difficulty of making electrical contact and the 70 μm Al foil was used to reduce wrinkles. Figure 7.11(a) shows an example of edge-press induced high contact resistance (non-busbar cell) laminated without frame.

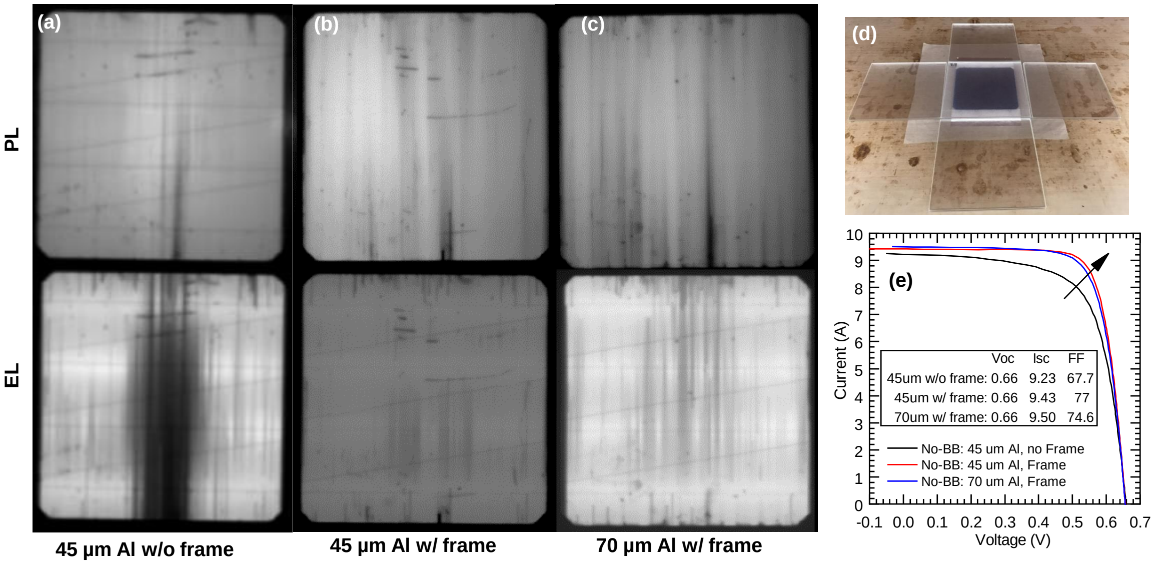

Figure 7.11: PL and EL of flex-circuit PV modules fabricated with (a) 45 μm foil without frame, (b) 45 μm foil with frame, and (c) 70 μm with frame; (d) photo of a flex-circuit laminate with frame sitting on the laminator bench; (d) IV curve of the three flex-circuit modules.

With the assistance of the frame, both (b) and (c) showed reduced contact resistance and more homogeneous EL distribution. The result is further confirmed by the IV curve where FF of 77 and 74.6% are measured compared to the value of 67.7% in the reference module, showing that the lamination frame is able to mitigate the edge pressing. On another note, the module (c) with thicker Al foil that demonstrated no wrinkling in the previous experiment, produced a lower FF than module (b). We attribute this FF drop to the thicker foil not being able to conform to the shape of the embossing die.

The above three modules were again subjected to the TC200 test. Unfortunately, all three failed due to increased contact resistance. Neither a lamination frame nor 70 μm Al foil is able to eliminate delamination in stress flex-circuit modules. Still, the reference lamination process needs to be modified to mitigate this loss of contact resistance. Since delamination is a result of the Al electrode losing electrical contact to the solar cell, three approaches are developed to increase interfacial adhesion in order to improve contact resistance.

The first approach adds a laser welding process to the end of module fabrication. The laser can provide local heat directly to the busbar areas on Al foil through the back glass and weld Al foil to Ag. By precisely controlling the laser power and pulse speed, the amount of heat could melt Al foil and possibly Ag, without damaging the other cell layers under Ag (confirmed by SEM cross-section images, not shown). This laser welding process works well with Zebra cells with busbars where the laser alignment can be readily carried out. However, it is challenging to laser wield on Ag fingers of no busbar Zebra cells.

In the second approach, a thin layer of adhesives is applied to the contact areas before lamination. Although the epoxy is not conductive, when the thickness of the epoxy is smaller than 30 μm, the rough surfaces (both surfaces have spikes) of Al foil and Ag are able to poke through the epoxy layer and make electrical contact to Ag (confirmed by X-ray tomography images). A deposition process using a paste dispenser was developed to achieve a uniform thin epoxy layer. By controlling the

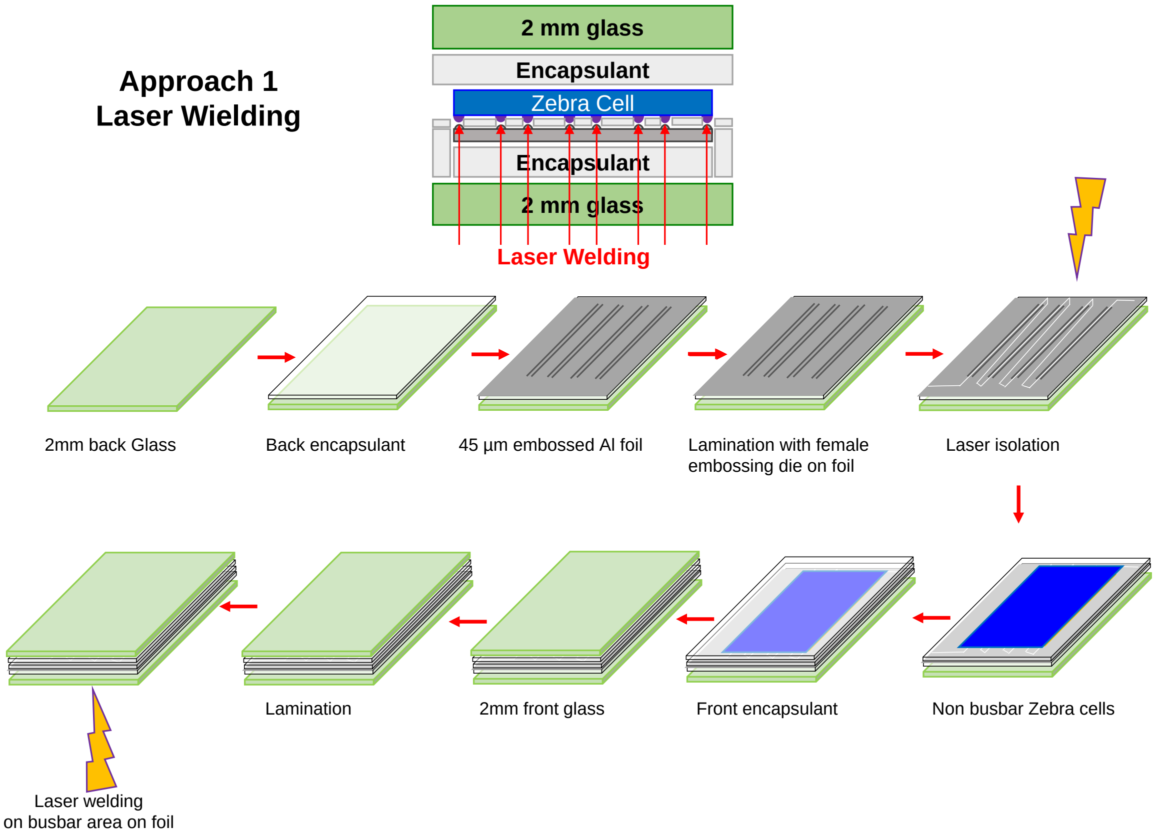

Figure 7.12: Fabrication process of flex-circuit modules using Approach 1 featuring a laser wielding process after lamination.

pressure, needle height, needle speed, and viscosity of epoxy, a thin epoxy layer of 30 μm can be successfully placed on the busbar areas.

In the final approach, to further promote interface adhesion and reduce process steps, the embossing step is taken out and a uniform thin epoxy layer (30 μm) is applied on the whole Al foil instead of just on the busbar areas (as used in approach 2). Full epoxy coverage should provide a lower chance of delamination. However, without embossing the Al foil and inner layer of encapsulant, the Al foil has full physical contact with the Zebra cell, both on the busbar areas as well as non-busbar areas through fingers. To provide electrical isolation on the non-busbar areas, the Zebra cells have full isolation paint/paste covering those areas.

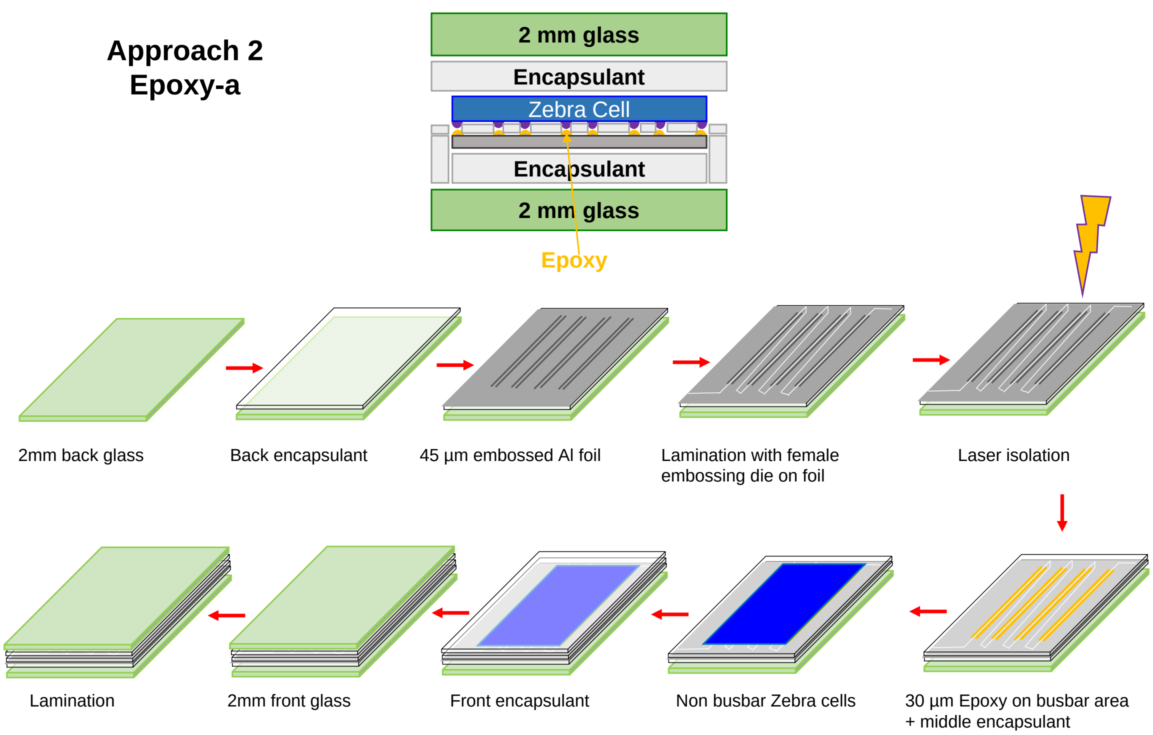

Figure 7.13: Fabrication process of flex-circuit module using Approach 2 featuring the isolation paste on selected Al foil areas.

The effectiveness of the approaches was evaluated again by IV and EL measurements through the TC200 test. Four flex-circuit modules following the reference method and Approach 1, 2 and 3 were fabricated and tested, as shown in Figure 7.15. Without adhesion strengthening, the center area of the solar cell is dark in the EL image shown in Figure 7.15, as expected. The module efficiency dropped by 19% (relative efficiency). On the contrary, modules fabricated with Approach 1, 2 and 3 demonstrated notably improved results after the TC200 test. The module with Approach 1 and 2 barely showed any change after TC200 in the EL images, indicating that less delamination occurred compared to previous approaches. The module efficiency dropped by 1.5 and 3%, respectively. The module fabricated with Approach 3 showed a shunted finger on the post lamination image, resulting in a module efficiency of 16.5%. The shunt could be caused by inhomogeneous isolation paste. However, the

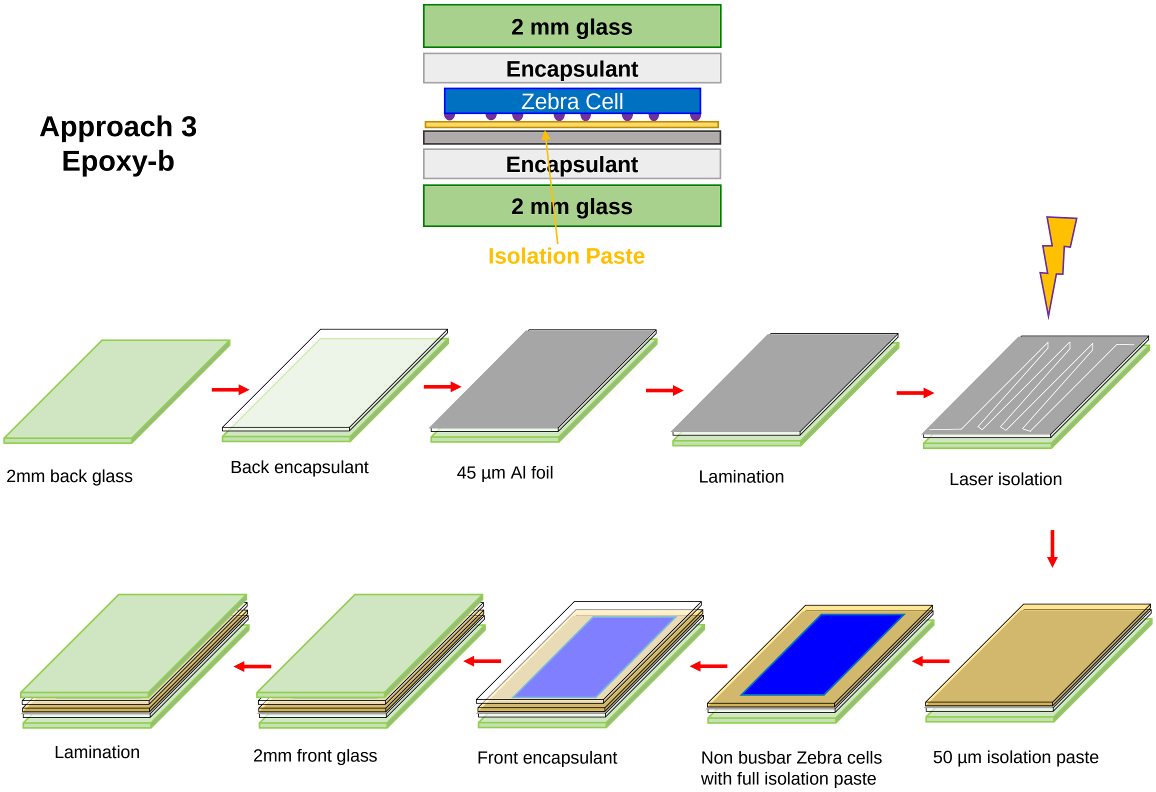

Figure 7.14: Fabrication process of flex-circuit module using Approach 3 featuring the isolation paste on the whole Al foil and no Al embossing.

shunt was ”cured” in the post-TC200 EL image, which could be a result of isolation paint movement/redistribution during the TC test. With the shunt elimination, that module’s efficiency increased to 19.5%. Thus, all modules fabricated with the proposed approaches passed the TC qualification test of less than 5% efficiency decrease, demonstrating the effectiveness of the approaches.

7.4 Stress of Different Module Configurations

As discussed in Chapter 5, traditional metal ribbons put stresses on the solar cell such that the solar cells have a higher chance of generating cracks in the future and eventually fail within the warranty period. This further motivates the use of this flex-circuit concept which reduces the stress values on solar cells. The fabrication

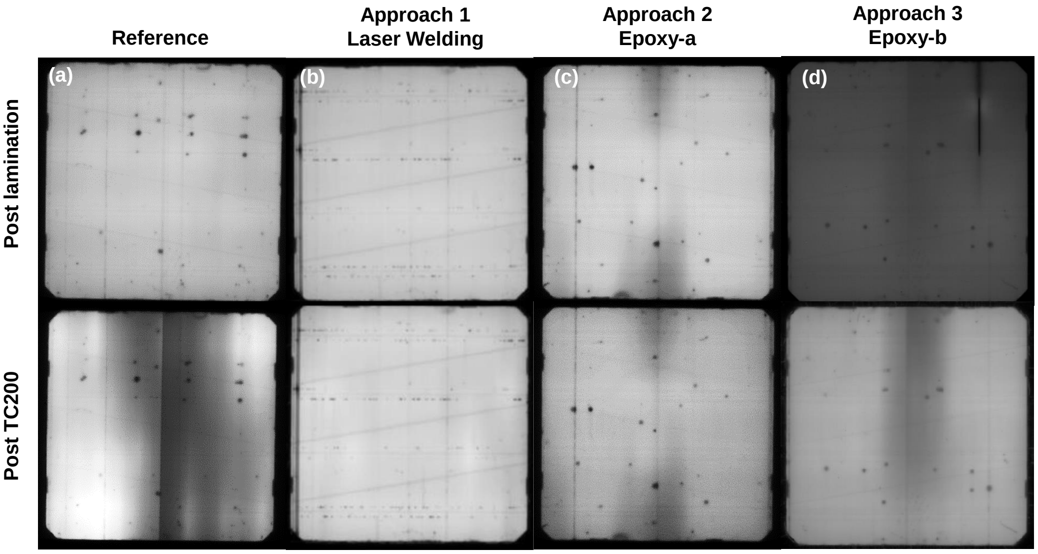

Figure 7.15: EL images of modules fabricated using (a) the reference, (b) Approach 1, (c) Approach 2, and (d) Approach 3.

of flex-circuit modules does not involve a high-temperature process (≥160°C), which means theoretically the solar cells in the flex-circuit module should have less stress than traditionally soldered modules. It is interesting to apply our newly developed XRT method to investigate the stress distribution on Zebra solar cells inside flex-circuit modules and compare the stress values to those in traditional PV modules.

Four PV modules following the PV stacks shown in Figure 7.16 were fabricated in glass/glass configuration and measured by XRT, using the methodology demonstrated in Chapter 3. Module Epoxy-a and Epoxy-b were fabricated using Approach 2 and Approach 3, representing two major configurations used in the flex-circuit concept (Approach 1 and 2 are expected to have similar stress distribution). Since Approach 2 has embossed Al pushing towards the solar cell, it is expected that module Epoxy-a has higher stress than module Epoxy-b, especially at the embossed areas. Module reference-Zebra used a Zebra cell but the cell was soldered with traditional metal ribbons on the back at ISC Konstanz. To counter the bowing effect introduced by the soldering process, a curved surface (curvature was calculated to eliminate bowing effect by soldering such that the soldered Zebra cell stays flat) was used during the soldering process. Module reference-PERC used a commercial PERC solar cell with ribbons on both sides to represent traditional PV modules.

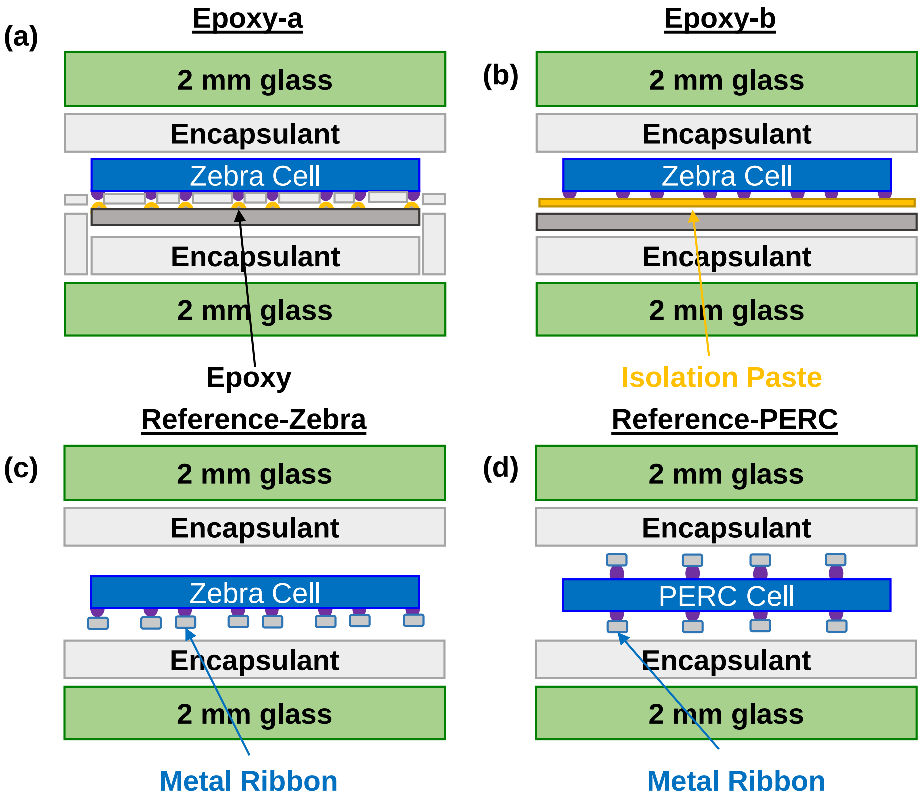

Figure 7.16: Lamination stack of (a) module Epoxy-a, (b) module Epoxy-b, (c) module reference-Zebra, and (d) module reference-PERC.

The deflections of the bottom-right corners of the four modules are shown in Figure 7.17. In this case, the bottom half of the right two sets of busbars will be displayed. In module Epoxy-a, the embossed busbars indeed push the Zebra cell toward the glass (blue areas in Figure 7.17(a)). The right set of busbars has smaller deflection values than the left set of busbars, indicating higher contact pressures by lamination. Since a flat Al electrode is used in module Epoxy-b (Figure 7.17(b)), no significant features associated with the busbars are identified compared to module Epoxy-a. The deflection of the module reference -Zebra has the most homogeneous deflection among all samples. The module reference-PERC, as discussed in Chapter 5.3, has most of the high deflection values at the end of busbars, which was caused by the lamination pressure pressing on the end of the back ribbons.

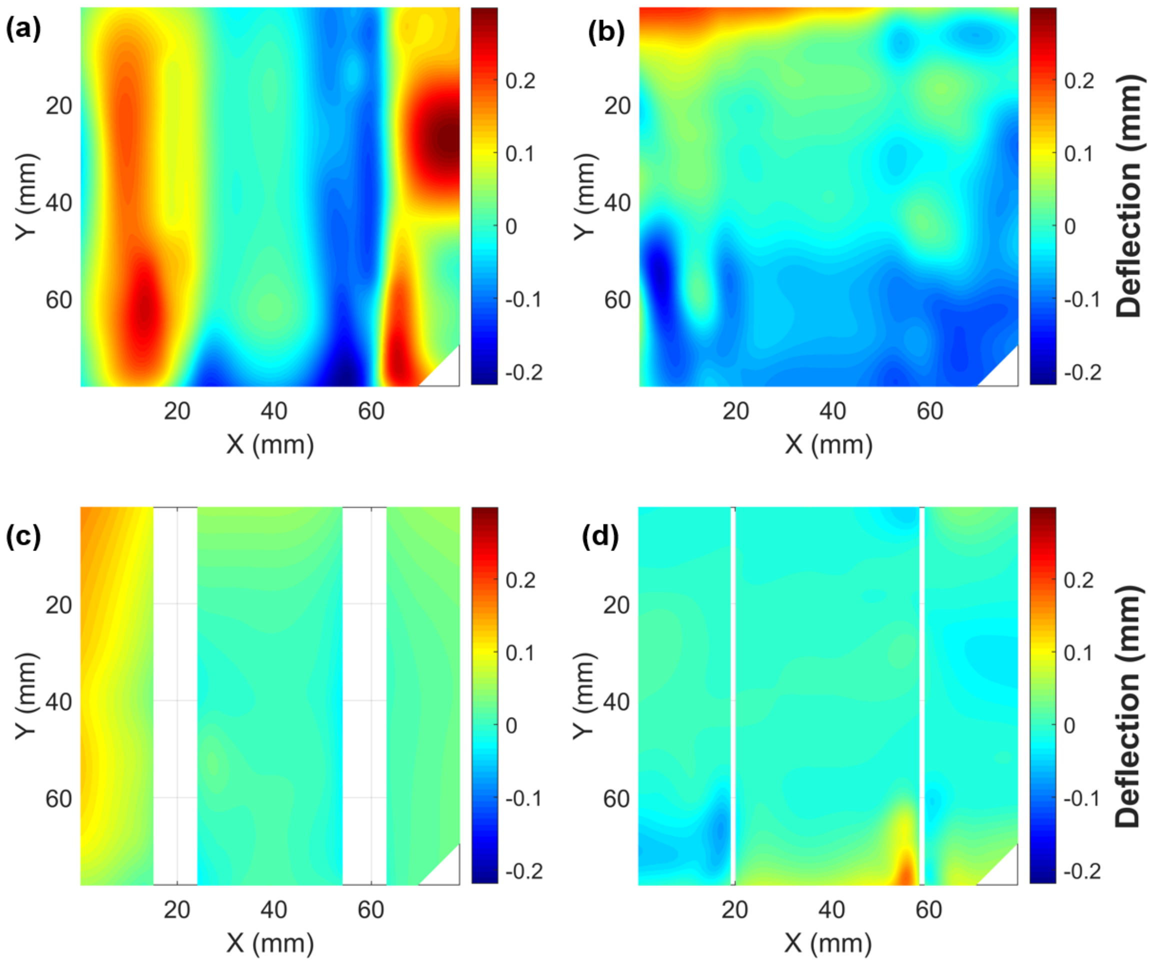

Figure 7.17: Deflection map of the bottom-right corner of (a) module Epoxy-a, (b) module Epoxy-b, (c) module reference-Zebra, and (d) module reference-PERC. Note that the solar cell areas between each pair of busbars in (c) are not displayed.

The $\sigma_{\mathrm{b},1}$ values of the bottom-right corners of the four modules are calculated using the thin-plate theory discussed in Chapter 5 and shown in Figure 7.18. As mentioned earlier, $\sigma_{\mathrm{b},1}$ demonstrates the highest stress values on each pixel which is positively correlated to the probability of failure. Module Epoxy-a has most of the high-stress values around the embossed busbar areas. Note that the $\sigma_{\mathrm{b},1}$ on the right busbar is

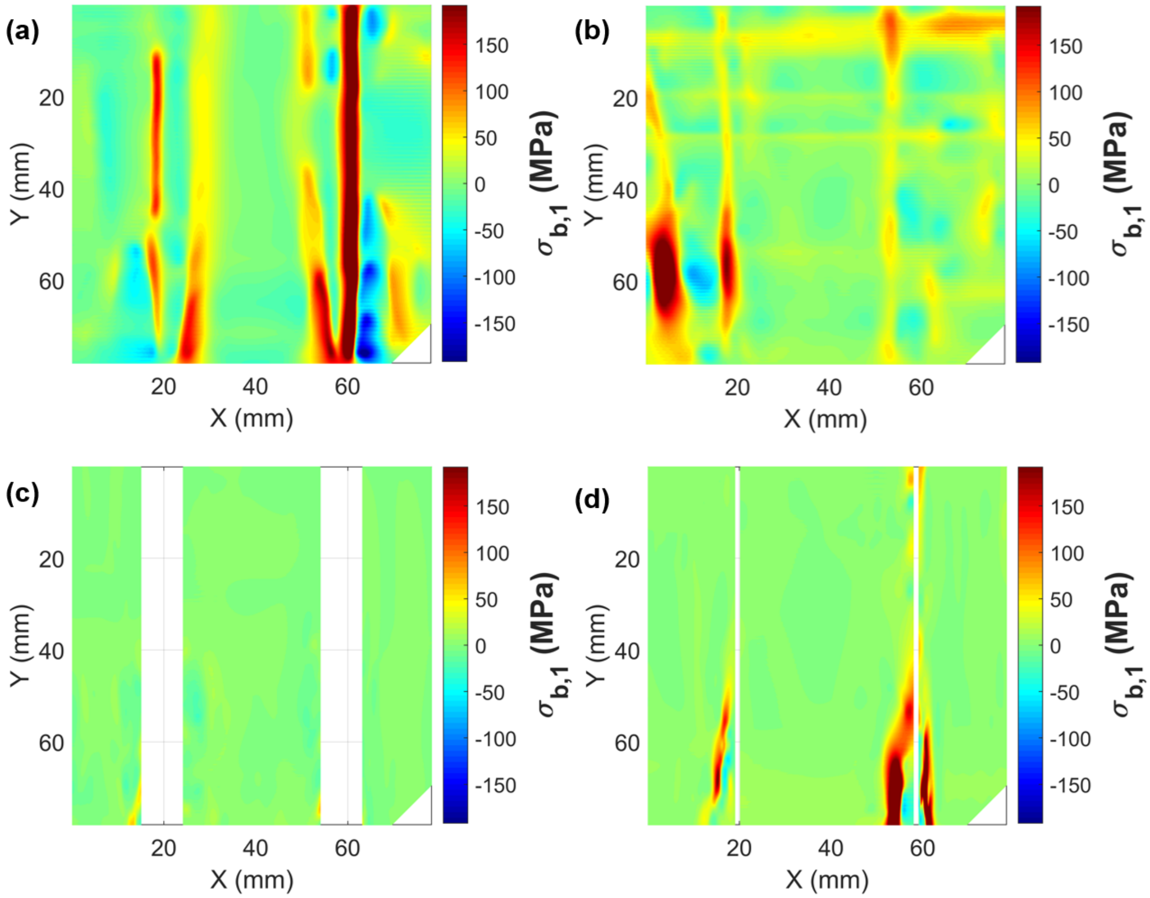

Figure 7.18: $\sigma_{\mathrm{b},1}$ maps of the bottom-right corner of (a) module Epoxy-a, (b) module Epoxy-b, (c) module reference-Zebra, and (d) module reference-PERC. Note that the solar cell areas between each pair of busbars in (c) are not displayed.

higher than the $\sigma_{\mathrm{b},1}$ on the left busbar, which is clearly a result of edge pressing. The module Epoxy-b, which used a flat Al foil, also shows high-stress values at random areas. We attribute them to the inhomogeneities in the isolation paste on the solar cell. That means the process of applying isolation paste needs to be improved. Since the metal ribbons in module reference-Zebra are soldered on the back-side of the cell, the $\sigma_{\mathrm{b},1}$ on it is expected to be the largest among all. Surprisingly, thanks to the special soldering process with a curved surface, module reference-Zebra shows the lowest stress values among all four modules in Figure 7.17(b). Using wider (2 mm) and thinner metal ribbons also contributes to this low-stress status. Red areas are observed at the left side of busbars, which is the same ribbon-press feature observed in module reference-PERC (discussed in Chapter 5). This is mostly introduced by the lamination instead of soldering.

The histogram of pixel counts on solar cells as a function of $\sigma_{\mathrm{b},1}$ values ($\geq$80 MPa) is shown in Figure 7.19. Higher pixel counts in higher $\sigma_{\mathrm{b},1}$ values indicate a higher probability of failure. In this case, the PERC cell with ribbons shows the largest amounts of bending stress values, followed by Zebra cell with embossed Al, Zebra cell with flat Al, and lastly Zebra cell with ribbons. The soldering process on the curved surface indeed significantly reduces the amounts of bending stresses on solar cells. Our proposed XRT method has successfully demonstrated the capability of analyzing the stress status of newly developed PV module concepts.

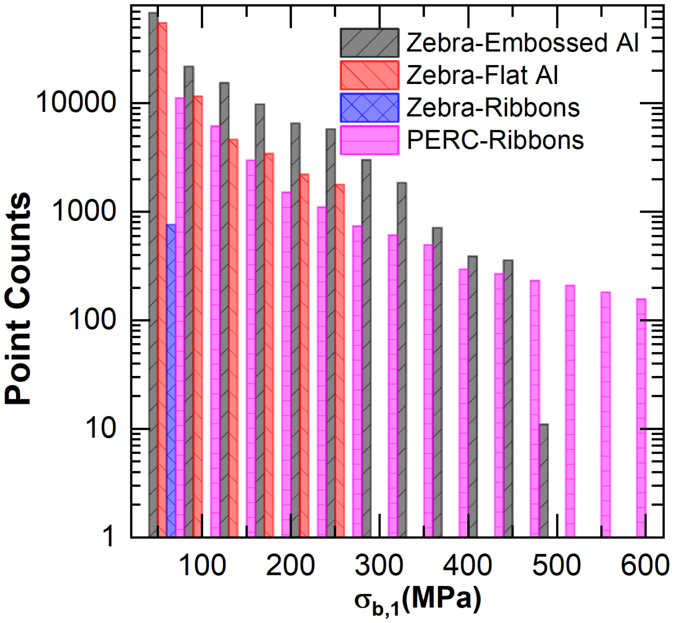

Figure 7.19: Histogram of the $\sigma_{\mathrm{b},1}$ values shown in Figure 7.18.

Chapter 8

PVMIRROR: CURVED PV MODULES WITH STORAGE CAPABILITY

Due to the intermittency of electricity generation, solar energy, as the most promising renewable energy source, is facing obstacles in replacing fossil energy. The efficiency is the major cost-driving factor for a PV system for decades, but the existence of the duck curve is promoting the indispensable demand for dispatchable electricity [76]. Utility-scale energy storage integrated with PV has been employed to increase PV's penetration into the grid. However, currently, most storage options like Lithium-ion batteries are still far from affordable. In this chapter, we introduce a novel PV/concentrating solar power (CSP) tandem system named PVMirror that combines the high efficiency of PV and storage capability of CSP using a dichroic film.

8.1 Introduction of PVMirror Concept

PVMirror enables a way of hybridizing PV and CSP technologies that can deliver 50% more power for only 30% more cost [77]. PV uses both diffused and direct incident light and converts solar energy into electricity; CSP only uses the direct normal irradiance (DNI) and converts solar energy into thermal energy. A PVMirror system is a CSP and PV hybrid tandem system. As shown in Figure 8.1, the system consists of a thermal receiver, a reflective mirror (PVMirror module) and a solar tracker, just like a normal CSP system. Instead of using Ag as the reflective mirror, PVMirror uses a band-pass dichroic film that reflects and transmits light of certain wavelengths. Note that the PV cells are working with no concentration and the film is located between the glass and solar cells instead of in front of the glass.

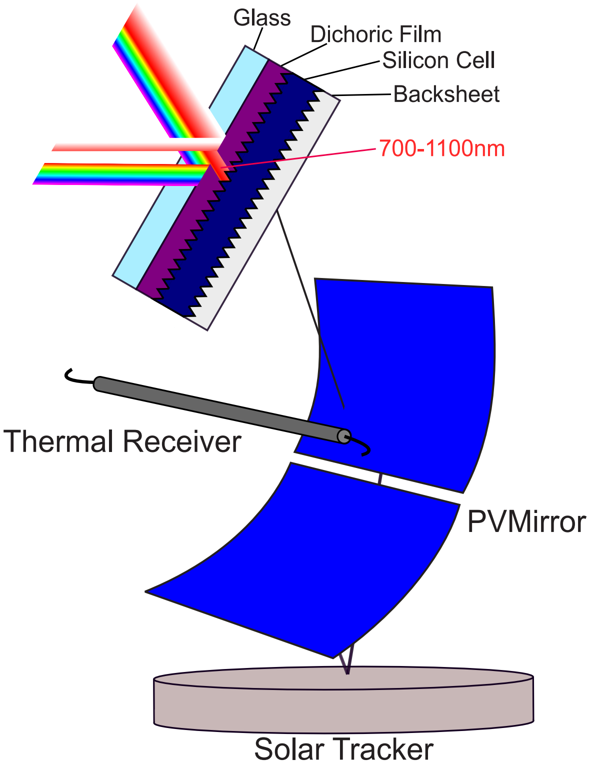

Figure 8.1: Schematic of the PVMirror system on a solar tracker including the thermal receiver and a PVMirror.

PVMirrors are designed on the basis of the spectral efficiency of silicon PV and CSP with respect to the AM1.5G spectrum, as shown in Figure 8.2. Spectral efficiency describes the solar energy conversion efficiency resolved by wavelength [78]. Silicon PV has higher spectral efficiency than CSP at wavelengths close to the bandgap of the cells. If both PV and CSP can work together at the wavelengths where they 'excel', a combined solar power system with storage capability that offers higher efficiency than CSP can be achieved. By tuning the cutoff wavelengths of the dichroic film, the PV/CSP split (the fraction of energy directed to either part of the system) can be tuned. Higher PV/CSP split brings higher system efficiency but decreased dispatchable electricity.

The dichroic film is the key component to realize the tandem function in PVMirror. This film, fabricated by 3M, is mostly made of PET and acrylic. It is a band-pass

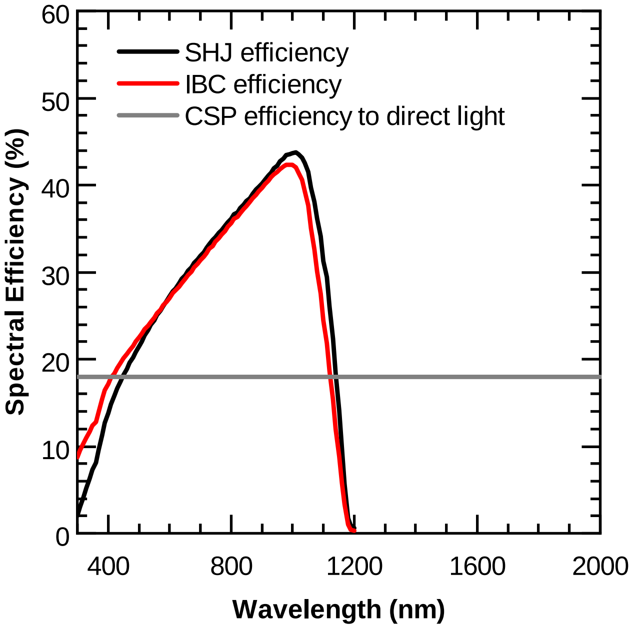

Figure 8.2: Spectral efficiency of IBC and SHJ solar cells with respect to global insolation and the wavelength-agnostic CSP efficiency with respect to DNI.

filter designed to transmit light between 700 to 1100 nm and reflects the remaining wavelengths (see Figure 8.3). As a comparison, the Ag (used in CSP trough) is a broadband reflector with an average reflectance of 94%. The film is positioned in front of the solar cells such that the reflected light will be collected by the thermal receiver as dispatchable thermal energy and stored in a steam tank, and the non-reflected light will be transmitted to the solar cells for DC output, where the solar cells have a better spectral efficiency than CSP [78]. The PVMirror system is expected to provide storage through a CSP system and hours of dispatchable electricity for peak hour usage [79]. By tuning the PV/CSP split (the fraction of AC power output that comes from the PV cells), a PVMirror system can vary its dispatchable electricity. The higher the PV/CSP split, the less dispatchable electricity is available. The reason why the dichroic film has a 700 nm and 1100 nm cut-off wavelength is to achieve a system efficiency (approximate 55% PV/CSP split) close to a pure PV system while retaining the same total dispatchable electricity capacity of pure CSP.

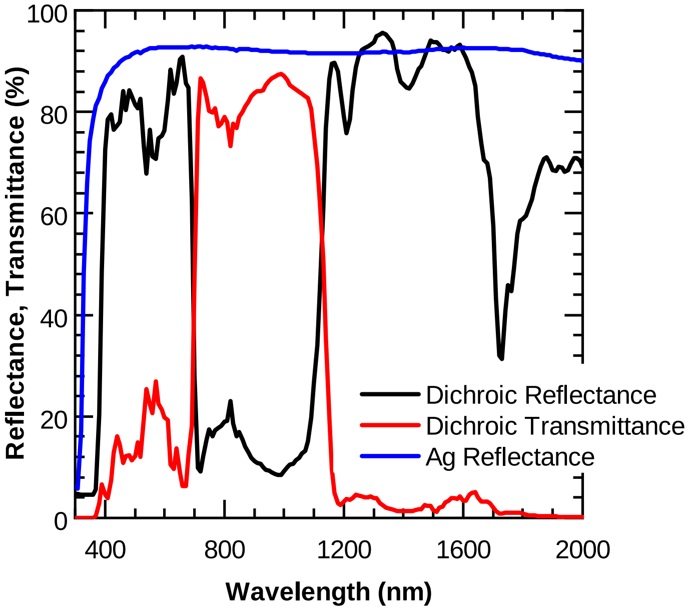

Figure 8.3: Transmittance and reflectance of the dichroic film and reflectance of Ag.

The PVMirror is designed with a north-south axis tracking system and the dichroic film is sensitive to the angle of incidence, particularly at grazing angles. At a low angle of incidence (winter), the system efficiency may be impacted. The reflectance and transmittance of a coupon (Glass/EVA/Film) is measured as a function of wavelength and angle of incidence, as shown in Figure 8.4 . The film absorbs most of the UV light ($\leqslant$380 nm) to protect the encapsulant. It has an absorptance (1-transmittance-reflectance) loss of approximately 0–3% through most of the remaining spectrum. The cutoff wavelengths of the film present a blue shift as the angle of incidence increases. From 0° to 60°, the shifts can be as large as ~120 nm (700 nm at 0°) and ~210 nm (1130 nm at 60°) and the cutoff wavelength gap shrinks from 430 nm to 340 nm. A higher angle of incidence will cause a lower PV/CSP split and thus more CSP output.

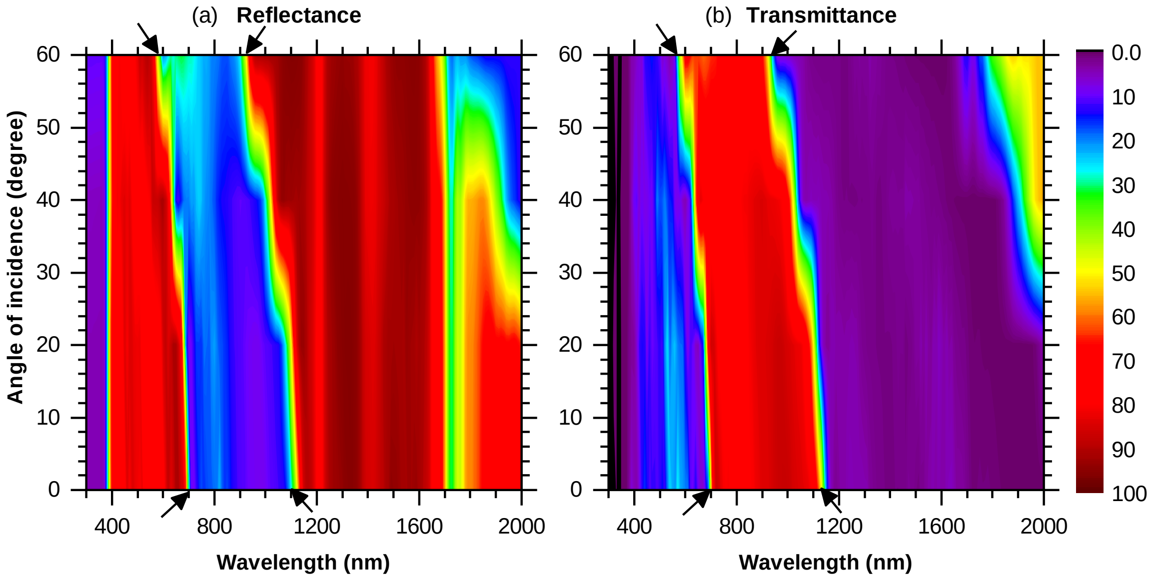

Figure 8.4: (a) Reflectance and (b) transmittance of dichroic film coupon (glass/EVA/film) as a function of light wavelength and angle of incidence.

8.2 Module Fabrication

Material Characterization

Although PET has been reported to be chemically stable below 150°C, its glass transition temperature (79°C) or crystallization temperature (149.86°C) can cause changes in its optical properties by lamination at 130–150°C [80; 81]. To characterize the thermal shrinkage of the film, ten identical pieces of film (400 mm × 400 mm) were laminated using the same lamination profile (16 min and 10^5 Pa) but at 10 different temperatures ranging from 60°C to 150°C at a 10°C interval. Using the same profile at 130°C, a piece of film (400 mm × 400 mm) was laminated sequentially for 3 lamination cycles. The area of the film was measured before and after each lamination. The shrinkage of the film was determined by taking the area ratio ($1 - \mathrm{A}_{\mathrm{after}} \div \mathrm{A}_{\mathrm{before}}$). Figure 8.5 shows the shrinkage of the dichroic film as a function of lamination temperature and the number of lamination cycles. When the lamination temperature is kept below 80°C, no shrinkage occurs. At 80°C, the film starts shrinking isotropically at a rate of 0.06%/°C such that at 150°C the film is 4% smaller in area. Repeating the lamination cycle at 130°C, the resulting sample showed little additional shrinkage, as shown on the right side of Figure 8.5, indicating that shrinkage is more a function of temperature than of the number of lamination cycles. Film shrinkage can cause movement and stress in adjacent EVA layers and solar cells, which is potentially responsible for system failure modes such as cell cracking and delamination [62; 82]. An optimized lamination recipe that minimizes film shrinkage would therefore deliver enough energy to cure the encapsulant ($\geq$ 80% gel content for EVA) at a relatively low temperature.

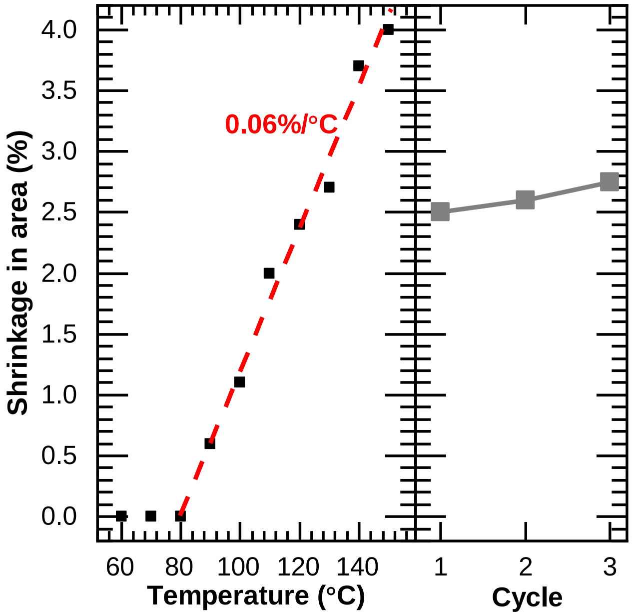

Figure 8.5: Dichroic film's shrinkage (% in area) as a function of lamination temperature and lamination cycle (at 130°C temperature).

Apart from physically shrinking the film, high lamination temperatures may induce compositional changes in the material, which would show up as new or reduced vibrational modes (peaks) in a Raman spectrum and/or changes in optical absorptance. A Renishaw Confocal InVia Raman Spectrometer was used to characterize any new/missing vibration mode in the film caused by lamination. Reflectance and transmittance of the film were measured by a PerkinElmer Lambda 950 S spectrophotometer. Raman and optical measurements performed on a piece of film before and after lamination at 145°C and 10^5 Pa for ∼16 min are shown in Figure 8.6. As expected, all signature peaks in the Raman spectrum match up with the known peaks of PET [83–85]. No change is observable in the Raman spectra after lamination. In the optical spectrum, a 3.5% absolute absorptance increase in the IR region between 1600–2000 nm is observed which is consistent with the film's crystallization behavior at elevated temperatures [80]. It should be noted that since the IR region contains only 2.6% of the total solar energy flux, the increased IR absorption has a negligible impact on electrical cell performance and on the thermal performance of the PVMirror.

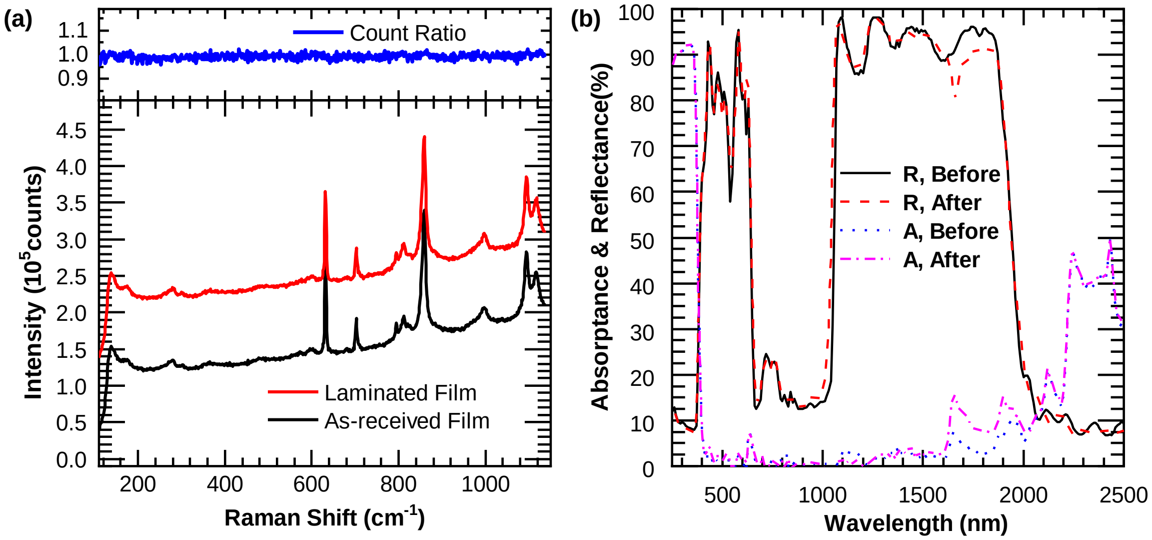

Figure 8.6: (a) Raman spectrum of the dichroic film before and after lamination offseted by 10^5 counts for clarity; (b) absorptance and reflectance of the dichroic film before and after lamination.

After confirming that lamination does not significantly degrade the film, a proper encapsulant has to be selected for best compatibility and integration. The adhesion strength between the encapsulant and the film is considered to be the major selection criterion [16; 62]. To determine the best encapsulant to use with the film, the adhesion strength between the film and different encapsulants was measured through a 180° peel test on a customized 180° peel setup with a 0.5 kN Instron load cell. In a standard peel test, the free end of the film is mounted to the actuator and then peeled off from the encapsulant at a speed of 5 mm/min following the ASTM (D3330 / D3330M - 04(2010)) standard [86]. Encapsulants tested in this study were: Ethyl Vinyl Acetate, EVA9100 from 3M (EVA), Polyolefin Elastomer, PO8100N from 3M (POE) and ionomer, PV5400 from DuPont (ION). Eighteen 180° peel test samples (peel width: 2.5 mm) were prepared following the stack: glass/encapsulant/film. Each encapsulant (EVA, POE and ION) was tested at two different lamination temperatures (130°C and 150°C for EVA and ION, 130°C and 160°C for POE), while using the same time (5 min vacuum time and 11 min press time) and pressure profile (10^5 Pa). Figure 8.7 shows the force required to separate the dichroic film from either EVA, POE, or ION processed at different lamination temperatures. ION does not adhere well to the film at either lamination temperature. This poor adhesion can be attributed to its thermoplastic bonding characteristics; thermoplastic interfaces rely on ionic, hydrogen, and/or Van der Waals forces for adhesion [13]. EVA and POE, which are cross-linking based encapsulants, have much higher peel strengths, around 10 N/mm. These values are consistent with previously reported values of 10–11 N/mm for encapsulant/glass interfaces [86].

Curved Lamination

To make curved laminates, an aluminum mold with the same radius of curvature as the curved glass was fabricated to support it during lamination and to conduct heat from the heating plate. Because of the curved nature of the mold, the center of a 450 mm × 450 mm mold (used with 450 mm × 450 mm curved glasses) is thicker than the edges (15.9 mm vs. 2 mm). This thickness variation across the mold could

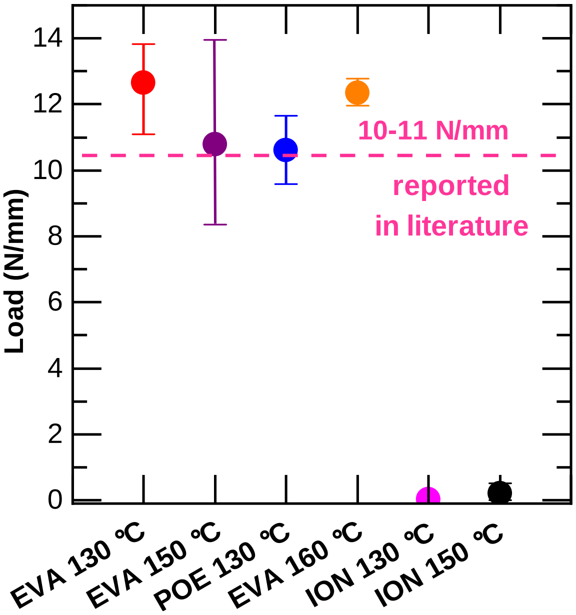

Figure 8.7: Maximum, mean and minimum of three 180° peel tests between the dichroic film and different encapsulants at two lamination temperatures.

cause an inhomogeneous temperature profile across the laminate resulting in different degrees of cross-linking across the encapsulant [27].

To quantify the temperature distribution across the laminate, one thermocouple was placed inside a flat laminate (no mold required) and two thermocouples, at the center and edge, were placed inside a curved laminate (Al mold required). The laminates were then processed together in the same lamination cycle (130°C lamination temperature, 5 min vacuum time and 11 min press time) and the measurement from each thermocouple is shown in Figure 8.8.

From Figure 8.8 one can observe that the temperature gradient across the mold, $\mathrm{T_{curved\text{-}center}} - \mathrm{T_{curved\text{-}edge}}$, is $\sim$ 4°C. Note that the temperature lag between the curved module and the flat one, especially during the vacuum step (0–5 min), is consistent with the heat transfer across the aluminum mold. As pressure is deployed on the laminates during the curing step, the temperature gap between the flat and curved laminate decreases and both $\mathrm{T_{curved\text{-}center}}$ and $\mathrm{T_{curved\text{-}edge}}$ are able to reach the target

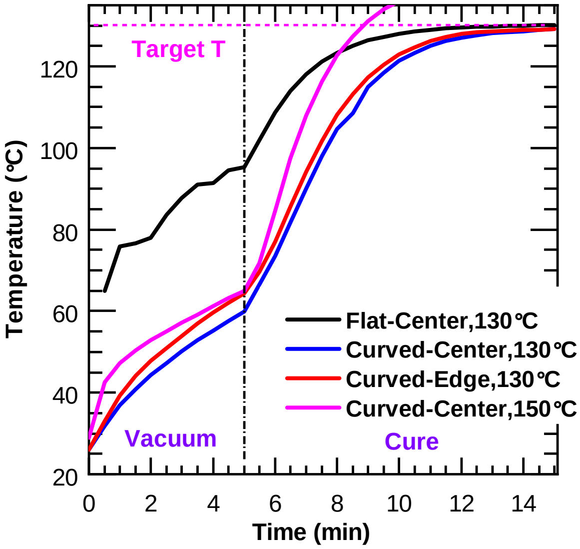

Figure 8.8: Temperature profile of the center of a flat laminate, the center and the edge of a curved laminate on top of a mold during the lamination cycle at two different temperatures. The dashed-dotted vertical line indicates the time of pressure initiation.

temperature. Possible solutions to compensate for the temperature lag induced by the mold are: (i) to preheat the mold on the flat-bed laminator before lamination starts (ii) to increase the heating rate and/or the lamination time/temperature – the latter would require fine-tuning to avoid overheating the polymers. Based on the peel test data shown in Figure 8.7, we selected EVA as the encapsulant in all PVMirror constructions, with a lamination temperature of 130°C (default temperature) for flat configurations and 150°C for curved modules (+20°C to compensate for the temperature lag during lamination, as shown in Figure 8.8).

Experimental Details

Five flat PVMirror modules for visual inspection, eight curved PVMirror modules for shape error measurement, and one utility-scale (144 cells) curved PVMirror module were fabricated with the stack shown in Fig. 8.9(b) and the lamination approaches shown in Table 8.1. Both 125 mm × 125 mm interdigitated back contacted (IBC) and

156 mm × 156 mm silicon heterojunction (SHJ) solar cells were used in the flat and curved PVMirror modules. The IBC cells were purchased from SunPower and SHJ cells were fabricated with the structure described in Ref. [87–93]. Flat PVMirror modules were laminated at 130°C and curved PVMirror modules were laminated at 150°C. Each lamination process has the vacuum time of 5 min and the press time of 11 min. More details regarding the difference of each approach will be discussed in Section 8.3. Flat modules were made with pieces of 400 mm × 400 mm, as-received, low iron B270 glass. To make curved PVMirror modules, pieces of 450 mm × 450 mm (for 4-SHJ and 9-IBC modules) and 1600 mm × 1600 mm (for 144-IBC modules) low iron B270 glass were slumped to parabolic shape with 1.7 m radius of curvature. All the lamination processes in this study were performed using a NPC LM-110X161-S module laminator except module U2, which was laminated using a commercial scale laminator at D2 solar. Note that no bubble formation was observed in any of the finished modules.

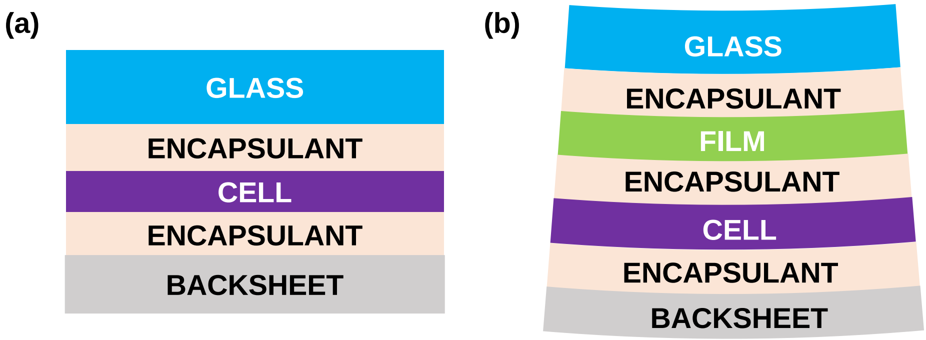

Figure 8.9: (a) Lamination stack of traditional modules and (b) a reference PVMirror PV module.

8.3 Optical Characterization and Lamination Optimization

As reported in Ref. [94], the curvature of the PVMirror is given by the CSP mirror requirements. The reflection from a PVMirror is required to be specular in order to reflect light to a thermal receiver at the focal point. During a standard lamination

Table 8.1: List of 5 flat and 9 curved PVMirror modules fabricated using different lamination approaches. Note that the flat modules have both IBC and SHJ cells in the same sample.

	Approaches	**Flat**	**Curved,9-IBC**	**Curved,4-SHJ**	**Curved,144-IBC**
1	Reference	F0	I0	S0	
2	Preheated film	F1			
3	Two lamination cycles	F2	I2	S2	U2
4	Thicker EVA on film	F3	I3	S3	
5	No EVA on glass	F4	I4	S4	

process, the entire module experiences an isostatic pressure from the laminator. At the same time, the EVA softens at temperatures above 80°C, causing the dichroic film to deform conformally over the tabbing ribbons and edges of the cells, as illustrated in Figure 8.10. Severe film deformation can change the specularity of the PVMirror surface, resulting in optical losses at the line focus. Figure 8.10 shows a flat PVMirror (F0) that was fabricated using the reference PVMirror approach (see Table 8.1). Film deformation can be identified as the distortion of the image reflected from a flat PVMirror module. For example, the red box on the photograph in Figure 8.10 indicates film deformation caused by the cell edges while the yellow box indicates film deformation caused by the metal ribbon.

The reference PVMirror approach was modified in four ways to eliminate film deformation and minimize optical losses. Figure 8.11(a) shows the first approach where the film is preheated at the lamination temperature and pressure before being incorporated into the module. Our preliminary experiments suggested that film shrinkage should be greatly reduced in a second lamination cycle at the same temperature (see Figure 8.5), however, the finished F1 module (in Figure 8.11(a)) shows a considerable amount of film wrinkling compared to the F0 reference module in Figure 8.10. In the F0 module, shrinkage during lamination causes the film to be under tension. In the

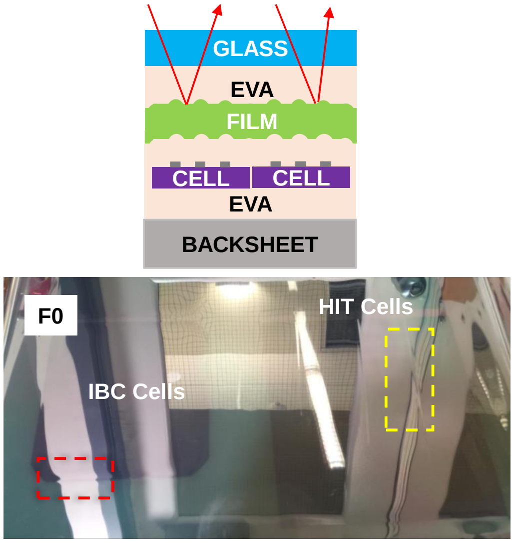

Figure 8.10: A schematic of the reference PVMirror lamination approach (top) highlighting film deformation induced by metal ribbons and cell edges (red arrows indicate light reflected by the film) and the photo of a flat PVMirror F0 (bottom).

F1 module laminate, the film was under tension during preheating and so is effectively ”free-floating” between two layers of EVA during lamination. This shows that film shrinkage is actually beneficial but not sufficient to eliminate film deformation.

The second approach employs two lamination cycles. The first cycle laminates the front of the stack (glass/EVA/film/EVA), and the second cycle laminates the entire stack. Note that the front portion of the stack is laminated twice, as shown in Figure 8.11(b). The dichroic film is fixed to the glass between adjacent cured EVA layers in the first cycle, such that film deformation is minimal in the second cycle. The effectiveness of the approach relies on the lamination quality of the EVA in the first cycle, and the assumption that cross-linked EVA does not significantly softens when heated during a second cycle. The F2 PVMirror module made with Approach 2 in Figure 8.11(b) shows little edge deformation (red box) but some ribbon deformation (yellow box).

To reduce film deformation using only one lamination cycle, the thickness of the EVA between the film and cells is increased in Approach 3, as shown in Figure 8.11(c).

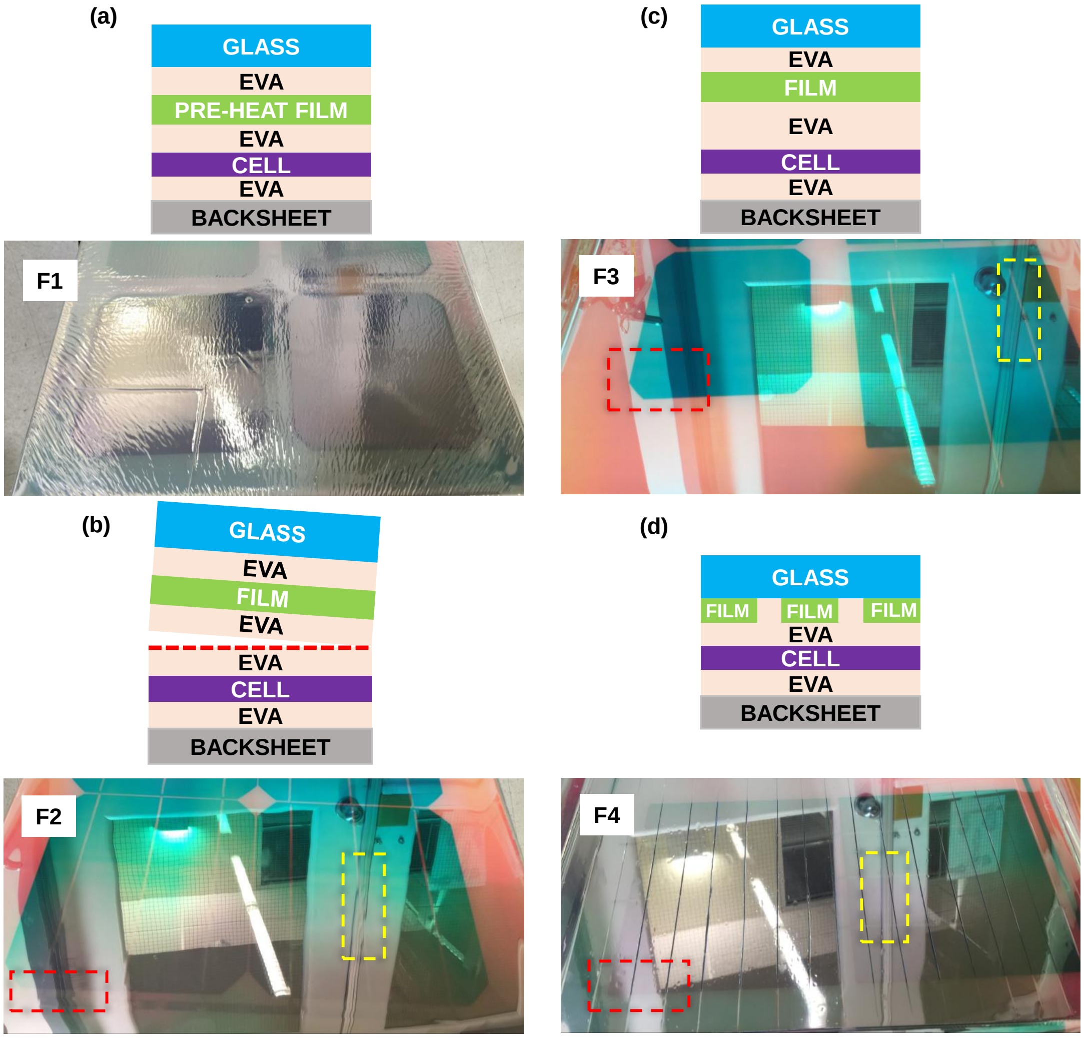

Figure 8.11: Diagram of the lamination stack (top) and photo of the corresponding flat PVMirror module (bottom) of different lamination approaches: (a) preheated film, (b) two lamination cycles, (c) thicker EVA layer between cells and film, (d) no EVA layer between glass and film.

Placing multiple layers of 400 µm thick EVA between the film and the cells showed that three or more layers can fully remove the deformation – the module in Figure 8.11(c) includes three EVA layers between the cells and the film.

Finally, Approach 4 consisted on eliminating the need for an EVA layer between the glass and the dichroic film by using a modified version of the film with holes or strips cut out of it, as shown in Figure 8.11(d). The cut-outs in the film, which take

10% of the film area, allows the EVA between the film and cells to adhere to the glass in a regularly spaced pattern across the module. Thanks to the high viscosity of the softened EVA, the EVA does not overflow between the film and glass. By removing the EVA layer on the glass side of the film, the film can accommodate no further deformation upon lamination. As a result, no film deformation is observed in Figure 8.11(d). This approach does not require a second lamination cycle and only uses a total of 2 layers of EVA.

Visual inspection in Figure 8.11 demonstrates that Approach 2, 3 and 4 reduce film deformation, but does not allow us to quantify the effectiveness of each approach. Here we use the Hartmann test [95] to quantify the optical performance of each approach against the reference PVMirror stack. Figure 8.12(a) demonstrates the methodology of the Hartmann test. A laser source is placed a known distance away from the sample, and a measurement screen is positioned (close-to-axis) where the light reflected off of the sample comes to a line focus. A measurement screen is set up to map the shape error (angular deviation from nominal) of the sample from transverse ray error at the image plane. Light from the screen is captured using a CCD camera close to the axis. The resulting images show the extent of transverse ray aberration at the image plane, which is mapped to shape error through grid lines on the measurement screen. If a perfectly smooth parabolic surface is measured, an extremely narrow line focus is observed in the image. Conversely, the line focus at the image plane can be spread out due to imperfections in the shape of the reflecting surface (e.g. bumps from lamination).

Figure 8.12(b) shows a typical image reflected on the measurement screen by a PVMirror module. The image is intentionally saturated to show details. To quantify the distribution of reflected light across the measurement screen, the image is translated into an intensity graph by summing the pixel intensities in each column in the

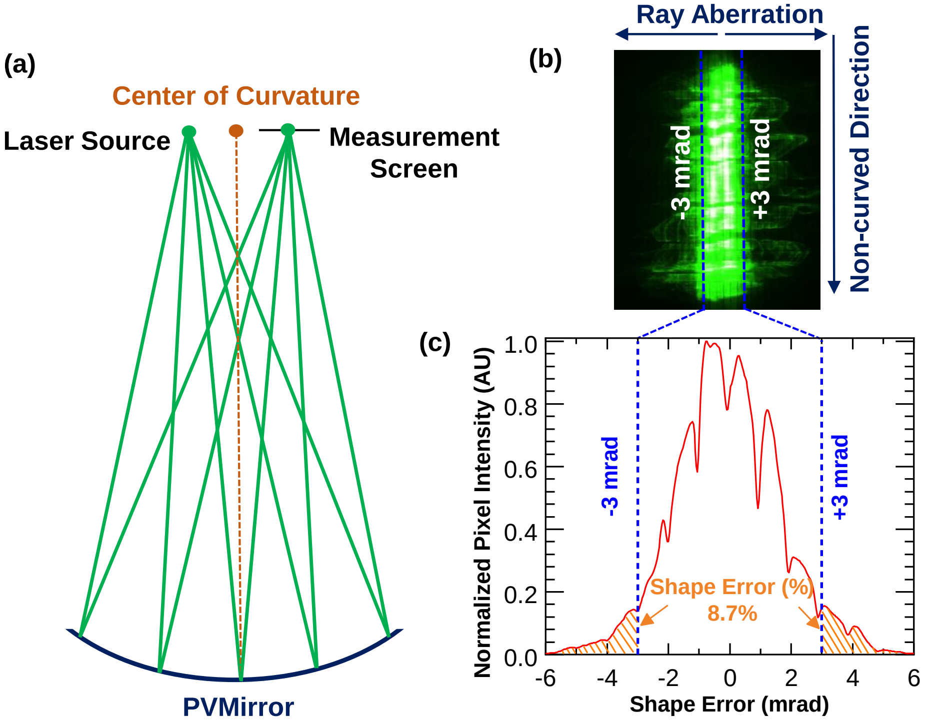

Figure 8.12: (a) Schematic of Hartmann test measuring the shape error of a PVMirror module; (b) image collected on the measurement screen from a PVMirror module; (c) normalized pixel intensity as a function of shape error, highlighting a shape error percentage of 8.7% in dash orange areas.

image and plotting the resulting sum as a function of the angle on the screen – see Figure 8.12(c). The blue dotted lines at ±3 mrad in Figure 8.12(b) and 8.12(c) corresponds to the shape error specification required for commercial CSP troughs, which is determined by the position and size of the thermal receiver [96]. The average shape error in actual systems is about 3.4 mrad [97]. We use this metric to determine how much of the incident light is lost by expressing the amount of light falling outside of the ±3 mrad spec as a percentage of the total, which in the case of Figure 8.12 is 8.7%.

In this study, eight curved PVMirror modules were prepared using two types of silicon cells (see Table8.1) and four different lamination approaches: the reference and Approach 2–4 (see Table 8.1). The curved glass used in each module and the finished laminates were measured using the Hartmann test described above. Note that the shape of the initial pieces of curved glass varies considerably. The effectiveness of each lamination approach is therefore quantified by calculating the increase of shape error percentage from glass to module, as shown in Figure 8.13. For the reference samples, the shape error percentage increases 8.3% (from 0.4% to 8.7%) for modules with IBC cells and 5.2% (from 0.4% to 5.6%) for modules with SHJ cells. All PVMirror modules made with Approach 2, 3 and 4 demonstrate a much smaller difference between the shape error of the glass and the module, indicating improvement in the lamination quality. Among them, S2 demonstrates the lowest shape error percentage increase of just 0.4%.

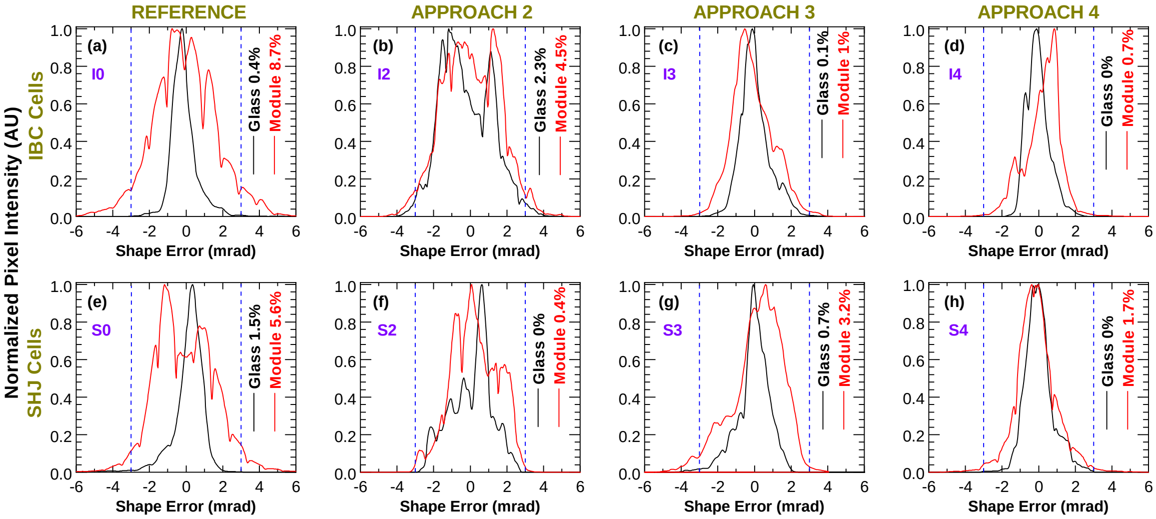

Figure 8.13: Shape error percentage (using ±3 mrad specification as indicated with blue dashed lines) of eight curved pieces of glass (Glass) measured before laminating them into modules and eight PVMirror modules (Module) with IBC and SHJ solar cells.

The increases in shape error of the curved PVMirror modules calculated as a function of shape error specification are shown in Figure 8.14. These values for SHJ cells are 0.59% higher on average than for IBC cells due to deformation from the front metal ribbons. The reference lamination approach has the highest shape error values in each cell category (module S0 and I0).

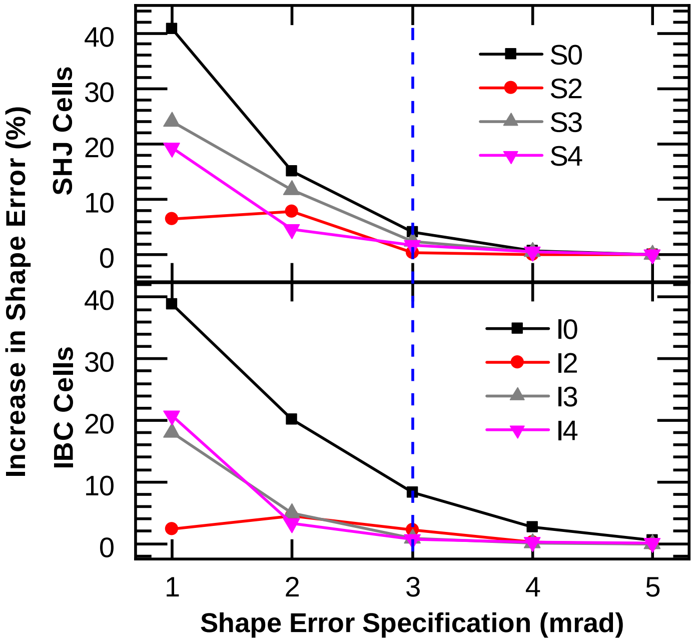

Figure 8.14: Shape error increase as a function of shape error specification for 8 curved PVMirror modules, ranging from ±1 mrad to ±5 mrad.

The proposed encapsulation approaches have been proven to effectively reduce the film deformation and thus increase the thermal output of PVMirror modules. However, one additional layer of EVA between the film and the cell in Approach 2 and 3 (one layer of EVA is considered essential) could cause potential parasitic absorption. To quantify this, the reflectance and transmittance of four mini-modules (stack: glass/EVA/dichroic film/EVA) were measured. Figure 8.15(a) and (b) show the absorptance spectra a and Figure 8.15(c) shows the effect that EVA thickness between the film and the cell has on the transmission of AM1.5G spectrum. The ratio of AM1.5G × (1-a) and the AM1.5G integrated over the wavelength 700–1100 nm indicates that each layer of EVA caused about 1% transmission reduction. However, it is not necessarily true that the best module has the lowest absorptance. For example, the PVMirror module with one layer of EVA between the film and the cell (I0 in Table 1) has an absorption of 3.5% and a shape error increase of 8.3% (Figure 8.13(a)). On the other hand, the PVMirror module with three layers of EVA between the film

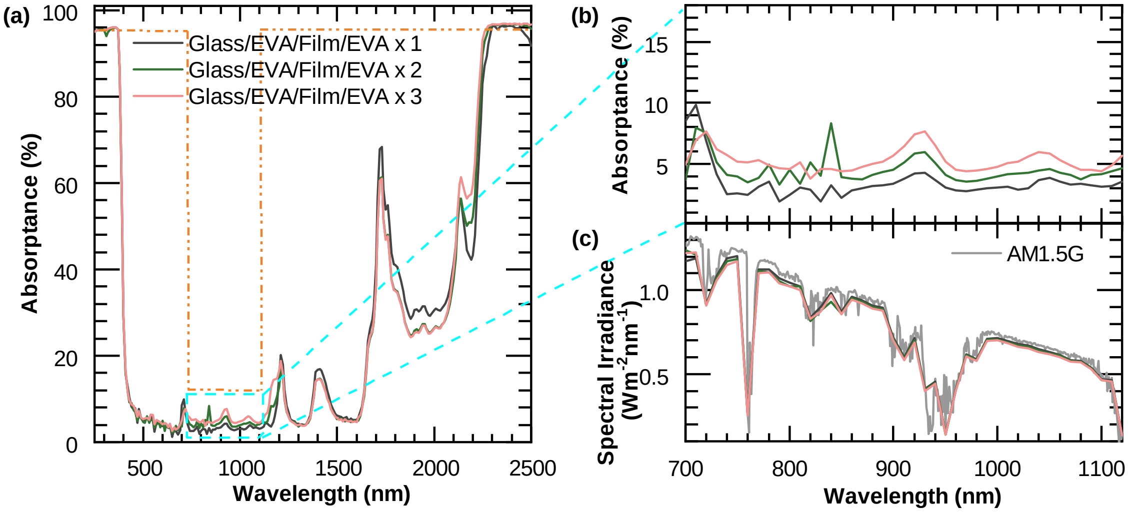

Figure 8.15: (a) Absorptance in three mini-modules with the stack: glass/EVA/Film/EVA×X, X=1, 2, 3 (yellow double dashed line approximately represents the reflectance of the dichroic film); (b) absorptance of the four aforementioned mini-modules in the range of 700–1100 nm; (c) intensity of AM1.5G spectrum and corresponding spectrum calculated by AM1.5G × (1-a), where a is the absorptance in (b).

and cell (I3 in Table 1) has an absorption of 5.3% and a shape error increase of only 0.9% (Figure 8.13(c)). Compared with the S0 module, the S2 module has 1.8% less transmittance to the cells but 7.4% more light reflects to the thermal receiver. Considering the effect from different EVA layers and shape errors, approach 2 seems to be the best approach with the lowest optical losses.

8.4 Electrical Performance and Upscaling Capability

After optimizing the lamination process by the Hartmann test, the optimum PVMirror module (I2 replica) was fabricated using Approach 2 and measured outdoor. Its performance is directly compared to an AgMirror (silver coated curved glass). The PVMirror and AgMirror are shown in Figure 8.16. 99.9% of the reflected light from the AgMirror is within the ±3 mrad specification, indicating the AgMirror is fabricated to standard. Though the image reflected from the PVMirror appears rough on the screen, 99.7% of the reflected light is within the ±3 mrad specification.

Thus, we assume that 100% of the reflected light from both AgMirror and PVMirror is within the ±3 mrad specification in the following discussion.

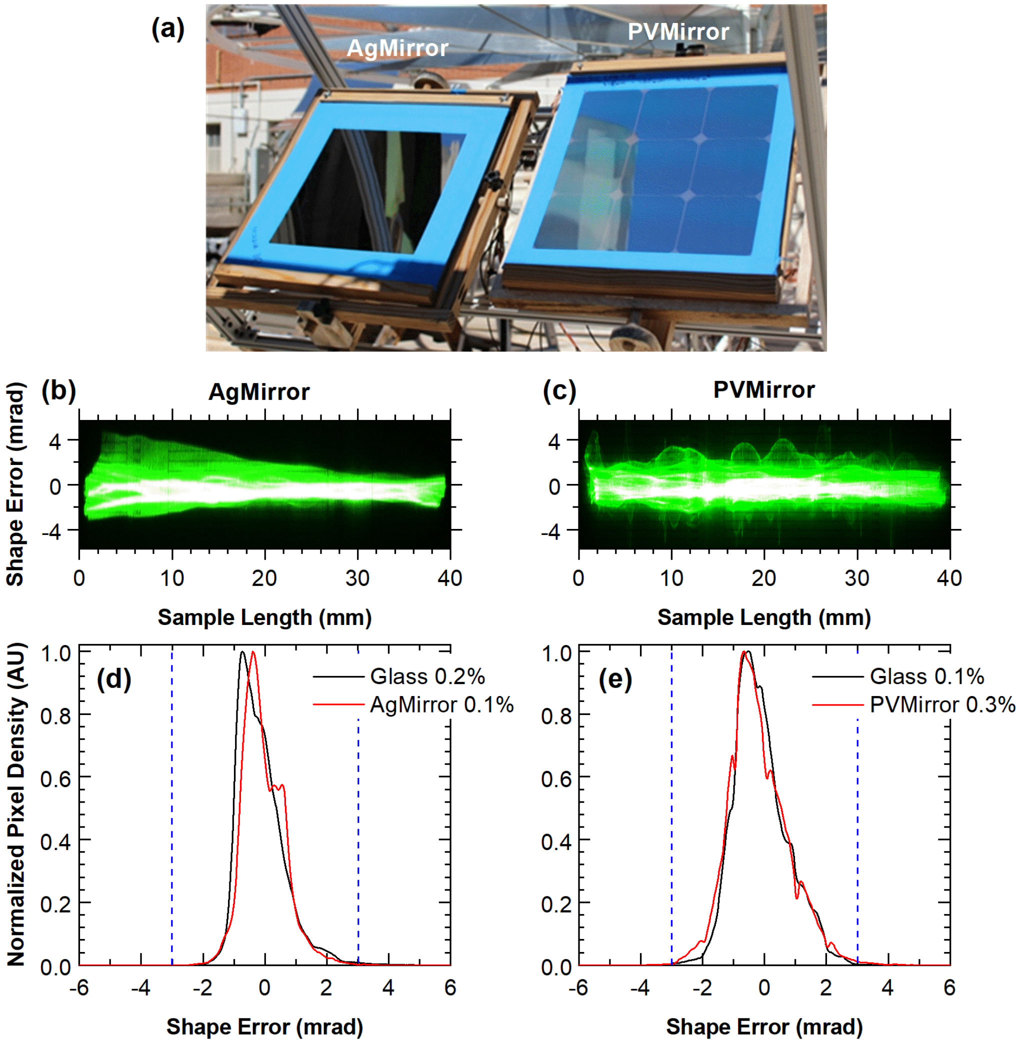

Figure 8.16: (a) Photo of a AgMirror and a PVMirror (I2 replica) on solar tracker; the reflected light on the Hartmann test screen from (b) the AgMirror and (c) the PVMirror; normalized pixel density as a function of transverse ray aberration of (d) the AgMirror and (e) PVMirror.

Outdoor measurement of the mirrors was carried out at the University of Arizona on 2-axis trackers with calorimeters mounted at the focus. The calorimeters were first calibrated against each other using two AgMirrors of known reflectance, shape error and area. The diffuse and DNI components of the incident irradiance were determined by the Observed Atmospheric and Solar Information System (OASIS), where the data was recorded 260 m west of the testing facility [98]. One of the AgMirrors was then replaced with the PVMirror and the two mirrors were measured at the same time in order to calculate the thermal efficiency of the PVMirror. The PVMirror thermal efficiency, with respect to the DNI, was calculated from the thermal measurement of the calorimeter and the OASIS measurement of the irradiance. The DC output of the PVMirror was measured at the same time by a Keithley source-measure unit (SMU) using a four-terminal measurement.

The outdoor measurement results of I2 replica and AgMirror are shown in Figure 8.17 as a function of measurement time. Based on their reflectivity, the thermal efficiencies of the AgMirror and I2 replica are 94% and 54.4% respectively, assuming all reflected light hits the thermal receiver. The PVMirror thermal output ranges from 412 to 517 $\mathrm{W/m^2}$ and the average efficiency with respect to DNI is determined to be 50.3%, which is 4.1% lower than what was modeled potentially due to improper module mounting. The highest DC output of 134 $\mathrm{W/m^2}$ was measured at 10:26 and the lowest output of 127.7 $\mathrm{W/m^2}$ at 13:30. The modeled PVMirror DC efficiency of 12.9% is calculated by the external quantum efficiency (EQE), average on-sun FF and temperature-corrected Voc, which is very close to the measured value of 12.6% to 13.4%. The DC efficiency decrease over time is caused by the voltage drop at elevated temperature. Overall, the measured performance of PVMirror has a good agreement with the modeled values with relative error within 7.5% (thermal) and 3.8% (DC), indicating that the measurement methodology can also be used to measure the performance of utility-scale PVMirrors.

To experimentally demonstrate the scalability of the PVMirror concept to utility-scale, larger 1.6 m x 1.6 m PVMirrors U2 were fabricated and measured outdoor on a solar tracker as shown in Figure 8.18(a). The 144 IBC cells are tabbed into two

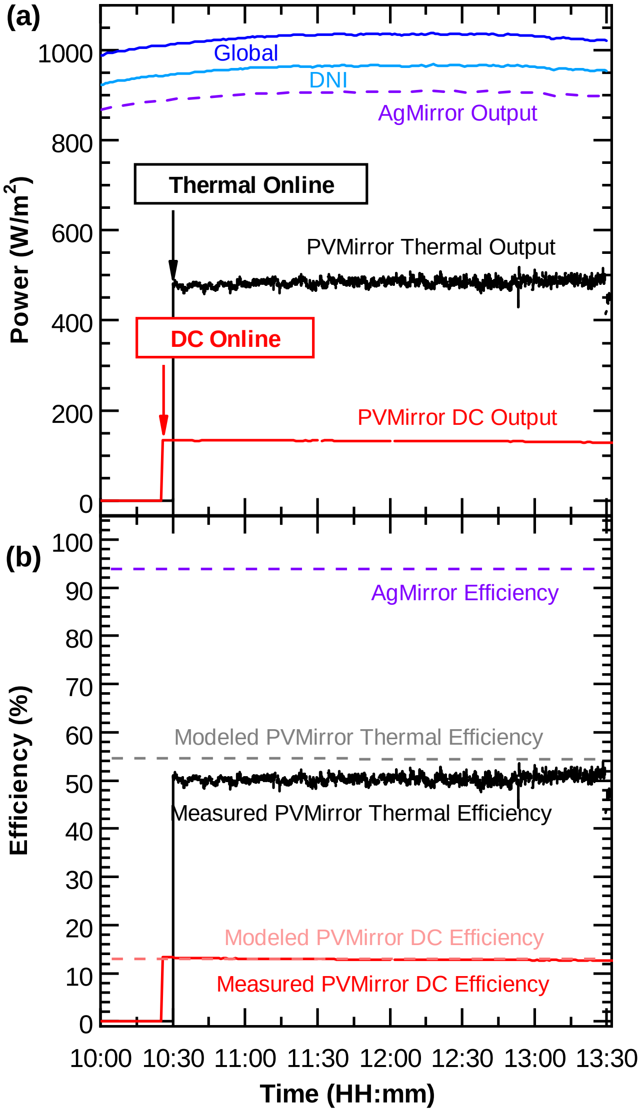

Figure 8.17: Modeled and outdoor measured (a) output and (b) efficiency of the PVMirror and AgMirror modules in Figure 8.16. The DC went online at 10:25 and the thermal went online at 10:30. Dashed lines are modeled.

separate strings. Indoor IV measurement shows that String-1 has a FF of 70.2% with 139 W maximum power (Pmp) and String-2 has a FF of 76.3% with 152 W Pmp. The low FF in the second string was caused by improper soldering and isolated solar cells, which is later confirmed by the EL images in Figure 8.18(b).

The outdoor performance of this PVMirror is carried out between 14:00 to 16:00 on a sunny day with an average air temperature of 39.3°C. The PV component is

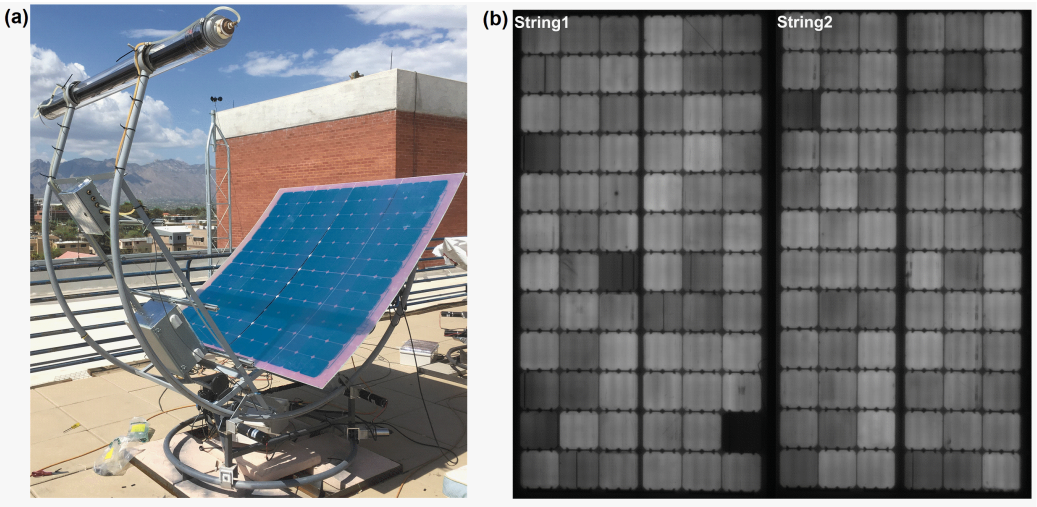

Figure 8.18: (a) Photo of the 144-IBC U2 PVMirror module mounted on a two-axis tracker; (b) EL image of the U2 PVMirror module.

measured with the two strings connected in series and a typical IV curve is shown in Figure 8.19. Due to the elevated air temperature and above-mentioned fabrication issues, the PV component delivers a FF of 73.3% with 253.8 W Pmp. The "kink" at 67V on the IV curve is caused by the current mismatch between two strings and the activation of reverse diodes. The average thermal efficiency of this PVMirror is 57.5%, which is relatively 5.6% higher than the modeled value.

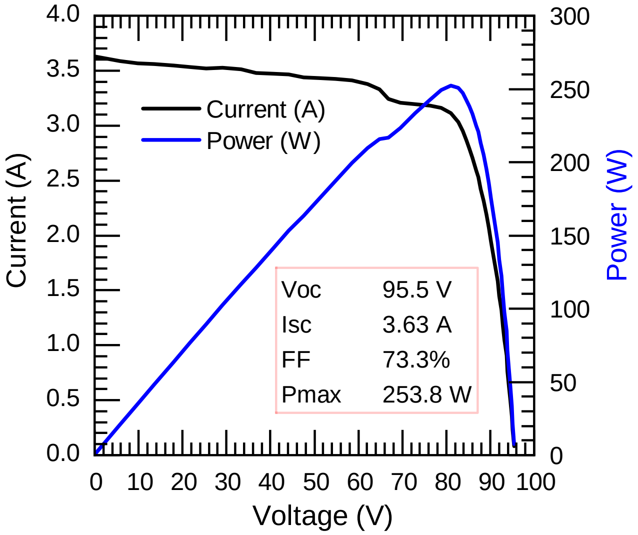

Figure 8.19: Electrical performance of the 144-cell U2 PVMirror module.

To determine the performance of the PVMirror concept at utility-scale, a detailed power plant farm model using 50 MW turbine is developed. The model determines the annual AC output from a PVMirror power plant with the option of tuning the thermal storage fraction as shown schematically in Figure 8.20(a). The model has four inputs: a radiation model, the dichroic film's measured optical properties, the PV cell's measured one-sun performance and a CSP thermal loss model. The PVMirror plant is designed with a north-south axis tracking system, which is similar to commercial CSP systems and simplifies the 3D radiation model into 2D. The radiance model takes hourly irradiance data from TMY326 data sets in Phoenix. The TMY3 are data sets of hourly values of solar radiation in the geographical location for a one-year period. The solar irradiance reaching the cell is calculated by the following steps: (1) divide the whole PVMirror (2.876m length) into flat segments of the size similar to IBC solar cell (0.127m length) while taking into account the rig angle effect (typical trough configuration) [99]; (2) determine the angle of incidence (AOI) between the sun and each flat segment of mirror surface using the method described here [100]; (3) generate AOI-corrected spectrum data from the "simple model of the atmospheric radiative transfer of sunshine" (SMARTS) [101]; (4) multiply the spectrum by the angular-dependent transmittance and reflectance of the dichroic film (Figure 8.4). The PV output is calculated by the solar irradiance transmitted through the film, EQE of the cell, average on-sun FF and temperature-corrected Voc. The cell model includes a 95% DC/AC conversion efficiency. The CSP output is calculated by the solar irradiance reflected by the film, and the measured thermal efficiency. The CPS model includes 14% tracking loss, 7% optical loss, 5% reflection loss, 8% radiation loss, 12% convection loss and 9% storage loss [77].

This model can be used to compare a PVMirror system with a PV only and a CSP only system, as shown in Figure 8.20(b). The PV only and CSP only system's

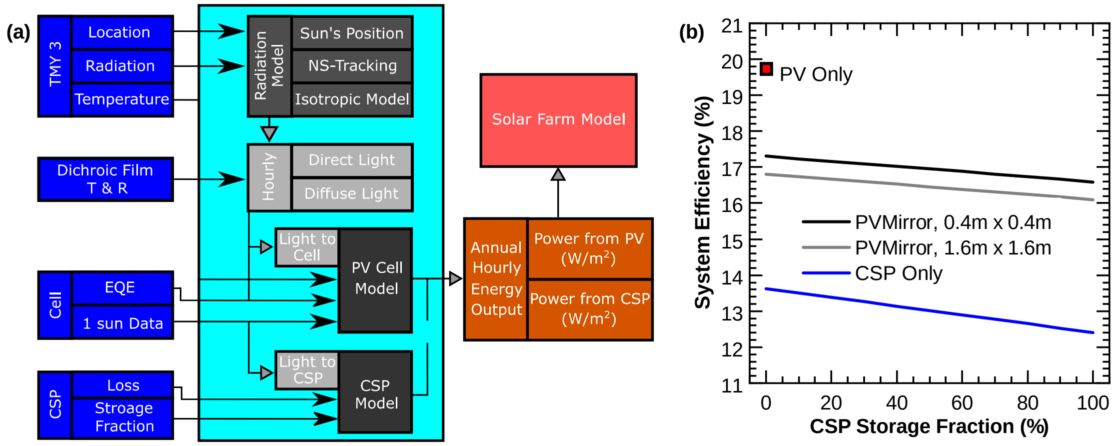

Figure 8.20: (a) Model of a PVMirror power plant system; (b) system efficiency of a PVMirror tandem system using I2-replica data, a PVMirror tandem system using U2 data, a CSP only system, and a PV only system as a function of the CSP storage fraction based on (a).

efficiencies are calculated by removing the dichroic film and using a broadband reflector (Ag), respectively. A PV only system will have an efficiency of 19.8% but zero dispatchable output as shown by the red square. The modeled annual AC output of the CSP only system is 1066.9 kW/m at 0% storage fraction and 970.9 kWh/m at 100% storage fraction. Storing all collected heat energy results in a 1.2% absolute system efficiency loss in the CSP only system as shown in the blue curve.

Scaling up the PVMirror from 9 cells to 144 cells caused a 0.5% absolute system efficiency decrease, as shown by the black and gray curves. We believe that proper R&D could effectively shrink that value close to zero. Using the on-sun performance measured on the I3 module (ie: assuming the issues we encountered at scale-up could be solved), the modeled annual AC output of the PVMirror plant is 728.7 kW/m from the PV side and 624.0 kWh/m at 0% storage fraction and 567.8 kWh/m at 100% storage fraction from the CSP side. Changing the storage fraction from 0% to 100% causes a 0.7% absolute system efficiency loss and the PV/CSP split to change from 55.3% to 57.6%. For a PVMirror system, the dispatchable energy is the combination of CSP storage fraction, PV/CSP slit and total DC energy output. A CSP only system with roughly 33% storage fraction (typical CSP power plant like Solana operates 12 hours a day and stores 6 hours of storage) will operate at 13.2% efficiency and have a 341.6 kWh/m annual dispatchable output based on the model. To match the same dispatchable annual output of the CSP only system, the PVMirror can work at 57% storage fraction with a much higher efficiency of 16.9%.

Chapter 9

CONCLUSIONS

The main goal of this dissertation is to develop a non-destructive method for mapping the deflection and stress in laminated solar cells based on X-ray topography. The cell deflection mapping is achieved by taking XRT images on the solar cells at different cell positions, followed by a reconstruction algorithm created in house. Error analysis has shown a maximum deviation of 3.3% from data processing and a 4.4% error induced by mounting. Currently, the main limiting factor of this method is the slow data acquisition rate. Though multiple approaches have been investigated in this dissertation, measuring a 6" silicon solar cell still takes approximately 8 hours. At this stage of development, this method is more suitable for R&D purposes than for a characterization tool in a production line. To further faciliate the data acquisition, the current XRT setup could be modified in the following ways: (1) larger first slit opening for bigger X-ray beam (expose X-rays to the whole sample); (2) larger sample holder that can natively hold and rotate 6" solar cell (reduce four measurements down to one); (3) larger X-ray detector enabled by a $\geq$ 6" scintillator. The above modifications could lead to a $\geq$ 80% reduction in measurement time. Meanwhile, a machine-learning assisted automatic thresholding could contribute to faster data processing.

Stress mapping is enabled by using Von Karman plate theory on the deflection maps. The theory is a combination of non-linear equations that calculate the bending stresses while assuming the solar cells are under pure bending and plane stress conditions. The effective mechanical properties instead of the isotropic properties are used because the sample's crystal orientation is known during the XRT measurement. In order to quantify the errors from those assumptions, in-situ four-point bending tests on Si wafers with layer(s) of sputtered Al are conducted. In those particular samples, deviations $\leq$18.3% between Von Karman stress and FEA simulated stress were observed, which are highly dependent on the position of the neutral plane. However, those four-point bending tests do not reflect the behavior of a real silicon solar cell, because: (1) thermal-induced uniform stresses on the samples are transferred into bending stresses during sample preparation (bowing effect) and the Von Karman bending stresses cannot be measured when the samples are flat; (2) the solar cells have more complex architectures than the samples used in the four-point bending test; (3) the sputtered Al is porous instead of solid (an effective media approach should be used to calculate the properties). For those reasons, further tests are needed to focus on the thermal-induced stress effect and extracting the effective mechanical properties. For example, a force measurement component such as a piezoelectric transducer can be added to the in-situ four-point bending setup, which can measure the bending force during each XRT measurement. Combining the bending stress with bending force at different bending distances, the effective Young's modulus and Possion's ratio of the sample can be obtained. In addition, temperature-dependent XRT experiments could be carried out on PV modules (for example, 0°C, 25°C, 60°C) to anlayze the effect of the viscoelasticity of each encapsulant on the silicon solar cell's stress behavior.

The deflection and bending stress mapping method was used to investigate PV modules of different architectures. This method is able to quantify the impact of lamination parameters, soldering, and packaging solutions on the mechanical properties of solar cells. For example, we found that glass/glass packaging introduces 190-320% more bending stress on the cells than traditional glass/backsheet packaging. This method is also able to characterize next-generation PV modules such as

Flex-circuit modules and PVMirror modules. However, the measured Von Karman stresses can only probe the relative stress values in the solar cell. When the cell's top and bottom surfaces have the same stress value, the Von Karman stress will be zero. This phenomenon is likely to take place during the soldering process where equal amounts of stress are introduced on both sides of the solar cell. This is considered to be the intrinsic limitation of this Von Karman stress calculation. In addition, the shear stresses are also important in cases including the soldering process. Equally, the shear stresses in the system dominates delamination. Reconstruction of the full stress tensor by FEA using a viscoelastical model is at the center of the needed work to move this technology forward.

REFERENCES

[1] K. Branker, M. J. Pathak, and J. M. Pearce, "A review of solar photovoltaic levelized cost of electricity," *Renewable and Sustainable Energy Reviews*, vol. 15, no. 9, pp. 4470–4482, 2011.

[2] C. Breyer, D. Bogdanov, A. Gulagi, A. Aghahosseini, L. S. Barbosa, O. Koskinen, M. Barasa, U. Caldera, S. Afanasyeva, M. Child, J. Farfan, and P. Vainikka, "On the role of solar photovoltaics in global energy transition scenarios," *Progress in Photovoltaics: Research and Applications*, vol. 25, pp. 727–745, aug 2017.

[3] W. J. Cole, B. A. Frew, P. J. Gagnon, J. Richards, Y. Sun, R. M. Margolis, and M. A. Woodhouse, "SunShot 2030 for Photovoltaics (PV): Envisioning a Low-cost PV Future," Tech. Rep. September, National Renewable Energy Laboratory (NREL), Golden, CO (United States), sep 2017.

[4] R. Jones-Albertus, D. Feldman, R. Fu, K. Horowitz, and M. Woodhouse, "Technology advances needed for photovoltaics to achieve widespread grid price parity," *Progress in Photovoltaics: Research and Applications*, vol. 24, pp. 1272–1283, sep 2016.

[5] ITRPV, "International Technology Roadmap for Photovoltaic (ITRPV)," *Itrpv*, no. 10th Edition, pp. 1–38, 2019.

[6] M. A. Green, Y. Hishikawa, E. D. Dunlop, D. H. Levi, J. Hohl-Ebinger, M. Yoshita, and A. W. Ho-Baillie, "Solar cell efficiency tables (Version 53)," *Progress in Photovoltaics: Research and Applications*, vol. 27, no. 1, pp. 3–12, 2019.

[7] M. Sander, B. Henke, H. Schwarz, S. Dietrich, S. Schweizer, M. Ebert, and J. Bagdahn, "Characterization of PV modules by combining results of mechanical and electrical analysis methods," vol. 777308, p. 777308, aug 2010.

[8] M. Woodhouse, R. Jones-Albertus, D. Feldman, R. Fu, K. Horowitz, D. Chung, D. Jordan, and S. Kurtz, "On the Path to SunShot: The Role of Advancements in Solar Photovoltaic Efficiency, Reliability, and Costs," *National Renewable Energy Laboratory (NREL)*, no. May, p. 44, 2016.

[9] K. Yoshikawa, H. Kawasaki, W. Yoshida, T. Irie, K. Konishi, K. Nakano, T. Uto, D. Adachi, M. Kanematsu, H. Uzu, and K. Yamamoto, "Silicon heterojunction solar cell with interdigitated back contacts for a photoconversion efficiency over 26%," *Nature Energy*, vol. 2, no. 5, 2017.

[10] F. J. Pern, "Ethylene vinyl acetate (EVA) encapsulants for photovoltaic modules: Degradation and discoloration mechanisms and formulation modifications for improved," *Die Angewandte Makromolekulare Chemie*, vol. 252, pp. 195–216, 1997.

[11] H. Li, *Open the Black Box: Understanding the Encapsulation Process of Photovoltaic Modules.* PhD thesis, 2013.

[12] M. Jaunich, M. Böhning, U. Braun, G. Teteris, and W. Stark, "Investigation of the curing state of ethylene/vinyl acetate copolymer (EVA) for photovoltaic applications by gel content determination, rheology, DSC and FTIR," *Polymer Testing*, vol. 52, pp. 133–140, 2016.

[13] M. Kempe, "Overview of scientific issues involved in selection of polymers for PV applications," in *2011 37th IEEE Photovoltaic Specialists Conference*, pp. 85–90, IEEE, jun 2011.

[14] D. C. Jordan and S. R. Kurtz, "Photovoltaic Degradation Rates—an Analytical Review," *Progress in Photovoltaics: Research and Applications*, vol. 21, pp. 12–29, oct 2013.

[15] M. Köntges and Others, "Review of Failures of Photovoltaic Modules. PVPS Task 13 - ST 3.2: Report," tech. rep., 2014.

[16] C. R. Osterwald and T. J. McMahon, "History of accelerated and qualification testing of terrestrial photovoltaic modules: A literature review," *Progress in Photovoltaics: Research and Applications*, vol. 17, pp. 11–33, oct 2009.

[17] J. Wohlgemuth, D. Cunningham, P. Monus, J. Miller, and A. Nguyen, "Long Term Reliability of Photovoltaic Modules," in *2006 IEEE 4th World Conference on Photovoltaic Energy Conference*, vol. 2, pp. 2050–2053, IEEE, 2006.

[18] E. L. Meyer and E. E. Van Dyk, "Assessing the reliability and degradation of photovoltaic module performance parameters," *IEEE Transactions on Reliability*, vol. 53, no. 1, pp. 83–92, 2004.

[19] A. Skoczek, T. Sample, and E. D. Dunlop, "The results of performance measurements of field-aged crystalline silicon photovoltaic modules," *Progress in Photovoltaics: Research and Applications*, vol. 17, pp. 227–240, jun 2009.

[20] S. Kajari-Schröder, I. Kunze, U. Eitner, and M. Köntges, "Spatial and orientational distribution of cracks in crystalline photovoltaic modules generated by mechanical load tests," *Solar Energy Materials and Solar Cells*, vol. 95, no. 11, pp. 3054–3059, 2011.

[21] M. Köntges, I. Kunze, S. Kajari-Schröder, X. Breitenmoser, and B. Bjørneklett, "The risk of power loss in crystalline silicon based photovoltaic modules due to micro-cracks," *Solar Energy Materials and Solar Cells*, vol. 95, pp. 1131–1137, apr 2011.

[22] W. Ma, C. Ke, M. Zhou, and X. Zhang, "Phase field crystal simulation of morphological evolution and propagation of microcracks in the intermetallic compound layer of Sn/Cu solder interconnects," in *2016 17th International Conference on Electronic Packaging Technology (ICEPT)*, pp. 963–967, IEEE, aug 2016.

[23] M. Sander, S. Dietrich, M. Pander, M. Ebert, and J. Bagdahn, "Systematic investigation of cracks in encapsulated solar cells after mechanical loading," *Solar Energy Materials and Solar Cells*, vol. 111, pp. 82–89, 2013.

[24] S. Pingel, Y. Zemen, O. Frank, T. Geipel, and J. Berghold, "Mechanical stability of solar cells within solar panels," *Proceedings of 24th European PV Solar Energy Conference*, vol. 91, pp. 3459–3464, 2009.

[25] A. M. Gabor, R. Janoch, A. Anselmo, and H. Field, "Solar panel design factors to reduce the impact of cracked cells and the tendency for crack propagation," *NREL PV Module Reliability Workshop, Denver, CO USA* -, pp. 1–11, 2015.

[26] D. M. Powell, M. T. Winkler, H. J. Choi, C. B. Simmons, D. B. Needleman, and T. Buonassisi, "Crystalline silicon photovoltaics: A cost analysis framework for determining technology pathways to reach baseload electricity costs," *Energy and Environmental Science*, vol. 5, no. 3, pp. 5874–5883, 2012.

[27] C. Hirschl, M. Biebl-Rydlo, M. Debiasio, W. Mühleisen, L. Neumaier, W. Scherf, G. Oreski, G. Eder, B. Chernev, W. Schwab, and M. Kraft, "Determining the degree of crosslinking of ethylene vinyl acetate photovoltaic module encapsulants - A comparative study," *Solar Energy Materials and Solar Cells*, vol. 116, pp. 203–218, 2013.

[28] H. Li, L.-E. Perret-Aebi, R. Théron, C. Ballif, Y. Luo, and R. F. M. Lange, "Towards in-line determination of EVA Gel Content during PV modules Lamination Processes," *Proceedings of the 25th PVSC Conference*, vol. 1, no. 20, p. 220, 2010.

[29] S. I. N. Ayutthaya and J. Wootthikanokkhan, "Investigation of the photodegradation behaviors of an ethylene/vinyl acetate copolymer solar cell encapsulant and effects of antioxidants on the photostability of the material," *Journal of Applied Polymer Science*, vol. 107, pp. 3853–3863, mar 2008.

[30] U. Eitner, M. Köntges, and R. Brendel, "Measuring thermomechanical displacements of solar cells in laminates using digital image correlation," *Conference Record of the IEEE Photovoltaic Specialists Conference*, pp. 001280–001284, 2009.

[31] U. Eitner, M. Köntges, and R. Brendel, "Use of digital image correlation technique to determine thermomechanical deformations in photovoltaic laminates: Measurements and accuracy," *Solar Energy Materials and Solar Cells*, vol. 94, no. 8, pp. 1346–1351, 2010.

[32] R. Meier, F. Kraemer, S. Wiese, K. J. Wolter, and J. Bagdahn, "Reliability of copper-ribbons in photovoltaic modules under thermo-mechanical loading," *Conference Record of the IEEE Photovoltaic Specialists Conference*, pp. 1283–1288, 2010.

[33] A. J. Beinert, A. Buchler, P. Romer, M. Heinrich, M. C. Schubert, J. Aktaa, and U. Eitner, "Stress Mapping by Confocal Raman Spectroscopy on Solar Cells and Modules," in *2018 IEEE 7th World Conference on Photovoltaic Energy Conversion (WCPEC) (A Joint Conference of 45th IEEE PVSC, 28th PVSEC & 34th EU PVSEC)*, pp. 3613–3617, IEEE, jun 2018.

[34] A. Büchler, A. Beinert, S. Kluska, V. Haueisen, P. Romer, F. D. Heinz, M. Glatthaar, and M. C. Schubert, "Enabling stress determination on alkaline textured silicon using Raman spectroscopy," *Energy Procedia*, vol. 124, pp. 18–23, sep 2017.

[35] M. Stoehr, G. Gerlach, T. Härtling, and S. Schoenfelder, "Analysis of Photoelastic Properties of Monocrystalline Silicon Analysis of Photoelastic Properties of Monocrystalline Silicon," no. June, 2019.

[36] C. Krüger, D. Heinert, A. Khalaidovski, J. Steinlechner, R. Nawrodt, R. Schnabel, and H. Lück, "Birefringence measurements on crystalline silicon," *Classical and Quantum Gravity*, vol. 33, no. 1, pp. 0–17, 2016.

[37] E. Citirik, T. Demirkan, and T. Karabacak, "Residual stress modeling of density modulated silicon thin films using finite element analysis," *Journal of Vacuum Science & Technology A: Vacuum, Surfaces, and Films*, vol. 33, p. 021503, mar 2015.

[38] S. K. Tippabhotla, I. Radchenko, W. Song, G. Illya, V. Handara, M. Kunz, N. Tamura, A. A. Tay, and A. S. Budiman, "From cells to laminate: probing and modeling residual stress evolution in thin silicon photovoltaic modules using synchrotron X-ray micro-diffraction experiments and finite element simulations," *Progress in Photovoltaics: Research and Applications*, vol. 25, pp. 791–809, sep 2017.

[39] W. M. Vetter and M. Dudley, "X-ray topographic dislocation contrast visible in reflections orthogonal to the Burgers vectors of axial screw dislocations in hexagonal silicon carbide," *Journal of Applied Crystallography*, vol. 34, no. 1, pp. 20–26, 2001.

[40] H. Klapper, N. Zaitseva, and L. Carman, "X-ray topographic study of growth defects of trans-stilbene crystals grown from solutions," *Journal of Crystal Growth*, vol. 429, pp. 74–81, 2015.

[41] Tsumoru Shintake, "Review of the worldwide SASE FEL development," in *2007 IEEE Particle Accelerator Conference (PAC)*, pp. 89–93, IEEE, 2007.

[42] R. Nave, "http://hyperphysics.phy-astr.gsu.edu/hbase/quantum/xrayc.html."

[43] T. Tuomi, K. Naukkarinen, and P. Rabe, "Use of synchrotron radiation in X-ray diffraction topography," *Physica Status Solidi (a)*, vol. 25, pp. 93–106, sep 1974.

[44] M. Moore, “White-beam X-ray topography,” *Crystallography Reviews*, vol. 18, pp. 207–235, jul 2012.

[45] H. N. Thi, H. Jamgotchian, J. Gastaldi, J. H rtwig, T. Schenk, H. Klein, B. Billia, J. Baruchel, and Y. Dabo, “ Preliminary in situ and real-time study of directional solidification of metallic alloys by x-ray imaging techniques ,” *Journal of Physics D: Applied Physics*, vol. 36, no. 10A, pp. A83–A86, 2003.

[46] X. Meng, M. Stuckelberger, L. Ding, B. West, A. Jeffries, and M. Bertoni, “Quantitative mapping of deflection and stress on encapsulated silicon solar cells,” *IEEE Journal of Photovoltaics*, vol. 8, no. 1, pp. 189–195, 2018.

[47] T. Jensen, T. Aljundi, J. N. Gray, and R. Wallingford, “A Model of X-Ray Film Response,” in *Review of Progress in Quantitative Nondestructive Evaluation*, pp. 441–448, Boston, MA: Springer US, 1996.

[48] E. V. Suvorov and I. A. Smirnova, “X-ray diffraction imaging of defects in topography (microscopy) studies,” *Uspekhi Fizicheskih Nauk*, vol. 185, no. 9, pp. 897–915, 2015.

[49] P. Rejmánková-Pernot, P. Cloetens, J. Baruchel, J.-P. Guigay, and P. Moretti, “Phase Retrieval by Combined Bragg and Fresnel X-Ray Diffraction Imaging,” *Physical Review Letters*, vol. 81, pp. 3435–3438, oct 1998.

[50] A. K. Freund, A. Munkholm, and S. Brennan, “X-ray diffraction properties of highly oriented pyrolytic graphite,” in *Optics for High-Brightness Synchrotron Radiation Beamlines II* (L. E. Berman and J. Arthur, eds.), vol. 2856, pp. 68–79, nov 1996.

[51] M. Dudley, X. R. Huang, and W. M. Vetter, “Contribution of x-ray topography and high-resolution diffraction to the study of defects in SiC,” *Journal of Physics D: Applied Physics*, vol. 36, no. 10 A, 2003.

[52] Z. B. Zhao, J. Hershberger, S. M. Yalisove, and J. C. Bilello, “Determination of residual stress in thin films: A comparative study of X-ray topography versus laser curvature method,” *Thin Solid Films*, vol. 415, no. 1-2, pp. 21–31, 2002.

[53] A. Bose, R. K. Vijayaraghavan, A. Cowley, V. Cherman, O. Varela Pedreira, B. K. Tanner, A. N. Danilewsky, I. De Wolf, and P. J. McNally, “Nondestructive Monitoring of Die Warpage in Encapsulated Chip Packages,” *IEEE Transactions on Components, Packaging and Manufacturing Technology*, vol. 6, no. 4, pp. 653–662, 2016.

[54] C. S. Wong, N. S. Bennett, D. Manessis, A. Danilewsky, and P. J. McNally, “Non-destructive laboratory-based X-ray diffraction mapping of warpage in Si die embedded in IC packages,” *Microelectronic Engineering*, vol. 117, pp. 48–56, 2014.

[55] A. Colli, K. Attenkofer, B. Raghothamachar, and M. Dudley, "Synchrotron X-Ray Topography for Encapsulation Stress/Strain and Crack Detection in Crystalline Silicon Modules," *IEEE Journal of Photovoltaics*, vol. 6, no. 5, pp. 1387–1389, 2016.

[56] A. N. Danilewsky, A. Rack, J. Wittge, T. Weitkamp, R. Simon, H. Riesemeier, and T. Baumbach, "White beam synchrotron topography using a high resolution digital X-ray imaging detector," *Nuclear Instruments and Methods in Physics Research, Section B: Beam Interactions with Materials and Atoms*, vol. 266, no. 9, pp. 2035–2040, 2008.

[57] X. Meng, M. Stuckelberger, L. Ding, B. West, A. Jeffries, and M. Bertoni, "Characterization of encapsulated solar cells by X-ray topography," in *2016 IEEE 43th Photovoltaic Specialist Conference, PVSC 2016*, pp. 0111–0114, IEEE, jun 2016.

[58] D. C. Wilson and B. A. Mair, "Thin-Plate Spline Interpolation," *Sampling, Wavelets, and Tomography*, pp. 311–340, 2011.

[59] R. F. M. Lange, Y. Luo, R. Polo, and J. Zahnd, "The lamination of (multi)crystalline and thin film based photovoltaic modules," *Progress in Photovoltaics: Research and Applications*, vol. 19, pp. 127–133, mar 2011.

[60] X. Meng, M. Stuckelberger, P. Hacke, and M. Bertoni, "Process Induced Deflection and Stress on Encapsulated Solar Cells," in *2017 IEEE 44th Photovoltaic Specialist Conference (PVSC)*, pp. 2854 – 2857, IEEE, jun 2017.

[61] W. J. Song, S. K. Tippabhotla, A. A. Tay, and A. S. Budiman, "Numerical Simulation of the Evolution of Stress in Solar Cells During the Entire Manufacturing Cycle of a Conventional Silicon Wafer Based Photovoltaic Laminate," *IEEE Journal of Photovoltaics*, vol. 8, no. 1, pp. 210–217, 2017.

[62] G. ORESKI and G. WALLNER, "Delamination behaviour of multi-layer films for PV encapsulation," *Solar Energy Materials and Solar Cells*, vol. 89, pp. 139–151, nov 2005.

[63] J. Kanatharana, T. Buckley, P. J. Mcnally, T. Tuomi, D. Lowney, W. Chen, L. Knuuttila, and J. Riikonen, "Mapping of mechanical stresses in silicon substrates due to lead – tin solder bump reflow process via synchrotron x-ray L Knuuttila and J Riikonen," vol. 36, 2003.

[64] X. Meng, R. Meier, M. Stuckelberger, A. Jeffries, S. Bernardini, and M. Bertoni, "Bending Stress Analysis of Encapsulated Silicon Solar Cells," in *7th World Conference on Photovoltaic Energy Conversion (WCPEC-7)*, p. In Press, 2018.

[65] X. Yu, P. Wang, X. Li, and D. Yang, "Thin Czochralski silicon solar cells based on diamond wire sawing technology," *Solar Energy Materials and Solar Cells*, vol. 98, pp. 337–342, 2012.

[66] J. Dolbow and M. Gosz, "Effect of out-of-plane properties of a polyimide film on the stress fields in microelectronic structures," *Mechanics of Materials*, vol. 23, no. 4, pp. 311–321, 1996.

[67] M. Hopcroft, "What is the Young ' s Modulus of Silicon?," *Physical Acoustics*, vol. 19, no. 2, pp. 229–238, 2007.

[68] F. Kaule, W. Wang, and S. Schoenfelder, "Modeling and testing the mechanical strength of solar cells," *Solar Energy Materials and Solar Cells*, vol. 120, pp. 441–447, 2014.

[69] C. Yang, F. Mess, K. Skenes, S. Melkote, and S. Danyluk, "On the residual stress and fracture strength of crystalline silicon wafers," *Applied Physics Letters*, vol. 102, no. 2, 2013.

[70] J. McLaughlin and A. Willoughby, "Fracture of silicon wafers," *Journal of Crystal Growth*, vol. 85, pp. 83–90, nov 1987.

[71] D. Hinken, K. Ramspeck, K. Bothe, B. Fischer, and R. Brendel, "Series resistance imaging of solar cells by voltage dependent electroluminescence," *Applied Physics Letters*, vol. 91, p. 182104, oct 2007.

[72] V. A. Popovich, A. C. Riemslag, M. Janssen, I. J. Bennett, and I. M. Richardson, "Characterization of Multicrystalline Silicon Solar Wafers Fracture Strength and Influenc- ing Factors," *International Journal of Material Science*, vol. 3, no. 1, pp. 9–17, 2013.

[73] K. Fisher, X. Meng, B. Hartweg, S. Mony, M. Bertoni, and Z. Holman, "Novel Foil Interconnects for Back-Contact Silicon Solar Cells," *2019 IEEE 446h Photovoltaic Specialist Conference (PVSC)*, vol. In Press, 2019.

[74] J. Geissbuhler, S. De Wolf, A. Faes, N. Badel, Q. Jeangros, A. Tomasi, L. Barraud, A. Descoeudres, M. Despeisse, and C. Ballif, "Silicon heterojunction solar cells with copper-plated grid electrodes: Status and comparison with silver thick-film techniques," *IEEE Journal of Photovoltaics*, vol. 4, no. 4, pp. 1055–1062, 2014.

[75] A. Halm, V. D. Mihailetchi, G. Galbiati, L. J. Koduvelikulathu, R. Roescu, R. Kopecek, K. Peter, and J. Libal, "The Zebra Cell Concept–Large Area n-type Interdigitated Back Contact Solar Cells and One-Cell Modules Fabricated Using Standard Industrial Processing Equipment," in *Proceedings of the 27th EUPVSC*, (Frankfurt), pp. 567–570, 2012.

[76] M. Obi and R. Bass, "Trends and challenges of grid-connected photovoltaic systems - A review," *Renewable and Sustainable Energy Reviews*, vol. 58, pp. 1082–1094, 2016.

[77] Z. J. Yu, K. C. Fisher, B. M. Wheelwright, R. P. Angel, and Z. C. Holman, "PVMirror: A New Concept for Tandem Solar Cells and Hybrid Solar Converters," *IEEE Journal of Photovoltaics*, vol. 5, no. 6, pp. 1791–1799, 2015.

[78] Z. Yu, M. Leilaeioun, and Z. Holman, "Selecting tandem partners for silicon solar cells," *Nature Energy*, vol. 1, no. 11, 2016.

[79] A. Richter, M. Hermle, and S. W. Glunz, "Reassessment of the limiting efficiency for crystalline silicon solar cells," *IEEE Journal of Photovoltaics*, vol. 3, no. 4, pp. 1184–1191, 2013.

[80] H. E. Bilal DEMİREL, Ali YARAŞ, "Crystallization Behavior of PET Materials," vol. 13, no. 1, pp. 26–35, 2011.

[81] L. H. Buxbaum, "The Degradation of Poly(ethylene terephthalate)," *Angewandte Chemie International Edition in English*, vol. 7, pp. 182–190, mar 1968.

[82] X. F. Brun and S. N. Melkote, "Analysis of stresses and breakage of crystalline silicon wafers during handling and transport," *Solar Energy Materials and Solar Cells*, vol. 93, no. 8, pp. 1238–1247, 2009.

[83] S. Yang and S. Michielsen, "Orientation distribution functions obtained via polarized Raman spectroscopy of poly(ethylene terephthalate) fibers," *Macromolecules*, vol. 36, no. 17, pp. 6484–6492, 2003.

[84] B. H. Stuart, "Polymer crystallinity studied using Raman spectroscopy," *Vibrational Spectroscopy*, vol. 10, no. 2, pp. 79–87, 1996.

[85] S. B. Roh, S. K. Oh, E. K. Park, and W. Z. Choi, "Identification of black plastics realized with the aid of Raman spectroscopy and fuzzy radial basis function neural networks classifier," *Journal of Material Cycles and Waste Management*, vol. 19, no. 3, pp. 1093–1105, 2017.

[86] G. J. Jorgensen, K. M. Terwilliger, J. A. DelCueto, S. H. Glick, M. D. Kempe, J. W. Pankow, F. J. Pern, and T. J. McMahon, "Moisture transport, adhesion, and corrosion protection of PV module packaging materials," *Solar Energy Materials and Solar Cells*, vol. 90, no. 16, pp. 2739–2775, 2006.

[87] E. Van Kerschaver and G. Beaucarne, "Back-contact solar cells: A review," *Progress in Photovoltaics: Research and Applications*, vol. 14, no. 2, pp. 107–123, 2006.

[88] S. DeWolf, A. Descoeudres, Z. C. Holman, and C. Ballif, "High-efficiency silicon heterojunction solar cells: A review," *Green*, vol. 2, no. 1, pp. 7–24, 2012.

[89] S. W. Glunz and F. Feldmann, "SiO2 surface passivation layers – a key technology for silicon solar cells," *Solar Energy Materials and Solar Cells*, vol. 185, pp. 260–269, oct 2018.

[90] J. Schmidt, R. Peibst, and R. Brendel, "Surface passivation of crystalline silicon solar cells: Present and future," *Solar Energy Materials and Solar Cells*, vol. 187, pp. 39–54, dec 2018.

[91] F. Schindler, A. Fell, R. Müller, J. Benick, A. Richter, F. Feldmann, P. Krenckel, S. Riepe, M. C. Schubert, and S. W. Glunz, "Towards the efficiency limits of multicrystalline silicon solar cells," *Solar Energy Materials and Solar Cells*, vol. 185, pp. 198–204, oct 2018.

[92] Q. Ren, S. Li, S. Zhu, H. Ren, X. Yao, C. Wei, B. Yan, Y. Zhao, and X. Zhang, "High near-infrared wavelength response planar silicon-heterojunction solar cells," *Solar Energy Materials and Solar Cells*, vol. 185, pp. 124–129, oct 2018.

[93] B. Gerdes, M. Jehle, N. Lass, L. Riegger, A. Spribille, M. Linse, F. Clement, R. Zengerle, and P. Koltay, "Front side metallization of silicon solar cells by direct printing of molten metal," *Solar Energy Materials and Solar Cells*, vol. 180, pp. 83–90, jun 2018.

[94] A. Mwesigye, Z. Huan, and J. P. Meyer, "Thermodynamic optimisation of the performance of a parabolic trough receiver using synthetic oil-Al2O3nanofluid," *Applied Energy*, vol. 156, pp. 398–412, 2015.

[95] D. Malacara-Hernández and D. Malacara-Doblado, "What is a Hartmann test?," *Applied Optics*, vol. 54, no. 9, p. 2296, 2015.

[96] A. Mwesigye, Z. Huan, T. Bello-Ochende, and J. P. Meyer, "Influence of optical errors on the thermal and thermodynamic performance of a solar parabolic trough receiver," *Solar Energy*, vol. 135, pp. 703–718, 2016.

[97] T. Wendelin, "Parabolic Trough VSHOT Optical Characterization in 2005-2006 (Presentation)," p. Size: 32 pp., 2006.

[98] A. Andreas and S. Wilcox, "Observed Atmospheric and Solar Information System (OASIS)," tech. rep., NREL Report No. DA-5500-56494., Tucson, Arizona (Data).

[99] B. Y. Liu and R. C. Jordan, "The long-term average performance of flat-plate solar-energy collectors," *Solar Energy*, vol. 7, no. 2, pp. 53–74, 1963.

[100] J. A. Duffie and W. A. Beckman, *Solar Engineering of Thermal Processes.* Hoboken, NJ, USA: John Wiley & Sons, Inc., apr 2013.

[101] D. R. Myers and C. A. Gueymard, "Description and availability of the SMARTS spectral model for photovoltaic applications," *Organic Photovoltaics V*, vol. 5520, no. November 2004, p. 56, 2005.

APPENDIX A

SUMMARY OF ACHIEVEMENT

Publications

1. **X. Meng**, R. Meier, M. Bertoni, "Insight into Thermal and Mechanical Stresses in Silicon Solar Cells", *IEEE J. Photovolt.*, In Preparation.

2. **X. Meng**, R. Meier, M. Bertoni, "Stress Analysis on Glass/Glass PV Modules with encapsulant and glass variations", *IEEE J. Photovolt.*, In Preparation.

3. **X. Meng**, K. C. Fisher, Z. J. Yu, J. Hyatt, W. Taylor, L. O. Reinhart, M. I. Bertoni, Z. C. Holman, "Outdoor Performance of a Hybrid PV/CSP System: PVMirror", *Prog. Photovolt. Res. Appl.*, To be Submitted.

4. **X. Meng**, K. C. Fisher, L. O. Reinhart, W. Taylor, M. Stuckelberger, Z. C. Holman, M. I. Bertoni, "Optical characterization of curved silicon PV modules with dichroic polymeric film", *Sol. Energy Mater. Sol. Cells*, vol. 201, pp. 110072, 2019.

5. **X. Meng**, R. Meier, M. Stuckelberger, A. Jeffries, S. Bernardini, M. Bertoni, "Bending Stress Analysis of Encapsulated Silicon Solar Cells", *in 2018 7th World Conference on Photovoltaic Energy Conversion (WCPEC-7)*, 2018, In Press.

6. **X. Meng**, M. Stuckelberger, L. Ding, B. West, A. Jeffries, M. Bertoni, "Quantitative Mapping of Deflection and Stress on Encapsulated Silicon Solar Cells", IEEE J. Photovolt., vol. 8, no. 1, pp. 189–195, 2018.

7. **X. Meng**, M. Stuckelberger, P. Hacke, M. Bertoni, "Process Induced Deflection and Stress on Encapsulated Solar Cells", *in 2017 IEEE 44rd Photovoltaic Specialists Conference (PVSC)*, 2017, pp. 2854-2857.

8. **X. Meng**, M. Stuckelberger, L. Ding, B. West, A. Jeffries, M. Bertoni, "Characterization of Encapsulated Solar Cells by X-ray Topography", *in 2016 IEEE 43rd Photovoltaic Specialists Conference (PVSC)*, 2016, pp. 0111-0114.

9. Z. Yu, K. Fisher, **X. Meng**, J. Hyatt, J. Angel, Z. Holman, "GaAs/Silicon PVMirror Tandem Photovoltaic Mini-Module with 29% Efficiency with Respect to the Outdoor Global Irradiance", Prog. Photovolt. Res. Appl., 2019, Accepted.

10. K. Fisher, X. Meng, B. Hartweg, S. Mony, M. Bertoni, Z. Holman, "Novel Foil Interconnects for Back-Contact Silicon Solar Cells", *in 2019 IEEE 46rd Photovoltaic Specialists Conference (PVSC)*, 2019, In Press.

11. M. Stuckelberger, T. Nietzold, G. Hall, B. West, **X. Meng**, J. Werner, B. Niesen, B. Lai, J. Maser, V. Rose, C. Ballif, M. Bertoni, "X-ray Beam Induced Degradation of Perovskite Solar Cells: Low Enough for Synchrotron Experiments", *Proc. MRS*, 2016.

Conference Presentations

1. **X. Meng**, et al., “Direct Imaging of Stress in Crystalline Silicon Modules - Imaging Deflection and Stress in Next Generation PV Modules ”, *2019 PVRW*, Denver (2019).
2. **X. Meng**, et al., “Stress Analysis of Encapsulated Silicon Solar Cells on Soldering, Lamination and Electrical Performance”, *WCPEC-7*, Waikoloa (2018).
3. **X. Meng**, et al., “Process Induced Deflection and Stress on Encapsulated Solar Cells”, *IEEE PVSC*, Washington DC (2017).
4. **X. Meng**, et al., “Monolithic silicon module manufacturing at <0.40 $/W”, *IEEE PVSC*, Washington DC (2017).
5. **X. Meng**, et al., “Revealing the deflection and stress on laminated solar cell: an X-ray topography study”, *9th CSSC Workshop*, Phoenix (2016).
6. **X. Meng**, et al., “Characterization of encapsulated solar cells by x-ray topography - Non destructive 3D deformation analysis”, *IEEE PVSC*, Portland (2016).
7. **X. Meng**, et al., “Deformation and defect analysis of encapsulated silicon solar cells by x-ray topography”, *MRS Spring Meeting & Exhibit*, Phoenix (2016).
8. **X. Meng**, et al., “Characterization of PV Modules: Imaging by X-ray topography”, *25th NREL Silicon Workshop on Crystalline Silicon Solar Cells and Modules*, Denver (2015).

Hornors & Awards

1. **Best student paper award WCPEC-7 2018 Finalist**, Area 5, ”Stress Analysis of Encapsulated Silicon Solar Cells on Soldering, Lamination, and Electrical Performance”
2. **Best student paper award IEEE PVSC 2016 Finalist**, Area 9, ”Characterization of encapsulated solar cells by X-ray topography - Non destructive 3D deformation analysis”
3. **University Graduate Fellowship**, Arizona State University, 2014.

Patent

1. Z. Holman, K. Fisher, **X. Meng**, ”Wavelength-Selective Specularly Reflecting Photovoltaic Module and Manufacture Thereof”, US20180053862A1, 2018, licensed.